Secondary coordination sphere contributions to primary sphere structure, bonding and reactivity

by

Cameron M. Moore

A dissertation submitted in partial fulfillment
of the requirements for the degree of
Doctor of Philosophy
(Chemistry)
in The University of Michigan
2015

Doctoral Committee:

      Assistant Professor Nathaniel K. Szymczak, chair
      Professor Vincent L. Pecoraro
      Professor Stephen W. Ragsdale
      Professor Melanie S. Sanford

Dedication

For my family

Acknowledgments

I would first like to thank Professor Nate Szymczak for mentoring me over the past five years. I feel fortunate to have been one of the first students in his group and help build the lab from the ground up. Nate has given me tremendous amounts of freedom during my graduate career to explore concepts and pursue wild ideas. He has also always had an open door while I've been in the group. I wouldn't be able to count the number of times I've come to his office in a panic and he's been there to help me keep my cool. I've learned how to write, think critically and practice good science from Nate, and for that I am very thankful.

I'd like to thank the members of my dissertation committee, both past and present: Prof. Melanie Sanford, Prof. Steve Ragsdale, Prof. Vince Pecoraro and Prof. Mi Hee Lim. During our meetings, I have very much appreciated your input and advice. I have valued the different perspectives you have all provided during these times and thank you for helping me to understand science in a more broad sense.

I would be remiss if I didn't thank Prof. Bart Bartlett. When I first arrived at Michigan, Bart was kind enough to lend me a hood to work in before our lab space was ready. Bart took me in as part of his lab for the summer and has had a much larger impact on my life and career than he may imagine. He's also been someone who was willing to lend an ear whenever I was in need of advice or had a naïve question.

Some of the chemistry presented in this thesis would not have been possible without valuable discussions from Prof. Nicolai Lehnert and Prof. Pavel Nagorny. I'm sure I've been quite the pest for Nicolai over the past few years with all of my questions, but I thank him very much for

his willingness to offer technical advice on copper chemistry, spectroscopy and computational chemistry. I gratefully thank Prof. Nagorny for some key suggestions in helping to synthesize some of the ligands presented in this thesis; I don't think I would have gotten there if not for his advice.

None of the crystallography would have been possible without the aid of Dr. Jeff Kampf. I've had a blast learning how to solve crystal structures from Jeff and I've accumulated a tremendous amount of knowledge from him over the past five years. Jeff's lab was also a great place to hide now and then when I needed a break and I thank him for being so willing to help me learn (and vent) about crystallography.

The Szymczak lab has been a great place to earn my degree thanks to a fun group of coworkers. I'd like to thank all members of the group, past and present, for always being there for helpful science discussions, advice and fun. I'd also like to thank the Chemistry Department and Rackham Graduate School for funding the first and final years of my graduate studies. I've also been fortunate to have been supported by the National Science Foundation Graduate Research Fellowship Program, and I'd like to thank them for their support.

Of course I'd like to thank my family for all of their love. I'd like to thank my parents, Mike Moore and Coral Holman, for supporting me every step of the way through my education. They have always encouraged me to pursue anything and everything I possibly can and I couldn't ask for more. I'd like to thank my sister Jen for always being available when I could use a phone call, and Kellan for giving me so many smiles over the last few months. Last not but not least, thank you Tanya for every moment of help, encouragement and love you have given me over the past five years. Much of my success has been due to you and I can't wait to see where our next adventure in life takes us.

Table of Contents

List of Figures

xiv

xvi

Abstract

Metalloenzymes are unique in their ability to mediate the transformations of relatively inert substrates with impressive selectivity and speed. Secondary interactions such as hydrogen bonding are broadly appreciated to promote enhanced reactivity in metalloenzymes and are proposed to operate through one of several modes of action; including binding and orienting substrates and stabilizing transition states. In this thesis, transition metal constructs were designed and synthesized to study how secondary coordination sphere perturbations can broadly affect primary sphere structure, bonding and reactivity changes in synthetic systems. Metal complexes supported by a tripodal ligand (*tris*[quinolyl-2-methyl-7-(morpholinomethanone)]amine, TQA') featuring hydrogen bond acceptor amide groups far removed from the metal center provided a unique example of hydrogen bonding with CH groups. Moreover, these hydrogen bonding interactions to the non-traditional acceptor were shown to influence the primary coordination sphere geometry. In separate studies, a proton-responsive tripodal ligand containing pendent hydroxyl groups (*tris*(6-hydroxypyrid-2-ylmethyl)amine, H_3thpa) was shown to alter coordination geometry and stability of copper halide complexes. Electronic perturbation at the metal center was shown to affect the hydrogen bonding manifold in the secondary coordination sphere of copper chloride complexes through combined crystallographic and computational studies. Copper fluoride complexes supported by H_3thpa were investigated and the network of hydrogen bonding interactions presented by the ligand scaffold enabled the isolation of a rare copper(I) fluoride adduct featuring a tripodal ligand. The ability of metal-H_3thpa constructs to deliver proton/electron equivalents to a reducible substrate

was also demonstrated by exposing a nitrite reduction pathway that is reminiscent of the metalloenzyme copper nitrite reductase. In a final set of studies, transition metal complexes supported by a pincer ligand framework containing tautomerizable hydroxyl groups (6,6'-dihydroxy terpyridine, dhtp) were investigated for catalytic heterolysis reactivity. Ruthenium complexes were studied in detail for catalytic ketone transfer hydrogenation. The role of the pendent hydroxyl groups during catalysis was elucidated and a catalytic cycle is proposed in which alkali metal cations engage substrate to achieve reduction. Together, the studies presented in this thesis demonstrate how secondary coordination sphere interactions can be used to stabilize otherwise reactive products and/or transition states, in analogy to metalloenzymes.

Chapter 1 Introduction

Portions of this chapter have been published:

Moore, C. M.; Dahl, E. W.; Szymczak, N. K. *Curr. Opin. Chem. Biol.*, **2015**, *25*, 9. Reprinted with permission; copyright 2015 Elsevier.

Moore, C. M.; Szymczak, N. K. "Appended Functionality in Pincer Ligands" in *Pincer and Pincer-Type Complexes: Applications in Organic Synthesis and Catalysis*, Szabó, K. J.; Wendt, O. F. (eds.), Wiley-VCH: Weinheim, Germany, 2014, pp 117-147. Reprinted with permission; copyright 2014 John Wiley and Sons.

1.1 [Fe]-hydrogenase and synthetic 2-hydroxypyridine catalysis

Metal-ligand cooperativity is often targeted as a synthetic strategy to (a) store H^+ equivalents in the ligand periphery and/or (b) couple the protonation/deprotonation events to modulate structural and electronic properties of the complex. Biology regularly exploits these principles to mediate multiple H^+ and/or e^- transfer reactions, often simultaneously (i.e. proton-coupled electron transfers). Hydrogenases, in particular, are a class of metalloenzymes that catalyze either the reversible oxidation of H_2 ([NiFe]- or [FeFe]-hydrogenase) or the heterolysis of H_2 ([Fe]-hydrogenase).[1] Key to their biochemical functions, hydrogenases utilize networks of amino

acids to accomplish H^+/e^- transfer reactions and/or evolutionarily designed ligand platforms to achieve facile H_2 heterolysis.

While unknown to biological hydrogenases, oxidative catalysis similarly requires the management of H^+/e^- inventories: a prime example being the oxidation of H_2O to yield 0.5 O_2, 2 H^+ and 2 e^-. Together, the efficient interconversion of H_2O, O_2, H^+ and e^- provides a foundation for a carbon-neutral energy scheme.[2] The design elements that biological systems have evolved to exploit are, therefore, of paramount interest to the synthetic chemistry community for catalyst development. In this review, we highlight [Fe]-hydrogenase; a metalloenzyme featuring a curious iron cofactor containing a 2-hydroxypyridine motif. We briefly describe aspects of its metallo-biochemistry that illustrate the utility of its unique primary and secondary coordination sphere environment. Noteworthy recent achievements in the field of homogeneous catalysis featuring 2-hydroxypyridine motifs are outlined. We detail the role of the 2-hydroxypyridine ligands for the management of H^+/e^- equivalents during reductive and oxidative catalysis, as well as the application of these catalysts in energy storage schemes.

[Fe]-hydrogenase is found in methanogenic archaea grown under nickel-limited conditions and functions within the metabolic pathway of CO_2 methanogenesis by making and breaking the H–H bond as a means to generate reducing equivalents (H^-) from H_2.[1] Unlike the other two hydrogenases ([FeFe] and [NiFe]), which catalyze the interconversion of H^+/e^- and H_2, [Fe]-hydrogenase catalyzes the reversible heterolytic cleavage of H_2 into H^+/H^- in the presence of methenyltetrahydromethanopterin (MPT^+), which acts as a H^- acceptor (Fig. 1-1).[1] The catalytically-active iron center in [Fe]-hydrogenase is contained within an unusual iron guanylyl-pyridinol cofactor (FeGP cofactor). The enzyme has been crystallographically characterized by Shima and co-workers from *Methanocaldococcus jannashii* and later, at a higher resolution from

2

a mutant protein (Fig. 1-1).[3,4] Combined, these studies revealed an octahedral iron center ligated by a cysteine, two carbon monoxide (CO) ligands, the guanylyl-pyridinol moiety and an unknown sixth ligand (most likely solvent water). Of note, the pyridinol unit coordinates to iron as a bidentate ligand through an appended acyl linkage as well as through the pyridinol nitrogen (Fig. 1-1).[4] The water coordination site, *trans* to the iron-acyl ligand (L in Fig. 1-1), serves as the site of H_2 oordination during catalysis, *vide infra*.
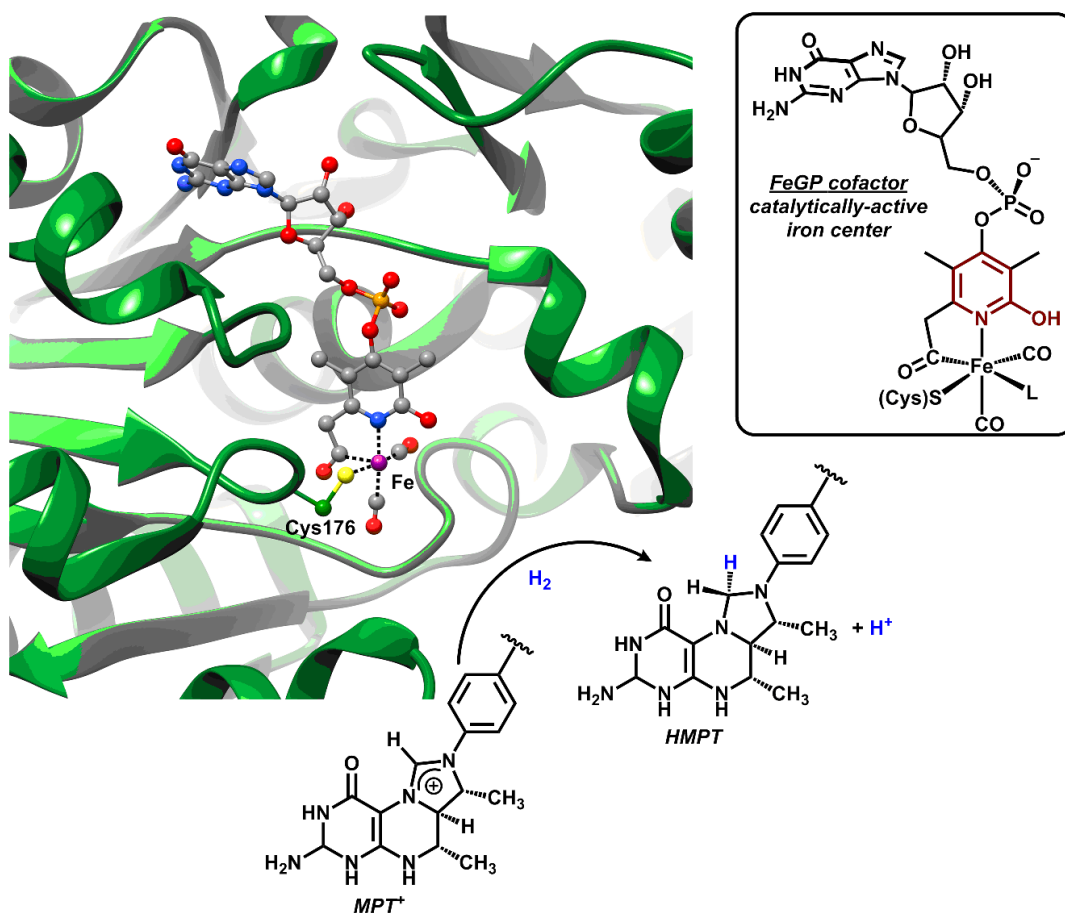
Figure 1-1: Active site of [Fe]-hydrogenase from Methanocaldococcus jannashii and the reduction of methenyltetrahydromethanopterin.

Inhibition studies by Shima and co-workers on [Fe]-hydrogenase unequivocally demonstrated the site of H_2 binding is *trans* to the pyridinol acyl group. The O-atom of the pyridinol is presumed to act as a base during the H_2 heterolysis step. Evidence of O-atom

3

nucleophilicity and interaction with Fe-coordinated substrates was obtained following the isolation of the isocyanide-bound [Fe]-hydrogenase from *Methanothermobacter marburgensis* and *Methanocaldococcus jannashii,* which revealed a covalent bond between the pyridinol oxygen and the iron-bound carbon of the isocyanide.[5]
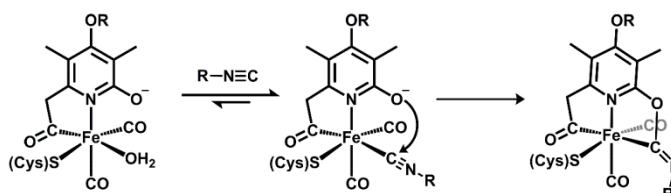
Figure 1-2:Mode of isocyanide inhibition in [Fe]-hydrogenase.

This bond is the direct result of nucleophilic attack of the pyridinol oxygen on the coordinated isocyanide (Fig. 1-2). These crystallographic results are consistent with inhibition studies by Shima and Ataka that determined a high affinity of isocyanides for [Fe]-hydrogenase (K_i ~ nanomolar) under catalytic conditions.[6] It is important to note that isocyanides do not inhibit [NiFe]- or [FeFe]-hydrogenases under the conditions tested, suggesting that the mode of isocyanide inhibition for [Fe]-hydrogenase is unique among the three metalloenzymes and further consistent with an active role of the pyridinoate group during substrate binding/activation.
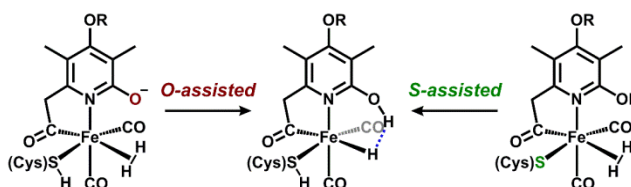
Figure 1-3: DFT-calculated H_2 heterolysis pathways using models of the FeGP cofactor.

Computational investigations into the mechanism of H_2 splitting and H^- delivery to MPT^+ have helped to further clarify the role of the pyridinol ligand at the active site. A resting state model of [Fe]-hydrogenase that features a strong $Fe-H\cdots H-O$ dihydrogen bond was calculated

4

by density functional theory (DFT) methods.[7] Two competing pathways for H_2 heterolysis were calculated: heterolysis involving H_2 deprotonation by (a) coordinated cysteine sulfur and (b) the pyridinoate oxygen (Fig. 1-3). The barriers for H_2 heterolysis involving the pyridinoate oxygen and cysteine sulfur were both found to be minimal (3.3 and 6.6 kcal/mol, respectively). From this study, the role of the unique pyridinol ligand on iron was proposed to be twofold: to facilitate the (1) H_2 heterolysis and (2) stabilization of the Fe−H through the formation of a dihydrogen bond.
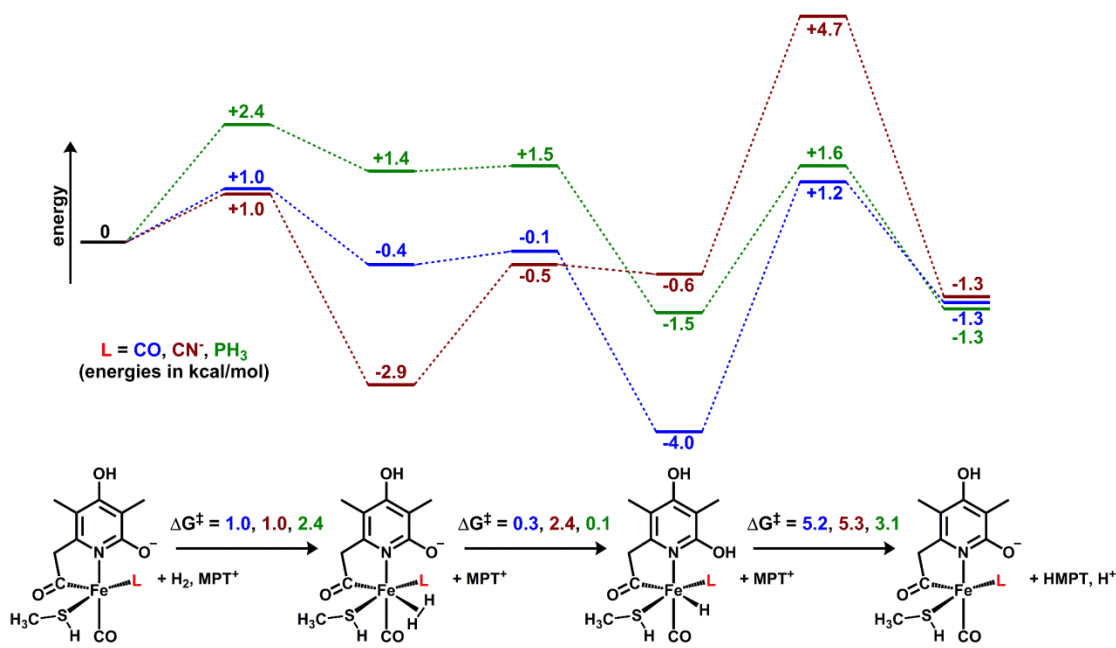
Figure 1-4: DFT-calculated energy profiles of H_2 splitting and transfer by model FeGP variants.

More recent DFT studies have shown that by including dispersion interactions between the FeGP active site and MPT[+], the barrier to H[-] transfer is less endergonic and the overall energy profile for the catalytic cycle is quite flat.[8] In contrast to previous DFT results, H_2 heterolysis *via* deprotonation by the pyridinoate oxygen was found to be kinetically favored. An especially intriguing finding of these studies is that the modification of ligands at iron can actually inverse the energetics of elementary reaction steps along the catalytic cycle. Reiher and co-workers

5

computationally substituted CO for cyanide (CN$^-$) and phosphine (PH$_3$) and examined the effect on the kinetic model of the catalytic cycle (Fig. 1-4). Overall, the energy profile for H$_2$ heterolysis and H$^-$ delivery for the phosphine variant is considerably flatter than the CO and (especially) cyanide variants. The presence of cyanide provides a highly stabilized Fe-(H$_2$) adduct (when compared to the other variants) and leads to a larger barrier for heterolysis and greater destabilization of the Fe-H product. For the synthetic chemist, the computational results from Reiher and co-workers provide an impetus for the systematic design of catalysts based on the 2-hydroxypyridine motif because the interconversion between H$^+$/H$^-$ and H$_2$ can be tuned based on the ancillary ligands at the metal center.

1.1.1 Reductive chemistry promoted by 2-hydroxypyridine catalysts

Germane to the aforementioned chemistry of [Fe]-hydrogenase, transition metal-catalyzed hydrogenation reactions are highly governed by the stability and reactivity of M-(H$_2$) and M-H intermediates. Given the strong H–H bond enthalpy of H$_2$ (104 kcal/mol), rapid formation of M-H species from H$_2$ is often a rate-limiting step for hydrogenation catalysis. Following the identification of a 2-hydroxypyridine motif within [Fe]-hydrogenase, transition metal complexes supported by similar ligand constructs have been targeted, especially for reactivity with H$_2$.
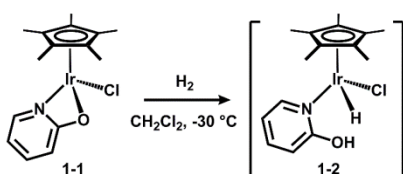
Figure 1-5: Spectroscopically observed H$_2$ heterolysis by an iridium-pyridinoate at low temperature.

Rauchfuss and co-workers demonstrated that the iridium complex Cp*Ir(κ^2-2-pyridinoate)Cl (**1-1**, Cp* = Me$_5$C$_5$) readily reacts with H$_2$ at -30 °C to form the iridium hydride species Cp*IrH(2-

hydroxypyridine)Cl (**1-2**, Fig. 1-5).[9] Complex **2** is transiently observable by NMR spectroscopy but is unstable with respect to dissociation of the 2-hydroxypyridine ligand.

To impart greater stability to M-H species featuring 2-hydroxypyridine motifs, and subsequently broaden their application in catalysis, multidentate versions of this ligand have been designed and implemented. Bidentate ligand scaffolds, in particular, are more faithful to the mode of coordination of the pyridinol ligand in [Fe]-hydrogenase. Iridium complexes supported by multidentate 2-hydroxypyridine ligands have been studied extensively for the hydrogenation of CO_2 in aqueous and non-aqueous media. The premier example of a 2-hydroxypyridine-derived system for CO_2 hydrogenation is the bimetallic tetrahydroxybipyrimidine-iridium complex **1-3**, which catalyzes the hydrogenation of CO_2 to formate (HCO_2^-) under mild conditions.[10] The impressive reactivity of **1-3** was attributed to (1) the ability of the 2-pyridinoate complex **1-4** to lower the barrier to H_2 heterolysis under basic conditions and (2) the strong π-donating ability of the deprotonated ligand framework (Fig. 1-6).
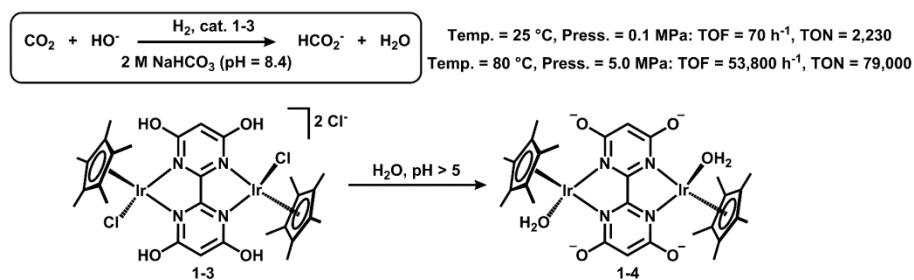
Figure 1-6: Hydrogenation of CO_2 catalyzed by bimetallic 2-hydroxypyridine-derived iridium complexes and proposed structure of the active species at high pH.

In order to investigate the mechanistic details of CO_2 hydrogenation catalyzed by iridium 2-hydroxypyridine-derived complexes, Himeda, Fujita and co-workers synthesized monometallic complexes **1-5** to **1-7**.[11] They found that, under basic conditions, **1-5** (featuring the 6,6'-

dihydroxybipyridine ligand; dhbp) far outperformed **1-6** and **1-7** (Fig. 1-7), and kinetic isotope effect (KIE) studies were used to gain a mechanistic understanding of these results.[12]
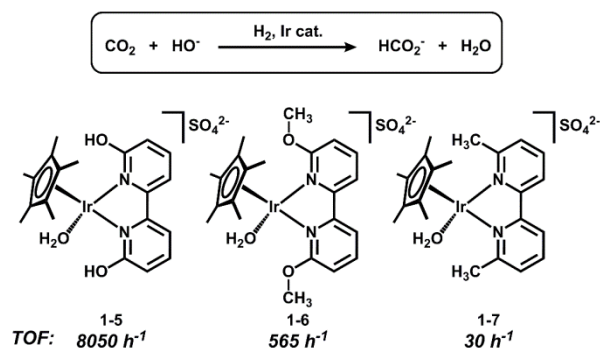
Figure 1-7: Monometallic CO_2 hydrogenation catalysts supported by bipyridine ligands.
The KIE was dependent on the origin of the deuterium (D_2 or D_2O) label. When the hydrogenation of CO_2 was performed with D_2 gas in basic H_2O, a KIE of 1.07 was found. However, when the hydrogenation was performed using H_2 in basic D_2O, a KIE of 1.14 was measured. The disparity between the two measured KIE's suggests that water plays a critical role in the rate-determining step of catalysis.
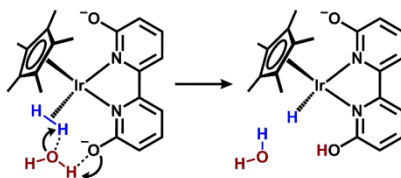
Figure 1-8: Role of solvent H_2O during rate-limiting H_2 heterolysis calculated by DFT.
Computational investigations into the mechanism of CO_2 hydrogenation have shown that solvent (H_2O) plays a critical role in these systems.[12,13] One of the roles of the dhbp ligand is to lower the barrier to rate-limiting H_2 heterolysis by forming a water 'bridge' between coordinated H_2 and the pendent 2-pyridinoate *via* hydrogen bonding (Fig. 1-8). This Grotthuss-type H^+ shuttling is consistent with the observed KIEs measured for **1-5**. Moreover, these findings

8

rationalize the significant entropic contributions to the H_2 heterolysis barrier for complex **1-5** determined by Himeda, Fujita and co-workers.[11]

   2-Hydroxypyridine-derived complexes are also useful transfer hydrogenation catalysts, which use 2-propanol or formate as H_2 surrogates (Fig. 1-9). Kelson and Phengsy found that the ruthenium-terpyridine complex **1-8** featuring two monodentate 2-pyridone ligands is an efficient ketone transfer hydrogenation catalyst under basic conditions with an initial turnover frequency (TOF) of 780 h^{-1} for acetophenone reduction.[14] Transfer hydrogenation catalyzed by **1-8** is also selective for ketones in the presence of alkene substrates. Papish and co-workers studied ruthenium-arene complexes, such as **1-9**, supported by the bidentate dhbp ligand as catalysts for transfer hydrogenation under basic conditions in aqueous and non-aqueous media.[15] Complex **1-9** is a competent transfer hydrogenation catalyst in basic, aqueous media at 90 °C with a TOF for acetophenone reduction of 16 h^{-1}. In basic, non-aqueous media (2-propanol) at 85 °C, catalysis is more sluggish, with a TOF for acetophenone reduction of 7 h^{-1}. Although mechanistic studies have not been conducted, the geometry and distance of the pyridinoate groups of **1-9** with respect to the metal center may require a water bridge (*vide supra*) to achieve H^+ transfer during catalysis would account for the observed enhanced catalytic activity of these complexes in aqueous media.
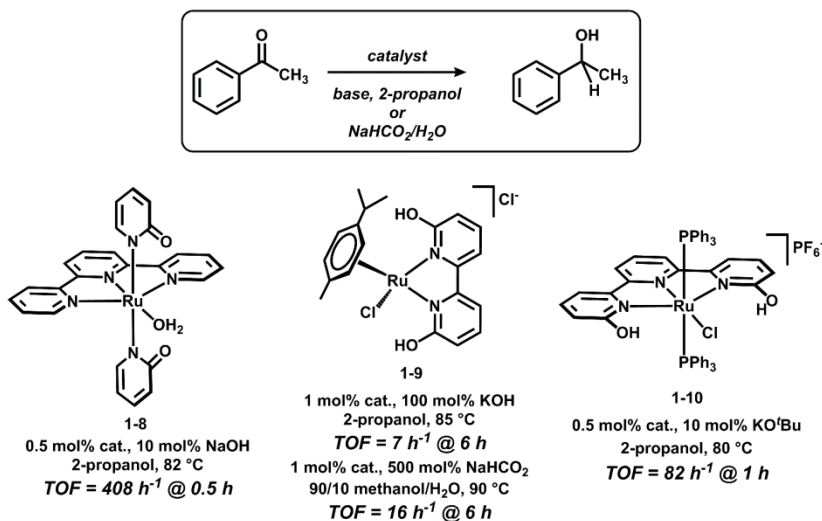
Figure 1-9: Ruthenium transfer hydrogenation catalysts featuring 2-hydroxypyridine-derived ligands.

To avoid the need for exogenous species (*i.e.* H_2O or ROH) to aid in H^+ transfer, and thus minimize the reorganization energy and entropy associated with H_2 splitting (*ca.* -9 kcal/mol for **1-5**) and transfer,[11] our group is developing transition metal complexes supported by rigid tridentate pincer frameworks that incorporate the 2-hydroxypyridine motif, such as 6,6'-dihydroxyterpyridine (dhtp). The confinement of the 2-hydroxypyridine motif within a pincer framework should ideally place the pyridinoate group in close proximity to the metal's active site to maintain an orientation more faithful to that of [Fe]-hydrogenase. Initially, we studied a ruthenium-dhtp complex (**1-10**) as a catalyst for the transfer hydrogenation of ketones (Fig. 1-9).[16] Under basic conditions, **1-10** is active for the reduction of a variety of ketone substrates, including aliphatic ketones, with TOF's ~100 h^{-1} at 80 °C. Complex **1-10** is also selective for polar bond reduction in the presence of alkene functional groups. It is important to note that these three systems (**1-8** to **1-10**) have been examined under slightly varying conditions and their rates for the reduction of acetophenone may reflect these subtle differences. However, a systematic study of the mechanisms of reduction by these catalysts is needed to fully elucidate

the effects of denticity, geometry of the 2-hydroxypyridine group (with respect to the open site of coordination) and metal electronics on the activity of the catalysts. These studies will aid in the design of future catalysts based on 2-hydroxypyridine for hydrogenation and/or splitting of H_2.

1.1.2 Oxidative chemistry promoted by 2-hydroxypyridine catalysts

The lowered kinetic barrier to reversible H_2 heterolysis by [Fe]-hydrogenase suggests that synthetic catalysts incorporating the 2-hydroxypyridine motif should likewise catalyze both reductive and oxidative transformations. The transfer hydrogenation catalysis described above has been extended to the dehydrogenative oxidation of many alcohols. A series of Cp*Ir complexes bearing 2-hydroxypyridine-derived ligands were found to catalyze the dehydrogenation of primary and secondary alcohols and the dehydrogenative lactonization of diols (Fig. 1-10).[9,17-22]
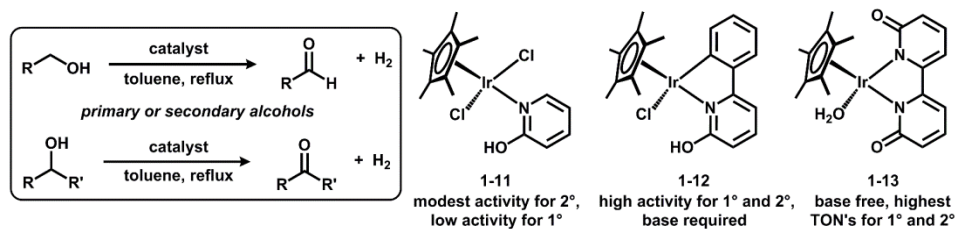
Figure 1-10: Dehydrogenative alcohol oxidation catalyzed by various 2-hydroxypyridine-derived iridium complexes.

Complex **1-11** containing monodentate 2-hydroxypyridine exhibits only modest activity for the dehydrogenation of secondary alcohols, and poor activity for primary alcohols. These low catalytic efficiencies, however, can be accelerated with bidentate variants, which parallels the bidentate 2-hydroxypyridine unit within the [Fe]-hydrogenase active site. For instance, by using complex **1-12**, efficient catalysis in the presence of added base was noted for primary and secondary alcohols. Alternatively, high catalytic efficiency and reaction scope was realized with

the fully deprotonated complex **1-13** for the oxidation of primary (TON ~ 47,500) and secondary alcohols (TON ~ 275,000) (Fig. 1-10).[21]

A comprehensive DFT study of the possible pathways for the acceptorless alcohol dehydrogenation reaction catalyzed by complex **1-13** revealed an outer-sphere mechanism where H^+ and H^- are transferred without substrate coordination and that formation of an Ir-(H$_2$) complex is rate-limiting.[23] Enhanced reactivity observed for complexes with dipyridinoate ligands are due to (1) an increased stabilization of an Ir-H intermediate by a protonated 2-hydroxypyridine (2) the electronic flexibility of the ligand backbone as a function of protonation state to allow for variable metal-ligand covalency as needed during catalysis and (3) the ability to form an alcohol 'bridge' to facilitate H–H bond formation through a H^+-shuttling mechanism (Fig. 1-11).
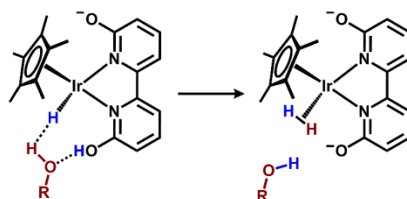
Figure 1-11: Role of alcohol during rate-limiting H−H bond formation calculated by DFT.
This latter Grotthuss-type mechanism is reminiscent of the role of H$_2$O during hydrogenation catalyzed by dhbp complexes (*vide supra*). These computational findings led the authors to use theory to guide the design of a highly active second-generation catalyst based on ruthenium. Their redesigned catalyst uses ruthenium as a cheaper and more abundant metal compared to iridium, and is structurally similar to catalysts that were previously reported by Papish and co-workers for transfer hydrogenation.[15]

1.1.3 H$_2$ storage schemes enabled by 2-hydroxypyridine catalysts

[Fe]-hydrogenases function, within a larger metabolic pathway, by making and breaking the H–H bond as a means to store and release energy. Acting in concert with F_{420}-dependent methylenetetrahydromethanopterin dehydrogenase, [Fe]-hydrogenase catalyzes the reduction of HMPT, *en route* to the reduction of coenzyme F_{420}, an energy carrier structurally reminiscent of a flavin, but functionally similar to NADP (nicotinamide adenine dinucleotide phosphate).[24] Coenzyme F_{420} is used as a reductant by methanogens in two of the steps along the methanogenesis pathway from CO_2 and thus serves as a biological H_2-storage system.

The interconversion of HMPT to MPT^+ by [Fe]-hydrogenase is approximately thermoneutral (ΔG = 1.3 kcal/mol),[24] and likewise, energy storage that relies on reversible hydrogenation for large-scale applications similarly requires highly reversible, thermoneutral reactions that also feature high H_2 storage capacities. For humans, the inability to safely store and transport meaningful quantities of H_2 has been a major hurdle toward realizing a hydrogen economy. A promising method for the storage of H_2 is in the form of chemical bonds to an organic H_2-carrier, where the storage (hydrogenation) and release (dehydrogenation) of H_2 is reversible.[25] The high activity of 2-hydroxypyridine-derived catalysts for hydrogenation and dehydrogenation implies that they should serve as effective mediators of reversible H_2 storage schemes. A reversible hydrogen storage system based on alcohols was developed by Fujita, Yamaguchi and Kawahara by expanding the acceptorless alcohol dehydrogenation reactivity of complex **1-13** (Fig. 1-12).[21] The system, simply composed of complex **1-13** in neat isopropanol, operates at mild temperature to quantitatively generate acetone. Upon addition of H_2, acetone is hydrogenated to isopropanol by the same catalyst in near quantitative yields, completing the H_2 storage scheme. The system could be cycled at least 8 times without any observed catalyst decomposition.
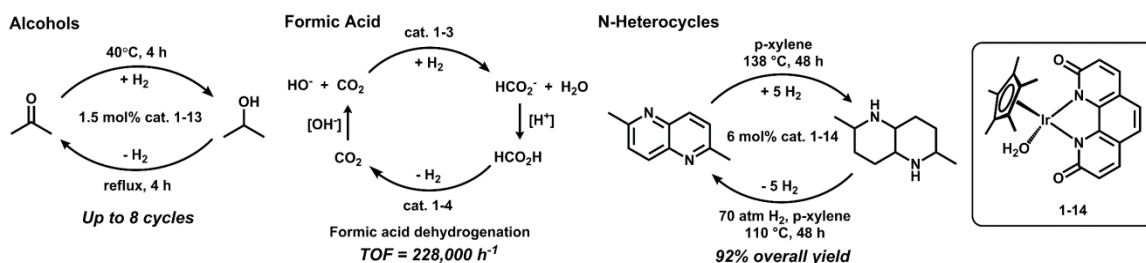
Figure 1-12: Reversible H$_2$ storage schemes mediated by iridium 2-hydroxypyridine catalysts.

In addition to alcohols, catalysts that reversibly interconvert CO$_2$ into formic acid are desirable for hydrogen storage applications as well as for CO$_2$ mitigation. The iridium CO$_2$ hydrogenation catalyst **1-3** described previously was also shown to function reversibly, which allowed for a reversible H$_2$ storage system based on formic acid (Fig. 3C).[10] Although these catalysts are highly robust for alcohol and formic acid dehydrogenation/rehydrogenation, the low H$_2$ gravimetric densities (<5 wt%) present a substantial limitation to their implementation as reversible H$_2$ carriers.

Hydrogen storage using N-heterocycles has grown in popularity due to their higher theoretical gravimetric densities and thermodynamic feasibility.[26] Recently, Fujita, Yamaguchi and coworkers showed reversible H$_2$ storage with N-heterocyclic compounds using complex **16** (Fig. 1-12).[27] The complete dehydrogenation/rehydrogenation of 2,6-dimethyl-1,5-naphthyridine (**1-14**) to **1-15** was performed in 92% yield under forcing conditions (130 °C, 70 atm H$_2$ for hydrogenation) with five equivalents of H$_2$ stored in the N-heterocycle and a gravimetric density of 6.6 wt.% H$_2$. 2-hydroxypyridine-based catalysts have thus demonstrated high activity in reversible H$_2$ storage systems due to their unique ability to lower kinetic barriers for H$_2$ delivery during hydrogenation and H$_2$ release during dehydrogenation. As the development of new compounds for H$_2$ storage continues to grow, the ease with which catalysts incorporating the 2-

hydroxypyridine motif manipulate H_2 makes them obvious contenders for future work in the field.

1.1.4 Water oxidation promoted by 2-hydroxypyridine catalysts

The efficient management and delivery of H^+ and e^- equivalents is a hallmark of [Fe]-hydrogenase and related synthetic systems containing the 2-hydroxypyridine motif. In extension to the reactions with H_2, analogous transformations of energy-relevant molecules related by H^+/e^- interconversions are also attractive targets for 2-hydroxypyridine-derived catalysis. The oxidation of water to O_2 comprises the half reaction of a water-splitting scheme that generates H^+ and e^- equivalents (or H_2) for use in alternative energy applications.[2] This energy-intensive reaction can be facilitated by an appropriate ligand environment around a metal that promotes H^+ and/or e^- transfer reactions to minimize energetic barriers. Indeed, some 2-hydroxypyridine-derived complexes display promising activity for catalytic water oxidation and exhibit significant improvements in activity when compared to systems containing unfunctionalized ligand variants. A series of Cp*Ir complexes bearing the 2-hydroxypyridine-derived dhbp scaffold have shown good efficacy for water oxidation when the oxidizing potential was delivered through a chemical oxidant (Fig. 1-13).[28-30]
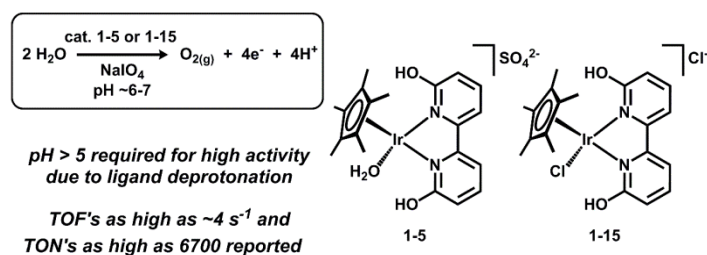
Figure 1-13: Chemical water oxidation catalysts supported by dhbp.

The activity for complexes **1-5** and **1-17** was highly pH-dependent and the highest activity was found for pH values greater than their pK_a of ~5. This effect was rationalized by considering

15

changes to the ligand's electronic environment upon deprotonation, which affords a strongly π-donating dipyridonate ligand that stabilizes a high-valent Ir(V)-oxo intermediate required for the key O-O bond-forming step. Consistent with this mechanism, water oxidation experiments with *para*-substituted dhbp also showed significant rate enhancement compared to the unfunctionalized bipy framework. Therefore, water oxidation with Cp*Ir-dhbp complexes is unique within our discussion of [Fe]-hydrogenase-inspired catalysis in that it relies more heavily on the electronic flexibility of the ligand rather than any direct interactions with substrate. Recently, water oxidation catalysis with dhbp and similar variants was extended to ruthenium complexes but no activity was observed in hydroxypyridine-containing scaffolds.[31] We note that 2- hydroxypyridine ligands do not always enhance catalytic activity and, although the 2-hydroxypyridine units are highly promising for catalysis involving proton-transfer events, further structure/function studies are required for each system or reaction.

In addition to chemical oxidation, electrochemical water oxidation is attractive because the operating potential can be selected to minimize the overpotential (applied potential in excess of the thermodynamically-limiting value) and hence, the energy input. This is in contrast to many examples of chemical water oxidation, where a fixed potential is used due to reagent constraints (e.g. $Ce(NH_4)_2(NO_3)_6$, IO_4^-) that is much greater than that required for catalysis. 2-hydroxypyridine-based metal complexes are well suited to achieve low-barrier (and low overpotential) water oxidation catalysis because the intimate metal-ligand cooperation allows for facile proton-coupled electron transfer (PCET) events. This concept was demonstrated by comparing copper complexes containing the bipy ligand (**1-18**) to an analogous dhbp complex (**1-19**, Fig. 1-14).
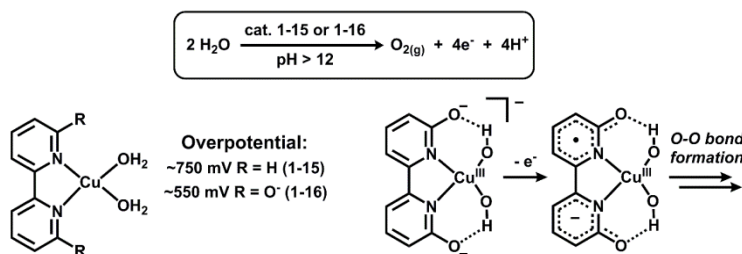
Figure 1-14: Electrochemical water oxidation catalyzed by copper dhbp and role of ligand in lowering overpotential, as calculated by DFT.

The latter catalyst, **1-19**, exhibited a diminution in the overpotential for water oxidation by ~200mV.[32,33] DFT calculations support a mechanism by which the pyridinoate groups promote two steps: (1) they assist in the removal of protons from a Cu bound H_2O through PCET events and (2) they allow the second oxidation of the system to occur at the ligand, which lowers the required potential for water oxidation (Fig. 1-14). The innate ability of 2-hydroxypyridine scaffolds to store both protons *and* electrons allows for reaction types that are far outside the realm of [Fe]-hydrogenase and should be considered as a model for future oxidation catalysis.

1.1.5 Outlook for 2-hydroxypyridine catalysis

The secondary coordination environment around a mononuclear iron site at the FeGP cofactor in [Fe]-hydrogenase plays an integral role in efficient H_2 heterolysis and delivery. To emulate the metal-ligand cooperativity found within the enzyme, synthetic chemists have targeted key design elements to generate highly active organometallic complexes. Catalysts incorporating the 2-hydroxypyridine motif use the pendent pyridinoate groups to aid in H^+ and e^- transfer steps for catalytic hydrogenation, dehydrogenation and water oxidation. Barriers to H^+ transfer can be minimized with an appropriate orientation of the pyridinoate groups to circumvent Grotthuss-type H^+ transfer mechanisms, and thus, lower the entropic contributions to rate-determining steps in catalytic cycles. The principles described for

17

hydrogenation/dehydrogenation will likely be adapted for hydrofunctionalization catalysis, or alternatively, many other reaction types that feature acidic/basic partners, as they may be cooperatively activated/transferred by 2-hydroxypyridine type units. Future frontiers in 2-hydroxypyridine-derived catalysis will involve the development of catalysts featuring earth-abundant metals,[34] structurally-faithful model complexes that exhibit catalytic reactivity of the native enzyme,[35] and the expansion of 2-hydroxypyridine ligands into other catalytic reactions.[36]

1.2 Appended functionality in synthetic pincer systems

Pincer-based metal complexes are capable of promoting remarkable reactivity toward small molecule substrates. To engage further substrate activation pathways, multifunctionality can be introduced within the secondary coordination sphere environment of a pincer-derived ligand. Secondary interactions are ubiquitous in biological systems and are responsible for promoting enhanced reactivity in many metalloenzymes, where a combination of hydrogen-bonding, steric and electrostatic interactions are used synergistically to augment reactivity profiles.[37,38] To emulate these principles, a growing number of synthetic complexes have targeted multifunctional ligand ensembles to directly probe how changes within a molecule's secondary coordination sphere can be used to influence and further modulate subsequent reactivity.[39] In addition to enhanced substrate activation, secondary coordination sphere interactions in synthetic systems have been utilized for the ground-state stabilization of otherwise unstable or reactive intermediates; the combination of both of these strategies can be exploited for small molecule transformations.[40] Examples of these principles have been detailed in the preceeding section for 2-hydroxypyridine-derived ligands. The proceeding discussion, therefore, will be concerned with a handful of examples of multifunctional ligand ensembles based on tridentate pincer scaffolds.

1.2.1 Design criteria

The title of this section merits the question; what defines *functionality*? For the purposes of the proceeding discussion a limited definition of *functionality* has been adopted as follows: a group, or groups, of polarizable units with an orientation suitable for cooperative substrate-directed interactions. In most cases, directed interactions should be considered to be toward a metal-bound substrate, however in some instances (i.e. supramolecular self-assemblies and sensors) metal-ions may be absent from this discussion.

Pincer ligand frameworks are ideally suited for "decoration" since these often rigid and redox-robust scaffolds preclude unproductive interaction of appended polar functional groups with the transition-metal center. Two limiting distinctions regarding the position of functionality relative to the plane defined by the donor atoms of the pincer framework can be made; functionality co-planar to the pincer chelate (Fig. 1-15a) and functionality not co-planar to the pincer chelate (Fig. 1-15b). In some cases these distinctions may become less straightforward, especially in the case of trigonal-bipyramidal coordination geometry, and these aspects will be treated in more detail where necessary.
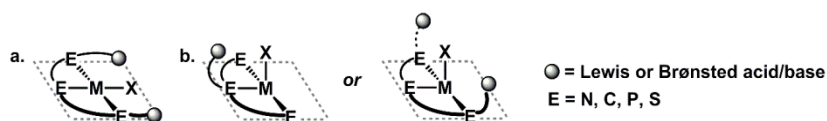
Figure 1-15: Representation of functionality coplanar (a) and not coplanar (b) to the pincer chelate.

1.2.2 Motivations

In contrast to unmodified pincer ligands, comparatively few examples of pincer ligand frameworks appended with polar functionality have been reported. The overarching goals

associated with such modifications are diverse and span the fields of catalysis, supramolecular assembly, and molecular recognition.

Metal complexes featuring directed secondary coordination sphere interactions are highly topical for complexes containing bidentate,[41] tripodal,[40] or phosphine ligands,[42] which can cooperatively promote a variety of catalytic transformations and/or stabilize highly reactive intermediate species. In contrast, limited examples of catalysis involving pincer-ligated adducts that contain appended functionality have been reported. One of the premier examples of cooperative catalysis that utilizes a pincer-derived framework for substrate-directed oxidation is the dimanganese complex **1** reported by Crabtree and Brudvig (Fig. 1-16).[43] The design strategy of **1-16** features an oxidatively-stable terpyridine ligand appended with a remote molecular recognition site (Kemp's triacid fragment) capable of binding a substrate such as ibuprofen, through hydrogen-bonding interactions; thus directing selective C-H oxygenation.
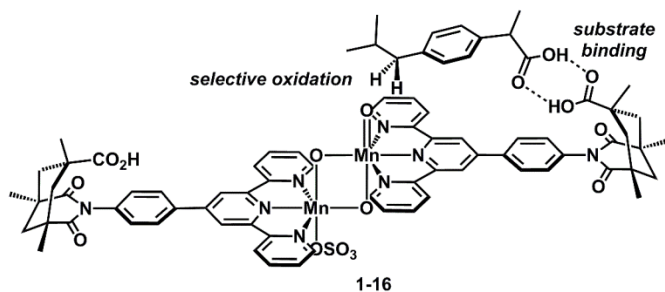
Figure 1-16: Selective C-H oxidation by a Mn-terpy complex featuring a remote molecular recognition site.

Oxygenation of ibuprofen using **1-16** as a catalyst and peroxomonosulfate as an oxidant provided >98% regioselectivity at the remote benzylic carbon with up to 700 turnovers. The substrate recognition is achieved through two hydrogen bonds between carboxylic acids of substrate and catalyst (Fig. 1-16), which is preserved throughout the C-H oxidation reaction.[44] In support of a cooperative binding event that precedes substrate oxidation, the addition of

exogenous carboxylic acids competitively inhibits the regioselectivity of ibuprofen oxygenation.[45] Furthermore, when the pendent carboxylic acid groups are removed from the terpyridine scaffold, the regioselectivity for oxygenation is diminished. This example highlights the potential to use secondary interactions to direct reactivity.
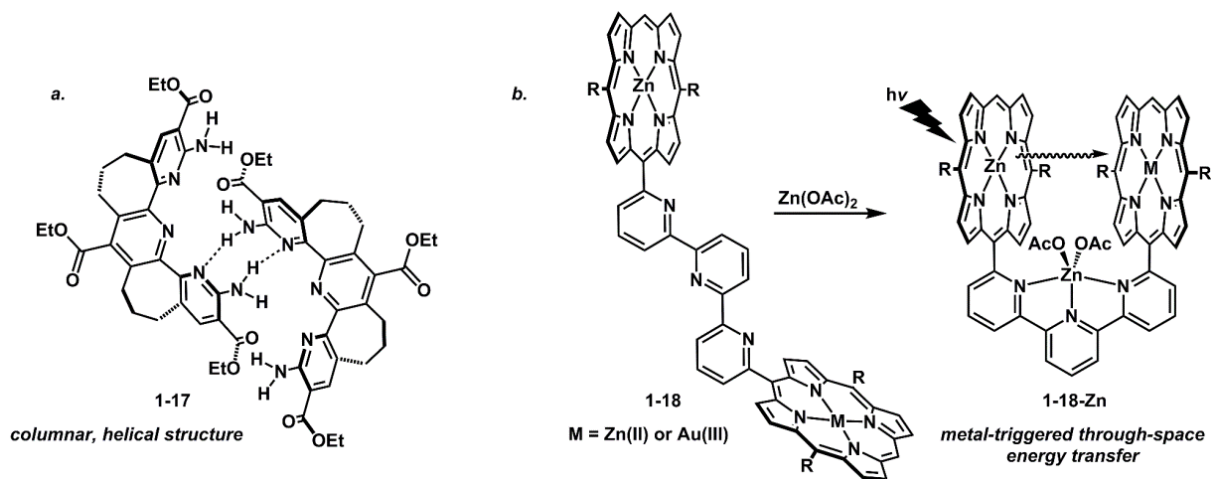
Figure 1-17: Self-complementary hydrogen bonding to yield a helical structure (a) and "butterfly-type" motion of a terpy complex to achieve through space energy transfer (b).

Several elegant examples of appended pincer frameworks can be found in the field of supramolecular chemistry, where tridentate ligands have been used to design functional three-dimensional architectures, both in the presence and absence of metal ions.[46,47] The ability to predict structural conformations *a priori* remains a key challenge within this field.[48] One strategy to overcome the apparent lack of predictability of self-assembly is to utilize non-covalent interactions to "guide" assembly into a predicted structure. For example, complimentary hydrogen-bonding interactions between two molecules of a highly decorated terpyridine-derived framework generate **1-17**, a columnar, helical scaffold in the solid-state (Fig. 1-17a). The appended NH_2 functionality engages in intermolecular hydrogen bonding interactions with the pyridine groups of another molecule, and the fixed orientation of the three pyridine rings within each ligand serves to propagate a helical structure. Further utility of this system may be limited

21

by its synthesis (8 steps, 5 % overall yield).[49] Complex architectures featuring pincer-type compounds have also been utilized as dynamic chemical devices which can respond to external stimuli, reminiscent of biological systems which undergo molecular-level changes to induce reactive states.[50,51] Lehn and co-workers have designed a sophisticated porphyrin-functionalized terpyridine-based ligand to study metalation-triggered geometry changes (**3**, Fig. 1-17b).[46] In addition to conformation modulation mediated by ligand binding events, efficient through-space energy transfer between the two porphyrin substituents was achieved when a metal-ion was coordinated to the terpyridine chelate (**1-18-Zn**). The coordination of a metal ion at the terpyridine induces a change in geometry and orients the two porpyhrin groups within close proximity to one another (Fig. 1-17b).

The highly complex systems presented by supramolecular architectures demonstrate the ability to control individual components within a larger molecular ensemble. The functions of these supramolecular motifs often mirror the functions found in biological enzymes; that is, the unique ability to bind and orient molecules (or substrates) in a specific manner to achieve a more reactive state. These concepts parallel the efforts of organometallic chemists to perform selective reactions on challenging substrates. Incorporating design elements found in supramolecular chemistry enables the possibility to confer enzymatic-type function, such as specificity and high reaction rates to synthetic systems.[52] Crabtree and Brudvig's dimanganese system exemplifies these principles upon which further systems may find inspiration. The following discussions will focus on pincer systems where functionality has been installed adjacent to the metal binding site, as opposed to remote sites, and the associated directed interactions that these functional groups provide to metal-bound substrates.

1.2.3 Appended functionality co-planar with the pincer chelate

Pincer-based ligands that incorporate the 2,2':6',2"-terpyridine (terpy) unit are attractive platforms upon which a diverse array of functional groups can be appended. Transition metal complexes supported by terpy and terpy-based ligands have been used in a wide array of applications, including sensitizers for solar cells[53] and as catalysts for water oxidation,[54,55] cross-coupling reactions,[56] hydrosilylation of alkenes[57,58] and transfer hydrogenation.[59-61] In addition to the high rigidity of the terpy scaffold, which serves to lock appended groups in place (limiting intramolecular chelation and inhibiting undesired structural reorganization), the ability to exploit highly modular synthetic routes alludes to the high utility of this ligand class.

Motivated by metal-free systems of "Frustrated Lewis Pairs" (FLPs) which bind and form adducts with small molecules, a strategy was recently described to couple the reactivity of FLPs to a transition metal fragment to afford a metal Lewis acid/base triad (LABT).[62] The combination of both partners with a transition metal center opens up the possibility to synergistically use these systems for further activation and/or redox transformations – currently a limitation of metal-free FLP systems.
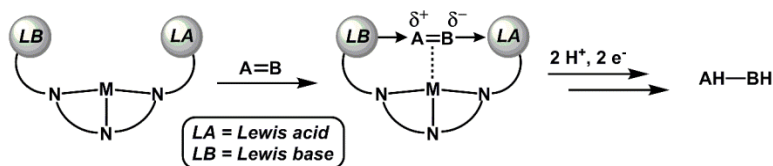
Figure 1-18: Hypothetical reduction of a substrate "A=B" using Lewis pairs in the secondary coordination sphere.

This concept is illustrated in Figure 1-18 where interaction of a hypothetical molecule "A=B" with the metal and FLP fragments in the secondary coordination sphere facilitates polarization of the A-B bond. Further weakening of the A-B bond may be promoted by interaction of a filled *d*-orbital on the metal into anti-bonding orbitals of the A-B bond. Coupling these interactions with

the ability of a redox-active metal center to promote proton and electron transfer events could lead to the release of the formally reduced A-B species. This strategy has been targeted to promote atypical reductive reactivity of typically inert substrates. To test these hypotheses, a ligand architecture based on the terpyridine framework was synthesized. A first generation design featuring a boronic ester and a morpholine group, as weakly Lewis acidic/basic partners appended to the terpy scaffold (Fig. 1-19), was synthesized.
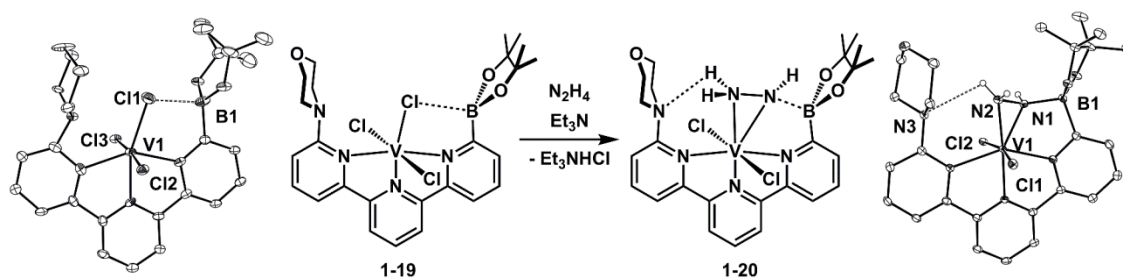
Figure 1-19: Reactivity of a vanadium complex featuring Lewis pairs in the secondary coordination sphere.

The ability of the appended functional groups to interact with a metal-bound substrate was confirmed by interrogation of associated V(III) adducts.[71] The structure of the VCl$_3$-adduct (**1-19**) contains an axial chloride ligand distorted toward the boronic ester group. The B1-Cl1 distance is consistent with a weak B-Cl interaction, and further supported by the low degree of pyramidalization at boron (ΣB_α=349.8(12)°). The appended functionality was confirmed as the major driver for these distortions; when the Lewis acid and base groups were replaced by *CH$_3$* units, the axial chloride ligand was roughly equidistant from both appended methyl groups. To synergistically engage both appended Lewis partners, hydrazine adducts were targeted, and a highly unusual complex (**1-20**) was obtained that features deprotonated hydrazine in an unprecedented side-on coordination, stabilized by Lewis acid/base and hydrogen bonding interactions. The N1-B1 separation is consistent with an elongated single bond, while the N3-H2

24

and N3-N2 separations are indicative of hydrogen-bonding. This complex also mediates N_2-centered redox reactivity, and in the presence of $CoCp_2^*$ and collidinium hydrochloride as a reductant and proton donor, respectively, ammonia was confirmed as a reduction product. The side-on binding mode and N-N bond scission reaction is of potential relevance to the N_2-fixation cycles since hydrazine is a known by-product of N_2 reduction to ammonia by V-nitrogenase.[63]

Complimentary to Lewis acidic/basic groups, Brønsted acid/bases have also been incorporated within the secondary coordination sphere of pincer frameworks. Incorporation of Brønsted acid/base functionality may be pursued to provide sites for proton transfer to/from metal coordinated substrates and/or to modify electronic properties of a metal/ligand complex. Commonly, such architectures are designed with the intent of ground state stabilization of coordinated substrates, such as metal-coordinated water or hydroxo molecules.[64-66] Recent reviews have detailed the effects of hydrogen bonding on metal-aquo ligands, especially within the context of hydrolysis reactivity.[67,68] A particularly noteworthy example of a terpy-like framework appended with Brønsted acid/base functionality was reported by Anslyn and co-workers,[69] who appended guanidinium groups to interact with metal-coordinated substrates. The zinc(II) complexes **1-21** and **1-22** (Fig. 1-20) were examined for their reactivity in the stoichiometric hydrolysis of adenylyl (3'→5') phosphoadenine (ApA).The enhancement in ester hydrolysis from the secondary coordination sphere interactions was confirmed by comparison with an analogous ligand structure that replaces the guanidinium units with functionally-inert *CH₃* groups; the rate of hydrolysis of Apa by **1-21** was *ca.*3300 times greater than that of **1-22**.
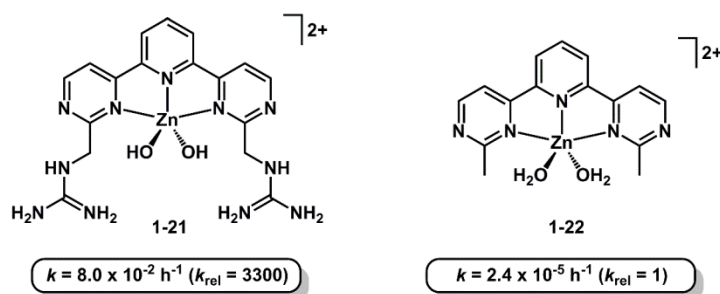
Figure 1-20: Zinc complexes reported by Anslyn and co-workers and their rate constants for the hydrolysis of ApA at pH 7.4.

Hydrolysis reactions measured as a function of pH of ApA by **1-21** established an optimal rate at a pH of 7.4, consistent with a zinc-bound hydroxo (pK_a independently measured as 7.3 in **1-21**) as the active species in the hydrolysis reaction. Although the pK_a of the zinc-bound aquo ligands in **1-22** was not determined, the guanidinium groups of **1-21** are thought to increase the rate of hydrolysis by: 1) using non-covalent interactions to a) acidify the zinc-bound aquo ligands, b) bind and orient the phosphate groups during hydrolysis and/or 2) acting as a general acid/base to facilitate proton transfer during hydrolysis. The impressive rate enhancement of ApA hydrolysis by appending guanidinium groups in the secondary coordination sphere demonstrates the utility of this approach.

Appended functionality was also investigated as a means to mediate further transformations of a metal-coordinated aquo ligand. For instance, one of the first mononuclear ruthenium complexes reported for water oxidation was complex **1-23**, by Thummel and co-workers (Fig. 1-21).[70] Of particular note with regard to this discussion is that only the aquo complex (in contrast to the chloro) was produced under the reaction conditions from $RuCl_3 \cdot 3H_2O$, presumably due to selective binding mediated by hydrogen bonding.
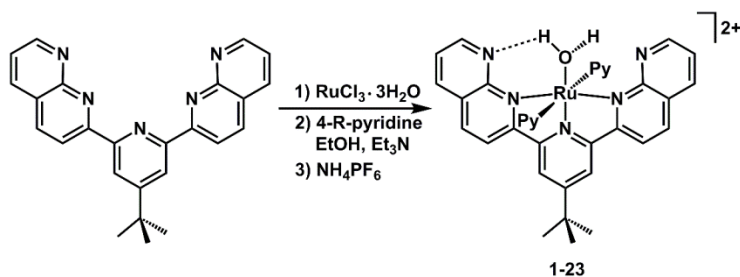
Figure 1-21: Mononuclear ruthenium water oxidation catalysts reported by Thummel and co-workers.

The axial water ligand was shown to participate in hydrogen-bonding interactions with the nearby naphthyridine nitrogen atoms, which likely affords increased stabilization compared to a chloro ligand, which cannot engage in similar secondary–sphere interactions. The role, if any, of the hydrogen-bonding interactions to promote water oxidation is not well-resolved, and recent reports demonstrate similar activity for water oxidation using several alternative mononuclear polypyridine complexes without additional assistance from the secondary coordination sphere.[71]

Terpyridine ligands containing amine groups at the 6- and 6'-positions provide a complementary platform that contains hydrogen-bonding functionality.[72] Interestingly, the platinum(II)-methyl complex containing this terpy pincer ligand (**1-24**, Fig. 1-22) can insert O_2 into the Pt–C bond and form a platinum(II)-methylperoxo species (**1-25**), which releases formaldehyde to afford a platinum(II)-hydroxo complex (**1-26**). A key intermediate in this transformation was identified; the amino groups of the terpyridine ligand participate in hydrogen bonding interactions with the proximal oxygen atom of the methylperoxo unit. These interactions can be visualized in the solid state by X-ray crystallography, and were also demonstrated to persist in solution using NMR experiments.
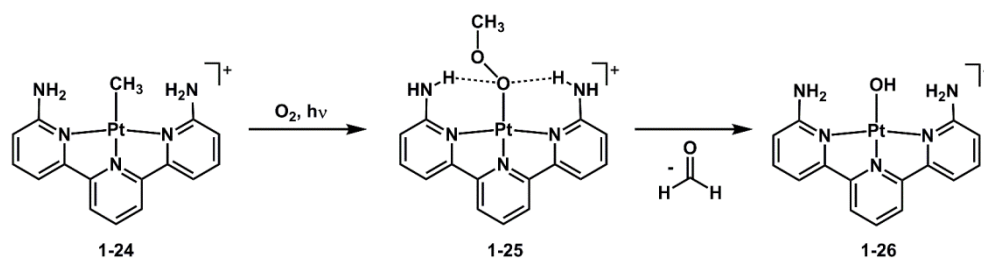
Figure 1-22: Insertion of O₂ into a Pt−CH₃ bond mediated by hydrogen bonding and the resultant terminal platinum-hydroxo complex.

The O_2 insertion reaction is light-dependent; the reaction proceeds to completion within minutes under ambient light, but only 50% conversion is obtained after prolonged reactions times in the absence of light. When the analogous unsubstituted terpyridine complex is subjected to similar reaction conditions, no O_2 insertion products are observed. This finding is rationalized by examination of the electronic absorption spectra and photophysical properties of **1-24** and the terpyridine analogue. While the terpyridine analogue is not photoluminescent at room temperature, the substituted terpyridine complex **1-24** exhibits photoluminescence under similar conditions. Additionally, the extinction coefficient for the metal-to-ligand charge transfer band in the electronic absorption spectrum of **1-24** (~400 nm) is an order of magnitude greater than that of the parent, unsubstituted terpyridine complex. These findings led Britovsek and co-workers to suggest that the observed reactivity of **1-24** is due to its ability to act as a photosensitizer for $^3O_2$ to afford $^1O_2$, the latter of which can insert into the Pt−CH₃ bond. An important, and not unexpected, conclusion that can be drawn from this study is that the introduction of functionality within pincer-derived ligands can modify not only the secondary coordination sphere properties, but also photophysical properties of resulting complexes.[73] As such, the enhanced reactivity of **1-24** can be attributed to the synergistic ability to photosensitize O_2 concomitant with the ground-state stabilization of the Pt-methylperoxo unit through hydrogen-bonding interactions.

28

Pyridine-2,6-dicarboxamide ligands are a versatile class of pincer ligands[74] that present a dianionic ligand field upon metal coordination and can be appended with a wide range of substituents around the flanking amide donor units. Limited monomeric transition-metal complexes supported by pyridine-carboxamide ligands with appended functionality have been structurally characterized. This is in large part due to the propensity of these ligands to form multi-nuclear species. Steric protection can inhibit higher nuclearity structures, but strategies to place these groups typically increase the synthetic complexity, and is likely a reason that so few monomeric pincer complexes exist in this class that feature appended functionality.
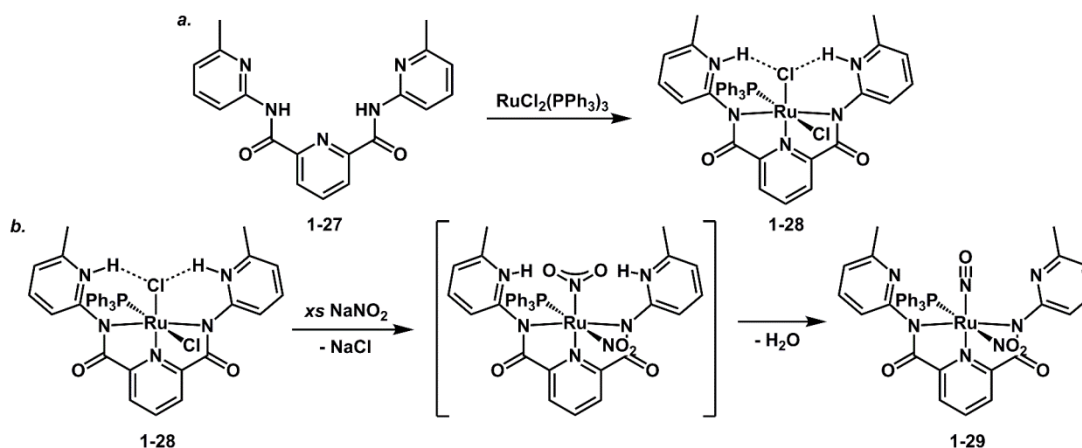
Figure 1-23: Metalation of a pyridine-2,6-dicarboxamide ligand appended with pyridine groups (a) and formation of a ruthenium nitrosyl via proton transfer and water elimination (b).

To enforce a monomeric complex of a pyridine-carboxamide ligand decorated with pyridine bases (**1-27**, Fig. 1-23), methyl groups at the 6-positions of the pyridine groups were effectively used to sterically block intermolecular association.[75] The utility of the appended functionality within this system was highlighted within the context of Ru-mediated nitrite conversion to nitrosyl. Reaction of **1-27** with $RuCl_2(PPh_3)_3$ produces a ruthenium pincer adduct (**1-28**) where intramolecular proton transfer afforded the pendent pyridinium groups. The solid-state structure of **1-28** reveals that these pyridinium groups participate in hydrogen-bonding interactions with

29

the ruthenium-bound chloride ligand. These secondary interactions were targeted to promote further reactivity of small molecules, for instance, the addition of nitrite furnished the ruthenium-nitrosyl complex **1-29**, presumably via a hydrogen-bonded intermediate. A traditional route to ruthenium-nitrosyls involves reaction of ruthenium-nitrite complexes with an exogenous acid. In this case, the pyridinium units likely serve as internal acids to promote the conversion of nitrite to nitrosyl. The relative ease of the synthesis of **1-27** (one step) along with the potential to promote intramolecular proton transfer events in the secondary coordination sphere makes future catalytic studies with this architecture intriguing.

1.2.4 Appended functionality not co-planar to the pincer chelate

ENE pincer systems containing a central pyridine ring have become prominent catalysts for numerous "hydrogen-borrowing" reactions; these systems exploit aromatization/dearomatization of the central pyridine for metal-ligand bifunctionality.[76] A remarkable mode of C-C bond formation was recently reported *via* nucleophilic attack of a deprotonated methylene sidearm on an electrophile such as CO_2, accompanied by concomitant aromatization of the central pyridine.[77,78] This mode of action was independently reported by two groups. Milstein and co-workers disclosed this reaction as an equilibrium process when using a symmetric pincer ligand (**1-30**, E = E' = P^{t}Bu$_2$, Fig. 1-24).[79] In a related study, Sanford and co-workers reported that the non-symmetric pincer ligand (**1-31**, E = NEt$_2$, E' = P^{t}Bu$_2$) provides two distinct Ru-bound carboxylate complexes when exposed to an atmosphere of CO_2,[80] consistent with single carboxylation events on each of the methylene side arms.

(1-30) E = E' = P^{t}Bu$_2$: *reversible*
(1-31) E = NEt$_2$, E' = P^{t}Bu$_2$: *irreversible*
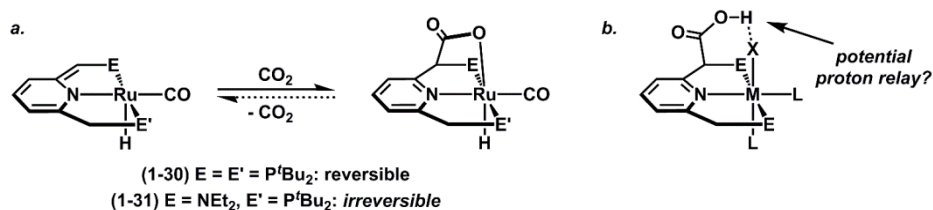
Figure 1-24: Formation of carboxylate compounds from CO$_2$ (a) and a hypothetical metal fragment supported by a pincer ligand with an appended carboxylic acid (b).

These two products have distinct stabilities; the kinetic product (adjacent to P^{t}Bu$_2$) undergoes facile exchange with isotopically-labeled ^{13}CO$_2$, whereas the thermodynamic product (adjacent to NEt$_2$) does not, and was stable toward exposure to vacuum. In the context of appended functionality, these reactions represent an intriguing approach to introduce a carboxylate group within the pincer framework. Although the emphasis of these reactions has been placed on their unique C-C bond forming mechanism, the ligand architectures accessed through this transformation are appealing to promote further small molecule manipulations. The carboxylate-appended pincer frameworks bear resemblance to Hangman porphyrin systems in which carboxylic acid groups were utilized as proton relays.[81] Thus, these ligands are well-suited to provide a new platform to examine catalytic reactions that feature a proton-transfer and/or proton coupled electron-transfer processes for the conversion of small molecule substrates.[82,83]
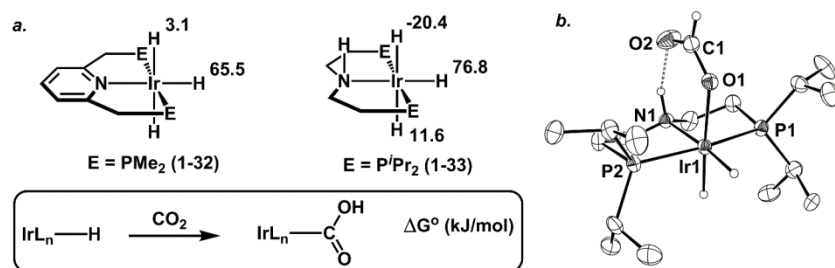
Figure 1-25: Gibb's free energies (kJ/mol) for the insertion of CO$_2$ into various Ir−H bonds (a) and the solid state structure of CO$_2$ insertion product of 1-33.

In addition to the reactivity directed at the methylene spacer in ENE pincers that contain a central pyridine unit, alternative catalytic reactivity can be promoted when the central *N*-donor is

31

a secondary amine. Although the N-H group of the central donor is not strictly "appended functionality", these systems merit discussion in light of recent reports where this N-H group serves to direct reactivity.[84-86] A notable example was described by Crabtree and Hazari[87] for CO_2 hydrogenation catalysis. The N-H functionality on a PNP pincer-ligated $Ir(H)_3$ fragment was found to substantially decrease the energy required for CO_2 insertion into an Ir-H bond. For example, insertion of CO_2 into the Ir-H bond *trans* to the central pyridine ring in **1-32** has a free energy change of +65.5 kJ/mol, while insertion of CO_2 into the mutually *trans* Ir-H bonds is more favorable (ΔG^o = 3.1 kJ/mol; Fig. 1-25a), and likely due to the potent *trans* hydride ligand. In contrast, insertion of CO_2 into the Ir-H bond *trans* to the N-H group in **1-33** has a higher energetic barrier than the pyridine variant (ΔG^o = 76.8 kJ/mol); consistent with the weaker *trans*-directing ability of the secondary amine. Unlike **1-32** where insertion of CO_2 into the mutually-*trans* Ir-H bonds is identical, insertion of CO_2 into the Ir-H bond in **1-33** nearest to the N-H group is energetically downhill (-20.4 kJ/mol), in contrast to the other mutually-*trans* Ir-H in **1-33** (+11.6 kJ/mol). Thus, the presence of the N-H group lowers the overall energy of CO_2 insertion by ~30 kJ/mol. This computational finding was supported with the structural characterization of the CO_2 insertion product (Fig. 1-25b), which shows hydrogen-bonding interactions between the formate carbonyl and the pincer N-H group. In addition to lowering the barrier of CO_2 insertion into a metal hydride, the adjacent NH group has been implicated as an active participant to assist in the heterolytic cleavage of H_2 for hydrogenation reactions promoted by metal ENE pincer (PNP and SNS) complexes.[88-90] As such, these systems are promising multifunctional catalysts for transformations involving H_2 activation/delivery strategies.

Unlike the majority of pincer ligands presented up to this point that are predominantly planar, Gelman recently reported $PC_{sp3}P$ pincer constructs that are three-dimensional.[91-93] These ligands

are based on dibenzobarrelene frameworks, and can be synthesized using highly modular Diels-Alder cycloaddition chemistry,[94] which allows for easy access into sterically and electronically varied sets of ligands within the same architecture. To highlight the potential of metal-ligand cooperativity within these systems, hydroxymethylene groups were incorporated within an Ir-PCP pincer to interact with metal-bound substrates (Fig. 1-26).[95] Solution-state NMR studies revealed an intramolecular close contact between the Ir-H and the methylene sidearm in **1-34**. This species is only transiently stable, and upon standing, H_2 is eliminated to form the "arm-closed" species, **1-35**, presumably through an intermediate dihydrogen bonded adduct (**1-34'**). The H_2 addition/elimination reaction is kinetically reversible, and the utility of this reaction was exploited for catalytic alcohol dehydrogenation. Both primary and secondary alcohols were dehydrogenated in the absence of an exogenous hydrogen acceptor to give esters and ketones, respectively. The structural versatility offered by this system, as well as the robustness presented by the highly-aromatic scaffold, make these systems exciting for future applications in catalysis.
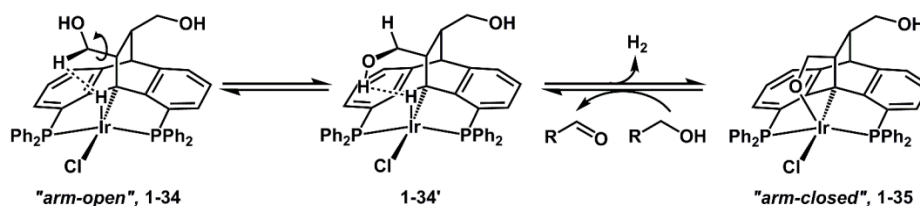
Figure 1-26: Acceptorless-dehydrogenation of alcohols by Gelman's Ir-PCP pincer complex.

The central atom of a pincer ligand can be modified with acidic and/or basic groups, which may later engage in cooperative metal/ligand interactions. Noted previously for the case of the N-H unit in ENE pincers, a central phosphorus or sulfur can be further elaborated in PEP pincers (where E = P, S). A recent example demonstrated that modification of the central atom of the pincer with acidic and basic functionality was possible with a mononuclear PPP pincer iridium(I)

complex (Fig. 18).[96] In contrast to a meridonal geometry typical of pincer ligands, the phosphido ligand in **1-37** is pyramidalized, and accordingly, affords a facial coordination mode. The geometry about the central phosphorus atom is consistent with predominantly σ-bonding character of the Ir-P unit, with an exposed lone pair. Further reactivity at this site provided pincer ligand manifolds that contain pendent acidic and basic groups. For example, **1-37** reacts with exogenous electrophiles, such as AuCl (**1-38**), BH$_3$•SMe$_2$, and NH$_4$PF$_6$ to provide discrete Lewis acid/base adducts. Alternatively, reaction with the O-atom transfer reagent, trimethylamine-N-oxide, furnished the phosphine oxide complex **1-36**, which highlights the ability of the phosphido unit to support both Lewis acidic and basic groups in the secondary coordination sphere of the PPP pincer framework. Further reactivity studies were hindered by the tight binding of the cyclooctadiene ligand, which could not be eliminated under reductive conditions.
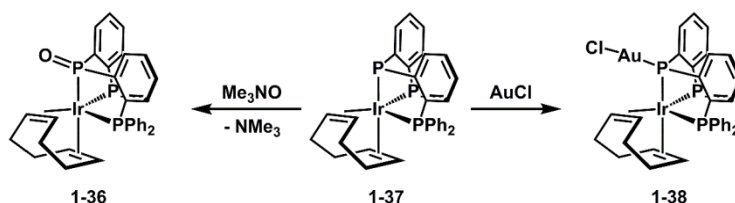
Figure 1-27: Functionalization of the central phosphide of a PPP pincer.

Although subsequent reactivity of the modified PPP ligands was not reported in this system, a related PP(O)P ligand featuring a central phosphine-oxide was recently reported by Bourissou and co-workers (Fig. 1-28a).[97]
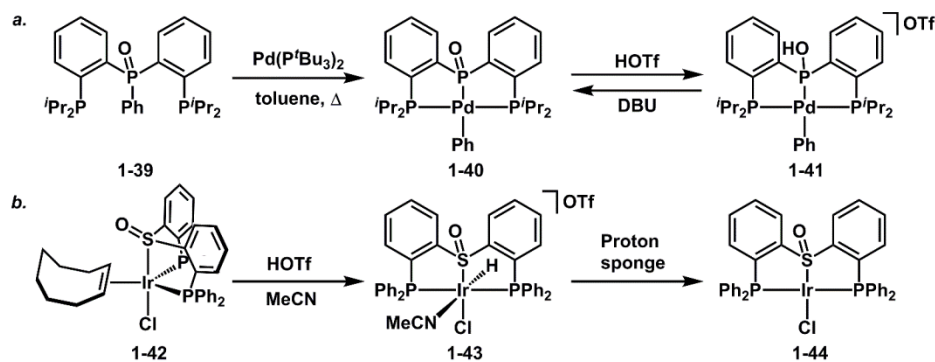
Figure 1-28: PP(O)P and PS(O)P pincer complexes and their reactions with Brønsted acids and bases.

Entry into the square-planar palladium(II) complex **1-40** can be achieved by formal insertion of the P-C bond of the free ligand **1-39** into a palladium(0) complex. The ability of the phosphine-oxide group in **1-40** to act as a Brønsted base was demonstrated by protonation using triflic acid to give the hydroxyl-phosphine complex, **1-41**. The addition of triflic acid to **1-40** modifies the ligand field of the central phosphorus atom from an X-type to an L-type donor, and is reversible using a sufficiently strong base such as DBU (DBU = 1,8-diazabicycloundec-7-ene). Phosphine oxides and sulfoxides are both potent hydrogen-bond acceptor units, thus pincer-based PEP ligands that contain a central sulfoxide unit are highly complementary to the phosphine oxide PP(O)P ligands shown above.

A PS(O)P pincer ligand was recently reported, in addition to its group 9 and 10 transition metal complexes (Fig. 1-28b).[98] Similar to the PP(O)P ligands, the PS(O)P ligand supports meridonal and facial coordination modes. Addition of Brønsted acids to iridium(I) complexes containing the PS(O)P ligand (**1-42**) results in the oxidative ligation of H$^+$ to afford an iridium(III) hydride species (**1-43**). This finding suggests that the sulfoxide moiety in PS(O)P-complexes has minimal Brønsted basicity, relative to the Ir(I) center. Protonation in this case is also reversible, and deprotonation affords a meridonal isomer (**1-44**). Thus, the

protonation/deprotonation sequence can effectively be used to induce facial/meridonal isomerization. The utility of the proton-responsive phosphine oxide in **1-40** and the S=O functionality in **1-42** currently have limited demonstrated proficiency; however these platforms might find application in catalytic cycles that feature proton-transfer events coupled with changes in the ligand field properties of a substrate. For this reason, future studies targeting proton-transfer reactivity in this complex, and related complexes, would be compelling.

Like Gelman's PC$_{sp3}$P pincer ligands, pyridine-2,6-diimine (PDI) ligands are a highly modular class of pincer ligands derived from commercially-available starting materials.[99] An additional attribute of this ligand class is the non-innocent nature of the scaffold with respect to redox chemistry.[100-102] The synthesis of PDI ligands is amenable to the facile introduction of functionality in a symmetric and non-symmetric manner, and can typically be achieved on multi-gram quantities. Symmetric PDI ligands featuring pendent Lewis basic (hydrazone) and acidic (pinacol boronate ester) sites have been reported with their iron(II) complexes, which were examined as catalysts for ethylene oligomerization.[103,104] The specific role of the pendent functional groups during catalysis is not fully understood, but appears to contribute to enhanced thermal stability of the catalysts.

A related non-symmetric PDI ligand that features a pendent amine was reported by Gilbertson and co-workers for metal-ligand cooperativity (**1-45**, Fig. 1-29).[105] In this case, the amine side-arm is flexible and can engage in interactions with metal-coordinated substrates. The amine unit can be readily protonated, which presents a potent hydrogen-bond donor group capable of further interactions with coordinated ligands, for example, metal halides. Intramolecular proton transfer was also possible in this system, and was effected from a transiently formed iron(II)-aquo complex, which allowed the isolation of a rare iron(II)-hydroxo

species, **1-46**. Of particular note, the subsequent hydrogen-bonding interaction with the protonated amine serves to stabilize the iron(II)-hydroxo complex. The highly flexible pendent amine is uniquely poised to act as a proton relay and/or to separately interact with a metal coordinated substrate at two distinct sites. These features, in addition to possible participation in proton-coupled electron transfer reactions *via* ligand-centered redox events make this a promising scaffold for further catalytic studies.
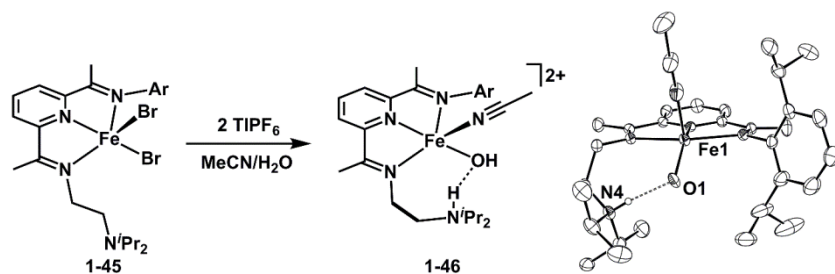
Figure 1-29: Formation of an iron-hydroxo from water and the solid-state structure of 1-46.

1.2.5 Outlook for multifunctional pincer complexes

Pincer frameworks provide a unique ligand scaffold that is amenable for further elaboration with appended functional groups, in large part due to the rigid nature of most pincer frameworks. Functionality can be directed collinear or orthogonal to a metal-coordinated substrate, and these distinct secondary structures can be targeted for substrate specificity within multifunctional architectures. Because of the potential coordinating ability of the introduced functionality, the selection of metalation conditions requires careful attention to limit multinuclear metal-ligand ensembles. Once metalated, appended functionality can serve to tune a ligand's physical properties and/or promote proton/electron transfer, which may concomitantly modify a pincer's ligand field strength. The recent explosion in reports of cooperative ligand frameworks demonstrates a high interest in the area of metal-ligand multifunctionality, and because of their

geometrical constraints as well as unique tunable reactivity, pincer-based ligands are poised to continue to emerge as premier platforms upon which further elaboration is possible to uncover new reactivity profiles for small molecule activation.

1.3 Outline and scope of this thesis

This thesis is structured around the synthesis, structure, and reactivity of transition metal complexes supported by ligand architectures appended with functional groups capable of engaging in hydrogen bonding interactions and/or H^+ transfer events. In Chapter 2, metal complexes supported by a tripodal ligand featuring hydrogen bond acceptor amide groups far removed from the metal center are described. Structural properties of these complexes are presented with an emphasis on how the secondary coordination sphere groups affect primary sphere coordination geometry. The design principle is highlighted by demonstrating selective hydrogen bonding interactions to a non-traditional CH donor. In Chapter 3, a proton-responsive tripodal ligand is described which is based on the 2-hydroxypyridine motif. The ability of the pendent hydroxyl groups to alter coordination geometry and stability is examined through the synthesis of copper complexes. Additionally, the ability of this ligand scaffold to facilitate proton and electron transfer reactivity is described. Chapter 4 details the catalytic applications of a pincer ligand which has been designed to confine 2-hydroxypyridine groups into a tridentate scaffold and allow for proton transfer reactivity. The discussion is largely based on ruthenium-catalyzed transfer hydrogenation reactivity and studies with H_2. These experiments are contextualized with regards to [Fe]-hydrogenase and an emphasis is placed on possible structure/function relationships. Lastly, Chapter 5 is dedicated to iridium hydride complexes supported by the pincer ligand presented in Chapter 4. Brief notes on reactivity as well as properties will be outlined and possible applications of these complexes are put forth.

1.4 References

1. Lubitz, W.; Ogata, H.; Rüdiger, O.; Reijerse, E. *Chem. Rev.* **2014**, *114,* 4081.

2. Lewis, N. S.; Nocera, D. G. *Proc. Natl. Acad. Sci.* **2006**, *103*, 15729.

3. Shima, S.; Pilak, O.; Vogt, S.; Schick, M.; Stagni, M. S.; Meyer-Klaucke, W.; Warkentin, E.; Thauer, R. K.; Ermler, U. *Science* **2008**, *321*, 572.

4. Hiromoto, T.; Ataka, K.; Pilak, O.; Vogt, S.; Stagni, M. S.; Meyer-Klaucke, W.; Warkentin, E.; Thauer, R. K.; Shima, S.; Ermler, U *FEBS Letters* **2009**, *583*, 585.

5. Tamura, H.; Stagni, M. S.; Fujishiro, T.; Warkentin, E.; Meyer-Klaucke, W.; Ermler, U.; Shima, S. *Angew. Chem. Int. Ed.* **2013**, *52*, 9656.

6. Shima, S.; Ataka, K: *FEBS Letters* **2011**, *585*, 353.

7. Yang, X.; Hall, M. B. *J. Am. Chem. Soc.* **2009**, *131*, 10901.

8. Finkelmann, A.R.; Stiebritz, M. T.; Reiher, M: *J. Phys. Chem. B* **2013**, *117,* 4806.

9. Royer, A. M.; Rauchfuss, T. B.; Gray, D. L. *Organometallics* **2010**, *29*, 6763.

10. Hull, J. F.; Himeda, Y.; Wang, W. H.; Hashiguchi, B.; Periana, R.; Szalda, D. J.; Muckerman, J. T.; Fujita, E. *Nat Chem* **2012**, *4,* 383.

11. Wang, W. H.; Hull, J. F.; Muckerman, J. T.; Fujita, E.; Himeda, Y. *Energy Environ. Sci.* **2012**, *5*, 7923.

12. Wang, W. H.; Muckerman, J. T.; Fujita, E.; Himeda, Y. *ACS Catal.* **2013**, *3,* 856.

13. Hou, C.; Jiang, J.; Zhang, S.; Wang, G.; Zhang, Z.; Ke, Z.; Zhao, C. *ACS Catal.* **2014**, *4*, 2990.

14. Kelson, E. P.; Phengsy, P. P. *J. Chem. Soc., Dalton Trans.* **2000**, 4023.

15.   Nieto, I.; Livings, M. S.; Sacci, J. B.; Reuther, L. E.; Zeller, M.; Papish, E. T. *Organometallics* **2011**, *30*, 6339.

16.   Moore, C. M.; Szymczak, N. K. *Chem. Commun.* **2013**, *49,* 400.

17.   Fujita, K.; Tanino, N.; Yamaguchi, R. *Org. Lett.* **2007**, *9*, 109.

18.   Fujita, K.; Yoshida, T.; Imori, Y.; Yamaguchi, R. *Org. Lett.* **2011**, *13,* 2278.

19.   Kawahara, R.; Fujita, K.; Yamaguchi, R. *J. Am. Chem. Soc.* **2012**, *134*, 3643.

20.   Fujita, K.; Uejima, T.; Yamaguchi, R. *Chem. Lett.* **2013**, *42,* 1496.

21.   Kawahara, R.; Fujita, K.; Yamaguchi, R. *Angew. Chem. Int. Ed.* **2012**, *51,* 12790.

22.   Fujita, K.; Ito, W.; Yamaguchi, R. *ChemCatChem* **2014**, *6*, 109.

23.   Zeng, G.; Sakaki, S.; Fujita, K.; Sano, H.; Yamaguchi, R. *ACS Catal.* **2014**, *4,* 1010.

24.   Thauer, R. K.; Kaster, A. K.; Goenrich, M.; Schick, M.; Hiromoto, T.; Shima, S. *Annu. Rev. Biochem.* **2010**, *79,* 507.

25.   Dalebrook, A. F.; Gan, W.; Grasemann, M.; Moret, S.; Laurenczy, G. *Chem. Commun.* **2013**, *49*, 8735.

26.   Crabtree, R. H. *Energy Environ. Sci.* **2008**, *1,* 134.

27.   Fujita, K.; Tanaka, Y.; Kobayashi, M.; Yamaguchi, R. *J. Am. Chem. Soc.* **2014**, *136*, 4829.

28.   DePasquale, J.; Nieto, I.; Reuther, L. E.; Herbst-Gervasoni, C. J.; Paul, J. J.; Mochalin, V.; Zeller, M.; Thomas, C. M.; Addison, A. W.; Papish, E. T. *Inorg. Chem.* **2013**, *52*, 9175.

29.   Zhang, T.; deKrafft, K. E.; Wang, J. L.; Wang, C.; Lin, W. *Eur. J. Inorg. Chem.* **2014**, 698.

30. Lewandowska-Andralojc, A.; Polyansky, D. E.; Wang, C. H.; Wang, W. H.; Himeda, Y.; Fujita, E. *Phys. Chem. Chem. Phys.* **2014**, *16,* 11976.

31. Marelius, D. C.; Bhagan, S.; Charboneau, D. J.; Schroeder, K. M.; Kamdar, J. M.; McGettigan, A. R.; Freeman, B. J.; Moore, C. E.; Rheingold, A. L.; Cooksy, A. L.; Smith, D. K.; Paul, J. J.; Papish, E. T.; Grotjahn, D. B.. *Eur. J. Inorg. Chem.* **2014** 676.

32. Zhang, T.; Wang, C.; Liu, S.; Wang, J. L.; Lin, W. *J. Am. Chem. Soc.* **2014**, *136,* 273.

33. Barnett, S. M.; Goldberg, K. I.; Mayer, J. M. *Nature Chem.* **2012**, *4*, 498.

34. Badiei, Y. M.; Wang, W. H.; Hull, J. F.; Szalda, D. J.; Muckermann, J. T.; Himeda, Y.; Fujita, E. *Inorg. Chem.* **2013**, *52*, 12576.

35. Hu, B.; Chen, D.; Hu, X. *Chem. Eur. J.* **2014**, *20,* 1677.

36. Ying, C. H.; Yan, S. B.; Duan, W. L. *Org. Lett.* **2014**, *16*, 500.

37. Lippard, S. J.; Berg, J. M. *Principles of Bioinorganic Chemistry*; University Science Books: Mill Valley, 1994.

38. Kaim, W.; Schwederski, B. *Bioinorganic Chemistry*; John Wiley & Sons Ltd: Chichester, 1994.

39. Crabtree, R. H. *New J. Chem.* **2011**, *35*, 18.

40. Shook, R. L.; Borovik, A. S. *Inorg. Chem.* **2010**, *49*, 3646.

41. Nieto, I.; Livings, M. S.; Sacci, J. B.; Reuther, L. E.; Zeller, M.; Papish, E. T. *Organometallics* **2011**, *30*, 6339.

42. Knapp, S. M. M.; Sherbow, T. J.; Yelle, R. B.; Zakharov, L. N.; Juliette, J. J.; Tyler, D. R. *Organometallics* **2013**, *32*, 824.

43. Das, S.; Incarvito, C. D.; Crabtree, R. H.; Brudvig, G. W. *Science* **2006**, *312*, 1941.

44. Balcells, D.; Moles, P.; Blakemore, J. D.; Raynaud, C.; Brudvig, G. W.; Crabtree, R. H.; Eisenstein, O. *Dalton Trans.* **2009**, 5989.

45. Das, S.; Brudvig, G. W.; Crabtree, R. H. *J. Am. Chem. Soc.* **2008**, *130*, 1628.

46. Linke-Schaetzel, M.; Anson, C. E.; Powell, A. K.; Buth, G.; Palomares, E.; Durrant, J. D.; Balaban, T. S.; Lehn, J.-M. *Chem.--Eur. J.* **2006**, *12*, 1931.

47. Huang, C.-Y.; Lynch, V.; Anslyn, E. V. *Angew. Chem., Int. Ed.* **1992**, *31*, 1244.

48. Disalvo, F. J. *Science* **1990**, *247*, 649.

49. Huang, C. Y.; Cabell, L. A.; Lynch, V.; Anslyn, E. V. *J. Am. Chem. Soc.* **1992**, *114*, 1900.

50. Barboiu, M.; Prodi, L.; Montalti, M.; Zaccheroni, N.; Kyritsakas, N.; Lehn, J.-M. *Chem.--Eur. J.* **2004**, *10*, 2953.

51. Barboiu, M.; Lehn, J.-M. *Proc. Natl. Acad. Sci. U. S. A.* **2002**, *99*, 5201.

52. Meeuwissen, J.; Reek, J. N. H. *Nat. Chem.* **2010**, *2*, 615.

53. Nazeeruddin, M. K.; Pechy, P.; Renouard, T.; Zakeeruddin, S. M.; Humphry-Baker, R.; Comte, P.; Liska, P.; Cevey, L.; Costa, E.; Shklover, V.; Spiccia, L.; Deacon, G. B.; Bignozzi, C. A.; Graetzel, M. *J. Am. Chem. Soc.* **2001**, *123*, 1613.

54. Concepcion, J. J.; Jurss, J. W.; Norris, M. R.; Chen, Z.; Templeton, J. L.; Meyer, T. J. *Inorg. Chem.* **2010**, *49*, 1277.

55. Polyansky, D. E.; Muckerman, J. T.; Rochford, J.; Zong, R.; Thummel, R. P.; Fujita, E. *J. Am. Chem. Soc.* **2011**, *133*, 14649.

56. Anderson, T. J.; Jones, G. D.; Vicic, D. A. *J. Am. Chem. Soc.* **2004**, *126*, 8100.

57. Kamata, K.; Suzuki, A.; Nakai, Y.; Nakazawa, H. *Organometallics* **2012**, *31*, 3825.

58.   Tondreau, A. M.; Atienza, C. C. H.; Darmon, J. M.; Milsmann, C.; Hoyt, H. M.; Weller, K. J.; Nye, S. A.; Lewis, K. M.; Boyer, J.; Delis, J. G. P.; Lobkovsky, E.; Chirik, P. J. *Organometallics* **2012**, *31*, 4886.

59.   Kelson, E. P.; Phengsy, P. P. *J. Chem. Soc. Dalton Trans.* **2000**, 4023.

60.   Enthaler, S.; Hagemann, B.; Erre, G.; Junge, K.; Beller, M. *Chem. Asian J.* **2006**, *1*, 598.

61.   Kroehnke, F. *Synthesis* **1976**, 1.

62.   Tutusaus, O.; Ni, C.; Szymczak, N. K. *J. Am. Chem. Soc.* **2013**, *135*, 3403.

63.   Dilworth, M. J.; Eady, R. R. *Biochem. J.* **1991**, *277*, 465.

64.   MacBeth, C. E.; Hammes, B. S.; Young, V. G., Jr.; Borovik, A. S. *Inorg. Chem.* **2001**, *40*, 4733.

65.   Mukherjee, J.; Lucas, R. L.; Zart, M. K.; Powell, D. R.; Day, V. W.; Borovik, A. S. *Inorg. Chem.* **2008**, *47*, 5780.

66.   Mareque-Rivas, J. C.; Prabaharan, R.; Martin, d. R. R. T. *Chem. Commun.* **2004**, 76.

67.   Berreau, L. M. In *Activation of Small Molecules*; Wiley-VCH Verlag GmbH & Co. KGaA: 2006, p 287.

68.   Ahmed, T. J.; Knapp, S. M. M.; Tyler, D. R. *Coord. Chem. Rev.* **2011**, *255*, 949.

69.   Ait-Haddou, H.; Sumaoka, J.; Wiskur, S. L.; Folmer-Andersen, J. F.; Anslyn, E. V. *Angew. Chem., Int. Ed.* **2002**, *41*, 4014.

70.   Zong, R.; Thummel, R. P. *J. Am. Chem. Soc.* **2005**, *127*, 12802.

71.   Kaveevivitchai, N.; Zong, R.; Tseng, H.-W.; Chitta, R.; Thummel, R. P. *Inorg. Chem.* **2012**, *51*, 2930.

72.   Taylor, R. A.; Law, D. J.; Sunley, G. J.; White, A. J. P.; Britovsek, G. J. P. *Angew. Chem., Int. Ed.* **2009**, *48*, 5900.

73.   Mutai, T.; Cheon, J.-D.; Tsuchiya, G.; Araki, K. *J. Chem. Soc., Perkin Trans. 2* **2002**, 862.

74.   Donoghue, P. J.; Tehranchi, J.; Cramer, C. J.; Sarangi, R.; Solomon, E. I.; Tolman, W. B. *J. Am. Chem. Soc.* **2011**, *133*, 17602.

75.   Redmore, S. M.; Rickard, C. E. F.; Webb, S. J.; Wright, L. J. *Inorg. Chem.* **1997**, *36*, 4743.

76.   Gunanathan, C.; Milstein, D. *Acc. Chem. Res.* **2011**, *44*, 588.

77.   Montag, M.; Zhang, J.; Milstein, D. *J. Am. Chem. Soc.* **2012**, *134*, 10325.

78.   Vogt, M.; Rivada-Wheelaghan, O.; Iron, M. A.; Leitus, G.; Diskin-Posner, Y.; Shimon, L. J. W.; Ben-David, Y.; Milstein, D. *Organometallics* **2013**, *32*, 300.

79.   Vogt, M.; Gargir, M.; Iron, M. A.; Diskin-Posner, Y.; Ben-David, Y.; Milstein, D. *Chem.--Eur. J.* **2012**, *18*, 9194.

80.   Huff, C. A.; Kampf, J. W.; Sanford, M. S. *Organometallics* **2012**, *31*, 4643.

81.   Rosenthal, J.; Nocera, D. G. *Prog. Inorg. Chem.* **2007**, *55*, 483.

82.   Piers, W. E. *Organometallics* **2011**, *30*, 13.

83.   Dempsey, J. L.; Esswein, A. J.; Manke, D. R.; Rosenthal, J.; Soper, J. D.; Nocera, D. G. *Inorg. Chem.* **2005**, *44*, 6879.

84.   Clarke, Z. E.; Maragh, P. T.; Dasgupta, T. P.; Gusev, D. G.; Lough, A. J.; Abdur-Rashid, K. *Organometallics* **2006**, *25*, 4113.

85.   Nielsen, M.; Kammer, A.; Cozzula, D.; Junge, H.; Gladiali, S.; Beller, M. *Angew. Chem., Int. Ed.* **2011**, *50*, 9593.

86.   Bertoli, M.; Choualeb, A.; Lough, A. J.; Moore, B.; Spasyuk, D.; Gusev, D. G. *Organometallics* **2011**, *30*, 3479.

87. Schmeier, T. J.; Dobereiner, G. E.; Crabtree, R. H.; Hazari, N. *J. Am. Chem. Soc.* **2011**, *133*, 9274.

88. Spasyuk, D.; Smith, S.; Gusev, D. G. *Angew. Chem., Int. Ed.* **2012**, *51*, 2772.

89. Spasyuk, D.; Gusev, D. G. *Organometallics* **2012**, *31*, 5239.

90. Spasyuk, D.; Smith, S.; Gusev, D. G. *Angew. Chem., Int. Ed.*, **2013**, *52*, 2538.

91. Azerraf, C.; Gelman, D. *Chem.--Eur. J.* **2008**, *14*, 10364.

92. Azerraf, C.; Gelman, D. *Organometallics* **2009**, *28*, 6578.

93. Gelman, D.; Romm, R. *Top. Organomet. Chem.* **2013**, *40*, 289.

94. Azerraf, C.; Shpruhman, A.; Gelman, D. *Chem. Commun.* **2009**, 466.

95. Musa, S.; Shaposhnikov, I.; Cohen, S.; Gelman, D. *Angew. Chem., Int. Ed.* **2011**, *50*, 3533.

96. Gloaguen, Y.; Jacobs, W.; de, B. B.; Lutz, M.; van, d. V. J. I. *Inorg. Chem.* **2013**, *52*, 1682.

97. Derrah, E. J.; Martin, C.; Mallet-Ladeira, S.; Miqueu, K.; Bouhadir, G.; Bourissou, D. *Organometallics*, **2013**, *32*, 1121.

98. Suess, D. L. M.; Peters, J. C. *Organometallics* **2012**, *31*, 5213.

99. Gibson, V. C.; Redshaw, C.; Solan, G. A. *Chem. Rev.* **2007**, *107*, 1745.

100. Tondreau, A. M.; Stieber, S. C. E.; Milsmann, C.; Lobkovsky, E.; Weyhermuller, T.; Semproni, S. P.; Chirik, P. J. *Inorg. Chem.* **2013**, *52*, 635.

101. Bart, S. C.; Chlopek, K.; Bill, E.; Bouwkamp, M. W.; Lobkovsky, E.; Neese, F.; Wieghardt, K.; Chirik, P. J. *J. Am. Chem. Soc.* **2006**, *128*, 13901.

102. Thammavongsy, Z.; Seda, T.; Zakharov, L. N.; Kaminsky, W.; Gilbertson, J. D. *Inorg. Chem.* **2012**, *51*, 9168.

103. Britovsek, G. J. P.; Gibson, V. C.; Kimberley, B. S.; Mastroianni, S.; Redshaw, C.; Solan, G. A.; White, A. J. P.; Williams, D. J. *J. Chem. Soc., Dalton Trans.* **2001**, 1639.

104. Ionkin, A. S.; Marshall, W. J.; Adelman, D. J.; Bobik, F. B.; Fish, B. M.; Schiffhauer, M. F. *Organometallics* **2008**, *27*, 1902.

105. Kendall, A. J.; Zakharov, L. N.; Gilbertson, J. D. *Inorg. Chem.* **2010**, *49*, 865

Chapter 2 Hydrogen bonding interactions far removed from the metal center

Portions of this chapter have been published:

Moore, C. M.; Szymczak, N. K. *Dalton Trans.* **2012**, *41*, 7886. Reprinted with permission; copyright 2012 The Royal Society of Chemistry.

2.1 Motivation and design criteria for the TQA' ligand

Biological metalloenzymes are unique in their ability to mediate the transformations of relatively inert substrates with impressive selectivity and speed. Secondary interactions such as hydrogen bonding are broadly appreciated to promote enhanced reactivity in metalloenzymes and are proposed to operate through one of several modes of action.[1] For instance, well-positioned networks of amino acid hydrogen bonds have been proposed to bind, orient, and activate substrates at an enzyme active site, or to stabilize a transition state.[2] Several recent breakthroughs have shown how appropriate hydrogen-bonding interactions can be utilized in synthetic inorganic systems to activate small molecules;[3,4] for example, to increase the acidity of coordinated aqua ligands,[5] or to stabilize typically reactive coordinated oxo,[6,7] hydroxo,[8] and hydroperoxo species.[9-12]

We sought to construct a series of metal-ligand adducts that feature well-defined primary and secondary coordination sphere environments to broadly investigate how the hydrogen-bonding network appended to a transition metal center may be used to augment substrate reactivity.

While numerous ligands have been constructed to enforce hydrogen-bonding interactions at positions that are 1-atom separated from the binding site,[7,9,13] few ligand architectures support directed interactions with a substrate that is ≥2 atoms removed from the metal center,[13,14] and moreover, ligand frameworks that incorporate hydrogen-bond acceptors are scarce.[15,16] Such scaffolds can be targeted to promote the activation of substrates for hydrolysis, or to stabilize typically reactive oxygenation intermediates (including a terminal hydroperoxo unit). Thus, our key ligand design criterion was to position hydrogen-bond acceptors at distances ≥ 4 Å from the primary metal site in order to favorably participate in substrate hydrogen-bonding interactions with atoms that are ≥ 2 bonds removed from the binding site. Other aspects of our design criteria included: (1) hydrogen bond acceptor groups that form DH − A adducts with weak basicity to limit proton-transfer and (2) a rigid ligand framework to prevent coordination of the peripheral hydrogen bond acceptor group to the metal center. It was envisioned that competitive coordination of the acceptor functionality could potentially deactivate a catalyst or prohibit binding of exogenous ligands or substrates, and this is most likely to occur when a flexible linker is used.
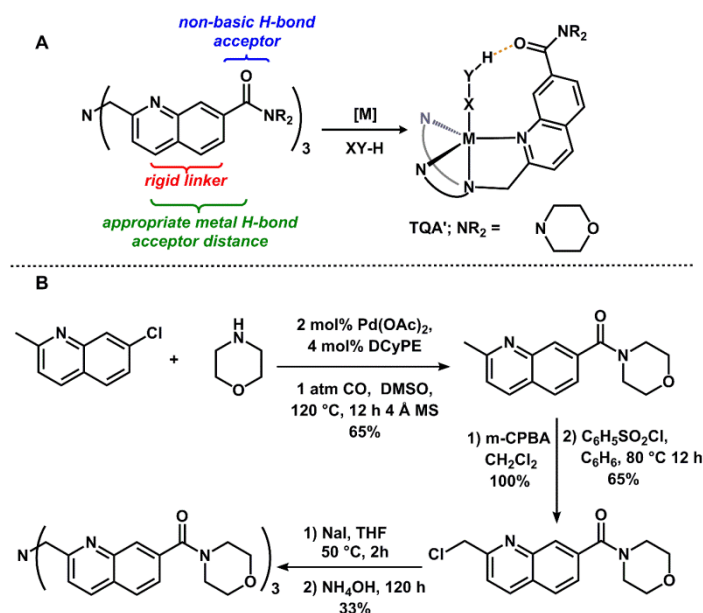
Figure 2-1. Design criteria and synthesis of the TQA' ligand.

To satisfy the above criteria, a tripodal ligand that incorporates 2-aminomethylquinoline units was targeted to enforce the desired secondary coordination sphere environment (Fig. 2-1A). The ligand, tris[quinolyl-2-methyl-7-(morpholinomethanone)]amine (TQA'), was prepared in four steps from commercially-available starting materials (Fig. 2-1B). Morpholine-derived amide groups were selected due to their facile syntheses as well as hydrogen-bonding ability, and access to appended morpholine amide groups proceeded smoothly using an aminocarbonylation protocol[17] from 7-chloro-2-(methyl)quinoline.

2.2 Hydrogen bonding interactions with a non-classical donor

We evaluated the salient structural features of the TQA' ligand by first preparing its Cu(I) complex. The cationic complex, [Cu(TQA')]X (**2.1**, $X^- = PF_6^-$ or ClO_4^-), was prepared by allowing equimolar amounts of TQA' and [Cu(MeCN)$_4$]X to react in acetonitrile for 30 minutes under an inert atmosphere. The light orange solid **2.1** exhibits stability similar to the previously prepared [Cu(TQA)]PF$_6$ (TQA = (tris(2-quinolylmethyl)amine));[18] it is relatively air stable in the

solid state (no appreciable decomposition after 12 hours).[18] Additionally, **2.1** is unreactive

toward O_2 in solutions of acetone or propionitrile at -78 °C, and -90 °C, respectively; in accord

with previously reported results on the reactivity of [Cu(TQA)]PF$_6$.[18] The solid-state structure

was interrogated by analysis of single crystals grown from acetonitrile/diethyl ether.

Figure 2-2. Synthesis and crystal structure of the Cu(I)-TQA' adduct 2.1. (30% ellipsoids, solvent molecules, counterions, morpholine rings and hydrogen atoms not participating in hydrogen bonding have been omitted for clarity)

The structure (Fig. 2-2) confirms C_3 symmetry and features a trigonal monopyramidal geometry

about copper (τ_4=0.85).[19] The 3-fold symmetry was retained in solution, as confirmed by a single

set of quinolyl resonances in the ^{1}H NMR spectrum.

2.2.1 Solid- and solution-state structures of copper(II)-TQA' adducts

In contrast to the trigonal monopyramidal, axially-vacant Cu(I) species described above, the

1-electron oxidized Cu(II) adducts of tetradentate-tripodal ligands generally feature 5-coordinate

geometry.[20] This coordination number allows for an axially-ligated substrate to interact most

constructively with the secondary coordination sphere of the TQA' scaffold when trigonal

bipyramidal (TBP) geometry is achieved. To examine this binding mode, the Cu(II) complex

was synthesized by treatment of an acetonitrile solution of **2.1** with [η^5-(C$_5$H$_5$)$_2$Fe][ClO$_4$],

providing [Cu(CH$_3$CN)TQA'][(ClO$_4$)$_2$] (**2.2**) as a green solid in 74% yield. For comparison, the

corresponding unmodified TQA complex [Cu(CH$_3$CN)TQA][(ClO$_4$)$_2$] (**2.3**) was also

prepared.[21,22] Comparative analyses of the solid-state structures of **2.2** and **2.3** expose notably distinct coordination environments around copper.
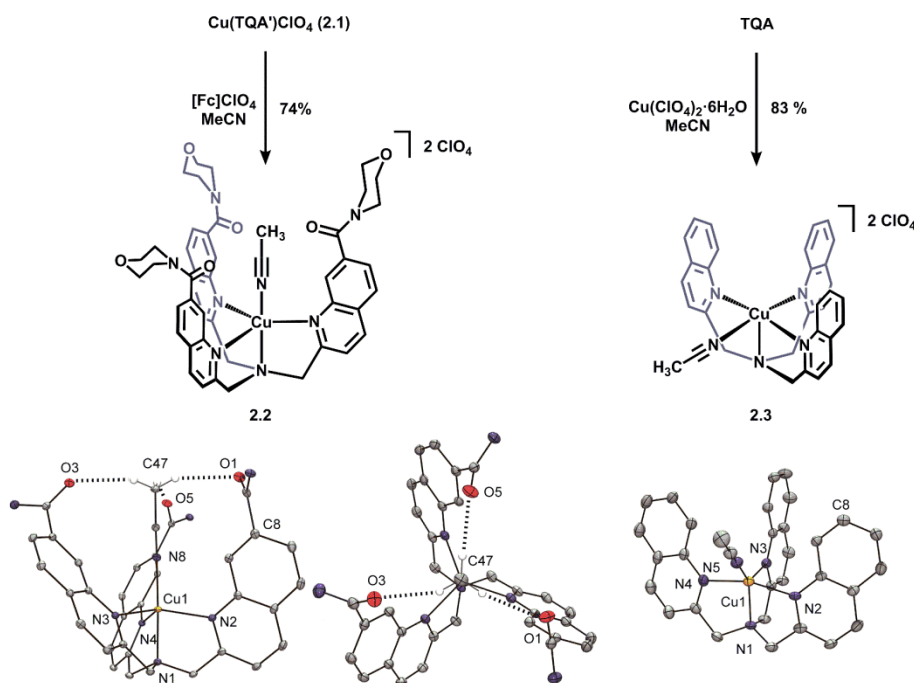
Figure 2-3. Synthesis and crystal structures of the Cu(II)-MeCN TQA' (2.2) and TQA (2.3) adducts. (30% ellipsoids, solvent molecules, counterions, morpholine rings and hydrogen atoms not participating in hydrogen bonding have been omitted for clarity)

The solid state structure of **2.2** (Fig. 2-3) reveals TBP geometry about the copper center ($\tau_5 = 0.95$), in contrast to the distorted square based pyramidal (SP) geometry in **2.3** (Fig. 2-3, $\tau_5 = 0.40$).[23] Additionally, close contact interactions were noted between the coordinated acetonitrile methyl (C47) group and the carbonyl of TQA' in 2. The C47–O distances are 3.42 Å (C47–O1), 3.26 Å (C47–O3) and 3.29 Å (C47–O5), and the O–H–C47 bond angles are ~ 150°; both metrics are indicative of weak hydrogen-bonding interactions.[24-27] Analysis of the solid state structure reveals the distance between the copper center and the plane defined by the three carbons at the 7-position of the quinoline ring (quinoline carbon to which the amide is appended, see Fig. 2-2 and 2-3) in **2.2** is 2.44 Å, which is significantly shorter than the distance found in **2.1** (3.12 Å)

51

and **2.3** (2.71 Å). This difference is a consequence of the "propeller-like" twisting (dihedral angle = 25 - 30°) that occurs in the structure of **2.2** to accommodate the coordinated acetonitrile ligand. The degree to which the quinoline rings can twist highlights the flexibility of the TQA' framework and ability to adapt to substrates whose binding might be otherwise precluded by steric interactions.[28]
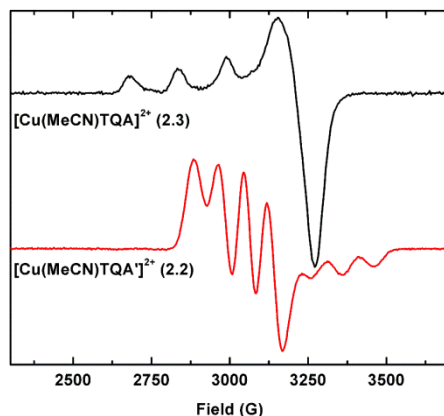
Figure 2-4. EPR spectra of 2.2 and 2.3 in MeCN/THF at 85 K.

To investigate whether the solid-state structures were retained in solution, comparative analyses of the solution-phase structures of **2.2** and **2.3** were performed using EPR spectroscopy. The X-band EPR spectra of both compounds in frozen CH_3CN/THF solutions were compared at 85 K and revealed notably distinct coordination environments around copper (Fig. 2-4). Complex **2.3** displays an axial spectrum ($g\perp$ = 2.05, $g\parallel$ = 2.27, $A\parallel$ = 153 G), consistent with a $d_{x^2-y^2}$ ground state, square pyramidal (SP) geometry.[22] In contrast, **2.2** displays an inverse axial spectrum ($g\perp$ = 2.18, $g\parallel$ = 2.00 $A\perp$ = 86 G, $A\parallel$ = 72 G), consistent with a d_{z^2} ground state, TBP geometry.[22] The results of these studies illustrate that although **2.3** converts from an intermediate (τ_5 = 0.40) to an SP geometry in solution, the solid-state structure of **2.2** (TBP) is retained in solution and, thus,

the observed coordination geometry of **2.2** in the solid state is not likely a consequence of crystal packing forces.[29]
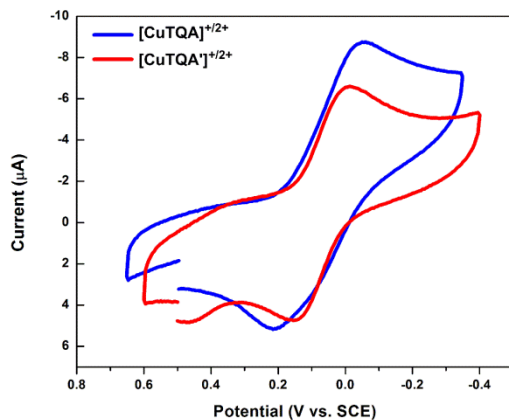
Figure 2-5. Cyclic voltammograms of Cu(TQA')$^{+/2+}$ and Cu(TQA)$^{+/2+}$ in DMF. (100 mV/s scan rate, 0.1 M [Bu$_4$N][PF$_6$] supporting electrolyte)

The only other structurally-characterized Cu(II) complex supported by a C_3 symmetric TQA-derived ligand is SP in solution and in the solid state ($\tau_5 = 0.06$).[21,22] This has been proposed to be a consequence of the steric influence of the C-H group at the 8-position of the quinaldine ring, which prohibits the fifth ligand from being bound in the axial pocket provided by the ligand framework.[21,22] Thus, the favored TBP geometry observed in the case of TQA' is noteworthy. This coordination preference could be directed by electronic or steric factors. To clarify whether the distinct coordination preferences of **2.2** and **2.3** could be dictated by differences in the ligand field environments of the two ligands, electrochemical studies were pursued. The cyclic voltammograms of **2.1** and Cu(TQA)PF$_6$[18] in dimethylformamide revealed an electrochemically-reversible 1e$^-$ oxidation event, consistent with a Cu^I/Cu^{II} redox couple (Fig. 2-5). Copper complexes with both TQA and TQA' exhibit similar redox couples (E$_{1/2}$ =0.16 and 0.18 V for **2.1** and Cu(TQA)PF$_6$, respectively; vs. SCE), indicating that both metal centers have comparable electronic environments. Thus, the electronic environment presented to the metal by both TQA

and TQA' are nearly identical, and variations in the primary coordination geometry cannot solely be ascribed to electronic differences.

2.2.2 Confirmation of CH−O hydrogen bonding in solution

The observation of close contacts in the solid state structure to the acetonitrile CH_3 groups in **2.2** is consistent with a non-covalent interaction, such as CH−O hydrogen bonding.[30] Since the solid-state structure of **2.2** was retained in solution (*vide supra*), we examined whether the postulated CH−O hydrogen-bonds were persistent in solution. Hydrogen bonds are typically identified in solution using IR and NMR spectroscopy.[27] Unfortunately, because the overlapping CH_2 vibrational modes of ligand morpholine groups obscured clear visualization of CH_3CN bands,[31] we sought to use NMR spectroscopy to investigate the proposed hydrogen-bonding interaction between the amide carbonyl groups of TQA' with the Cu-bound acetonitrile CH_3 groups. ^2H NMR spectroscopy was selected as a viable technique because the quadrupolar ^2H nucleus typically affords resonances that are observable even in the presence of paramagnetic metal centers, such as Cu(II).[32,33] Thus, the deuterated acetonitrile isotopologues of **2.2** and **2.3** were prepared (denoted **2.2-d** and **2.3-d**), as was the corresponding TPA (tris(2-pyridylmethyl)amine) copper(II) complex (**2.4-d**). Complex **2.4-d** was selected as a geometrically identical (TBP, $\tau_5=0.96$)[34] control species to evaluate whether chemical shift differences between **2.2-d** and **2.3-d** could be attributed to the overall coordination geometry rather than differences in the local deuteron environments.
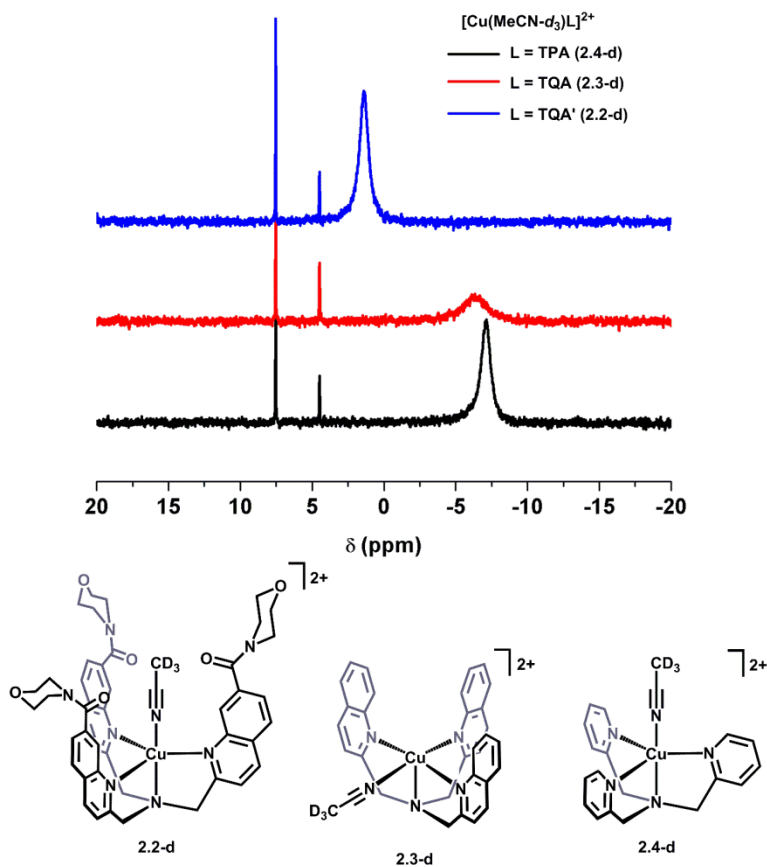
Figure 2-6. Room temperature ^{2}H NMR spectra of Cu(II)-MeCN-d_3 adducts.

At room temperature, the paramagnetically-shifted ^{2}H NMR spectra of **2.4-d** and **2.3-d** are similar (Fig. 2-6). In contrast, the CD$_3$CN resonance of **2.2-d** is shifted downfield by 7.6 ppm from **2.3-d**. The absolute chemical shifts of the CD$_3$CN resonances at room temperature reflect differences in local deuteron environments; this difference is decoupled from both copper coordination geometry as well as ligand field (i.e. **2.3-d** vs. **2.4-d**). Furthermore, the downfield shift noted for **2.2-d** is consistent with proton (or deuterium) deshielding as a result of hydrogen-bonding interactions, although the magnitude of this downfield shift is less meaningful in paramagnetic systems.[27,35]
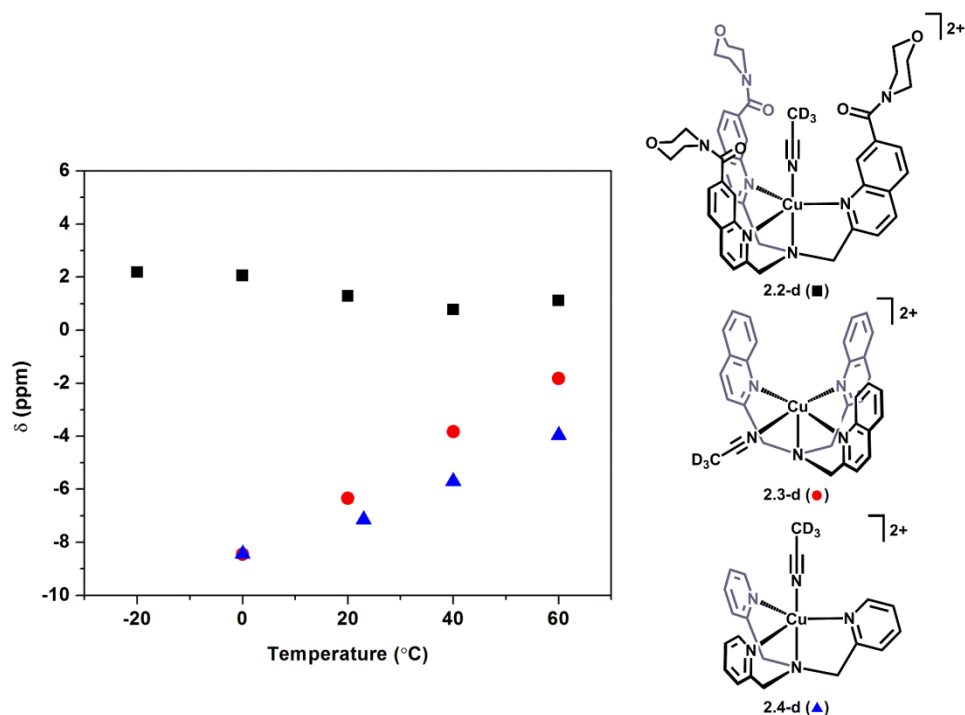
Figure 2-7. Variable temperature ^{2}H NMR chemical shifts of the coordinated CD$_3$CN resonance in 2.2-d (■), 2.3-d (●) and 2.4-d (▲) (0.038 M in MeNO2

We further tested the possibility of persistent hydrogen-bonding interactions in **2.2-d** by measuring the temperature-dependent behavior of the paramagnetically-shifted ^{2}H NMR resonances. We anticipated that the ^{2}H NMR temperature profiles would allow for the differentiation between hydrogen bonding interactions and dynamic exchange processes (rapid equilibration of free and coordinated CD$_3$CN). As shown in Fig. 2-7, **2.3-d** and **2.4-d** display an upfield chemical shift trend in a response to decreasing temperature, whereas **2.2-d** undergoes a slight downfield chemical shift with decreasing temperature.[36] Notably, the spectra at -20 °C are drastically different between **2.2-d** and both **2.3-d** and **2.4-d**. At this temperature, the CD$_3$CN resonance for both **2.3-d** and **2.4-d** has reached the coalescence point and broadened into the baseline, as opposed to **2.2-d** where the CD$_3$CN signal remains sharp and well defined. Together, the room temperature and variable-temperature ^{2}H NMR spectra support markedly distinct local

coordination environments and dynamic behavior of the coordinated CD$_3$CN ligands between **2.2-d** and both **2.3-d** and **2.4-d**. These preliminary results are consistent with a persistent hydrogen-bonding interaction for **2.2** in solution and dynamic CD$_3$CN exchange behavior in **2.3** and **2.4**.

2.3 Lewis acid encapsulation within the secondary coordination sphere

Copper(II) complexes supported by the TQA' ligand favor C_3-symmetric structures when an appropriate hydrogen bond donor substrate is coordinated to the metal center (*vide supra*). As such, we sought to investigate substrates which cannot engage the ligand scaffold in non-covalent interactions to further understand how these interactions might influence coordination geometry. An ideal substrate for this purpose is cyanide, since it cannot form hydrogen bonds with the ligand scaffold. Moreover, we envisioned that the ability of cyanide to act as a bridging ligand between two metal centers would allow us to potentially modulate the structure of the TQA' complexes by introducing metal ions capable of interacting with the cyanide group (as illustrated in Fig. 2-8). In this way, the properties of the metal center (i.e. coordination geometry and electronic ground state) could be modulated between two states depending on an external stimulus.

square pyramidal (SP)   trigonal bipyramidal (TBP)
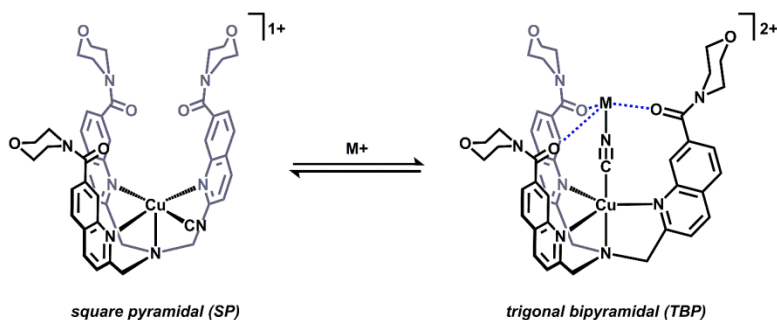
Figure 2-8. Interconversion of coordination geometry via secondary coordination of a metal ion.

We first evaluated the coordination of cyanide to copper-TQA' constructs by performing a spectrophotometric titration of complex **2.2** with sodium cyanide (NaCN) in a nitromethane/methanol solution. The resulting UV/vis spectra are shown in Fig. 2-9 and display a binding event which is complete after approximately one equivalent of NaCN has been added, consistent with tight binding of cyanide to **2.2**. With this information in hand, a synthetic procedure was pursued to generate the product of this titration in significant quantities in order to interrogate the mode of cyanide binding and coordination geometry at copper.
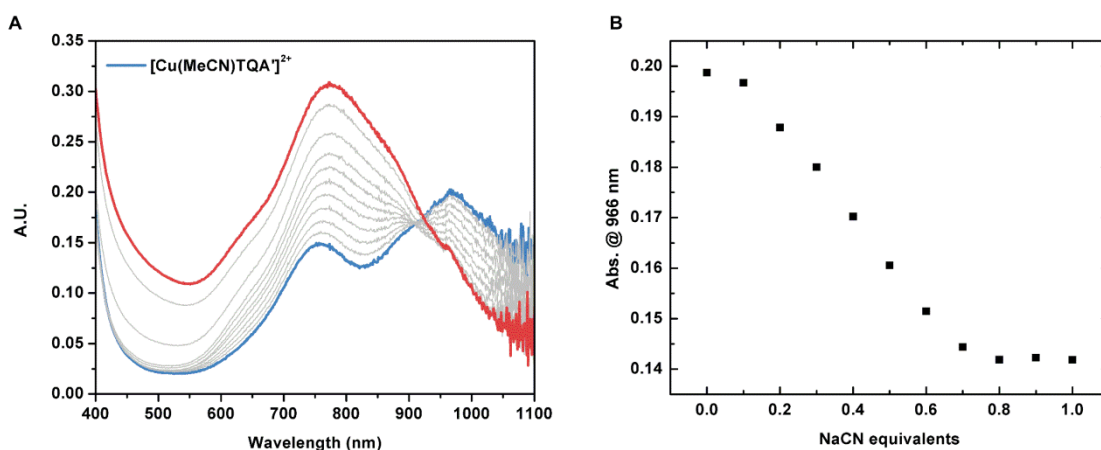
Figure 2-9. Spectrophotometric titration of 2.2 with NaCN. (MeNO$_2$ solvent)

This was achieved by generating complex **2.2** in situ (by allowing TQA' to react with Cu(ClO$_4$)$_2$ 6H$_2$O in acetonitrile solution) and exposing it to one of equivalent of NaCN. This procedure allowed for the isolation of a dark green microcrystalline powder upon vapor diffusion of diethyl ether into the filtered reaction solution. The UV-vis spectrum of the above material (complex **2.5**) was identical to the endpoint spectrum of the aforementioned titration of **2.2** with NaCN. A crystal of complex **2.5** suitable for X-ray diffraction was grown by vapor diffusion of diethyl ether into a solution of **2.5** in acetonitrile.
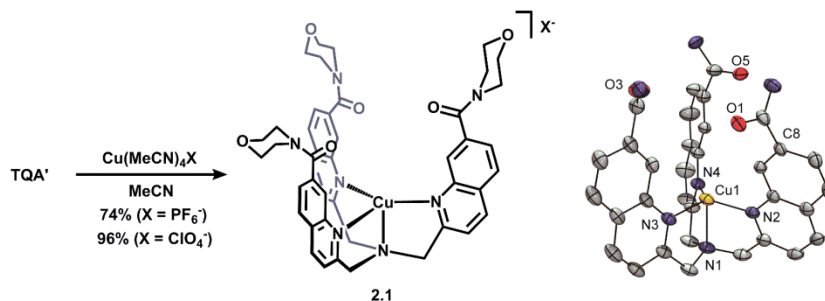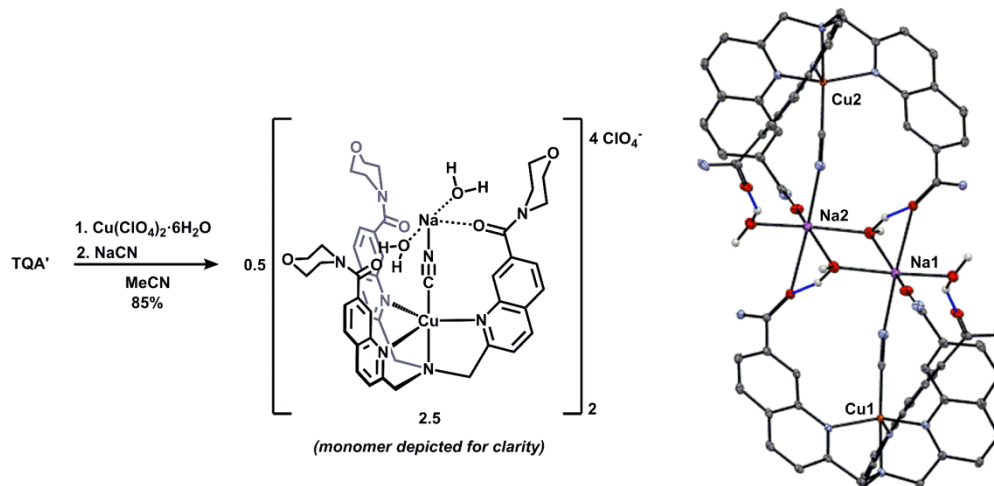
Figure 2-10. Synthesis and crystal structure of the NaCN adduct 2.5. (30% ellipsoids, solvent molecules, counterions, morpholine rings and hydrogen atoms not participating in hydrogen bonding have been omitted for clarity)

The structure of **2.5** is presented in Fig. 2-10 and reveals that the complex adopts a dimeric structure assembled through hydrogen bonding interactions between water molecules and nearby hydrogen bond acceptor groups from the ligand. Additionally, the sodium cation has been incorporated into the structure, stabilized by Lewis acid-base interactions with the TQA' scaffold and water coordination. Overall the structure contains a rich network of intramolecular Lewis and Brønsted acid/base interactions that result in the copper center maintaining a TBP coordination geometry ($\tau_5 = 0.99$).[23]

The encapsulation of Na$^+$ ions within complex **2.5** reveals a binding motif for Lewis acids that might be exploited to isolate other diatoms within a metal-ligand ensemble. To date, efforts to synthesize copper-cyanide constructs devoid of cations have led to the isolation of ill-defined materials. As such, the synthesis of a well-defined copper-cyanide construct in the absence of cations is needed in order to explicitly determine how cations might regulate the coordination geometry around copper.

59

2.4 Reactivity toward hydrogen peroxide

Copper hydroperoxo compounds have been targeted primarily to emulate the chemistry of the copper-containing metalloenzyme dopamine β-monooxygenase (DβM). The DβM enzyme is responsible for catalyzing the oxidation of dopamine to norepinephrine using O_2 as a terminal oxidant.[37] A mechanism for this transformation has been proposed that proceeds through a copper-hydroperoxo species, and as such, there have been many efforts to understand the fundamental chemistry of these species.[38] Pioneers in this field, such as the Karlin and Masuda groups, have described the reactivity of numerous synthetic copper-hydroperoxo complexes.[11,39] In general, these complexes are highly reactive and can only be characterized in solution at low temperature. Typical decomposition pathways are through intramolecular ligand hydroxylation. This reaction is directly analogous to the function of DβM, although an exogenous substrate is hydroxylated, rather than the ligand.
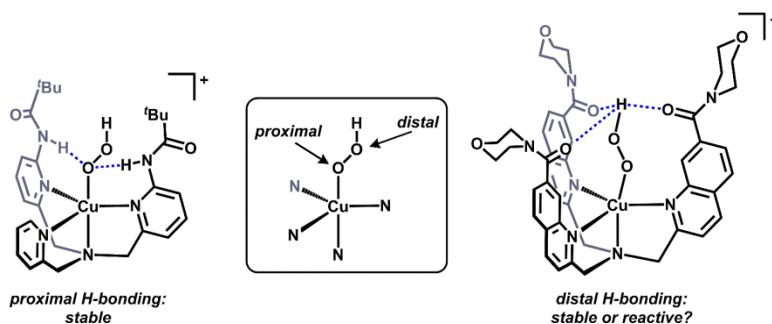
Figure 2-11. Directed hydrogen bonding toward copper-coordinated hydroperoxide.

To stabilize these reactive intermediates, Masuda and co-workers, among others, have introduced hydrogen bonding groups in the secondary coordination sphere of their ligand constructs in an effort to form stabilizing non-covalent interactions with coordinated hydroperoxide.[11,39] In fact, this approach has led to the isolation and structural characterization of a terminal copper-hydroperoxo complex featuring hydrogen bonding interactions directed at the

proximal oxygen atom of the hydroperoxide ligand (Fig. 2-11). The ability to fully characterize this complex however came at a cost; it was found to be completely unreactive toward exogenous substrates.[11] The subtle interplay between stability and reactivity therefore is crucial when designing ligand scaffolds to interact with reactive, metal bound substrates such as hydroperoxide. Based on the above stabilization of hydroperoxide by hydrogen bonding, we hypothesized that targeting the distal OH group of coordinated hydroperoxide might offer a disparate reactivity pattern than that observed by Masuda and co-workers. We envisioned that the pendent amide groups of TQA' would be ideally suited to engage in hydrogen bonding interactions with coordinated hydroperoxide since the hydrogen bond donor would be three atoms removed from the metal center (in analogy to the Na^+ interactions described above, Fig. 2-11).

We examined the reactivity of copper-TQA' complexes toward hydrogen peroxide (H_2O_2) in order to test the above hypotheses. When the copper(II) complex **2.2** is treated with excess H_2O_2 and base (triethylamine) in acetone solution at -78 C, a new complex is formed. This reaction was monitored using UV-vis spectroscopy and the product could be identified by a new weak absorption at 390 nm ($\varepsilon \sim 1700$ $M^{-1}cm^{-1}$), which is consistent with a hydroperoxide to copper ligand-to-metal charge transfer (LMCT) band. For instance, this peak position and intensity are similar to that of a mononuclear, TPA-based copper-hydroperoxo complex reported by Karlin and co-workers ($\lambda_{max} = 393$ nm, $\varepsilon = 1600$ $M^{-1}cm^{-1}$).[39] Based on this data, the product of the reaction of complex **2.2** with H_2O_2/triethylamine is therefore proposed to be a terminal copper-hydroperoxo complex (**2.6**, Fig. 2-12).
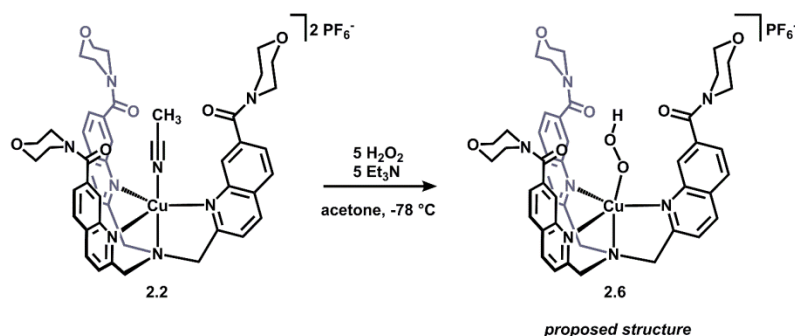
Figure 2-12. Proposed copper-hydroperoxide complex supported by the TQA' ligand.

To understand the importance of the pendent hydrogen bonding functionality on the outcome of the H_2O_2 reaction, the unmodified TQA complex **2.3** was subjected to identical reaction conditions with H_2O_2 and base. The resulting UV-vis spectrum of this reaction product (**2.7**) is distinct from that of the TQA' complex **2.6** and exhibits a more intense absorption at 379 nm ($\varepsilon \sim$ 3400 $M^{-1}cm^{-1}$). Although the peak position is very close to that of complex **2.6**, the intensity is significantly higher than the TQA' analogue and is consistent with a different oxidized species. Unfortunately, the spectral features of **2.6** are not comparable with previously reported oxidized copper-oxygen species. Regardless of the exact nature of the oxidized product **2.7**, we examined the thermal stability of the two compounds generated *in situ*. Warming the acetone solutions containing **2.6** and **2.7** to -40 °C causes a bleaching of the spectral features over time for each species. In the case of **2.6**, the half-life for decomposition was approximately 110 min. In contrast, the half-life for the decomposition of **2.7** was much shorter, approximately 20 min. Both complexes display distinct thermal stability, which illustrates a difference in their chemical composition. These differences may be due to non-covalent interactions promoted by the TQA' ligand, however more experiments are necessary to validate this hypothesis.
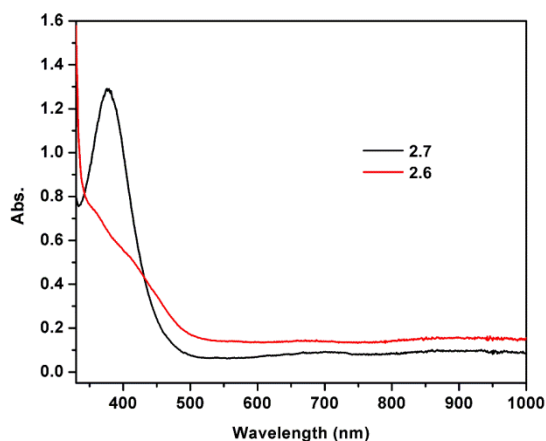
Figure 2-13. UV-vis spectra of complexes 2.6 and 2.7. (-78 ° C, acetone)

Further characterization of these complexes at low temperature is required in order to fully verify their structures and to examine their reactivity toward exogenous substrates. Preliminary results have shown that these spectral features can be bleached in the presence of *O*-atom acceptors, such as triphenylphosphine, and further work is necessary to understand their respective reactivity profiles. Additionally, characterization of the products of decomposition will be useful to understand the nature of the oxidized intermediate. These studies will likely require the use of resonance Raman spectroscopy and low temperature mass spectroscopy.

2.5 Urea coordination and hydrogen bonding interactions

Inspired by the chemistry of the nickel-containing metalloenzyme urease,[40] nickel complexes supported by the TQA' ligand were pursued. Urease catalyzes the hydrolysis of urea to carbon dioxide with remarkable efficiency; showing a rate enhancement of 10^{14}-fold increase over the uncatalyzed elimination reaction.[40] While the mechanism of this transformation is still somewhat debated, it is widely accepted that the secondary coordination sphere around the dinuclear nickel active site of the enzyme plays a vital in the catalytic activity. In particular, two nearby histidine residues are believed to be involved during catalysis by regulating urea binding/coordination

63

and/or acting as a general acid/base to facilitate H^+ transfer events during hydrolysis. These hypotheses have been confirmed through mutation studies in which replacement of the histidine residues with residues not capable of engaging in hydrogen bonding interactions leads to decreased catalytic rates, as compared to the native enzyme.[40] The aforementioned hydrogen bonding interactions involving nearby histidine residues have been proposed to be with the distal NH_2 group of nickel-bound urea (a group three bonds removed from the metal center) and aid in polarizing urea and generating hydroxide for attack on the carbonyl group.[40]

At the outset, we hypothesized that coordination of urea to a nickel complex supported by TQA' would lower the activation energy for H_2O attack and subsequent hydrolysis through hydrogen bonding interactions, akin to the mode of operation of the nearby histidine residues in the native enzyme. Hydrolysis of urea promoted by homogeneous, synthetic transition metal complexes has proven to be a daunting task:[41] the highest reported turnover number (TON) for the metal catalyzed urea hydrolysis is four and was achieved by an abiological palladium complex.[42] When considering the high hydrolytic stability of urea (*ca.* 40 kcal/mol resonance stabilization energy), it is no surprise that catalysts for this reaction are few and far between. Furthermore, the nitrogen-containing product of urea hydrolysis, ammonia (NH_3), is an excellent ligand for most transition metals and therefore catalyst poisoning *via* product inhibition is an even more challenging task to overcome when considering possible catalyst designs. One approach to overcoming the challenge of product inhibition is to design a catalyst that preferentially binds substrate in the presence of product. This, in principle, should be possible to achieve by promoting specific hydrogen bonding interactions with the substrate. The TQA' ligand scaffold seemed ideal to test this hypothesis given that the hydrogen bonding acceptor

groups are far-removed from the metal center and most likely unable to interact with metal-coordinated ammonia.
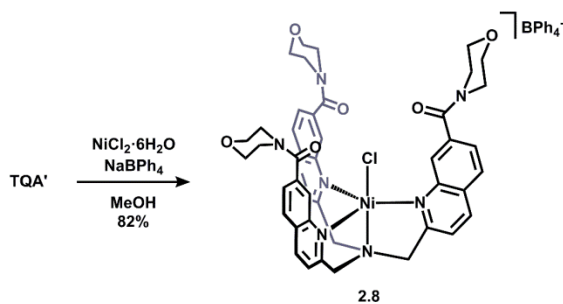
Figure 2-14. Synthesis of a Ni(II)-chloride TQA' complex.

To assess the cooperative binding of urea to a nickel center, a nickel complex supported by TQA' was synthesized. When TQA' is allowed to react with $NiCl_2 \cdot 6H_2O$ in methanol, the nickel complex **2.8** is obtained in 82% yield as a pale green powder after metathesis with $NaBPh_4$. Although **2.8** is paramagnetic, it could be characterized by ^{1}H NMR spectroscopy. The ^{1}H NMR spectrum (acetone-d_6) of **2.8** displays a single set of paramagnetically-shifted ligand resonances, which is consistent with three-fold symmetry in solution. When a solution (acetone-d_6) of **2.8** is titrated with urea, tight binding can be observed by ^{1}H NMR spectroscopy. The ^{1}H NMR spectra of solutions containing varied amounts of urea are presented in Fig. 2-15 and demonstrate nearly complete conversion to a new complex (**2.9**) upon introduction of approximately one equivalent of urea.
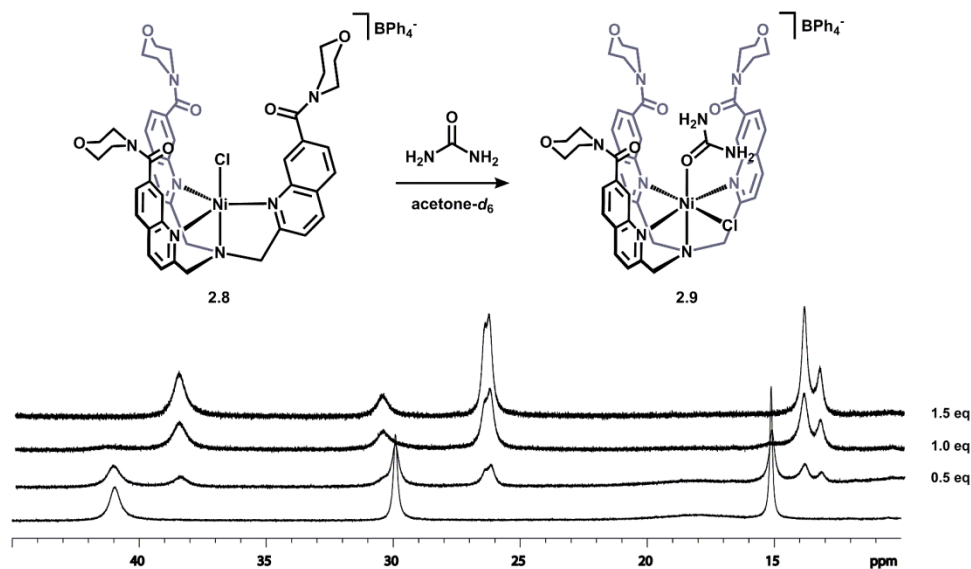
Figure 2-15. ¹H NMR titration of 2.8 with urea.

The tight binding ($K_a > 10^4$) is confirmed by the presence of non-exchanging (on the NMR timescale) resonances for **2.8** and the new complex **2.9**, indicative of a binding event that is not reversible. Also apparent from the spectra is the loss of symmetry upon introduction of urea, consistent with a change in coordination geometry at nickel from TBP to octahedral. Based on the complete conversion of **2.8** upon addition of one equivalent of urea and the lowering of symmetry, the product of the reaction with urea was proposed to be the octahedral urea adduct **2.9**.
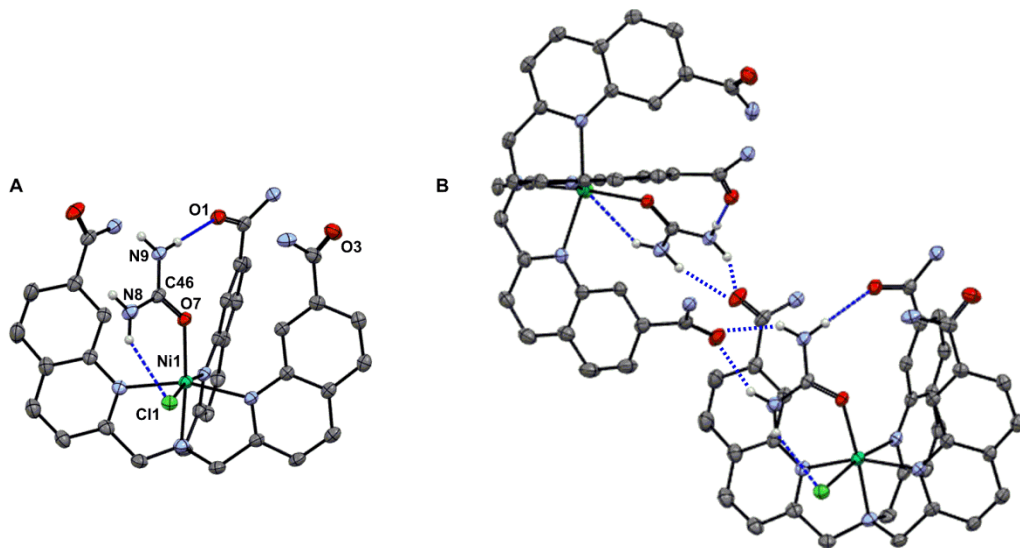
Figure 2-16. Solid-state structure of the urea-adduct 2.9 and intermolecular hydrogen bonding. (30% ellipsoids, solvent molecules, counterions, morpholine rings and hydrogen atoms not participating in hydrogen bonding have been omitted for clarity)

To further assess the above supposition, a crystal of complex **2.9** suitable for an X-ray diffraction experiment was grown by diffusing diethyl ether into the NMR tube from the above titration experiment. The crystal structure of **2.9** exhibits the predicted structure from the NMR experiments: an octahedral nickel complex with a single urea molecule bound to the metal center (Fig. 2-16A). In addition, the structure displays a rich network of inter- and intramolecular hydrogen bonding interactions with adjacent amide groups of the TQA' scaffold (Fig. 2-16B).

The tight binding of urea to the nickel complex **2.8** prompted us to investigate the ability of **2.8** to promote the hydrolysis of urea. Aqueous solutions (acetone-d_6/H_2O; pH 7) of **2.8** were treated with excess urea and subsequently heated at reflux for extended time periods (up to 3 days). Unfortunately, no urea hydrolysis products could be observed under the aforementioned conditions. These results initially suggest that the TQA' ligand does not appreciably lower the activation energy required for H_2O attack on urea and/or generate sufficient concentrations of hydroxide necessary for hydrolysis.

2.6 Experimental section for Chapter 2

Warning: Perchlorate complexes are potentially explosive and should be handled with extreme care. Cyanide salts are highly toxic and should be used in a well-ventilated fume hood.

General Considerations

All commercially-available reagents were used as received without further purification. TQA,[18] TPA,[43] DCyPE,[44] $Cu(CH_3CN)_4X$,[45] $Cu(TQA)PF_6$[18] and$[Cu(CH_3CN)TPA][(ClO_4)_2]$[46] were prepared as previously described. All manipulations were carried out in the air unless otherwise stated. Air sensitive reactions were performed either using standard Schlenk techniques or in an MBraun Lab Master 130 or Innovative Technologies Pure Lab[HE] GP-1 glovebox. NMR spectra were recorded on either a Varian MR400 or a Varian vnmrs 500 spectrometer and are referenced to residual solvent peaks. IR spectra were collected using a Nicolet *i*S10 spectrometer equipped with a diamond attenuated total reflectance (ATR) accessory. UV-vis measurements were carried out using a Varian Cary50 spectrophotometer equipped with an all-quartz dip probe using fiber optic cables. Electrochemical measurements were performed using a Pine WaveNow potentiostat. The electrochemical cell consisted of a modified three electrode set-up with a glassy carbon working electrode, a platinum counter electrode and a silver wire pseudo-reference electrode. Ferrocene was used as an internal reference and introduced at the end of the experiment, then voltammograms were referenced to SCE (ferrocene/ferrocenium$^+$ = 0.45 V / SCE). Voltammograms were measured in DMF with 0.1 M tetrabutylammonium hexafluorophosphate as the supporting electrolyte. X-band EPR spectra were recorded on a Bruker EMX spectrometer equipped with a Bruker 4102-ST general purpose cavity at 85 K. The spectra were recorded at a frequency of 9.258 GHz, modulation frequency of 100 kHz, modulation amplitude of 10.0 G, and 205.1 mW of power.

(2-methylquinolinyl)(morpholino)methanone

To a 300 mL Schlenk flask charged with a stirbar, 4 Å molecular sieves (11.6 g) were added and activated under vacuum and heat. The flask was moved into the glovebox and charged with sodium phenoxide (15.10 g, 130 mmol) and 1,2-bis(dicyclohexylphosphino)ethane (1.10 g, 2.60 mmol). The flask was removed from the glovebox and palladium(II)acetate (0.29 g, 1.29 mmol) and 7-chloroquinaldine (11.60 g, 65.3 mmol) were added quickly against an outflow of nitrogen. The flask was sealed with a septum and tape, and DMSO (125 mL) was then introduced, followed by morpholine (17.0 mL, 194 mmol) under vigorous stirring. The headspace of the flask was evacuated and exchanged for carbon monoxide and a bubbler was attached to the flask. The flask was heated to 120 °C and allowed to stir while carbon monoxide continued to bubble through the solution. After 12 h, the brown mixture was allowed to cool to room temperature and was diluted with EtOAc (100 mL) and filtered through a pad of silica (4 cm tall x 5 cm diam.) , eluting with EtOAc (400 mL). The eluent was extracted with 1 M aqueous NaOH (6 x 100 mL), dried over anhydrous Na_2SO_4 and concentrated to afford a beige solid. The combined aqueous layers were extracted with Et_2O (4 x 100 mL) and the organic extracts were then washed with brine and concentrated to a yellow oil. The yellow oil was lyophilized using benzene until a yellow gummy solid was obtained, which was triturated with cold Et_2O to provide a beige solid. This solid was combined with the original portion to give the title compound (10.8 g, 65 %) in ~ 95 % purity (as assessed by ^{1}H NMR spectroscopy; the major impurity is phenol), and was used without further purification. A crystalline sample was obtained by slow evaporation from a saturated Et_2O solution. ^{1}H NMR 500 MHz ($CDCl_3$), δ (ppm): 8.06 (d, J = 8.5 Hz, 1H), 7.99 (s, 1H), 7.84 (J = 8 Hz, 1H), 7.55 (dd, J = 8.5, 1.5 Hz, 1H), 7.34 (d, J = 8.5 Hz, 1H), 3.4 − 3.8 (br m, 8H), 2.76 (s, 3H). 13C NMR 125 MHz ($CDCl_3$), δ (ppm): 169.9, 160.4, 147.2, 136.13,

136.10, 128.6, 127.2, 127.1, 124.7, 123.3, 67.1, 25.6. IR, neat (cm^{-1}): 2976, 2921, 2844, 1628, 1615, 1431, 1270, 1110, 856.

(2-methylquinolinyl)(morpholino)methanone-N-oxide

In a 500 mL round bottom flask charged with a stirbar and CH$_2$Cl$_2$ (250 mL) was added I (8.94 g, 34.9 mmol). With stirring, m-CPBA (~ 77 wt.%, 11.7 g, 68.0 mmol) was added and the solution was allowed to stir for 12 h. Saturated aqueous K2CO3 (200 mL) was then added and the solution was vigorously stirred for 2 h. The layers were then separated and the aqueous layer was extracted with CH$_2$Cl$_2$ (5 x 20 mL). The combined organic layers were washed with brine (50 mL) and dried over anhydrous Na$_2$SO$_4$, then concentrated to give the title compound as a beige powder (9.47 g, 99.7%). ^{1}H NMR 500 MHz (CDCl3), δ (ppm): 8.78 (s, 1H), 7.91 (d, J = 8.5 Hz, 1H), 7.68 (overlapping d's, J = 8.5 Hz, 2H), 7.39 (d, J = 8.5 Hz, 1H), 3.4 − 3.9 (br m, 8H), 2.73 (s, 3H). ^{13}C NMR 125 MHz (CDCl$_3$), δ (ppm): 169.1, 146.9, 141.0, 136.9, 129.8, 129.2, 127.0, 124.8, 124.4, 118.4, 67.0, 18.9. IR, neat (cm^{-1}): 2964, 2913, 2863, 1627, 1615, 1471, 1434, 1334, 1251, 1110, 852.

(2-(chloromethyl)quinolinyl)(morpholino)methanone

In a 100 mL Schlenk flask charged with a stir bar, tosyl chloride (1.24 g, 6.50 mmol) was dissolved in deoxygenated 1,2-DCE (60 mL) under a dry dinitrogen atmosphere. To the stirring solution was added II (1.61 g, 5.91 mmol). The mixture was allowed to reflux under nitrogen overnight. After this time, the reaction was allowed to cool to room temperature and was quenched with saturated aqueous K$_2$CO$_3$. The phases were separated and the aqueous phase was extracted with DCM (3 x 25 mL). The combined organic layers were dried over anhydrous Na$_2$SO$_4$, filtered and concentrated to afford a yellow oil. The oil was dissolved in CH$_3$CN and filtered through a pad of silica (3 cm tall x 4 cm diam.) eluting with CH$_3$CN. The eluent was

concentrated to provide a yellow oil and triturated with Et_2O to give the title compound (1.12 g, 65 %) as a beige powder in ~95% purity (as assessed by ^{1}H NMR spectroscopy; the major impurity is tosyl chloride). ^{1}H NMR 500 MHz ($CDCl_3$), δ (ppm): 8.23 (d, J = 8.5 Hz, 1H), 8.06 (s, 1H), 7.91 (d, J = 8 Hz, 1H), 7.68 (d, J = 8.5 Hz, 1H), 7.63 (dd, J = 8.5, 1.5 Hz, 1H), 4.84 (s, 2H), 3.4 − 3.9 (br m, 8H). ^{13}C NMR 125 MHz ($CDCl_3$), δ (ppm): 169.6, 158.1, 146.8, 137.3, 136.8, 128.6, 128.0, 127.8, 126.0, 121.8, 67.1, 47.3. IR, neat (cm-1): 2983, 2868, 1623, 1436, 857.

TQA'

In a 50 mL round bottom flask, III (0.52 g, 1.8 mmol) and NaI (0.54 g, 3.6 mmol) were added followed by acetone (20 mL) with stirring. The solution was heated to reflux and stirred for 2 h resulting in a slightly yellow, cloudy solution. The mixture was allowed to cool to room temperature and was concentrated to afford a yellow oil. The oil was taken up in DCM (20 mL) and water was added (20 mL). The layers were separated and the aqueous layer was extracted with DCM (3 x 20 mL) and the organic extracts were combined and dried over anhydrous Na_2SO_4, filtered and concentrated to an orange oil corresponding to the iodo-substituted product. ^{1}H NMR spectra recorded of this compound show clean and complete conversion from the chloride to iodide compound: ^{1}H NMR 400 MHz ($CDCl_3$), δ (ppm): 8.14 (d, J = 8.4 Hz, 1H), 8.03 (s, 1H), 7.86 (d, J = 8.8 Hz, 1H), 7.59 (app. t, J = 8.5 Hz, 2H), , 4.67 (s, 2H), 3.4 − 3.9 (br m, 8H). The iodo-compound thus prepared was used directly in the next step of the synthesis due to the instability of this compound. Storage on the bench top or in a freezer in the dark results in the slow decomposition of this product leading to a purple oil within less than a week.

The freshly prepared iodo-compound from above was dissolved in THF (20 mL) and NH_4OH was then added (0.24 mL, 14.8 M, 3.6 mmol). The flask was sealed and allowed to stir for 5

days. After that period, a white precipitate had appeared and was collected on a medium-porosity glass frit and washed with MeOH and then Et_2O and dried to a white powder (0.15 g, 33%). ^{1}H NMR 500 MHz ($CDCl_3$), δ (ppm): 8.14 (d, J = 8 Hz, 3H), 8.06 (s, 3H), 7.85 (d, J = 8.5 Hz, 3H), 7.77 (d, J = 8.5 Hz, 3H), 7.56 (d, J = 8 Hz, 3H), 4.15 (s, 6H), 3.4 – 3.9 (br m, 24H). ^{13}C NMR 125 MHz ($CDCl_3$), δ (ppm): 169.8, 161.1, 147.0, 136.4, 128.5, 128.0, 127.8, 125.2, 122.4, 67.1, 61.0. IR, neat (cm-1): 2847, 1628, 1457, 1238, 854.

[CuTQA'][PF6] (2.1)

In a nitrogen-filled glovebox, TQA' (82 mg, 0.11 mmol) and $Cu(CH_3CN)_4PF_6$ (39 mg, 0.11 mmol) were dissolved in 5 mL of CH_3CN in a 20 mL scintillation vial and stirred for 30 min. Et_2O (~ 2 mL) was added to the yellow solution and then was filtered through 545 Celite. Et_2O (15 mL) was added to the filtrate and the cloudy yellow mixture was placed in a -35 °C freezer overnight to produce the title compound as a light orange powder (83 mg, 74%). Crystals suitable for a single crystal X-ray diffraction experiment were grown by vapor diffusion of Et_2O into a saturated solution of the title compound in CH_3CN. ^{1}H NMR 400 MHz (CD_2Cl_2), δ (ppm): 8.72 (s, 3H), 8.35 (d, J = 8 Hz, 3H), 7.96 (d, J = 8.4 Hz, 3H), 7.65 (d, J = 8.4 Hz, 3H), 7.56 (d, J = 8 Hz, 3H), 4.62 (s, 6H), 3.3 – 4.1 (br m, 24H). IR, neat (cm^{-1}): 2859, 1637, 1435, 1301, 1277, 1244, 1113, 835. ESI-MS: 841.9 $[M-PF_6]^+$ (calc. 842.3).

Replacement of $Cu(CH_3CN)_4PF_6$ for $Cu(CH_3CN)_4ClO_4$ yields the corresponding perchlorate complex in high yield: In a nitrogen-filled glovebox, TQA' (50 mg, 0.064 mmol) and $Cu(CH_3CN)_4ClO_4$ (19 mg, 0.058 mmol) were dissolved in 10 mL of CH_3CN in a 20 mL scintillation vial and stirred for 30 min. Et_2O (100 mL) was added to the solution and the cloudy yellow mixture was filtered on a medium porosity frit. The orange solid was washed with Et_2O and dried to an orange powder (53 mg, 96%). ^{1}H NMR 400 MHz (CD_2Cl_2), δ (ppm): 8.72 (s,

3H), 8.35 (d, J = 8 Hz, 3H), 7.96 (d, J = 8.4 Hz, 3H), 7.65 (d, J = 8.4 Hz, 3H), 7.56 (d, J = 8 Hz, 3H), 4.67 (s, 6H), 3.3 – 4.1 (br m, 24H). IR, neat (cm^{-1}): 2854, 1630, 1433, 1301, 1276, 1242, 1084, 858.

[Cu(CH$_3$CN)TQA'][(ClO$_4$)$_2$] (2.2)

Method A:

In a 20 mL scintillation vial with a stir bar, Cu(ClO$_4$)$_2$•6H$_2$O (12.2 mg, 0.0329 mmol) was dissolved in 5 mL of CH$_3$CN. To the stirring pale blue solution was added solid TQA' (25.1 mg, 0.0322 mmol). The green mixture was stirred until all the solids had dissolved, then the solution was concentrated to minimal volume and filtered. Vapor diffusion of Et$_2$O directly into the filtrate provided bright green crystals which were washed with Et$_2$O and dried (32.1 mg, 92%). Crystals suitable for a single crystal X-ray diffraction experiment were grown by slow vapor diffusion of Et$_2$O into a saturated solution of the title compound in CH$_3$CN.

Method B:

In a nitrogen filled glovebox, CH$_3$CN (2 mL) was added to the solids Cu(TQA')ClO$_4$ (20 mg, 0.021 mmol) and ferrocenium perchlorate (7 mg, 0.03 mmol) with stirring. The initial blue color immediately became green and, once all of the solids dissolved, Et$_2$O (20 mL) was added to give a green precipitate. The green solid was collected on a medium porosity frit and washed with THF, then Et$_2$O, and dried to give a mint-green powder (17 mg, 74%). UV-vis, λ_{max} (ε M^{-1} cm^{-1}): 690 sh (110), 900 (290). X-band EPR 85 K (1:1 THF:CH$_3$CN): g$_\parallel$ = 2.00, g$\perp$ = 2.18, A$_\parallel$ = 72 G, A$\perp$= 86 G. IR, neat (cm^{-1}): 2860, 2322, 2293, 2250, 1622, 1604, 1441, 1301, 1280, 1251, 1081. ESI-MS (performed for **2.2-d**): 887.0 [M−2 ClO$_4$]$^+$ (calc. 886.3). Note: The use of Cu(TQA')PF$_6$ and ferrocenium hexafluorophosphate yields identical results; a green powder exhibiting identical EPR and UV-vis characterization. In our hands, we found that the synthesis of **2.2** by

Method A was less reproducible than Method B. However, **2.2** can be prepared reproducibly using Method B and therefore we advise the use of Method B for the consistent synthesis of **2.2**.

[Cu(CH₃CN)TQA][(ClO₄)₂] (2.3)

In a 20 mL scintillation vial with a stir bar, $Cu(ClO_4)_2 \cdot 6H_2O$ (17.7 mg, 0.0478 mmol) was dissolved in 5 mL of CH_3CN. To the stirring pale blue solution was added solid TQA (21.3 mg, 0.0483 mmol). The teal mixture was stirred until all the solids had dissolved, then the solution was concentrated to minimal volume and filtered. Et_2O (20 mL) was added to produce a light blue precipitate which was collected and washed with Et_2O. The solid was dried to give the title compound as a pale turquoise powder (29.4 mg, 83%). Crystals suitable for a single crystal X-ray diffraction experiment were grown by slow vapor diffusion of Et_2O into a saturated solution of the title compound in CH_3CN. UV-vis, λ_{max} (ε M^{-1} cm^{-1}): 660 (170), 845 sh (100). X-Band EPR 85 K (1:1 $THF:CH_3CN$) $g\perp$ = 2.05, $g\parallel$ = 2.27, $A\parallel$ = 153 G. IR, neat (cm^{-1}): 2317, 2288, 1603, 1515, 1433, 1084, 822. Anal calcd. for $C_{32}H_{27}Cl_2CuN_5O_8$: C, 51.66; H, 3.66; N, 9.41. Found: C, 51.71; H, 3.72; N, 9.42.

²H NMR Studies

The preparation for the CD_3CN isotopologues was analogous to the above syntheses except that CH_3CN was replaced with CD_3CN. For the analysis of the CD_3CN isotopologues, a solution containing the complex (0.02 mmol) and 0.50 mL of $MeNO_2$ with an internal C_6D_6 standard (0.002 mmol) was prepared. The spectra were recorded at 77 MHz using a Varian vnmrs 500 MHz spectrometer. Samples were allowed to fully equilibrate at the desired temperature for 5 minutes before spectra were recorded.

[(Cu(NaCN)TQA') 2H$_2$O]$_2$[(ClO$_4$)$_4$] (2.5)

In a scintillation vial in the open air, acetonitrile (5 mL) was added to solid TQA' (25.6 mg; 0.0328 mmol) and Cu(ClO$_4$)$_2$·6H$_2$O (12.6 mg; 0.0340 mmol) and stirred until a homogeneous, bright green solution was obtained. To the stirring solution, NaCN (34 μL of 0.1 M in H$_2$O; 0.034 mmol) was added and allowed to stir for 30 minutes. The solution was then concentrated to a minimal volume and diethyl ether was allowed to vapor diffuse into the solution over night to provide dark green microcrystals of the title compound (31.5 mg; 85%). UV-vis (MeCN): 645 (sh), 780 nm. A crystal of **2.5** suitable for an X-ray diffraction experiment was grown by vapor diffusion of diethyl ether into an acetonitrile solution of **2.5**.

[NiCl(TQA')][BPh$_4$] (2.8)

TQA' (100 mg; 0.13 mmol) was dissolved in methanol (20 mL) and stirred. To the stirring suspension, solid NiCl$_2$ 6H$_2$O (31 mg; 0.13 mmol) was added resulting in a light green, cloudy solution. After stirring for 2 h the solution became homogeneous, at which time NaBPh$_4$ (44 mg; 0.13 mmol, dissolved in *ca.* 2 mL methanol) was added to produce a light green precipitate. The solid was collected and dried to give the title compound as a pale green powder (125 mg; 82% yield). ^{1}H NMR 500 MHz (acetone-d_6), δ (ppm): 40.96, 29.91, 18 (v br), 15.12, 7.35 (BPh$_4$), 6.87 (BPh$_4$), 6.69 (BPh$_4$), 6.09, 3.6-4.8 (m, v br), 2.66.

Urea NMR titration of 2.8 (2.9)

Complex **2.8** (8.9 mg; 0.0075 mmol) was dissolved in acetone-d_6 (0.600 mL) in an NMR tube. To the NMR tube, aliquots of urea (0.020 μL of 0.05 M solution in acetone-d_6; 0.001 mmol) were successively added and the ^{1}H NMR spectrum was recorded at each point. A total of 9 aliquots were added (1.2 eq). After the titration, the contents of the tube were transferred to a small vial and Et$_2$O was allowed to diffuse into the solution, providing crystals of **2.9** suitable for

X-ray diffraction. ^{1}H NMR 500 MHz (acetone-d_6), δ (ppm): 38.58, 30.53, 26.40, 13.97, 13.36, 7.36 (BPh$_4$), 6.91 (BPh$_4$), 6.76 (BPh$_4$), 6.42, 5.76, 3.3-4.4 (m, v br).

Reactions with H$_2$O$_2$

In a glass UV-vis cell containing a stir bar, the copper complex (either **2.2** or **2.3**, 0.0084 mmol) was dissolved in acetone (2.5 mL). A quartz UV-vis dip probe was inserted into the cell and the apparatus was cooled in an acetone/CO$_2$ bath with stirring. Triethylamine (210 μL of a 0.2 M acetone solution; 0.042 mmol) was added and the solution was stirred briefly, then H$_2$O$_2$ (80 μL of a 0.51 M solution in acetone; 0.041 mmol) was added and the solution was stirred for 15 min while maintaining the temperature and UV-vis spectra were then recorded.

2.7 Notes and References

1.   Christianson, D. W.; Cox, J. D. *Annu. Rev. Biochem*. **1999**, *68*, 33.

2.   Jeffery, G. A.; Saenger, W. *Hydrogen Bonding in Biological Structures*; Springer-Verlag: Berlin, 1991.

3.   Hart, J. S.; White, F. J.; Love, J. B. *Chem. Commun.* **2011**, 5711.

4.   Tubbs, K. J.; Fuller, A. L.; Bennett, B.; Arif, A. M.; Berreau, L. M. *Inorg. Chem.* **2003**, *42*, 4790.

5.   Feng, G.; Mareque-Rivas, J. C.; Williams, N. H. *Chem. Commun.* **2006**, 1845.

6.   Lacy, D. C.; Gupta, R.; Stone, K. L.; Greaves, J.; Ziller, J. W.; Hendrich, M. P.; Borovik, A. S. *J. Am. Chem. Soc.* **2010**, *132*, 12188.

7.   Shook, R. L.; Borovik, A. S. *Chem. Commun.* **2008**, 6095.

8.   Mukherjee, J.; Lucas, R. L.; Zart, M. K.; Powell, D. R.; Day, V. W.; Borovik, A. S. *Inorg. Chem.* **2008**, *47*, 5780.

9.   Yamaguchi, S.; Wada, A.; Nagatomo, S.; Kitagawa, T.; Jitsukawa, K.; Masuda, H. *Chem. Lett.* **2004**, *33*, 1556.

10. Yamaguchi, S.; Nagatomo, S.; Kitagawa, T.; Funahashi, Y.; Ozawa, T.; Jitsukawa, K.; Masuda, H. *Inorg. Chem.* **2003**, *42*, 6968.

11. Wada, A.; Yamaguchi, S.; Jitsukawa, K.; Masuda, H. *Angew. Chem., Int. Ed.* **2005**, *44*, 5698.

12. Cheruzel, L. E.; Cecil, M. R.; Edison, S. E.; Mashuta, M. S.; Baldwin, M. J.; Buchanan, R. M. *Inorg. Chem.* **2006**, *45*, 3191.

13. Collman, J. P.; Gagne, R. R.; Reed, C.; Halbert, T. R.; Lang, G.; Robinson, W. T. *J. Am. Chem. Soc.* **1975**, *97*, 1427.

14. Yeh, C.-Y.; Chang, C. J.; Nocera, D. G. *J. Am. Chem. Soc.* **2001**, *123*, 1513

15. Park, Y. J.; Ziller, J. W.; Borovik, A. S. *J. Am. Chem. Soc.* **2011**, *133*, 9258.

16. Shirin, Z.; Carrano, C. J. *Polyhedron* **2004**, *23*, 239.

17. Martinelli, J. R.; Clark, T. P.; Watson, D. A.; Munday, R. H.; Buchwald, S. L. *Angew. Chem., Int. Ed.* **2007**, *46*, 8460.

18. Wei, N.; Murthy, N. N.; Chen, Q.; Zubieta, J.; Karlin, K. D. *Inorg. Chem.* **1994**, *33*, 1953.

19. Yang, L.; Powell, D. R.; Houser, R. P. *Dalton Trans.* **2007**, 955.

20. Hathaway, B. J.; Billing, D. E. *Coord. Chem. Rev.* **1970**, *5*, 143.

21. Wei, N.; Murthy, N. N.; Karlin, K. D. *Inorg. Chem.* **1994**, *33*, 6093.

22. Karlin and co-workers have previously described the synthesis and properties of $[Cu(Cl)TQA]^+$, see reference 21.

23. Addison, A. W.; Rao, T. N.; Reedijk, J.; Van, R. J.; Verschoor, G. C. *J. Chem. Soc., Dalton Trans.* **1984**, 1349.

24. Hydrogen-bonding interactions involving coordinated or free acetonitrile, while uncommon, are known. For selected examples, see refs. 25 and 26.

25. Zheng, G.-l.; Zhang, H.-J.; Song, S.-Y.; Li, Y.-Y.; Guo, H.-D. *Eur. J. Inorg. Chem.* **2008**, 1756.

26. Herres-Pawlis, S.; Floerke, U.; Henkel, G. *Acta Crystallogr., Sect. E: Struct. Rep. Online* **2006**, *E62*, m2138.

27. Steiner, T. *Angew. Chem., Int. Ed.* **2002**, *41*, 48.

28. Karlin's [Cu(Cl)TQA]PF_6 complex adopts a distorted square-pyramidal geometry, which is thought to be due to steric interactions of the bulky quinoline arms of the ligand, see reference 21.

29. Xu, X.; Maresca, K. J.; Das, D.; Zahn, S.; Zubieta, J.; Canary, J. W. *Chem.--Eur. J.* **2002**, *8*, 5679.

30. Scheiner, S. *Adv. Mol. Struct. Res*. **2000**, *6*, 159.

31. CD_3CN bands were similarly obscured by other bands. Additionally, the carbonyl vibrations of **2.1** (1630 cm^{-1}) and **2.2** (1622 cm^{-1}) in the solid state were compared. These values provide additional support for the proposed CH–O hydrogen bonding interaction, although confirmation of hydrogen bonding by Δν of a hydrogen-bond acceptor is generally less reliable than other spectroscopic methods.

32. Tsai, Y.-C.; Stephens, F. H.; Meyer, K.; Mendiratta, A.; Gheorghiu, M. D.; Cummins, C. C. *Organometallics* **2003**, *22*, 2902.

33. Johnson, A.; Everett, G. W., Jr. *J. Amer. Chem. Soc.***1972**, *94*, 1419.

34.   Lim, B. S.; Holm, R. H. *Inorg. Chem.* **1998**, *37*, 4898.

35.   Tucker, E. E.; Lippert, E. In *The Hydrogen Bond: Recent Developments in Theory and Experiments*; Schuster, P., Zundel, G., Sandorfy, C., Eds.; North-Holland: New York, 1976; pp 791−830.

36.   The observed behavior of **2.3-d** and **2.4-d** is consistent with a ligand exchange process (between free and coordinated CD_3CN) that is suppressed at low temperatures. Note that **2.2-d** does not readily undergo exchange, further supporting a hydrogen-bond stabilized CD_3CN. Additionally, the temperature dependence of **2.2-d** is consistent with intramolecular hydrogen bonding interactions previously observed for N−H resonances using ^{1}H NMR spectroscopy (i.e. small $\Delta\delta/\Delta T$ values), see Gellman, S. H.; Dado, G. P.; Liang, G.-B.; Adams, B. R. *J. Am. Chem. Soc.* **1991**, *113*, 1164.

37.   Tian, G.; Berry, J. A.; Klinmann, J. P. *Biochemistry*, **1994**, *33*, 226.

38.   Klinmann, J. P. *J. Biol. Chem.* **2006**, *281*, 3013.

39.   Kim, S.; Saracini, C.; Siegler, M. A.; Drichko, N.; Karlin, K. D. *Inorg. Chem.* **2012**, *51*, 12603.

40.   Carter, E. L.; Flugga, N.; Boer, J. L.; Mulrooney, S. B.; Hausinger, R. P. *Metallomics*, **2009**, *1*, 207.

41.   Fenton, D. A. *Proc. Indian Natn. Sci. Acad.* **2004**, *70*, 311.

42.   Kaminskaia, N. V.; Kostić, N. M. *Inorg. Chem.* **1997**, *36*, 5917.

43.   Beni, A.; Dei, A.; Laschi, S.; Rizzitano, M.; Sorace, L. *Chem.--Eur. J.* **2008**, *14*, 1804.

44.   Issleib, K.; Doell, G. *Chem. Ber.* **1963**, *96*, 1544.

45.   Kubas, G. J. *Inorg. Synth.* **1990**, *28*, 68.

46.   Lim, B. S.; Holm, R. H. *Inorg. Chem.* **1998**, *37*, 4898.

Chapter 3 Tautomerizable ligands in 3-fold symmetry

Portions of this chapter have been published:

Moore, C. M.; Quist, D. A.; Kampf, J. W.; Szymczak, N. K. *Inorg. Chem.*, **2014**, *53*, 3278. Reprinted with permission; copyright 2014 American Chemical Society.

Moore, C. M.; Szymczak, N. K. *Chem. Commun.*, **2015**, *51*, 5490. Reprinted with permission; copyright 2015 The Royal Society of Chemistry.

Moore, C. M.; Szymczak, N. K. *Chem. Sci.*, **2015**, *6*, 3373. Reprinted with permission; copyright 2015 The Royal Society of Chemistry.

3.1 Constraining the 2-hydroxypyridine motif within a tripodal framework

3.1.1 Motivation and ligand design

   Non-covalent interactions are ubiquitous in biological systems and are used to augment reactivity in many metalloenzymes through a combination of hydrogen-bonding, steric and electrostatic interactions. As a means to mimic these key aspects of metallo-biochemistry, a burgeoning number of synthetic metal complexes have been designed to include directed non-covalent interactions in order to investigate how perturbations to a metal's secondary coordination sphere can influence the reactivity at the metal's primary coordination sphere.[1]

Furthermore, directed secondary coordination sphere interactions in synthetic systems have proven to be effective for the stabilization and characterization of otherwise unstable or reactive intermediates.[2] In addition to promoting non-covalent interactions, proton transfer reactivity can also be directed by positioned acidic/basic groups.[3] Such proton-responsive ligands are attractive features of bio-inspired complexes[4] and catalysts.[5]

The recent structural elucidation of the active site of the iron-only hydrogenase enzyme revealed a derivative of 2-hydroxypyridine coordinated to iron (see Section 1.1).[6] This motif might reveal the blueprint of an evolutionarily-designed cooperative M-L proton-responsive fragment. In addition to biological relevance, complexes containing 2-hydroxypyridine units feature ligand fields that may be modulated as a function of protonation state.[7] To further extend the coordination chemistry of 2-hydroxypyridine-derived ligands, a framework was targeted that incorporates the 2-hydroxypyridine motif within an ostensibly 3-fold symmetric ligand environment reminiscent of the classic tris(2-pyridylmethyl)amine (tpa) ligand.[8]
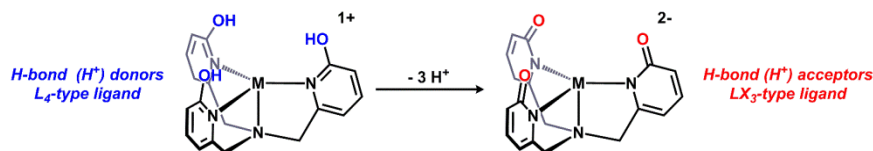
Figure 3-1. Proton-responsive ligand field presented by H$_3$thpa.

By incorporating three 2-hydroxypyridine units into a tripodal ligand, multiple metal oxidation states and/or electronic environments should be accessible by exploiting the tautomerization of the 2-hydroxypyridine units. Additionally, the ability to adapt to either hydrogen bond acceptors or donors depending on the protonation state of the ligand might be exploited to stabilize highly reactive units *via* non-covalent interactions (Fig. 3-1).

3.1.2 Ligand synthesis and solution/solid state speciation

The ligand, tris(6-hydroxypyrid-2-ylmethyl)amine (H$_3$thpa), can be synthesized in three steps

starting from commercially available 2-methoxy-6-methylpyridine (Fig. 3-2). Bromination of the

pyridine methyl group[9] and subsequent condensation with ammonium carbonate in acetonitrile at

75 °C affords tris(6-methoxypyrid-2-ylmethyl)amine (tpaOMe) in 45% isolated yield over two

steps. Deprotection of the OCH$_3$ groups could not be achieved using traditional methods (acid

hydrolysis, BBr$_3$, Me$_3$SiI, etc.).
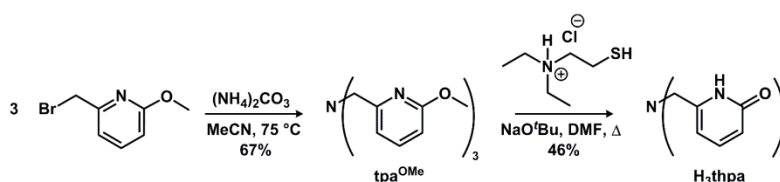
Figure 3-2. Synthesis of H$_3$thpa.

However, we found that the desired hydroxyl variant can be accessed in 46% isolated yield by

deprotection using 2-diethylaminoethanethiol hydrochloride and base in refluxing

dimethylformamide (Fig. 3-2). Given the array of substituted tpa derivatives synthesized with

hydrogen bonding functionality,[10] it is surprising that this compound has not been, to our

knowledge, previously reported,[11] and perhaps this can be attributed to the required deprotection

conditions.
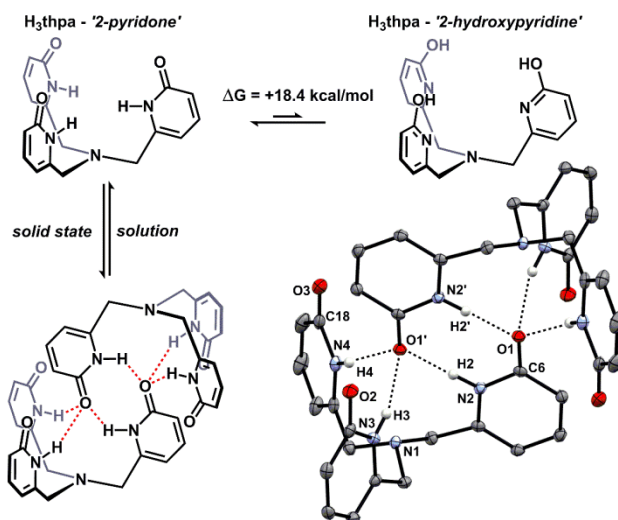
Figure 3-3. Tautomerization equilibrium for H$_3$thpa and the solid-state structure of the H$_3$thpa dimer (50% ellipsoids, H atoms not involved in hydrogen bonding omitted for clarity).

The 2-pyridone form of H$_3$thpa is favored both in DMSO-d_6 or CD$_3$OD solutions and the solid state (Fig. 3-3), as evidenced from the lack of OH bands and an intense amide C=O band in the solid state (1659 cm^{-1}) and DMSO solution (1669 cm^{-1}) IR spectra of H$_3$thpa. Density functional theory (DFT) calculations support this tautomeric form and reveal that the pyridone form is favored by 18.4 kcal/mol (Fig. 3-3). The solid state structure of H$_3$thpa is presented in Fig. 3-3 and is best described as a dimer formed via intermolecular hydrogen bonding interactions. The carbonyl group of one H$_3$thpa molecule resides within the binding pocket of its symmetry-generated duplicate and forms three hydrogen bonds with pseudo-threefold symmetry around O1'. The C-O distances in the solid state structure of H$_3$thpa (1.235(2), 1.236(2) and 1.264(2) Å) are consistent with amide-type C=O double bonds. Additionally, one arm of H$_3$thpa exhibits a slightly elongated C-O distance (C6-O1: 1.264(2) Å) due to a 'base-pair like' hydrogen bonding interaction between O1 and N2'-H2'. In contrast to the chemically-dissimilar

amide environments noted above, the ^{1}H NMR spectrum of H$_3$thpa in DMSO-d_6 or CD$_3$OD reveals 3-fold symmetry, which suggests distinct solution and solid-state stuctures.[12]

3.1.3 Coordination to copper(I) chloride

Although the amide tautomer was isolated, metalation was hypothesized to induce tautomerization to the 2-hydroxypyridine form. In a trigonal bipyramidal coordination environment, the hydroxyl groups of H$_3$thpa are ideally suited to interact with a metal-bound substrate. Given the rich coordination chemistry of copper with polyamine ligands,[13] we targeted a Cu(I) halide complex supported by the H$_3$thpa ligand to examine the influence of hydrogen bonding interactions on the metal primary coordination sphere. Reaction of CuCl and H$_3$thpa in benzene at 70 °C affords a yellow slurry, which after filtration and concentration provides CuCl(H$_3$tpha) (**3.1**) as a microcrystalline yellow powder.
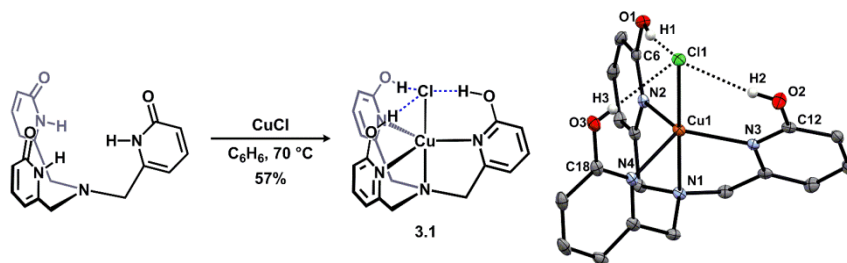
Figure 3-4. Synthesis and solid state structure of 3.1. (H atoms not involved in hydrogen bonding omitted)

The solid state IR spectrum of **3.1** confirms the tautomerization of the ligand upon metalation: a new OH band is present at 3139 cm^{-1} and the amide C=O band is absent. Vapor diffusion of diethyl ether into a dichloromethane solution of **3.1** afforded yellow crystals, which were subjected to an X-ray diffraction experiment. The solid state structure of **3.1** is depicted in Fig. 3-4 and reveals a trigonal bipyramidal coordination geometry about Cu (τ = 0.95).[14] Comparison of the Cu-Cl bond distance with the parent CuCl(tpa) (2.3976(5) Å),[15] reveals an

elongated Cu-Cl bond distance of 2.5661(6) Å in **3.1**. The lengthened Cu-Cl bond is consistent with hydrogen bonding interactions between the three hydroxyl groups of H$_3$thpa and the chloride ligand (O---Cl separations: 3.045(2), 3.057(2) and 3.042(2) Å).[4c,16] As a result of these hydrogen bonding interactions, the Cu1-N1 distance in **3.1** is also shortened relative to that of CuCl(tpa) (2.283(2) vs. 2.437(1) Å, respectively).[17] The C-O bond distances (1.335(3), 1.334(3) and 1.344(3) Å) are also consistent with single C-O bonds, further confirming the tautomeric form.

The solution structure (CD$_2$Cl$_2$) confirms retention of C_3-symmetry of **3.1** in solution, by the chemical equivalence of the three pyridine arms, as monitored by ^{1}H NMR spectroscopy at room temperature. In contrast to reports of dynamic solution behavior of Cu(tpa)X (X = Cl- or Br-) at room temperature,[17] the solution structure of **3.1** remains static, as evidenced by the narrow peak widths of the methylene resonances at room temperature ($\nu_{1/2}$ = 3.3 Hz) and invariance when measured from 40 °C to -50 °C.[18] The OH resonances of **3.1** also appear as a single, sharp resonance at 10.57 ppm ($\nu_{1/2}$ = 6.8 Hz). The static solution behavior is consistent with persistent hydrogen bonding interactions, which engage the axial chloride ligand and prevent dissociation.

3.1.4 Oxidation to copper(II)

Based on the highly directed interactions observed for **3.1**, we sought to investigate how the hydrogen bonding manifold would be modified upon electronic perturbation. Electrochemical experiments guided oxidative studies: the cyclic voltammogram of **3.1** displayed a reversible Cu(I/II) redox wave centered at 95 mV vs. SCE (Fig. 3-5).
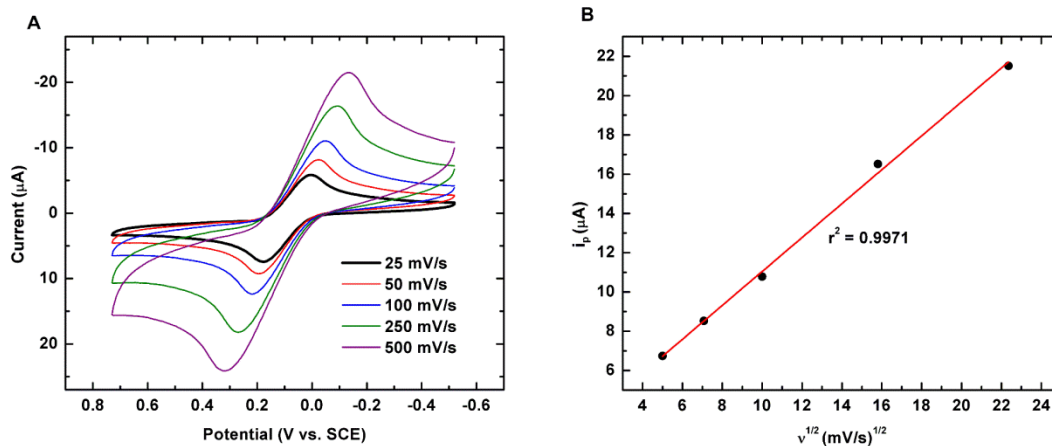
Figure 3-5. Cyclic voltammograms of 3.1 at varying scan rates (A) and scan rate dependence of the peak current (B).

Accordingly, oxidation of **3.1** was effected with one equiv. of ferrocenium hexafluorophosphate in dichloromethane to afford the Cu(II) complex **3.2** (Fig. 3-6). The X-band EPR spectrum of **3.2** in frozen dichloromethane (Fig. 3-7A) features an 'inverse-axial' spectrum ($g_\parallel = 2.010$, $A_\parallel = 81$ G, $g_\perp = 2.165$, $A_\perp = 64$ G) consistent with a Cu(II) ion in a trigonal bipyramidal coordination environment.[19]
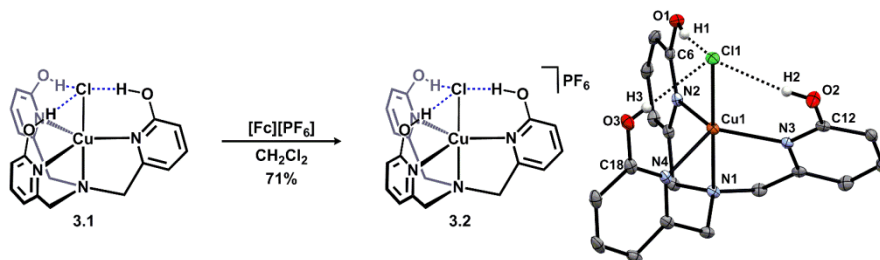
Figure 3-6. Synthesis and solid state structure of 3.2. (30% ellipsoids, counterions, solvent and H atoms not involved in hydrogen bonding interactions omitted)

As further confirmation of the solution-state structure, the electronic absorption spectrum of **3.2** (Fig. 3-7B) in dichloromethane exhibits d–d bands consistent with a trigonal bipyramidal geometry in solution ($\lambda_{max} = 913$ nm (300 mol^{-1}cm^{-1}), 740 nm (90 mol^{-1}cm^{-1})).[19] Green crystals

suitable for an X-ray diffraction experiment were obtained from vapor diffusion of diethyl ether into a dichloromethane solution of **3.2**.
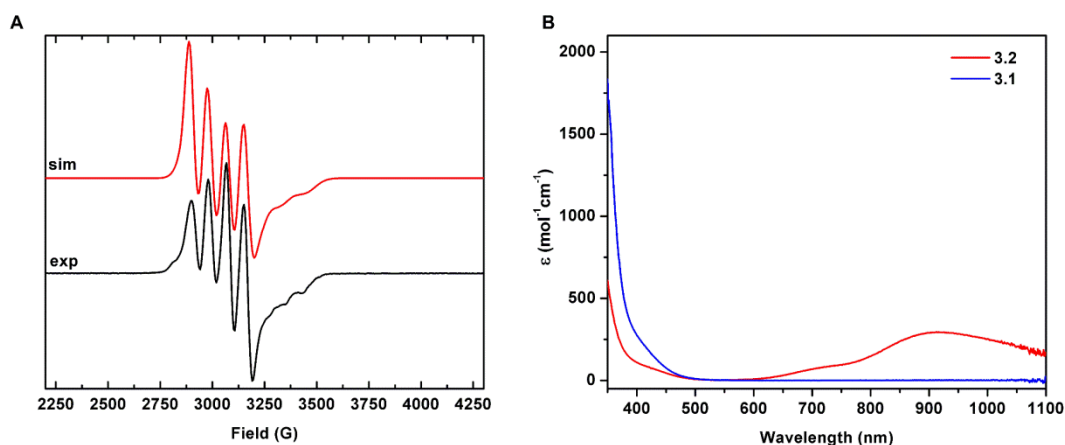
Figure 3-7. X-band EPR spectrum (A: CH$_2$Cl$_2$, 85K) and UV-vis spectrum of 3.2 (B; CH$_2$Cl$_2$).

The solid state structure of **3.2** contains two independent molecules in the unit cell. One cation is depicted in Fig. 3-6 and reveals a trigonal bipyramidal geometry ($\tau = 0.93$), similar to **3.1**, with key differences. The Cu-Cl bond in **3.2** (2.263(2) Å) is, as expected, much shorter than **3.1**. The O---Cl separations (2.876(6), 2.912(5) and 2.997(5) Å) are also consistent with intramolecular hydrogen bonding interactions as in **3.1**.[16] Comparison with the corresponding CuCl(tpa)$^+$ complex reveals a marginal elongation of the Cu-Cl distance in **3.2** (2.263(2) vs. 2.233(2) Å, respectively).[20,21] These results indicate hydrogen bonding interactions between the OH groups and the Cl ligand may be weaker in **3.2** compared to **3.1** due to decreased electron density at the chloride ligand adjacent to a more electropositive Cu(II) ion. The Cu1-N1 distance in **3.2** is also drastically shortened (1.990(3) Å) in relation to **3.1**, consistent with the increased electrophilicity at copper.

3.1.5 Quantifying hydrogen bonding interactions

In order to further quantify effects of hydrogen bonding interactions of H$_3$thpa, **3.1** and **3.2**, and effects on substrate binding, DFT calculations were employed. Optimization and frequency calculations were performed on the hydroxy tautomer of H$_3$thpa to determine the OH stretching frequency in the absence of intermolecular hydrogen bonds (3620 cm^{-1}). Similarly, the asymmetric OH stretching frequencies for **3.1** and **3.2** were calculated as 3228 cm^{-1} and 3377 cm^{-1}, respectively. Although the absolute frequency shift was overestimated[4c] as compared to the experimental values for **3.1** and **3.2** (3139 cm^{-1} and 3273 cm^{-1}), the difference in shifts upon oxidation of **3.1** to **3.2** is well reproduced by the calculations ($\Delta v = 149$ cm^{-1} vs. 134 cm^{-1}). The bathochromic shift of the OH bands relative to free H$_3$thpa is consistent with hydrogen bonding interactions: the shift arising from electron donation from the chloride ligand into the O-H σ^* orbitals, thus weakening the bond. In **3.1**, the OH stretch is even further shifted than in **3.2**, consistent with stronger hydrogen bonding interactions in **3.1** due to the increased nucleophilic character on the Cl atom.[4c,22] The shift of the OH bands, relative to free H$_3$thpa, can be used to approximate the strength of the hydrogen bonding interactions using a methodology described by Iogansen, yielding values of 6.1 kcal/mol for **3.1** and 4.8 kcal/mol for **3.2** per each hydrogen bond.[22,23] As a structural manifestation of hydrogen bonding effects, the Cu-Cl bond in **3.2** is significantly shorter, and likely stronger, than the Cu-Cl bond in **3.1**. The weakening of the Cu-Cl bond in **3.1** enhances the ionic nature of the chloride ligand and promotes stronger donation into the O-H σ^* orbital.

The structural data allude to an axial Cu-Cl bond whose stability might be regulated by secondary interactions. To further quantify this effect, the thermodynamics of the H-bonding interactions in **3.1** were examined using CuCl(tpa) to benchmark our studies. The ionization

reaction shown in Fig. 3-8 was investigated for both complexes. For CuCl(tpa), dissociation of the chloride ligand to afford the axially-vacant [Cu(tpa)]$^+$ was found to be an overall uphill reaction by 6.3 kcal/mol. For **3.1**, chloride dissociation to afford [Cu(H$_3$thpa)]$^+$ was endergonic by 24.3 kcal/mol. While the Cu-Cl bond distance in **3.1** is significantly lengthened in comparison to CuCl(tpa), *vide supra*, the results from our calculations demonstrate that chloride dissociation from **3.1** is energetically more costly than in CuCl(tpa).

$\Delta G = + 6.3$ kcal/mol (R = H)
$\Delta G = + 24.3$ kcal/mol (R = OH)
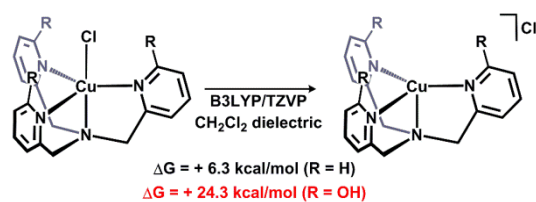
Figure 3-8. DFT-calculated chloride dissociation energies.

This difference (18 kcal/mol) is likely attributable to chloride stabilization through non-covalent interactions and can be used to estimate an upper limit of the strength of the hydrogen bonding interactions in **3.1** (~6 kcal/mol per H-bond). Furthermore, the C_3-symmetry of **3.1** is maintained in solution. In contrast, dissociation of the pyridyl-arms has been reported for Cu(tpa)Cl.[17] These data are consistent with stabilization of the primary coordination geometry of **3.1** *via* hydrogen bonds to the chloride ligand, which are responsible for maintaining the 3-fold symmetric structure.

3.2 Stabilization of copper fluoride adducts via hydrogen bonding

Although transition metal fluoride complexes featuring early metals have been well-described in the literature, examples with late metals are considerably rarer.[24] Recent reports have implicated such species as key actors in catalytic fluorination chemistry.[25] Specifically, copper complexes have received considerable interest as cheap, abundant reagents for (catalytic) C-F bond formation[26] and thus, there is a high interest in synthetic strategies that afford Cu-F

intermediates.[27] The disparity between the π-donating nature of fluoride and the filled d-orbitals of low valent group 11 metals generally leads to highly labile M-F bonds.[28] Despite this, a handful of monomeric copper(I) fluoride complexes have been reported. Prior examples use N-heterocyclic carbenes,[29] bipyridine,[30] and/or phosphines[31] as supporting ligands. Metal fluorides are prolific hydrogen bond acceptors,[32] and in all of the prior reported terminal Cu-F adducts (both Cu^I and Cu^{II}), inter- or intramolecular H-bond interactions with the fluoride ligand accompany metal coordination in the solid state.[33] These interactions are so favorable that even very weak hydrogen bond donors, such as weakly acidic C-H groups participate in non-covalent interactions with the M-F unit.[34] Unfortunately, strategies that incorporate the rational design of these interactions to promote F- binding in close proximity to a metal site (that might support M-F binding) are not well explored.[35]

We postulated that an axial fluoride ligand would show enhanced hydrogen bonding interactions when compared to the chloride congener (i.e. **3.1** or **3.2**) and provide entry into a predictive platform to construct and evaluate M-F interactions. Furthermore, we hypothesized that the highly directed hydrogen bonding interactions provided by H_3thpa would be ideally suited to stabilize reactive, low valent Cu-F units. In this section, the synthesis of copper fluoride complexes supported by H_3thpa is described and we demonstrate that upon reduction from copper(II) to copper(I), Cu-F bond dissociation occurs to yield a remarkable copper(I) complex with a fluoride anion encapsulated in the secondary coordination sphere *via* hydrogen bonding.

3.2.1 Synthesis and characterization of a copper(II) fluoride

We first interrogated H-bonding interactions between H_3thpa and coordinated fluoride by preparing a copper(II) fluoride complex. Treatment of H_3thpa with $Cu(SO_4) \cdot 5H_2O$ and $NaBF_4$ in

methanol, followed by CsF cleanly provided the copper(II) fluoride complex $CuF(H_3thpa)BF_4$ (**3.3**) in 77% yield.
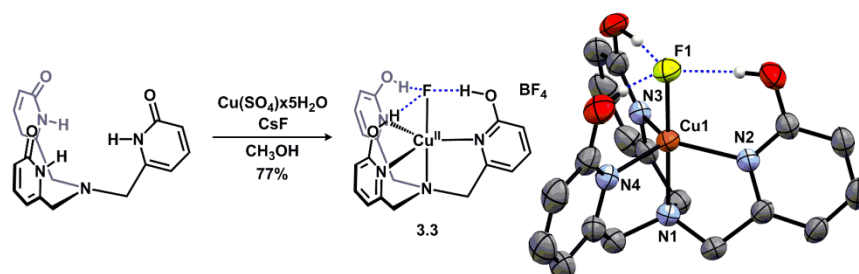
Figure 3-9. Synthesis and solid state structure of 3.3. (30% ellipsoids, counterion and H atoms not involved in hydrogen bonding omitted)

The absence of C=O stretches and presence of sharp O-H stretches in the IR spectrum of **3.3** confirms ligand tautomerization (2-pyridone/2-hydroxypyridine) upon metalation. By using the methodology described in the previous section for copper chloride complexes, the position of the OH stretching frequency can be used to approximate the upper limit of hydrogen bonding strength in **3.3**.[23] As anticipated for the potent hydrogen bond accepting fluoride ligand, each hydrogen bonding interaction in **3.3** is significantly stronger ($\Delta H^o_{H\text{-bond}}$ = -6.0 kcal/mol) than in the corresponding $CuCl(H_3thpa)^+$ complex **3.2** ($\Delta H^o_{H\text{-bond}}$ = -3.8 kcal/mol). Furthermore, the solution state structure of **3.3** was interrogated by UV-vis and EPR spectroscopies, both revealing that **3.3** is trigonal bipyramidal (TBP) in solution, very similar to **3.2** (Fig 3-10).[19]
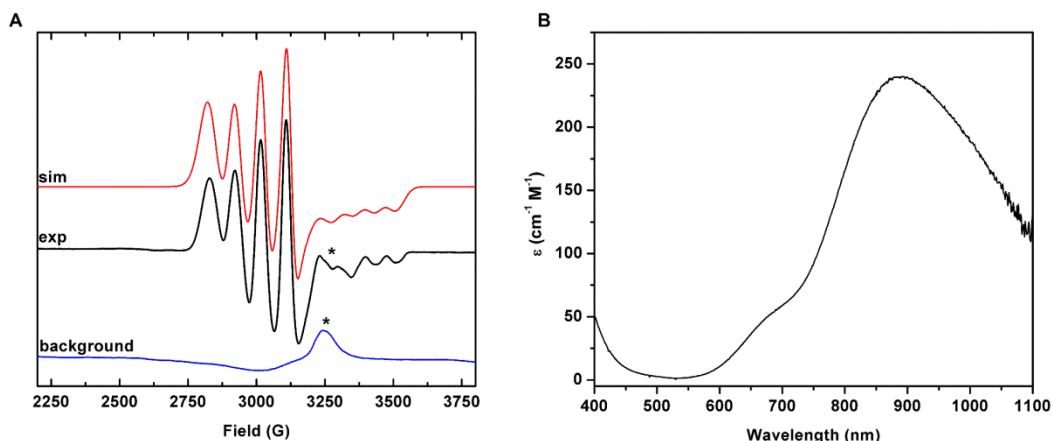
Figure 3-10. EPR spectrum (A; CH_2Cl_2, 85K) and UV-vis spectrum of 3.3 (B; CH_2Cl_2).

Crystals of **3.3** were subjected to an X-ray diffraction experiment and the solid state structure is depicted in Fig. 3-9. The TBP coordination geometry in **3.3** is maintained in the solid state structure. Notably, the F---O separations in **3.3** (2.578(5), 2.641(5) and 2.668(4) Å) are consistent with intramolecular hydrogen bonding interactions.[16] The Cu-F bond distance in **3.3** (1.925(2) Å) is elongated in comparison to the 'parent' tpa (tpa = tris(2-pyridylmethyl)amine) complex $CuF(tpa)PF_6$ (1.852 Å),[36] and consistent with intramolecular hydrogen bonding interactions serving to remove electron density from the fluoride ligand.

3.2.2 Isolation of a copper(I) fluoride complex

Cyclic voltammetry experiments were conducted in order to ascertain the stability of a putative Cu(I) fluoride supported by H_3thpa. Fig. 3-11 shows the cyclic voltammograms of **3.3** in CH_2Cl_2 solution with $[^nBu_4N][PF_6]$ as supporting electrolyte. The reduction of **3.3** is reversible ($i_{pa}/i_{pc} = 1.02$) and has a peak separation similar to that of ferrocene under identical conditions (Fig. 3-11C).
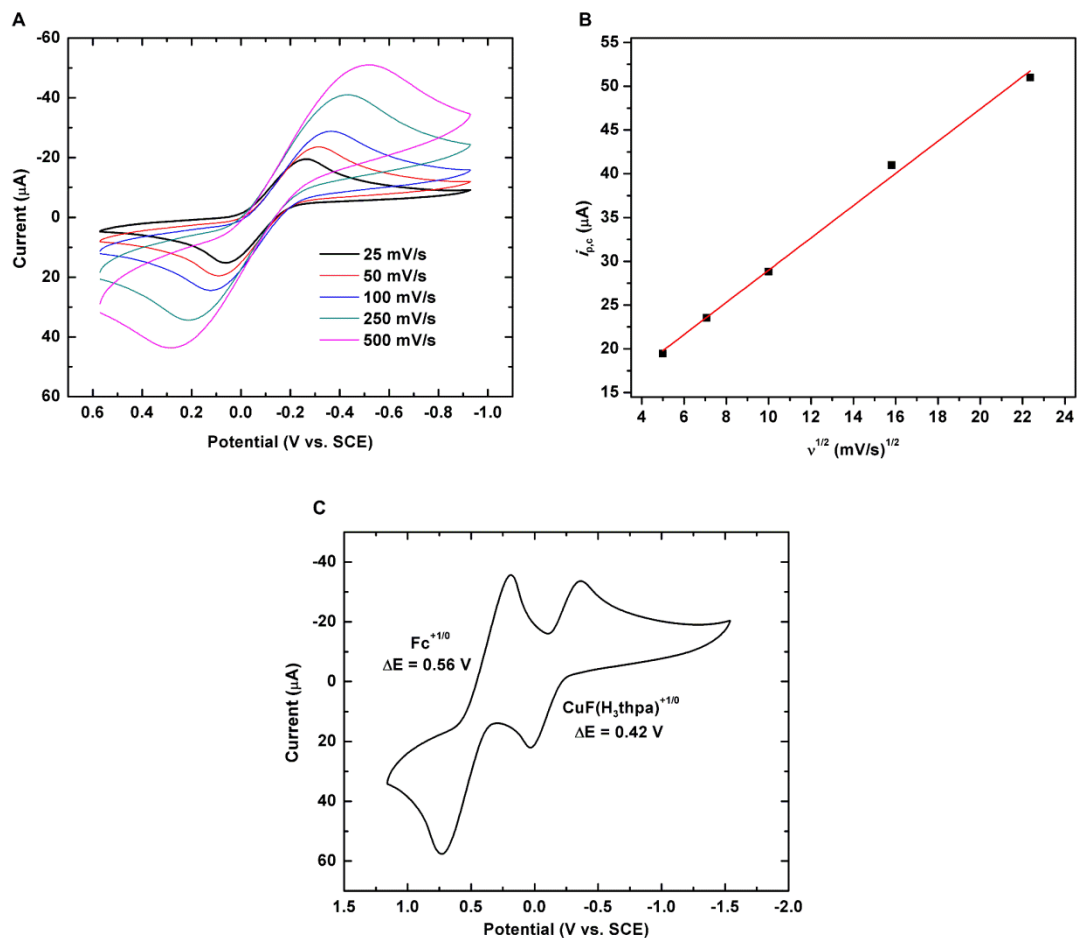
Figure 3-11. Cyclic voltammograms of 3.3 at varying scan rates (A) the scan rate dependence of the peak current (B) and comparison of peak separation to ferrocene (C).

The redox potential of **3.3** ($E_{1/2}$ = -0.195 V vs. SCE) is cathodic of the corresponding CuCl(H$_3$thpa)$^+$ complex **3.2** ($E_{1/2}$ = +0.095 V vs. SCE), and consistent with the higher electronegativity of the fluoride ligand compared to chloride.
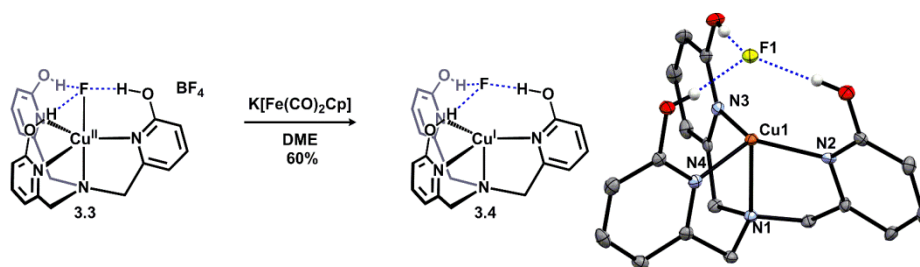
Figure 3-12. Synthesis and crystal structure of 3.4. (30% ellipsoids, H atoms not involved in hydrogen bonding omitted)

Chemical reduction of **3.3** with K[Fe(CO)$_2$Cp] afforded the neutral, copper(I) fluoride adduct **3.4** (Fig. 3-12). Solution (CD$_2$Cl$_2$) ^{1}H NMR spectra of **3.4** display ligand resonances characteristic of 3-fold symmetry.[37] The OH resonances in **3.4** appear at 12.90 ppm as a broad singlet ($v_{1/2}$ = 26.7 Hz) at 25 °C. Cooling the sample to -25 °C, the OH signal evolves into a doublet with a coupling constant of 49.5 Hz (Fig. 3-13A; bottom). Upon ^{19}F-decoupling at -25 °C, the doublet collapses into a singlet, confirming the observed coupling is due to F (Fig. 3-13A; top). The magnitude of $^1J_{H-F}$ (49.5 Hz) is comparable to that observed for the [F(HF)$_3$]$^-$ anion ($^1J_{H-F}$ = 41 Hz), which has D_{3h} symmetry.[38] The ^{19}F NMR spectrum of **3.4** displays a single, broad ($v_{1/2}$ = 110 Hz) resonance at -109 ppm (Fig. 3-13B), which is drastically different than previously reported Cu(I)-F complexes (^{19}F NMR signals ranging from -200 to -250 ppm)[29,31] and more closely resembles the ^{19}F chemical shift of hydrated F$^-$ (δ = -119).[39]

94
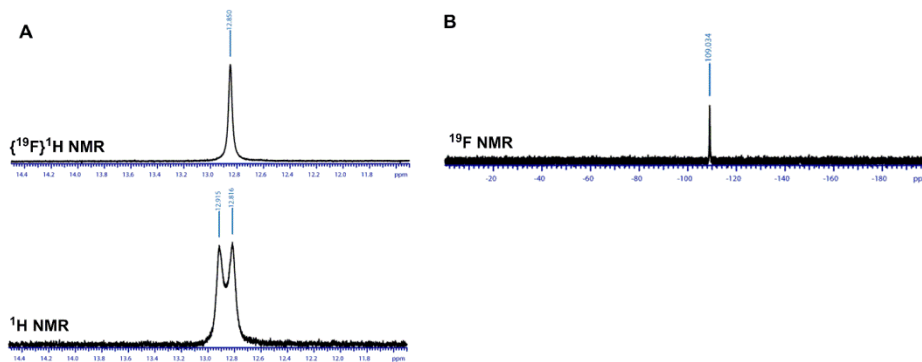
Figure 3-13. ^{1}H NMR spectra of 3.4 at -25 ° C (A; ^{19}F decoupled on top, coupled on bottom) and the ^{19}F NMR spectrum of 3.4 (B).

The NMR spectroscopic analysis of **3.4** above alludes to a magnetic environment around fluorine that is weakly (or not) interacting with a copper center. This interaction was clarified by analysis of the solid state structure of **3.4**, which displays approximate C_{3V} symmetry (Fig. 3-12). The separation between Cu and F in the solid state structure is 2.469(2) Å. This value is significantly longer than the sum of the Shannon ionic radii of Cu and F (1.885 Å),[40] suggesting little to no covalent bonding between the two atoms in the solid state structure. The Cu-N1 distance of 2.218(3) Å in **3.4** is also elongated with respect to **3.3** (1.995(3) Å), consistent with a decreased Lewis acidic metal center upon reduction. The O---F distances in **3.4** (2.576(4), 2.581(4) and 2.585(3) Å) are, on average, shorter than those found in **3.3** (*vide supra*), highlighting the increased electron density on F and stronger H-bonding interactions in **3.4** with respect to **3.3**.

To further support the absence of bonding interactions between Cu and F, density functional theory (DFT) calculations of **3.4** were undertaken. The B3LYP functional[41] and TZVP basis set[42] were employed and all calculations used an implicit CH_2Cl_2 solvation through a polarizable continuum model.[43] Good agreement between the X-ray structure and calculated structure of **3.4** was found. Fig. 3-14 shows a qualitative molecular orbital diagram of **3.4**. The highest occupied

molecular orbital (HOMO) of **3.4** primarily arises from the $3d_{z^2}$ orbital on Cu (80.4%) with only a small contribution from the F $2p_z$ orbital (3.9%). The interactions between filled Cu $3d$ (d_{xz}, d_{yz}, d_{xy}, $d_{x^2-y^2}$ and d_{z^2}) orbitals and F $2p$ orbitals all are of anti-bonding character.
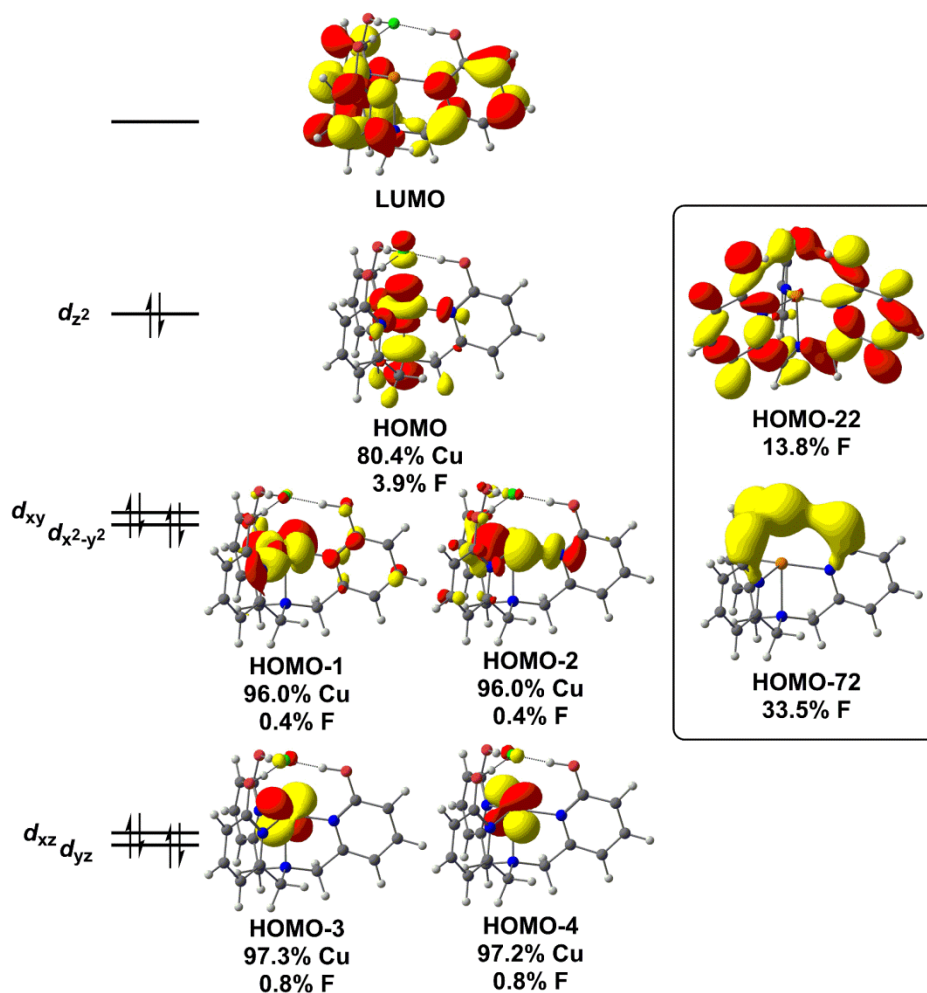
Figure 3-14. DFT-calculated qualitative molecular orbital (MO) diagram and orbital compositions of 3.4 (isovalue 0.03) and representative MO's involved in hydrogen bonding with F⁻ in 3.4 (inset; isovalue 0.03).

The lowest unoccupied molecular orbital (LUMO) of **3.4** primarily consists of π^* orbitals on the pyridine rings of the H$_3$thpa ligand. Representative molecular orbitals (HOMO-22 and HOMO-72) involved in hydrogen bonding are also depicted in Fig. 3-14: the σ interactions of F $2p$ and $2s$ orbitals (respectively) with the OH groups of H$_3$thpa. A natural population analysis[44] of **3.4**

found electrostatic charges of +0.54 for Cu and -0.77 for F. The H atoms involved in hydrogen bonding with F were found to have electrostatic charges of +0.523. When the F was removed and natural population analysis was carried out on the cationic fragment $Cu(H_3thpa)^+$, the H atoms were found to have electrostatic charges of +0.470, highlighting the polarization of the H atoms due to hydrogen bonding to F. A natural bond orbital (NBO) analysis[44b] on **3.4** found no covalent bonding interactions between Cu and F. Additionally, the donor-acceptor interactions for hydrogen bonding in **3.4** were found to have a total second order stabilization energy of 65.7 kcal/mol (*ca.* 22 kcal/mol per OH group). A Wiberg bond index[45] between Cu and F was calculated to be 0.12. Taken together, the DFT calculations are consistent with interactions between Cu and F as primarily electrostatic in nature with little covalency between the two atoms.
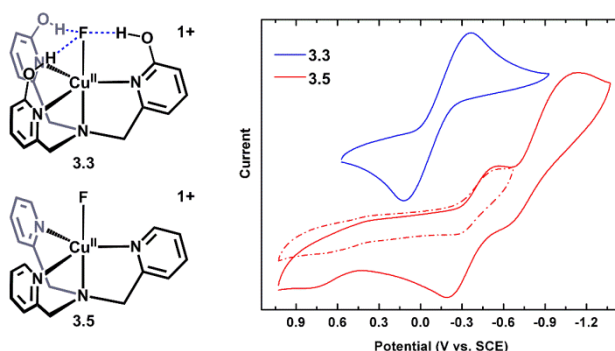
Figure 3-15. Comparison of the cyclic voltammograms of 3.3 and 3.5 at 100 mV/s scan rate in 0.1 M [$^nBu_4N$][PF_6] CH_2Cl_2.

Given the unusual accessibility and stability of both Cu(II) and Cu(I) fluoride species, we sought to evaluate the degree to which stability is imparted by the ligand's secondary coordination environment. Unsubstituted tpa was selected as a comparative tripodal ligand that does not contain groups capable of engaging in non-covalent interactions. We prepared Karlin's CuF(tpa)PF_6 (**3.5**)[36] *via* a modified procedure and examined its reductive electrochemistry.

Unlike **3.3**, the cyclic voltammogram of **3.5** displays two irreversible reductive events (Fig. 3-15). The first reductive wave centered at *ca.* -0.5 V vs. SCE may be due to an irreversible Cu(II/I) redox couple (see dashed inset in Fig. 3-15) and we propose the second feature centered at *ca.* -1.1 V is due to deposition of Cu^0 on the electrode surface based on the appearance of a stripping wave (*ca.* -0.2 V) upon reversal of potential during the cyclic voltammetry experiment. This reductive instability of the 'parent' $CuF(tpa)^+$ complex is in stark contrast to **3.3**, which is reductively stable to -1.5 V vs SCE. Furthermore, attempts to chemically reduce **3.3** with reductants such as $[Co(C_5H_5)_2]$ have led to intractable mixtures containing highly insoluble black material, most consistent with Cu^0. Thus, the presence of the OH groups in **3.3** serve to greatly enhance the reductive stability of the tripodal copper fluoride complexes and are required for the generation of stable copper(I) fluoride adducts.

3.3 Reactivity toward nitrite

3.3.1 Motivation from Nature: Nitrite reductase

Nitrite reductases (NiRs) are enzymes found in prokaryotic organisms which catalyze the one-electron (e^-) reduction of nitrite to nitric oxide (NO).[46] Copper nitrite reductases (CuNiRs) are homotrimeric enzymes with each monomer containing two copper centers: a T1 site for electron transfer, and a catalytically-active T2 site.[47] Although X-ray crystallographic studies have provided structural snapshots of intermediates along the reduction pathway,[48] the precise mechanism by which CuNiR catalyzes nitrite reduction has been disputed.[46c] In one proposed pathway, nitrite coordinates to the reduced T2 center, then following two proton (H^+) transfer events, water is released and a copper-nitrosyl species is generated (described as either Cu(I)-NO^+ or Cu(II)-NO); Fig. 3-16A).[48c,49]
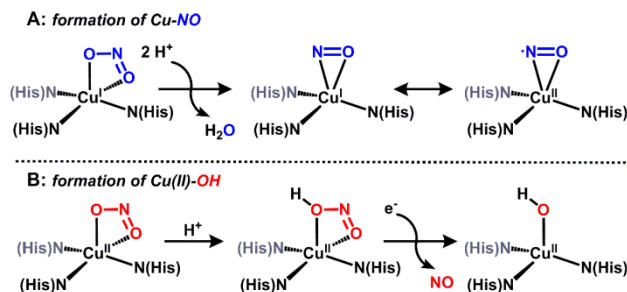
Figure 3-16. Proposed pathways for nitrite reduction in CuNiR.

In support of this mechanism, a crystal structure of CuNiR with NO bound to the reduced T2 site was reported with an unusual side-on binding mode of NO,[50] which suggests that NO coordination to copper is at least possible under reducing conditions.[51] However, an oxidized Cu(NO) unit (i.e. Fig. 3-16A) would be capable of nitrosylating nearby amino acid residues,[52] and thus is unlikely to be formed under catalytic conditions. An alternative pathway for nitrite reduction catalyzed by CuNiR has been described wherein nitrite first coordinates to the oxidized T2 center followed by H^+ transfer from a nearby aspartic acid residue to protonate the coordinated nitrite.[53] In this case, protonation of nitrite triggers e^- transfer from the T1 center to the T2 center, with release of NO to form a copper-hydroxide (Fig. 3-16B). This mechanism is consistent with isolated crystal structures of CuNiR with nitrite bound to the oxidized T2 center,[48c] steady-state kinetics and pulsed radiolysis experiments,[54] and computational modeling.[55] Although the intimate pathway of nitrite reduction may be disputed, the network of hydrogen bonds provided by nearby amino acid residues is widely accepted to play a key role in positioning substrate and facilitating e^- transfer.[46c]

With the goal of clarifying the fundamental pathways of nitrite reduction, the reactivity of synthetic copper complexes toward nitrite has been extensively studied,[46c] although limited examples have been reported that demonstrate secondary sphere interactions with a copper nitrite

complex.[56] Prior reports have largely focused on the preparation of copper(I) nitrite adducts and subsequent reactivity with exogenous H^+ sources to release NO. One critical distinction between synthetic copper(I) nitrite adducts and CuNiR is the observed mode of nitrite coordination: there are no reported synthetic copper(I) complexes supported by biologically-relevant ligands that feature the κO-nitrite coordination observed in CuNiR, and instead exclusively feature κN-coordination.[57]

While select systems have been shown to produce NO from a copper(I) nitrite complex,[46c,58] the mechanism by which these reactions proceed are often not fully resolved, thus precluding direct mechanistic comparisons to CuNiR. One reason for limited mechanistic insight has been the isolation of terminal copper(II) complexes which do not contain the inorganic products of nitrite reduction (i.e. H_2O or NO).[58b,58d,58f] Although copper(II)-nitrosyls have been implicated in many synthetic nitrite reduction pathways, their isolation has remained elusive,[52b,59,60] thus calling into question their role in synthetic and biological copper nitrite reduction schemes.

A nitrite reduction pathway that circumvents the formation of a highly reactive copper-nitrosyl species is likely operative in CuNiR (Fig. 3-16B). In this section, we demonstrate that nitrite reduction by a copper complex supported by a proton-responsive ligand proceeds through a parallel pathway. A mechanism is described whereby a H^+/e^- transfer pathway to nitrite releases NO, which bypasses the formation of an unstable copper(II)-nitrosyl species, and provides a synthetic mechanistic analogue for nitrite reduction in CuNiR.

3.3.2 Reactivity toward silyl-nitrite

We envisioned that anions capped by SiR_3^+ units would react with **3.4** *via* metathesis to provide new copper complexes in which we could interrogate hydrogen bonding and H^+/e^- transfer reactivity toward reducible substrates. Specifically, we sought to exploit this

methodology to examine the reactivity of **3.4** with nitrite in an effort to experimentally distinguish between two mechanistic pathways of nitrite reduction. Given the capability of the H_3thpa ligand scaffold to deliver H^+ and subsequently provide hydrogen bond donors and acceptors, we hypothesized that the inorganic products of nitrite reduction would be captured within a hydrogen bonding network surrounding the copper center.
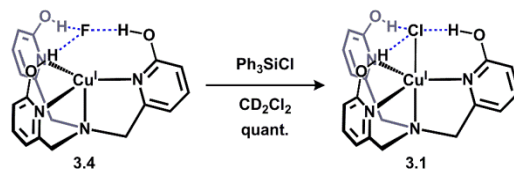
Figure 3-17. Reaction of 3.4 with Ph₃SiCl yields 3.1.

In order to assess the ability of **3.4** to engage in metathesis reactivity with silyl-anions, we first examined the substitution of the fluoride anion in **3.4** for chloride. When **3.4** was treated with an equivalent of Ph_3SiCl at room temperature, the previously described $CuCl(H_3thpa)$ complex **3.1** and Ph_3SiF were generated quantitatively; both of which were confirmed by ^1H and ^{19}F NMR spectroscopy. Based on the clean reactivity observed with Ph_3SiCl, we synthesized a reagent capable of transferring nitrite to **3.4** by preparing $Ph_3Si(ONO)$ *via* salt metathesis of Ph_3SiCl and $AgNO_2$ in benzene solvent.[61]

The reaction of **3.4** with $Ph_3Si(ONO)$ occurs immediately in dichloromethane solvent: when $Ph_3Si(ONO)$ is added to a yellow solution of **3.4**, a rapid color change to green occurs. ^{19}F NMR spectra of the resulting solution confirm the quantitative formation of Ph_3SiF, indicating metathesis of fluoride. The color change is indicative of oxidation from copper(I) to copper(II), a supposition confirmed by EPR and UV-vis spectra collected of reaction solutions. For instance, UV-vis spectra collected during the reaction between **3.4** and $Ph_3Si(ONO)$ at 0 °C are presented in Fig. 3-18A. The spectra reveal a clean formation (isosbestic point near 525 nm) to a new

copper(II) containing product. Additionally, the EPR spectrum of a reaction mixture of **3.4** and Ph$_3$Si(ONO) shows an inverse-axial signal characteristic of a TBP copper(II) complex (Fig. 3-18B).[19]
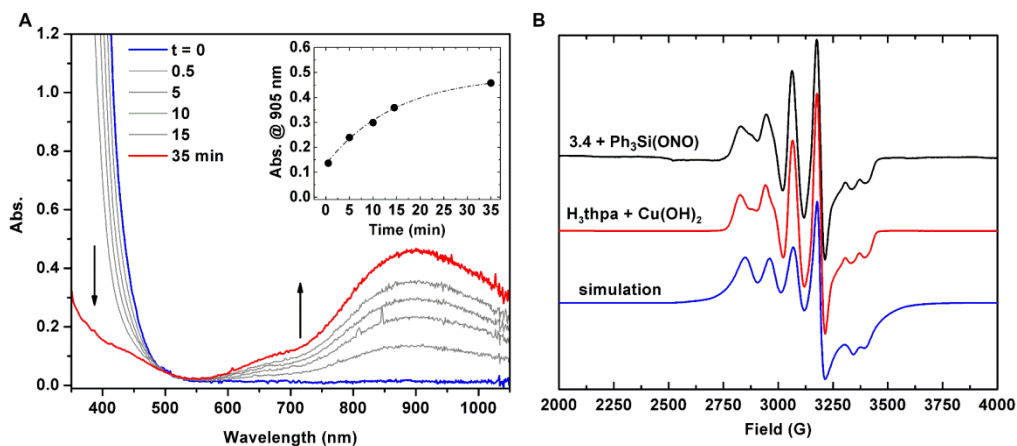
Figure 3-18. UV-vis monitoring of the reaction of 3.4 with Ph$_3$Si(ONO) at 0 °C (A; CH$_2$Cl$_2$) and EPR spectra of the reaction mixture (B; CH$_2$Cl$_2$, 85 K).

Solid state IR spectra of the isolated green material from this reaction do not show bands associated with nitrite or a metal-nitrosyl species, however a new ligand C=O stretch at 1658 cm^{-1} was visualized (consistent with a change in protonation state of the ligand), along with broadened OH bands. Based on the above findings, we hypothesized that the terminal copper-containing product in this reaction was a copper(II)-aquo complex (Cu(OH$_2$)Hthpa, **3.6**, Fig. 3-19).
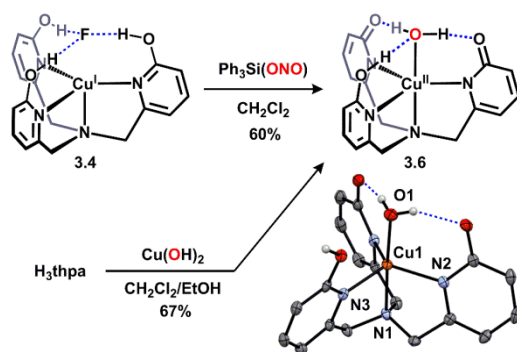
Figure 3-19. Syntheses and crystal structure of 3.6. (30% ellipsoids, solvent and H atoms not involved in hydrogen bonding interactions omitted)

3.3.3 Characterization of copper-containing product upon nitrite reduction

We sought an alternative preparation of **3.6** to confirm its formation during the reaction of **3.4** with Ph$_3$Si(ONO). Authentic samples of complex **3.6** were prepared by allowing equimolar amounts of the ligand, H$_3$thpa, and Cu(OH)$_2$ to react in dichloromethane/ethanol solution. The solution characterization data (UV-vis and EPR) for **3.6** prepared in this manner were identical to those from the reaction of **3.4** with Ph$_3$Si(ONO), as shown in Fig. 3-18B. The crystal structure of **3.6** contains two independent molecules along with an ethanol solvate which is engaged in H-bonding interactions with only one of the molecules. The solid state structure of one of the independent molecules of **3.6** is presented in Fig. 3-19 and reveals a trigonal bipyramidal coordination geometry at copper, consistent with the solution state coordination geometry as determined by EPR and UV-vis spectroscopy. The Cu-OH$_2$ unit is coordinated at a distance of 1.956(2) Å from copper and features hydrogen bonds (O---O separations 2.567(3) and 2.664(3) Å) to the asymmetric Hthpa ligand. The asymmetry of the ligand environment is confirmed by examination of the ligand's C-O bond lengths (1.299(3) Å and 1.284(3) Å for the deprotonated 'arms' and 1.325(3) Å for the protonated 'arm') which reflect the anionic nature of the two ligand 'arms'. The protonated 'arm' (N3) is engaged in intermolecular hydrogen bonding

103

interactions with another molecule of **3.6**, as opposed to the Cu-bound O atom. This network of intermolecular hydrogen bonding, which forms a 1-D chain in the extended structure, is presumably a manifestation of crystal packing and unlikely to persist in solution under dilute conditions.[62]

3.3.4 Confirmation of NO formation and control experiments

In addition to the formation of **3.6** from **3.4** and Ph$_3$Si(ONO), NO was also confirmed as a reaction product by gas-phase IR spectroscopy, as well as by trapping experiments with CoTPP (TPP = tetraphenylporphyrin) and quantification using UV-vis spectroscopy.[63] Headspace analysis of reaction mixtures revealed two broad bands at 1904 and 1844 cm^{-1} in the IR spectrum, consistent with NO, as well as bands associated with dichloromethane solvent vapors (Fig. 3-20).
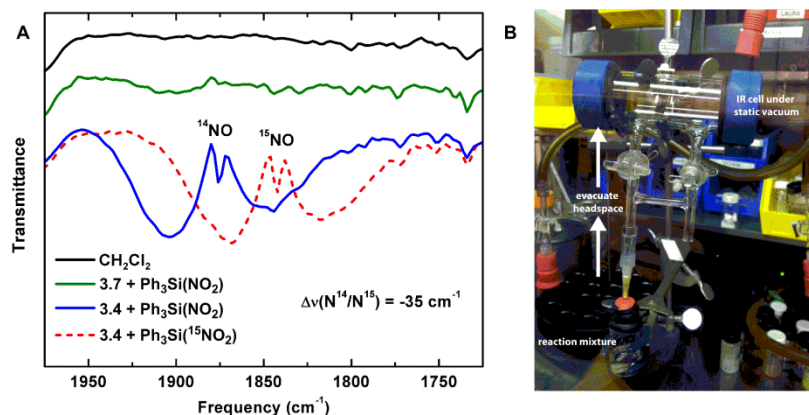
Figure 3-20. Gas-phase IR spectra of reaction products (A) and set-up used to collect headspace measurements (B).

To further support the assignment of gaseous NO as a by-product, we prepared the ^{15}N isotopologue, Ph$_3$Si(O^{15}NO), and allowed it to react with **3.4**. Headspace analysis of the reaction mixture by IR spectroscopy showed two broad bands at 1868 and 1817 cm^{-1}, consistent with

[15]NO, further substantiating NO formation during the reaction of **3.4** and Ph$_3$Si(ONO). The formation of NO was quantitative, as revealed by CoTPP trapping experiments.

Control reactions confirmed that the quantitative generation of NO was unique to **3.4**. For instance, to examine whether a direct reaction of the silyl-reagent with a metal fluoride induced NO extrusion, we performed a control experiment where the known copper(I) fluoride CuF(PPh$_3$)$_3$ (**3.7**)[64] was allowed to react with Ph$_3$Si(ONO).[65] Headspace analysis of this reaction mixture by IR spectroscopy revealed negligible bands associated with NO (Fig. 3-20). Trapping experiments with CoTPP did not reveal any significant formation of NO above the background during the reaction of **3.7** and Ph$_3$Si(ONO).

The quantitative yield of NO from complex **3.4** cannot be attributed solely to a disproportionation reaction of nitrite. Under sufficiently acidic conditions, nitrite disproportionates to form NO, along with other NO$_x$ species.[66] To examine a possible acid-promoted nitrite disproportionation pathway that produces NO, we probed the reactivity of Ph$_3$Si(ONO) with CuF(H$_3$thpa)BF$_4$ (**3.3**).

Complex **3.3** serves as an ideal platform to test the ability of the ligand framework to deliver H$^+$ equivalents to nitrite since (1) e$^-$ transfer is not possible and (2) the OH groups within the putative Cu(H$_3$thpa)$^{2+}$ dication are expected to be more acidic than in the analogous Cu(H$_3$thpa)$^+$ monocation.
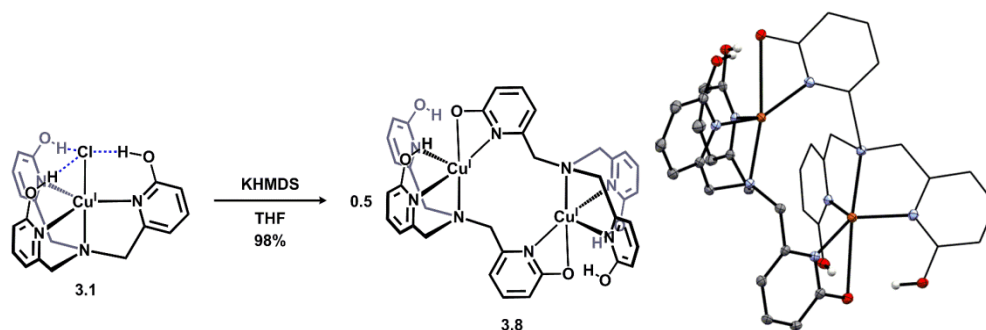
Figure 3-21. Synthesis and solid state structure of dimer 3.8. (30% ellipsoids, H atoms not involved in hydrogen bonding omitted)

Note that $CuCl(H_3thpa)$, complex **3.1**, can be deprotonated with weak bases such as sodium acetate, suggesting an upper limit for the first pK_a of $CuX(H_3thpa)$ complexes is ~4. The product of the deprotonation reaction of **3.1** is the dimeric structure **3.8** where one 'arm' has dissociated to coordinate a neighboring copper center. The formation of this dimeric structure precluded a precise pK_a determination since an equilibrium between protonated and deprotonated structures could not be established. However, based on the ability to deprotonate with weak bases, we have estimated an upper limit for the pK_a.

Although NO was detected by IR spectroscopy in the headspace of reaction samples containing **3.3** and $Ph_3Si(ONO)$, quantification using CoTPP revealed formation of NO in only *ca.* 10% yield above the background decomposition. Taken together, these results confirm the necessity of the H_3thpa ligand framework on copper(I) to mediate nitrite reduction in the absence of any exogenous H^+ source. The quantitative formation of NO from **3.4** and $Ph_3Si(ONO)$ confirms that **3.4** serves to deliver H^+ *and* e^-, as opposed to initiating acid-mediated disproportionation.

3.3.5 Possible reaction pathway for nitrite reduction

The generation of a copper(II)-(OH_x) species from copper(I) and nitrite is reminiscent of a proposed pathway for biological nitrite reduction in CuNiR (Fig. 3-16B). We sought to

106

investigate key intermediates along the nitrite reduction pathway in our system to provide insight into the reaction sequence that may be applied to CuNiR. However, no intermediates were detected by ^{1}H NMR spectroscopy during the reaction of **3.4** with Ph₃Si(ONO) at or below -50 °C, which precluded mechanistic analysis in solution. For instance, when Ph₃Si(ONO) is layered onto a frozen CD_2Cl_2 solution of **3.4** and allowed to thaw at -78 °C inside an NMR spectrometer, no reaction is observed (Fig. 3-22A.) However, when the solution is warmed to -50 °C, **3.4** begins to immediately react with the nitrite reagent, without the appearance of any intermediates (Fig. 3-22B). At this temperature, the paramagnetic copper(II) product, **3.6**, can be visualized as a broad singlet centered near 9.2 ppm. After 15 minutes at -50 °C, consumption of **3.4** is complete without any detectable formation of a diamagnetic intermediate throughout the experiment.
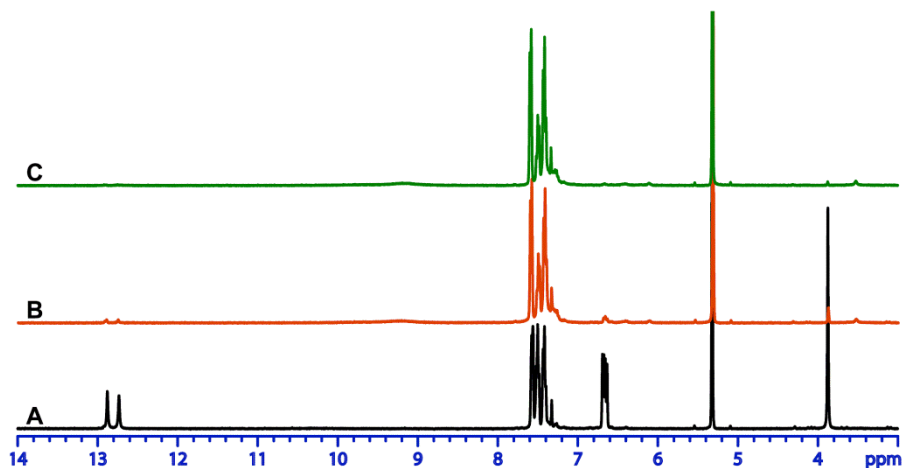
Figure 3-22. Low temperature ^{1}H NMR spectra of the reaction of 3.4 and Ph₃Si(ONO) at -78 °C (A), immediately warming to -50 °C (B) and 15 minutes later at -50 °C (C).

Since we were unable to detect intermediates along the nitrite reduction pathway, we examined the reaction profile using density functional theory (DFT) calculations. The initial nitrite binding step was first interrogated for a series of possible Cu(H₃thpa)-nitrite adducts.

Three nearly isoenergetic (<0.5 kcal/mol difference) structures were computationally identified that feature an interaction of nitrite with the putative $Cu(H_3thpa)^+$ cation (Fig. 3-23).[67] These included an 'encounter' complex (I) where, reminiscent of the F[-] binding in **3.4**, nitrite is positioned in the second coordination sphere by hydrogen bonding interactions. Additionally, two other isomers were located containing two nitrite coordination modes; an $\eta1$-κO isomer (I') and an η^1-κN isomer (I'', Fig. 3-23).

I   I'   I"
E = 0.0 kcal/mol   E = +0.1 kcal/mol   E = -0.3 kcal/mol
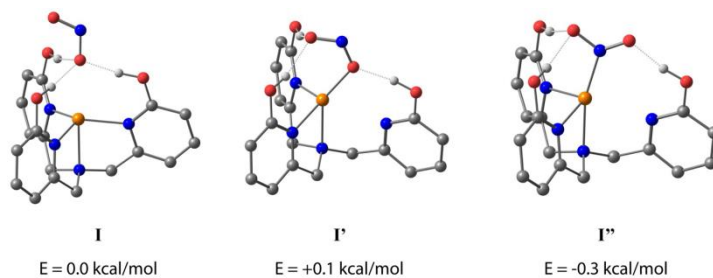
Figure 3-23. DFT-calculated copper(I)-nitrite adducts supported by H$_3$thpa and their relative energies.

The nitrite reduction sequence subsequent to the initial binding event was evaluated. In analogy to Fig. 3-16A, nitrite reduction *via* water elimination from the η^1-κN isomer (I'') to provide a copper-nitrosyl (III, Fig. 3-24A) was found to be an endothermic process by 17.9 kcal/mol, presumably due to the formation of a high energy copper(II)-nitrosyl. In contrast, and in analogy to Fig. 3-16B, reduction via NO elimination from the η^1-κO isomer (I') was found to be an exothermic process by 3.8 kcal/mol to generate the experimentally observed copper(II)-aquo (II) species (Fig. 3-24B).
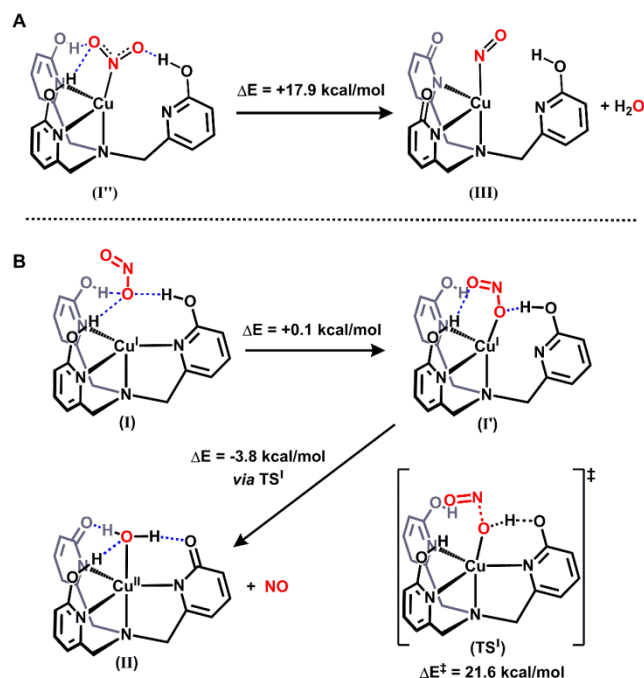
Figure 3-24. DFT-calculated nitrite reduction pathways.

The transition state for the critical N-O bond breaking step (TS^I) was located computationally and is 21.6 kcal/mol above the starting 'encounter' complex I. In the calculated transition state TS^I, H$^+$ transfer from the H$_3$thpa scaffold to the coordinated nitrite is accompanied by elongation of the O–NO bond. There is substantial Mulliken spin density on the Cu-O fragment (0.565) in the transition state. This value is intermediate between the Mulliken spin density of the starting species I (0.0) and the Mulliken spin density on the Cu-O fragment in the product II (0.929). The spin density on the Cu-O fragment in the transition state (along with spin density of the opposite sign on NO, Fig. 3-25) indicates charge transfer from copper to nitrite concomitant with H$^+$ transfer from H$_3$thpa to nitrite. This H$^+$/e$^-$ transfer, accompanied by NO ejection, is followed by an additional H$^+$ transfer from the H$_2$thpa ligand to copper-bound hydroxide to form the final copper(II)-aquo product II.

109
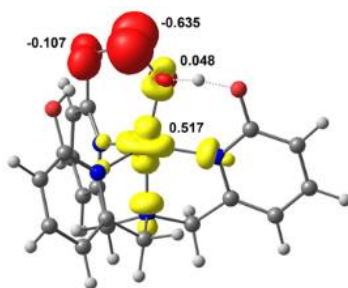
Figure 3-25. Mulliken spin density plot of TS^I (isovalue 0.05).

To understand the impact of the binding mode of nitrite in our system as compared to CuNiR we analyzed the frontier molecular orbitals of structures along the O-NO bond cleavage reaction coordinate. The empty σ*O-NO orbital overlaps with the filled Cu d_{z2} orbital (Fig. 3-26A). This is in contrast to CuNiR, where the highest occupied molecular orbital (HOMO) is primarily d_{x2-y2} character and subsequently nitrite coordinates in a bidentate manner to maximize orbital overlap between d_{x2-y2} and σ*O-NO for electron transfer.[55] For Cu(H$_3$thpa)$^+$, the HOMO is d_{z2} and favors an alternative mode of nitrite binding. The binding of nitrite as a monodentate ligand κO maximizes overlap between d_{z2} and σ*O-NO for electron transfer (Fig. 3-26B). The d_{z2} ground state predicted for II, subsequent to electron transfer and NO release, is in agreement with the experimental EPR data for **3.6**.
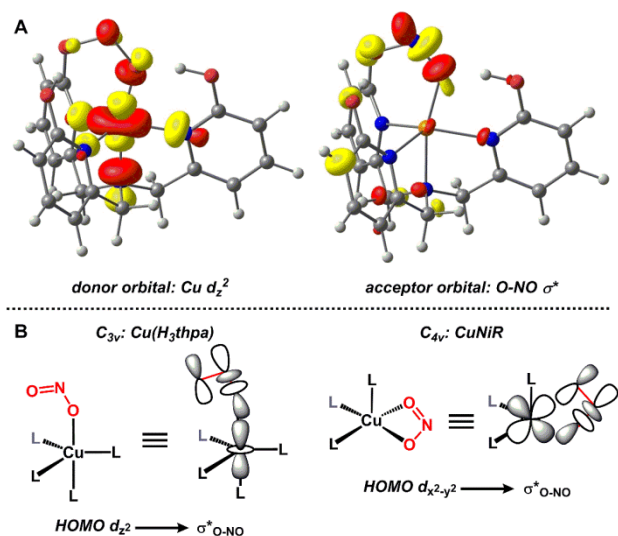
Figure 3-26. Donor and acceptor molecular orbitals along the N-O bond cleavage reaction coordinate (A, isovalue = 0.05) and comparison of nitrite binding mode and donor/acceptor orbitals for Cu(H₃thpa)⁺ (B, left) and CuNiR (B, right)

The difference in mode of nitrite binding between our synthetic system and CuNiR has ramifications on the calculated barrier height for O-NO bond cleavage. In CuNiR, bidentate coordination of nitrite to copper maximizes back-bonding interactions and significantly lowers the calculated barrier to O-NO bond cleavage (16 kcal/mol).[55] Moreover, bidentate coordination in CuNiR stabilizes a transiently formed copper-NO adduct which is bound κ*O*. When a monodentate coordination was examined *in silico*, the extent of back-bonding between copper and nitrite was significantly lower and consequently, a higher barrier to O-NO bond cleavage was observed (26 kcal/mol).[55] The barrier in the present system (21 kcal/mol) is intermediate of these regimes in CuNiR. The hydrogen bonding interactions in TS^I between the distal oxygen of the nitrite anion and the OH groups of the H₃thpa ligand serves to lower the σ*O-NO orbital energy, similar in fashion to bidentate coordination to copper in CuNiR.

Although the reduction pathway described by DFT methods here is distinct from the proposed pathway in CuNiR, two key features of the present proposal which may have biological

relevance are the reduction of nitrite circumventing a copper-nitrosyl adduct and H^+ delivery to substrate which initiates reduction. Unlike CuNiR, the reduction sequence demonstrated here proceeds at a reduced copper center, whereas nitrite is bound to a copper(II) center in CuNiR prior to reduction, which is initiated via H^+ transfer. Moreover, bidentate nitrite coordination in CuNiR was shown to lower the barrier to reduction, potentially due to stabilizing interactions with a transient copper-nitrosyl adduct. In contrast to energetic consequences on orbital energies imposed by geometric constraints, the hydrogen bonding interactions in H_3thpa provide an alternative means by which to lower the σ*O-NO orbital energy, and this approach may well be exploited as a general strategy to minimize energetic costs associated with substrate reduction. Such strategies have been thoroughly described for biological systems.[68,69]

3.4 Experimental section for Chapter 3

General Considerations

All commercially-available reagents were used as received without further purification with the exception of Ph_3SiCl, which was purified by sublimation (100 °C, 0.1 torr) prior to use. $K[Fe(CO)_2Cp]$[70], 2-(bromomethyl)-6-methoxypyridine[71] and $CuF(PPh_3)_3$[64] were synthesized as previously described. All manipulations were carried out under a purified atmosphere of nitrogen using standard Schlenk techniques or in an MBraun Lab Master 130 or Innovative Technologies Pure LabHE GP-1 glovebox, unless otherwise stated. NMR spectra were recorded on either a Varian MR400 or a Varian vnmrs 500 spectrometer and are referenced to residual solvent peaks. Reported ^{19}F NMR chemical shifts are relative to $CFCl_3$ and ^{15}N NMR chemical shifts are relative to $MeNO_2$. Solid-state IR spectra were collected using a Nicolet iS10 spectrometer using a diamond attenuated total reflectance (ATR) accessory. Gas-phase IR spectra were collected using a Perkin-Elmer Spectrum BX spectrometer using a custom gas cell with an 11 cm path

length and BaF_2 windows. EPR spectra were collected on a Bruker EMX EPR spectrometer. Electronic absorption spectra were collected on a Varian Cary-50 spectrophotometer. Voltammetry experiments were conducted under N_2 in a cell consisting of a glassy carbon working electrode, platinum counter electrode and a silver wire reference electrode using a Pine WaveNow potentiostat. Ferrocene was used as an internal reference and introduced at the end of the experiment, then voltammograms were referenced to SCE (ferrocene/ferrocenium = 0.46 V / SCE in CH_2Cl_2). Elemental analyses were performed by Midwest Microlabs, LLC, Indianapolis, IN. Powder X-ray diffraction measurements were performed on a Bruker D8 Advance powder X-ray diffractometer.

tris(6-methoxypyrid-2-ylmethyl)amine (tpa^{OMe})

In a thick-walled Schlenk tube in the open air, acetonitrile (50 mL) was added to 2-(bromomethyl)-6-methoxypyridine (3.89 g; 19.25 mmol) and ammonium carbonate (9.20 g; 95.74 mmol) and then was sealed with a Teflon stopper. The mixture was heated to 75 °C with vigorous stirring for 16 h. The mixture was then allowed to cool to room temperature and *very carefully vented in a fume hood* to release ammonia pressure. The solids were filtered, and washed with copious amounts of dichloromethane. The combined filtrates were concentrated to an oily yellow residue. Addition of cold ethanol produced a white solid, which was washed with small amounts of cold ethanol, then copious amounts of hexanes and dried to give the title compound as a white powder (1.43 g). An additional crop of product (0.21 g) was obtained by concentrating the combined ethanol/hexanes washes to a minimal volume and cooling to -25 °C overnight (total yield 1.64 g; 67%). ^{1}H NMR, 400 MHz (CD_3Cl): 7.53 (t, J = 7.2, 3 H), 7.23 (d, J = 6.8, 3 H), 6.59 (d, J = 7.6, 3 H), 3.92 (s, 9 H), 3.83 (s, 6 H). ^{13}C NMR, 100 MHz (CD_3Cl):163.7, 157.9, 139.0, 115.2, 108.6, 59.9, 53.4. IR (ATR, cm^{-1}): 2814, 1573, 1463, 1411,

1312, 1270, 1026, 986, 798. ESI-MS: 381.08 (100; M+H$^+$). Anal. cald (C$_{21}$H$_{24}$N$_4$O$_3$): 66.30 C, 6.36 H, 14.73 N%. Found: 65.97 C, 6.31 H, 14.34 N%.

tris(6-hydroxypyrid-2-ylmethyl)amine (H$_3$thpa)

In a 50 mL Schlenk flask, 2-diethylaminoethanethiol hydrochloride (2.68 g; 15.79 mmol) was suspended in dimethylformamide (15 mL) and cooled to 0 °C. To this stirring mixture, sodium *tert*-butoxide (3.16 g; 32.88 mmol) was added and stirred for 30 min. The resulting slurry was then allowed to warm to room temperature and stirred an additional 15 min, at which point **tpa^{OMe}** (1.00 g; 2.63 mmol) was added and the pink slurry was heated to a gentle reflux for 20 h. The resulting brown slurry was allowed to cool to room temperature and acetic acid (1.88 mL; 32.84 mmol) was added. All volatiles were then removed *in vacuo* to yield a brown oily residue. Ethanol (25 mL) was then added to give a precipitate, which was collected with the aid of a pad of 521 Celite (4.5 cm diam. x 2 cm) and washed with ethanol (3 x 25 mL) then acetone (2 x 25 mL). ^{1}H NMR, elemental analysis and powder XRD revealed that this material was free of organic contaminants but contained *ca*. 10% NaCl impurity. To isolate material free of NaCl impurity, the above solid was extracted with 200 mL boiling pyridine and filtered through Celite while hot. The filtrate was concentrated to *ca*. 25 mL and diethyl ether (100 mL) was added to produce a white solid. The solid was collected on a sintered glass frit, washed with 1:1 acetone:ethanol (40 mL) then copious amounts of acetone, and finally dried at 100 °C (0.1 torr) for 1 h to give the title compound as a white powder (0.41 g; 46%). Crystals suitable for a single-crystal X-ray diffraction experiment were grown by vapor diffusion of diethyl ether into a methanol solution of **H$_3$thpa**. ^{1}H NMR, 400 MHz (DMSO-d_6): 11.84 (br s, 3 H), 7.33 (dd, $J = $ 6.8, 9.2, 3 H), 6.22 (d, $J = 9.2$, 3 H), 6.11 (d, $J = 5.6$, 3 H), 3.40 (s, 6 H). ^{13}C NMR, 100 MHz (DMSO-d_6): 163.4, 144.5, 140.8, 118.9, 105.1, 54.9. IR (ATR, cm^{-1}): 3369, 3116, 2806, 1660,

1608, 1122, 997, 813, 795. ESI-MS: 339.05 (100; M+H$^+$). Anal. cald (C$_{18}$H$_{18}$N$_4$O$_3$): 63.89 C, 5.36 H, 16.56 N%. Found: 63.68 C, 5.68 H, 15.76 N%. Although the %N is outside the range viewed as establishing analytical purity, the analysis is provided to illustrate the best values obtained to date.

CuCl(H$_3$thpa) (3.1)

In a scintillation vial, H$_3$thpa (73.1 mg; 0.216 mmol) and CuCl (21.8 mg; 0.220 mmol) were suspended in benzene (10 mL). The vial was sealed with a Teflon-lined cap and heated to 70 °C with vigorous stirring for 2 h, then allowed to cool to room temperature. Dichloromethane (*ca.* 5 mL) was added to the yellow slurry and then filtered, and the filter cake was rinsed with a minimal amount of dichloromethane (*ca.* 1 mL). The combined yellow filtrates were concentrated and dried *in vacuo* to provide the title compound as a microcrystalline yellow powder (53.8 mg; 57%). Crystals suitable for a single-crystal X-ray diffraction experiment were grown by vapor diffusion of diethyl ether into a dichloromethane solution of **3.1** at 5 °C. ^{1}H NMR, 400 MHz (CD$_2$Cl$_2$): 10.57 (s, 3 H), 7.56 (t, *J* = 8.0, 3 H), 6.72 (d, *J* =7.2, 3 H), 6.68 (d, *J* = 8.0, 3 H), 3.66 (s, 6 H). ^{13}C NMR, 100 MHz (CD$_2$Cl$_2$): 165.5, 154.2, 140.5, 115.8, 111.3, 57.2. IR (ATR, cm^{-1}): 3139 (OH), 1645, 1613, 1439, 1197, 1152, 998, 796, 682. Anal. cald (C$_{18}$H$_{18}$ClCuN$_4$O$_3$): 49.43 C, 4.15 H, 12.81 N%. Found: 49.12 C, 4.15 H, 12.61 N%.

CuCl(H$_3$thpa)PF$_6$ (3.2)

In a scintillation vial, **3.1** (20.1 mg; 0.0460 mmol) was dissolved in dichloromethane (*ca.* 5 mL) and then a solution of ferrocenium hexafluorophosphate (15.4 mg; 0.0465 mmol) in dichloromethane (*ca.* 1 mL) was added causing an immediate color change to green. The solution was stirred for 5 min, then filtered and concentrated to a minimal volume. Diethyl ether (*ca.* 5 mL) was added to cause a precipitation, and the solid was collected and washed with

diethyl ether (*ca.* 5 mL) and benzene (*ca.* 2 mL). The green solid was then redissolved in a minimal amount of dichloromethane, filtered and concentrated to give a green oil which, after trituration with diethyl ether, and drying *in vacuo* provided the title compound as an emerald green powder (19.0 mg; 71%). Crystals suitable for a single-crystal X-ray diffraction experiment were grown by vapor diffusion of diethyl ether into a dichloromethane solution of **3.2** at 5 °C. X-band EPR (DCM, 77 K): $g_{\parallel}$ = 2.010, $A_{\parallel}$ = 81 G, $g_{\perp}$ = 2.165, $A_{\perp}$ = 64 G. UV-vis (DCM): 740 nm (sh, 90 mol^{-1} cm^{-1}), 913 nm (300 mol^{-1} cm^{-1}). IR (ATR, cm^{-1}): 3273 (OH), 1628, 1578, 1489, 1445, 1160, 833 (PF$_6$). Anal. cald (C$_{18}$H$_{18}$ClCuF$_6$N$_4$O$_3$P): 37.13 C, 3.12 H, 9.62 N%. Found: 37.38 C, 3.34 H, 9.37 N%.

CuF(H$_3$thpa)BF$_4$ (3.3)

In the open air, methanol (30 mL) was added to H$_3$thpa (0.400 g; 1.18 mmol) and NaBF$_4$ (0.285 g; 0.259 mmol) and stirred. Cu(SO$_4$)·5H$_2$O (0.295 g; 1.18 mmol) was added to the mixture and stirred for *ca.* 5 min, producing a cloudy green mixture, at which time CsF (0.198 g; 1.30 mmol) was added and stirring was continued for 2 h. The turquoise mixture was then filtered and the filtrate was concentrated to dryness. The residue was extracted with dichloromethane (*ca.* 30 mL) and filtered. The filtrate was concentrated to yield the title compound as a microcrystalline turquoise solid (0.462 g; 77%). Crystals of **3.3** suitable for X-ray diffraction were grown from vapor diffusion of diethyl ether into a dichloromethane solution of **3.3**. IR (ATR, cm^{-1}): 3159 (OH), 3125 (OH), 1629, 1578, 1459, 1312, 1046 (BF$_4$), 717. EPR (1:1 CH$_2$Cl$_2$:toluene, 77 K): g_x = 2.210, g_y = 2.182, g_z = 1.945, A_x = 100 G, A_y = 103 G, A_z = 67 G. UV-vis (CH$_2$Cl$_2$): 889 nm (240 cm^{-1}M^{-1}), 683 (53). Anal. cald (C$_{18}$H$_{18}$BCuF$_5$N$_4$O$_3$): 42.58 C, 3.57 H, 11.04 N%. Found: 43.05 C, 3.67 H, 11.13 N%.

CuF(H₃thpa) (3.4)

Complex **3.3** (199.5 mg; 0.393 mmol) was suspended in dimethoxyethane (*ca.* 25 mL) and K[Fe(CO)₂Cp] (81.0 mg dissolved in *ca.* 2 mL dimethoxyethane; 0.375 mmol) was added dropwise to the mixture and stirred for *ca.* 15 min. The dark orange mixture was then filtered and the filtrate was concentrated to dryness. The residue was washed with 1:1 dimethoxyethane:diethyl ether (*ca.* 10 mL) and filtered, then the filter cake was washed with diethyl ether until the eluent became colorless. The collected solids were then extracted with tetrahydrofuran and filtered until the eluent became colorless. The tetrahydrofuran filtrate was then concentrated to give a yellow solid, which after trituration with pentane and drying under vacuum yielded the title compound as a yellow powder (94.4 mg; 60%). Analytical samples and crystals of **3.4** suitable for X-ray diffraction were grown from vapor diffusion of diethyl ether into a dichloromethane solution of **3.4**. ^{1}H NMR, 400 MHz (CD₂Cl₂): 12.90 (br s, 3 H), 7.51 (t, *J* = 7.6, 3 H), 6.67 (d, *J* = 8, 6 H), 3.90 (s, 9 H). ^{13}C NMR, 100 MHz (CD₂Cl₂):164.5, 154.0, 139.7, 114.4, 111.3, 58.5. ^{19}F NMR, 377 MHz (CD₂Cl₂): -109.0 (br s). IR (ATR, cm^{-1}): 2909, 2848, 2644, 2609, 2570, 2536, 2501, 2473, 1614, 1570, 1440, 1154, 789. Anal. cald (C₁₈H₁₈CuFN₄O₃): 51.36 C, 4.31 H, 13.31 N%. Found: 51.05 C, 4.29 H, 13.23 N%.

CuF(tpa)PF₆ (3.5)

This compound was previously prepared by reaction of Cu(tpa)$^+$ with O₂ in the presence of PF₆$^-$.[36] This procedure provided low and variable yields and we therefore sought an alternative, more reliable preparation. Acetonitrile (*ca.* 5 mL) was added to a mixture of tpa (48.9 mg; 0.168 mmol), CuF₂ (17.5 mg; 0.172 mmol) and NaPF₆ (30.4 mg; 0.181 mmol) and stirred for 2 h. Over this time, the mixture gradually became blue and nearly homogeneous. The mixture was filtered and the filtrate was concentrated to a blue oil under vacuum. The oil was extracted with

dichloromethane (*ca.* 5 mL), filtered and concentrated to again give a blue oil. The oil was triturated with copious amounts of diethyl ether and dried under high vacuum, giving a blue foam. Prolonged drying of the foam under high vacuum and crushing provided the title compound as a sky blue powder (50.2 mg; 58%). IR (KBr, cm^{-1}): 1614, 1446, 838 (PF$_6$), 767, 558, 498 (Cu-F). EPR (1:1 CH$_2$Cl$_2$:toluene, 77 K): g$_\perp$ = 2.210, g$_\parallel$ = 1.940, A$_\perp$ = 92 G, A$_\parallel$ = 67 G. UV-vis (CH$_2$Cl$_2$): 894 nm (170 cm^{-1}M^{-1}), 700 (84). The characterization data are consistent with those previously reported by Karlin and co-workers.[36]

Reaction of 3.4 with Ph$_3$SiCl:

In a small vial, **3.4** (5.2 mg; 0.012 mmol) was dissolved in CD$_2$Cl$_2$ (700 μL). To this yellow solution, Ph$_3$SiCl (4.0 mg; 0.014 mmol, dissolved in 700 μL CD$_2$Cl$_2$) was added dropwise *via* syringe. An aliquot (*ca.* 0.6 mL) was immediately transferred to an NMR tube and the reaction mixture analyzed by ^{1}H and ^{19}F NMR, which showed quantitative conversion to CuCl(H$_3$thpa) **3.1** along with Ph$_3$SiF and excess, unreacted Ph$_3$SiCl.

Preparation of Ph$_3$Si(ONO)

Benzene (*ca.* 10 mL) was added to a mixture of AgNO$_2$ (80.0 mg; 0.520 mmol) and Ph$_3$SiCl (139.0 mg; 0.471 mmol). The mixture was stirred protected from light for 24 h then filtered and concentrated to a white solid. The solid was redissolved in a minimal amount of pentane, filtered and concentrated to *ca.* 2 mL and placed in a –35 °C freezer overnight. The deposited colorless crystals (70.4 mg; 49%) were collected and dried briefly (*ca.* 10 min) under vacuum and used without further purification. This material slowly decomposes at room temperature over the course of *ca.* 2 days and was therefore stored at –35 °C. We have found samples stored at this temperature have remained unchanged for *ca.* 1 month. Note that we have been unable to obtain satisfactory combustion analyses for this material to date, presumably due to decomposition prior

118

to analysis. ^{1}H NMR (400 MHz, CD$_2$Cl$_2$): 7.64-7.66 (m, 6H), 7.51-7.55 (m, 3H), 7.43-7.47 (m, 6H). ^{13}C{^{1}H} NMR (100 MHz, CD$_2$Cl$_2$): 136.1, 132.4, 131.5, 128.8. IR (ATR, cm^{-1}): 3069, 3016, 1631 (N=O)[4], 1589, 1428, 1119, 997, 908.

The ^{15}N isotopologue, Ph$_3$Si(O[15]NO), was prepared in an identical manner using Na[15]NO$_2$ and dimethoxyethane solvent. Note that material obtained in this manner contained small amounts (*ca.* 5%) of unreacted Ph$_3$SiCl. ^{15}N NMR (51 MHz, CD$_2$Cl$_2$): 188.0. IR (ATR, cm^{-1}): 3068, 3016, 1603 (N=O), 1589, 1428, 1118, 997, 899.

Cu(OH$_2$)Hthpa (3.6)

Method A: In a scintillation vial, **3.4** (21.3 mg; 0.051 mmol) was dissolved in dichloromethane (*ca.* 10 mL) to give a yellow solution. With stirring, Ph$_3$Si(ONO) (16.2 mg; 0.053 mmol, dissolved in *ca.* 1 mL dichloromethane) was added dropwise immediately producing a color change to green. The reaction was stirred for 15 min, then pentane (*ca.* 10 mL) was added to produce a precipitate. The supernatant was decanted and the solid was triturated with pentane, then dried to an olive green powder (12.7 mg; 60%).

Method B: In the open air, a mixture of dichloromethane and ethanol (*ca.* 20 mL, 1:1) was added to solid H$_3$thpa (100.8 mg; 0.298 mmol) and Cu(OH)$_2$ (28.9 mg; 0.296 mmol). The suspension was stirred for 24 h and then filtered. The green filtrate was concentrated to a green residue and diethyl ether (*ca.* 10 mL) was added. The resulting green powder was collected on a sintered glass frit, washed with copious amounts of diethyl ether and dried to afford a mint green powder (83.4 mg; 67%). Crystals of **3.6** suitable for X-ray diffraction were grown from vapor diffusion of diethyl ether into a 1:1 dichloromethane/ethanol solution of **3.6** at 5 °C. IR (ATR, cm^{-1}): 1658 (C=O), 1614, 1488, 1437, 1155, 998, 796. EPR (1:1 CH$_2$Cl$_2$:EtOH, 77 K): $g_x = g_y = 2.177$, $g_z =$

1.955, $A_x = A_y = 103$ G, $A_z = 50$ G. UV-vis (CH$_2$Cl$_2$): 438 nm (50 cm^{-1}M^{-1}), 680 (35), 905 (160).

Anal. calc'd (C$_{18}$H$_{18}$CuN$_4$O$_4$): 51.73 C, 4.34 H, 13.41 N%. Found: 51.58 C, 4.19 H, 13.20 N%.

Low temperature reaction of 3.4 with Ph$_3$(ONO):

In a screw cap NMR tube, **3.4** (2.1 mg; 5.0 µmol) was dissolved in CD$_2$Cl$_2$ (700 µL). The tube

was placed in a cold well (liquid N$_2$) and frozen. To the frozen solution, Ph$_3$Si(ONO) (200 µL of

a 27 mM solution in CD$_2$Cl$_2$; 5.4 µmol) was layered onto the frozen solution using a syringe and

sealed. The frozen tube was transferred directly into a pre-cooled NMR spectrometer and spectra

were recorded immediately. The recorded spectra showed no reaction at -75 °C, upon warming

to -50 °C immediate conversion of **3.4** to paramagnetic **3.6** (broad resonance at *ca.* 9.2 ppm) was

observed without the appearance of a diamagnetic intermediate. Note any diamagnetic

intermediates would be distinguishable by (1) a new $-CH_2$ resonance between 3.5 and 4.5 ppm

and/or (2) a new $-OH$ resonance >8 ppm.

Headspace measurements

IR spectroscopy: In a 20 mL scintillation vial with a Teflon stirbar in a glovebox, the copper

fluoride (either **3.4**, **3.7** or **3.3** *ca.* 0.035 mmol) was dissolved in dichloromethane (5 mL) and

then sealed using a septum and electrical tape. To the stirring solution, the nitrite (either

Ph$_3$Si(ONO) or Ph$_3$Si(O^{15}NO), *ca.* 1.05 equivalents dissolved in 1.0 mL dichloromethane) was

added *via* syringe through the septum. The solution was allowed to stir for 30 min and the

headspace was then evacuated by attaching the IR cell (*ca.* 105 mL) under vacuum (0.25 torr) *via*

a needle. IR spectra were recorded directly on the collected headspace samples in the IR cell.

UV-vis: In a small Schlenk tube with a Teflon stirbar in a glovebox, the copper fluoride (either

3.4, **3.7** or **3.3** *ca.* 5.0 µmol) was dissolved in dichloromethane (2 mL). Separately, CoTPP (5.0

μmol dissolved in 3 mL dichloromethane) was added to a small vial with a stir bar, and placed inside the Schlenk tube such that the two solutions could not mix, and the tube was sealed using a septum. To the stirring copper solution, the nitrite (Ph$_3$Si(ONO) *ca.* 1.05 equivalents dissolved in 1.0 mL dichloromethane) was added *via* syringe through the septum. The solution was allowed to stir for 60 min to assure complete diffusion of NO. After this time, 0.25 mL of the CoTPP solution was removed, diluted with dichloromethane (final volume 3.0 mL) and then a UV-vis spectrum was recorded. The yield of NO was determined by fitting the position of the Q-band of the resultant UV-vis spectrum. The position of the Q-band in authentic UV-vis spectra of CoTPP (528 nm) and CoTPP-NO (538 nm) were used for the fitting procedure.

[Cu(H$_2$thpa)]$_2$ (3.8)

In a scintillation vial, **CuCl(H$_3$thpa)** (105.0 mg; 0.240 mmol) was dissolved in tetrahydrofuran (*ca.* 20 mL) to give a yellow solution. With stirring, potassium hexamethyldisilylazide (KHMDS, 49.6 mg; 0.249 mmol) was slowly added immediately producing a precipitate. The reaction was stirred for 15 min, then diethyl ether (*ca.* 10 mL) was added. The precipitate was collected and washed with diethyl ether. The solid was redissolved in a minimal amount of dichloromethane, filtered, then concentrated to give the title compound as a pale yellow powder (94.4 mg; 98%). Note that the deprotonation can be achieved using a weak base such as sodium acetate (pK_a = 4.8), which suggests a minimum pK_a value.

Crystals of **3.8** suitable for X-ray diffraction were grown by vapor diffusion of diethyl ether into a dichloromethane solution of **3.8**.

Characterization data for **[Cu(H$_2$thpa)]$_2$**: ^{1}H NMR (400 MHz, CD$_2$Cl$_2$): 12.92 (s, 4H), 7.59 (t, J = 6.8, 2H), 7.41 (t, J = 7.2, 4H), 6.79 (d, J = 7.6, 4H), 6.61 (d, J = 8, 4H), 6.42 (d, J = 6.8, 4H), 4.38 (s, 4H), 4.20 (d, J = 15.6, 4H), 3.21 (d, J = 14.8, 4H). ^{13}C{^{1}H} NMR (100 MHz, CD$_2$Cl$_2$):

171.0, 164.2, 153.4, 139.9, 138.7, 129.7, 115.3, 114.2, 112.9, 111.2, 62.2, 57.4. IR (ATR, cm^{-1}): 1657, 1611, 1567, 1470, 1425, 1274, 1201, 1150, 1013, 788.

Computational details

All calculations were performed using Gaussian 09[72] and visualized using GaussView 5.0.[73] Becke's three-parameter hybrid function using Lee, Yang and Parr's correlation function (B3LYP)[41] was used for all calculations. Initial optimizations utilized the LanL2DZ[74] basis set, however poor agreements between optimized geometries and experimental structures were found. Better agreement was found using the triple-zeta basis set TZVP[42] and only the optimizations using this basis set are reported. Structures were freely optimized in C_1 symmetry and were confirmed to be minima based on the absence of imaginary frequencies in the calculated vibrational spectra. Computed vibrational frequencies have been scaled according to the appropriate factors reported by Merrick and co-workers.[75] Transition states were confirmed based on the presence of one imaginary frequency in the calculated vibrational spectra. All reported energies are enthalpies in kcal/mol. Spin densities were calculated using Mulliken population analyses.[44] Appropriate spin polarization of the ground state wavefunction was ensured by examining closed-shell and open-shell wave functions when calculating intermediates along the N-O bond cleavage pathways. For the formation of **II**, the intermediates along the N-O cleavage pathway from **I** are best described as open-shell singlet (broken symmetry) states until NO dissociation. Compound **III** is best described as a Cu(II)-NO·species with an open-shell (broken symmetry) ground state wavefunction.

3.5 Notes and references

1.   (a) Widger, L. R.; Davies, C. G.; Yang, T.; Siegler, M. A.; Troeppner, O.; Jameson, G. N. L.; Ivanović-Burmazović, I.; Goldberg, D. P. *J. Am. Chem. Soc.* **2014**, *136*, 2699. (b)

Cheruzel, L. E.; Cecil, M. R.; Edison, S. E.; Mashuta, M. S.; Baldwin, M. J.; Buchanan, R. M. *Inorg. Chem.* **2006**, *45*, 3191. (c) Tubbs, K. J.; Fuller, A. L.; Bennett, B.; Arif, A. M.; Berreau, L. M. *Inorg. Chem.* **2003**, *42*, 4790. (d) Feng, G.; Mareque-Rivas, J. C.; Williams, N. H. *Chem. Commun.* **2006**, 1845. (e) Shook, R. L.; Borovik, A. S. *Chem. Commun.* **2008**, 6095. (f) Tutusaus, O.; Ni, C.; Szymczak, N. K. *J. Am. Chem. Soc.* **2013**, *135*, 3403. (g) Wada, A.; Honda, Y.; Yamaguchi, S.; Nagatomo, S.; Kitagawa, T.; Jitsukawa, K.; Masuda, H. *Inorg. Chem.* **2004**, *43*, 5725.

2.   Borovik, A. S. *Acc. Chem. Res.* **2004**, *38*, 54.

3.   (a) Rosenthal, J.; Nocera, D. G. *Acc. Chem. Res.* **2007**, *40*, 543. (b) Rakowski DuBois, M.; DuBois, D. L. *Chem. Soc. Rev.* **2009**, *38*, 62.

4.   (a) Hart, J. S.; Nichol, G. S.; Love, J. B. *Dalton Trans.* **2012**, *41*, 5785. (b) Hart, J. S.; White, F. J.; Love, J. B. *Chem. Commun.* **2011**, *47*, 5711. (c) Sickerman, N. S.; Park, Y. J.; Ng, G. K. Y.; Bates, J. E.; Hilkert, M.; Ziller, J. W.; Furche, F.; Borovik, A. S. *Dalton Trans.* **2012**, *41*, 4358. (d) Park, Y. J.; Sickerman, N. S.; Ziller, J. W.; Borovik, A. S. *Chem. Commun.* **2010**, *46*, 2584.

5.   (a) Grotjahn, D. B.; Incarvito, C. D.; Rheingold, A. L. *Angew. Chem., Int. Ed.* **2001**, *40*, 3884. (b) Royer, A. M.; Rauchfuss, T. B.; Gray, D. L. *Organometallics* **2010**, *29*, 6763. (c) For a recent review on 2-hp-derived catalysts, see: Wang, W.-H.; Muckerman, J. T.; Fujita, E.; Himeda, Y. *New J. Chem.* **2013**, *37*, 1860. (d) DePasquale, J.; Nieto, I.; Reuther, L. E.; Herbst-Gervasoni, C. J.; Paul, J. J.; Mochalin, V.; Zeller, M.; Thomas, C. M.; Addison, A. W.; Papish, E. T. *Inorg. Chem.* **2013**, *52*, 9175. (e) Breit, B.; Seiche, W. *J. Am. Chem. Soc.* **2003**, *125*, 6608.

6.   (a) Hiromoto, T.; Ataka, K.; Pilak, O.; Vogt, S.; Stagni, M. S.; Meyer-Klaucke, W.; Warkentin, E.; Thauer, R. K.; Shima, S.; Ermler, U. *FEBS Lett.* **2009**, *583*, 585. (b) Hiromoto, T.; Warkentin, E.; Moll, J.; Ermler, U.; Shima, S. *Angew. Chem., Int. Ed.* **2009**, *48*, 6457.

7.   Letko, C. S.; Rauchfuss, T. B.; Zhou, X.; Gray, D. L. *Inorg. Chem.* **2012**, *51*, 4511.

8.   Anderegg, G.; Wenk, F. Helv. *Chim. Acta* **1967**, *50*, 2330.

9.   Gray, M. A.; Konopski, L.; Langlois, Y. *Synth. Commun.* **1994**, *24*, 1367.

10.   Berreau, L. M. *Eur. J. Inorg. Chem.* **2006**, 273.

11.   Although we have found no prior reports of H$_3$thpa, a related tridentate ligand was described by Rauchfuss and co-workers (ref. 7).

12.   Note that H$_3$thpa has low solubility in less polar organic solvents.

13.   Lewis, E. A.; Tolman, W. B. *Chem. Rev.* **2004**, *104*, 1047.

14.   Addison, A. W.; Rao, T. N.; Reedijk, J.; van Rijn, J.; Verschoor, G. C. *J. Chem. Soc., Dalton Trans.* **1984**, 1349.

15.   Eckenhoff, W. T.; Pintauer, T. *Inorg. Chem.* **2007**, *46*, 5844.

16.   Steiner, T. *Angew. Chem., Int. Ed.* **2002**, *41*, 48.

17.   (a) Eckenhoff, W. T.; Garrity, S. T.; Pintauer, T. *Eur. J. Inorg. Chem.* **2008**, 563. (b) Hsu, S. C. N.; Chien, S. S. C.; Chen, H. H. Z.; Chiang, M. Y. *J. Chin. Chem. Soc.* **2007**, *54*, 685.

18.   Sandström, J. *Dynamic NMR spectroscopy*; Academic Press Inc.: London, 1982.

19.   Hathaway, B. J.; Billing, D. E. *Coord. Chem. Rev.* **1970**, *5*, 143.

20.   Karlin, K. D.; Hayes, J. C.; Juen, S.; Hutchinson, J. P.; Zubieta, J. *Inorg. Chem.* **1982**, *21*, 4106.

21.   For a similar Cu(II)-Cl elongation, see: Jitsukawa, K.; Harata, M.; Arii, H.; Sakurai, H.; Masuda, H. *Inorg. Chim. Acta* **2001**, *324*, 108.

22.   For a similar analysis, see: Rivas, J. C. M.; Hinchley, S. L.; Metteau, L.; Parsons, S. *Dalton Trans.* **2006**, 2316.

23.   Iogansen, A. V.; Kurkchi, G. A.; Furman, V. M.; Glazunov, V. P.; Odinokov, S. E. *Zh. Prikl. Spektrosk.* **1980**, *33*, 460.

24.   (a) N. M. Doherty, N. W. Hoffmann, *Chem. Rev.* **1991**, *91*, 553; (b) E. F. Murphy, R. Murugavel, H. W. Roesky, *Chem. Rev.* **1997**, *97*, 3425.

25.   (a) A. J. Hickman, M. S. Sanford, *Nature* **2012**, *484*, 177, and references cited therein; (b) V. V. Grushin, *Acc. Chem. Res.* **2010**, *43*, 160, and references cited therein; (c) P. Tang, T. Furuya, T. Ritter, *J. Am. Chem. Soc.* **2010**, *132*, 12150; (d) J. A. Akana, K. X. Bhattacharyya, P. Mueller, J. P. Sadighi, *J. Am. Chem. Soc.* **2007**, *129*, 7736.

26.   For selected recent examples, see: (a) X. Mu, H. Zhang, P. Chen, G. Liu, *Chem. Sci.* **2014**, *5*, 275; (b) Y. Ye, S. D. Schimler, P. S. Hanley, M. S. Sanford, *J. Am. Chem. Soc.* **2013**, *135*, 16292; (c) T. Truong, K. Klimovica, O. Daugulis, *J. Am. Chem. Soc.* **2013**, *135*, 9342; (d) P. S. Fier, J. F. Hartwig, *J. Am. Chem. Soc.* **2012**, *134*, 10795.

27.   (a) P. S. Fier, J. Luo, J. F. Hartwig, *J. Am. Chem. Soc.* **2013**, *135*, 2552; (b) A. Casitas, M. Canta, M. Sola, M. Costas, X. Ribas, *J. Am. Chem. Soc.* **2011**, *133*, 19386.

28.   K. Fagnou, M. Lautens, *Angew. Chem., Int. Ed.* **2002**, *41*, 26.

29.   (a) J. R. Herron, Z. T. Ball, *J. Am. Chem. Soc.* **2008**, *130*, 16486; (b) J. R. Herron, V. Russo, E. J. Valente, Z. T. Ball *Chem. - Eur. J.* **2009**, *15*, 8713; (c) T. Fujihara, T. Xu, K. Semba, J. Terao, Y. Tsuji, *Angew. Chem., Int. Ed.* **2011**, *50*, 523; (d) C. M. Wyss, B. K.

Tate, J. Bacsa, M. Wieliczko, J. P. Sadighi *Polyhedron*, **2014**, DOI: 10.1016/j.poly.2014.06.039.

30. Y. Liu, C. Chen, H. Li, K.-W. Huang, J. Tan, Z. Weng, *Organometallics* **2013**, *32*, 6587.

31. D. J. Gulliver, W. Levason, M. Webster, *Inorg. Chim. Acta* **1981**, *52*, 153.

32. L. Brammer, E. A. Bruton, P. Sherwood, *Cryst. Growth Des*. **2001**, *1*, 277.

33. Cambridge crystallographic database search (CSD version 5.35, updated November 2013).

34. A. Almesaker, P. Gamez, J. Reedijk, J. L. Scott, L. Spiccia, S. J. Teat, *Dalton Trans.* **2009**, 4077.

35. (a) G. A. van Albada, S. Nur, M. G. van der Horst, I. Mutikainen, U. Turpeinen, J. Reedijk, *J. Mol. Struct.* **2008**, *874*, 41; (b) G. Ambrosi, M. Formica, V. Fusi, L. Giorgi, A. Guerri, M. Micheloni, P. Paoli, R. Pontellini, P. Rossi, *Chem. - Eur. J.* **2007**, *13*, 702.

36. R. R. Jacobson, Z. Tyeklar, K. D. Karlin, J. Zubieta, *Inorg. Chem*. **1991**, *30,* 2035.

37. Note the peak positions and linewidths in the ^{1}H NMR spectra of **3.2** in 1,2-dichloroethane are unchanged between -25 °C and +75 °C, and suggestive of a static solution structure.

38. I. G. Shenderovich, S. N. Smirnov, G. S. Denisov, V. A. Gindin, N. S. Golubev, A. Dunger, R. Reibke, S. Kirpekar, O. L. Malkina, H. H. Limbach, *Ber. Bunsen-Ges.* **1998**, *102*, 422.

39. K. O. Christe, W. W. Wilson, R. D. Wilson, R. Bau, J. A. Feng, *J. Am. Chem. Soc.* **1990**, *112*, 7619.

40. R. D. Shannon, *Acta Crystallogr., Sect. A* **1976**, *A32*, 751.

41.   (a) A. D. Becke, *J. Chem. Phys.* **1993**, *98*, 5648; (b) C. Lee, W. Yang, R. G. Parr, *Phys. Rev. B: Condens. Matter* **1988**, *37*, 785.

42.   (a) A. Schaefer, H. Horn, R. Ahlrichs, *J. Chem. Phys.* **1992**, *97*, 2571; (b) A. Schaefer, C. Huber, R. Ahlrichs, *J. Chem. Phys.* **1994**, *100*, 5829.

43.   S. Miertus, E. Scrocco, J. Tomasi, *Chem. Phys.* **1981**, *55*, 117.

44.   (a) A. E. Reed, R. B. Weinstock, F. Weinhold, *J. Chem. Phys.* **1985**, *83*, 735; (b) A. E. Reed, L. A. Curtiss, F. Weinhold, *Chem. Rev.* **1988**, *88*, 899.

45.   K. B. Wiberg, *Tetrahedron* **1968**, *24*, 1083.

46.   (a) B. A. Averill, *Chem. Rev.* **1996**, *96*, 2951; (b) W. G. Zumft, *Microbiol. Mol. Biol. Rev.* **1997**, *61*, 533; (c) A. C. Merkle, A. C., N. Lehnert, *Dalton Trans.* **2012**, *41*, 3355 and references therein.

47.   S. Suzuki, K. Kataoka, K. Yamaguchi, T. Inoue, Y. Kai, *Coord. Chem. Rev.* **1999**, 190-192, 245.

48.   (a) M. E. P. Murphy, S. Turley, E. T. Adman, *J. Biol. Chem.* **1997**, *272*, 28455; (b) M. J. Ellis, M. Prudencio, F. E. Dodd, R. W. Strange, G. Sawers, R. R. Eady, S. S. Hasnain, *J. Mol. Biol*. **2002**, *316*, 51; (c) S. V. Antonyuk, R. W. Strange, G. Sawers, R. R. Eady, S. S. Hasnain, *Proc. Natl. Acad. Sci. U. S. A.* **2005**, *102*, 12041.

49.   B. A. Averill, *Angew. Chem. Int. Ed.* **1994**, *33*, 2057.

50.   E. I. Tocheva, F. I. Rosell, A. G. Mauk, M. E. P. Murphy, *Science* **2004**, *304*, 867.

51.   Note that the NO adduct of reduced CuNiR can also be generated in solution, see: O. M. Usov, Y. Sun, V. M. Grigoryants, J. P. Shapleigh, C. P. Scholes, *J. Am. Chem. Soc.* **2006**, *128*, 13102.

52.   (a) C. L. Hulse, J. M. Tiedje, B. A. Averill, *J. Am. Chem. Soc.* **1989**, *111*, 2322; (b) M. Sarma, B. Mondal, *Inorg. Chem.* **2011**, *50*, 3206.

53.   K. Kataoka, H. Furusawa, K. Takagi, K. Yamaguchi, S. Suzuki, *J. Biochem.* **2000**, *127*, 345.

54.   (a) Y. Zhao, D. A. Lukoyanov, Y. V. Toropov, K. Wu, J. P. Shapleigh, C. P. Scholes, *Biochemistry* **2002**, *41*, 7464; (b) S. Suzuki, K. Kataoka, K. Yamaguchi, *Acc. Chem. Res.* **2000**, *33*, 728; (c) K. Kobayashi, S. Tagawa, Deligeer, S. Suzuki, *J. Biochem.* **1999**, *126*, 408.

55.   S. Ghosh, A. Dey, Y. Sun, C. P. Scholes, E. I. Solomon, *J. Am. Chem. Soc.* **2009**, *131*, 277.

56.   For select Cu(II) examples, see: (a) F. Hueso-Ureña., A. L. Peñas-Chamorro, M. N. Moreno-Carretero, M. Quirós-Olozábal, J. M. Salas-Peregrín, *Polyhedron*, **1999**, *18*, 351; (b) M. Harata, K. Jitsukawa, H. Masuda, H. Einaga, *Bull. Chem. Soc. Jpn.*, **1998**, *71*, 637.

57.   Note that copper(I)-nitrite adducts featuring κO-coordination have been observed using phosphine ligands, see: J. A. Halfen, W. B. Tolman, *Acta Cryst.* **1995**, *C51*, 215, along with ref. 12d and 12e.

58.   For selected examples, see: (a) J. A. Halfen, S. Mahapatra, M. M. Olmstead, W. B. Tolman, *J. Am. Chem. Soc.* **1994**, *116*, 2173; (b) J. A. Halfen, S. Mahapatra, E. C. Wilkinson, A. Gengenbach, V. G., Jr. Young, L. Que, W. B. Tolman, *J. Am. Chem. Soc.* **1996**, *118*, 763; (c) J. A. Halfen, W. B. Tolman, *J. Am. Chem. Soc.* **1994**, *116*, 5475; (d) W.-J. Chuang, I. J. Lin, H.-Y. Chen, Y.-L. Chang, S. C. N. Hsu, *Inorg. Chem.* **2010**, *49*, 5377; (e) S. C. N. Hsu, Y.-L. Chang, W.-J. Chuang, H.-Y. Chen, I. J. Lin, M. Y. Chiang, C.-L. Kao, H.-Y. Chen, *Inorg. Chem.* **2012**, *51*, 9297; (f) M. Kujime, H. Fujii, *Angew.*

Chem. Int. Ed. **2006**, *45*, 1089; (g) P. P. Paul, K. D. Karlin, *J. Am. Chem. Soc.* **1991**, *113*, 6331. For an example of catalytic nitrite reduction using a synthetic de novo protein design, see: (h) Tegoni, M.; Yu, F.; Berseloni, M.; Pecoraro, V. L. *Proc. Nat. Acad. Sci. U. S. A.* **2012**, *109*, 21234.

59.   (a) M. Sarma, A. Kalita, P. Kumar, A. Singh, B. Mondal, *J. Am. Chem. Soc.* **2010**, *132*, 7846; (b) M. Sarma, A. Singh, G. S. Gupta, G. Das, B. Mondal, *Inorg. Chim. Acta* **2009**, *363*, 63.

60.   A. M. Wright, G. Wu, T. W. Hayton, *J. Am. Chem. Soc.* **2010**, *132*, 14336.

61.   For a similar synthesis to generate Si^{i}Pr$_3$(ONO), see: M. Weidenbruch, F. Sabeti, *Z. Naturforsch., B: Anorg. Chem., Org. Chem.* **1976**, *31B*, 1212.

62.   DFT optimizations of **3.6** using a CH$_2$Cl$_2$ dielectric predict that all OH groups engage in intramolecular H-bonding interactions. Under dilute conditions where intermolecular interactions are less favored, we presume this is an accurate depiction of the solution structure and have therefore represented **3.6** in accordance with the computational results.

63.   M. Kumar, N. A. Dixon, A. C. Merkle, M. Zeller, N. Lehnert, E. T. Papish, *Inorg. Chem.* **2012**, *51*, 7004.

64.   F. H. Jardine, L. Rule, A. G. Vohra, *J. Chem. Soc. A* **1970**, 238.

65.   CuF(PPh$_3$)$_3$ was selected as a viable copper(I) fluoride given its reported synthesis and characterization, in contrast to CuF(tpa), which is not known.

66.   M. S. Rayson, J. C. Mackie, E. M. Kennedy, B. Z. Dlugogorski, *Inorg. Chem.* **2012**, *51*, 2178.

67. Note that the presence of nearly isoenergetic coordination isomers is in accordance with previous studies on copper-nitrite adducts, see: N. Lehnert, U. Cornelissen, F. Neese, T. Ono, Y. Noguchi, K. Okamoto, K. Fujisawa, *Inorg. Chem.* **2007**, *46*, 3916.

68. (a) G. A. Jeffery, W. Saenger, *Hydrogen Bonding in Biological Structures*; Springer-Verlag: Berlin, 1991; (b) K. M. Lancaster, *Struct. Bonding* **2012**, *142*, 119.

69. Note that a similar mechanism for iron-mediated nitrite reduction was recently reported, see: E. M. Matson, Y. J. Park, A. R. Fout, *J. Am. Chem. Soc.* **2014**, *136*, 17398.

70. Ohishi, T.; Shiotani, Y.; Yamashita, M. *J. Org. Chem.* **1994**, *59*, 250.

71. Gray, M. A.; Konopski, L.; Langlois, Y. *Synth. Commun.* **1994**, *24*, 1367.

72. Gaussian 09, Revision D.01, Frisch, M. J.; Trucks, G. W.; Schlegel, H. B.; Scuseria, G. E.; Robb, M. A.; Cheeseman, J. R.; Scalmani, G.; Barone, V.; Mennucci, B.; Petersson, G. A.; Nakatsuji, H.; Caricato, M.; Li, X.; Hratchian, H. P.; Izmaylov, A. F.; Bloino, J.; Zheng, G.; Sonnenberg, J. L.; Hada, M.; Ehara, M.; Toyota, K.; Fukuda, R.; Hasegawa, J.; Ishida, M.; Nakajima, T.; Honda, Y.; Kitao, O.; Nakai, H.; Vreven, T.; Montgomery, J. A., Jr.; Peralta, J. E.; Ogliaro, F.; Bearpark, M.; Heyd, J. J.; Brothers, E.; Kudin, K. N.; Staroverov, V. N.; Kobayashi, R.; Normand, J.; Raghavachari, K.; Rendell, A.; Burant, J. C.; Iyengar, S. S.; Tomasi, J.; Cossi, M.; Rega, N.; Millam, N. J.; Klene, M.; Knox, J. E.; Cross, J. B.; Bakken, V.; Adamo, C.; Jaramillo, J.; Gomperts, R.; Stratmann, R. E.; Yazyev, O.; Austin, A. J.; Cammi, R.; Pomelli, C.; Ochterski, J. W.; Martin, R. L.; Morokuma, K.; Zakrzewski, V. G.; Voth, G. A.; Salvador, P.; Dannenberg, J. J.; Dapprich, S.; Daniels, A. D.; Farkas, Ö.; Foresman, J. B.; Ortiz, J. V.; Cioslowski, J.; Fox, D. J. Gaussian, Inc., Wallingford CT, 2009.

73.   GaussView, Version 5, Dennington, R.; Keith, T.; Millam, J. Semichem Inc., Shawnee Mission KS, 2009.

74.   (a) Dunning, T. H., Jr.; Hay, P. J. In: *Modern Theoretical Chemistry*; Schaefer, III. H. F., Ed.; Plenum: New York, 1976. (b) Hay, P. J.; Wadt, W. R. *J. Chem. Phys.* **1985**, *82*, 270 and 299. (c) Wadt, W. R.; Hay, P. J. *J. Chem. Phys.* **1985**, *82*, 284.

75.   Merrick, J. P.; Moran, D.; Radom, L. *J. Phys. Chem. A*, **2007**, *111*, 11683.

Chapter 4 Protonation state-dependent reactivity with pincer ligands

Portions of this chapter have been published:

Moore, C. M.; Szymczak, N. K. *Chem. Commun.*, **2013**, *49*, 400. Reprinted with permission; copyright 2013 The Royal Society of Chemistry.

4.1 Transfer hydrogenation catalysis promoted by a proton-responsive ligand

4.1.1 Motivation and ligand design

Metal-ligand cooperativity is a key aspect of H_2 activation/transfer by bifunctional catalysts. These systems exploit intramolecular proton transfer as a means to (a) store proton equivalents in the ligand periphery and/or (b) utilize the protonation/deprotonation event to modulate the structural and electronic properties of the ligand.[1] Biological systems similarly engage metal-ligand cooperativity to mediate multi-electron redox events, proton-coupled electron-transfer reactions, and substrate activation.[2] A biologically-relevant metal-ligand platform for bifunctional activation was recently visualized following the discovery of a 2-hydroxypyridine-derived cofactor in the active site of the hydrogenase metalloenzyme, [Fe]-hydrogenase,[3] and subsequently, synthetic transition-metal complexes supported by 2-hydroxypyridine-derived ligands have been demonstrated to promote (de)hydrogenation catalysis.[4] While the intimate details of the role of the 2-hydroxypyridine unit in [Fe]-hydrogenase are still under investigation,

the tautomeric pair 2-hydroxypyridine and 2-pyridone likely function to facilitate H_2 cleavage and transfer (see Chapter 1).[3b,5]

Approaches to synthetic systems that seek to emulate a cooperative H_2 activation pathway, reminiscent of [Fe]-hydrogenase, have targeted bidentate ligand frameworks, such as bipyridine and bipyrimidine, that incorporate 2-hydroxypyridine units.[6] Piano-stool type complexes containing such appended 2-hydroxypyridine structural units have shown promising hydrogenation activity; however, the orientation of the appended OH groups with respect to the metal-bound substrate limits their utility as efficient hydrogenation catalysts due to a necessary reorganization required for H_2 heterolysis. Accordingly, we targeted hydrogen-transfer reactivity using a ligand framework that promotes directed interactions between the secondary coordination sphere environment and metal-bound substrates. The ligand, 6,6'-dihydroxy terpyridine was selected as a rigid, pincer-based framework that enforces interactions of the ligand hydroxyl groups with metal-bound substrates, and is capable of promoting bifunctional catalysis.[7]
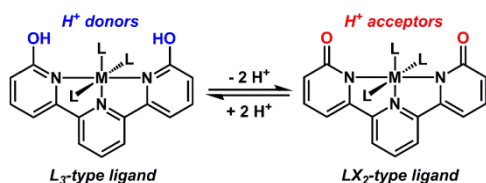
Figure 4-1. Proton-responsive dhtp ligand and differences in ligand field upon deprotonation.

The tautomerism of 6,6'-dihydroxy terpyridine(dhtp) provides accessible proton donors and acceptors in the secondary coordination sphere of the metal center, when maintaining a meridonal N,N,N-coordination mode. The ligand binding modes of the two tautomeric forms of dhtp also present drastically different ligand fields; the hydroxy-tautomer serving as an L_3-type

133

ligand, while the deprotonated pyridone tautomer (dhtp'') acting as an LX_2-type ligand (Fig. 4-1). Such proton-responsive ligand-field dependence is a common feature of catalysis involving proton-transfer events.[1c,d,8]
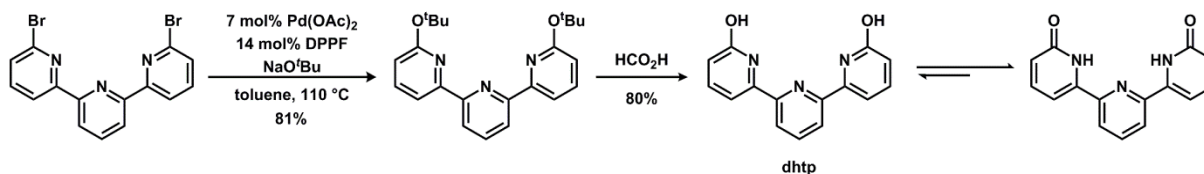
Figure 4-2. Synthesis of dhtp.

We targeted a straightforward synthesis of dhtp, amenable to gram quantity scalability. Because this compound was previously synthesized using F_2-derived reagents[9] and multi-step ring-closing metathesis routes,[10] we devised an alternative two-step route that proceeds from the commercially-available 6,6'-dibromo terpyridine (Fig. 4-2). Palladium(II)-catalyzed coupling of 6,6'-dibromo terpyridine with sodium tert-butoxide afforded 6,6'-di-tert-butoxy terpyridine in 81% yield. Conveniently, hydrolysis of the tert-butoxide groups proceeds within minutes at room temperature upon addition of formic acid, and cleanly provides dhtp in 80% yield as a microcrystalline powder; the preparation can be scaled to gram quantities. In solution and the solid state, dhtp adopts the pyridone tautomeric state.

4.2 Ketone transfer hydrogenation catalyzed by ruthenium-dhtp constructs

4.2.1 First generation catalyst studies

The ability of metal-dhtp adducts to promote hydrogen-transfer reactivity was probed by examining Ru(II) complexes containing PPh_3 as an auxiliary ligand. Reaction of equimolar quantities of $RuCl_2(PPh_3)_3$ and dhtp in refluxing methanol under an inert atmosphere provided trans-RuCl(dhtp)$(PPh_3)_2PF_6$ (**4.1**) after anion metathesis with $[NH_4][PF_6]$.
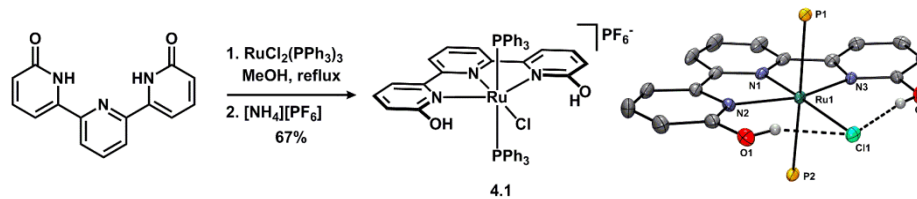
Figure 4-3. Synthesis and solid state structure of 4.1. (30% ellipsoids, counterions, solvent, PR₃ C atoms and H atoms not involved in hydrogen bonding omitted)
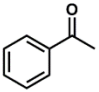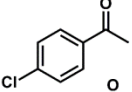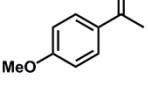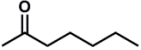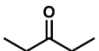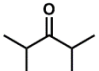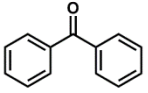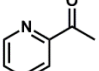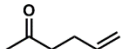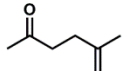
The solid state structure of **4.1** (Fig. 4-3) reveals octahedral coordination around ruthenium(II), with mutually trans PPh₃ ligands. Notably, both of the pendent hydroxyl groups engage in close-contact interactions to the Ru-bound chloride (O1-Cl1 and O2-Cl of 3.017(3) and 2.966(3) Å, respectively); consistent with intramolecular hydrogen-bonding interactions. Additionally the solid-state structure of **4.1** reveals C-O distances of the terpyridine fragment (1.336(5) and 1.335(5) Å) consistent with C-O single bonds and a neutral ligand scaffold.[11]

The orientations of the hydroxyl groups in **4.1** with respect to the Ru-bound chloride can be used to approximate subsequent metal-substrate interactions. For a relevant comparison, Ru-based piano-stool complexes featuring 6,6'-dihydroxy bipyridine (dhbp), $[(\eta^6$-arene)Ru(dhbp)Cl]$^+$,[6d] were selected. In **4.1**, the torsion angles between the Ru-Cl and C-O bond vectors are 2.93° and 4.22° (avg. 3.58°), which demonstrates that the two bond vectors lie nearly co-planar. In contrast, the torsion angles are significantly greater in the case of the dhbp adduct: 65.45° and 62.44° (arene = C₆Me₆, avg. 63.95°), and 82.71° and 82.31° (arene = p-cymene, avg. 82.51°). The OH---Cl interaction was further investigated by comparison of the average distances between the hydroxyl groups and the Cl atom between **4.1** and the $[(\eta^6$-arene)Ru(dhbp)Cl]$^+$ complexes; 3.007 Å for **4.1**, 3.489Å (arene = C₆Me₆) and 3.773Å (arene = p-cymene), the former is consistent with an intramolecular hydrogen-bonding interaction. The differences in distances, as well as geometry, between hydroxyl groups and the ruthenium-bound

chloride atom (a surrogate for a metal-bound hydride) suggest that the ligand geometry imposed by **4.1** is predisposed to offer a strongly coupled hydride/hydroxyl system for hydride and proton transfer.

To confirm the utility of the favorable orientations of the hydroxyl groups in **4.1**, we examined transfer hydrogenation reactivity of acetophenone using complex **4.1** as a catalyst. Using 0.5 mol% **4.1** and 10 mol% KO^{t}Bu in neat 2-propanol, acetophenone is reduced to 1-phenylethanol in nearly quantitative (98%) yield over the course of 12 hours at 80 °C (Table 4-1, entry 1).[12,13] Substitution of the 4-position with electron donating groups (entry 3) was found to slightly decrease hydrogenation, while electron withdrawing groups (entry 2) slightly promoted hydrogenation. Aliphatic ketones were hydrogenated with yields highly sensitive to the ketone steric environment (entries 4-6). Additionally, when benzophenone is used as a substrate no hydrogenation product is observed (entry 7). The catalytic system of **4.1** and KO^{t}Bu tolerates heteroaromatics such as 2-acetylpyridine, which can be reduced to the corresponding alcohol in good yield (79%) over 24 h (entry 8). This finding is noteworthy because the product, 1-(2-pyridinyl)ethanol, is a strongly chelating bidentate ligand,[14] which could coordinate an active hydrogenation catalyst that contains more than one accessible coordination site.

Table 4-1. Scope of transfer hydrogenation catalyzed by 4.1 and KO^{t}Bu.^{a}

Entry	Substrate	Yield (%)[b]	TOF (h^{-1})[c]
1		98	82
2		100	100
3		92	42
4		100	64
5		78	66
6		17	10
7		0	0
8[d]		79	26
9[d]		57[e,f]	n.d.
10[d]		66[e]	n.d.

[a]General conditions: 0.05 mmol ketone, 0.00025 mmol **4.1**, 0.005 mmol KO^{t}Bu, 0.500 mL ^{i}PrOH, 0.029 mmol PhTMS, 80 °C, 12 h. [b]NMR yield calculated against PhTMS internal standard. [c]TOF calculated after 2 h, TOF = 0.5 x [(mmol ketone)$_o$-(mmol ketone)$_{t=2}$]/(mmol **4.1**). [d]Reaction time 24 h. [e]Yield determined by GC/MS; yield of carbonyl hydrogenation product. Note other products are observed, see text. [f]1 mol% PPh$_3$ added.

Given that one of the hallmarks of outer-sphere hydrogenation catalysts is the ability to perform chemoselective hydrogenations, we examined the transfer hydrogenation of unsaturated ketone substrates by **4.1** and KO^{t}Bu. Using our general conditions for transfer hydrogenation, 5-

hexen-2-one is converted to a mixture of hydrogenation products with high conversion (95%) over 24 h; the ratio of 1:0.55:0.71 obtained for 5-hexen-2-ol, 2-heptanone and 2-hexanol, respectively, with a 42% yield of 5-hexen-2-ol. We hypothesized that this low observed selectivity may be due to a competitive inner-sphere hydrogenation pathway which could be suppressed using PPh$_3$. In support, addition of 1 mol% PPh$_3$ provided an increase in selectivity for the carbonyl hydrogenation product, giving a ratio of the aforementioned products of 1:0.16:0.30 after 24 h, with 57% yield of 5-hexen-2-ol (Table 4-1, entry 9).[15] This finding is consistent with suppression of an alternative, non-selective hydrogenation mechanism, however further studies are merited to elucidate the intimate details.

Based on our results illustrating a high steric dependence on hydrogenation, we hypothesized that the chemoselectivity of transfer hydrogenation by **4.1**/KO^{t}Bu could be further increased by introducing steric differentiation between the carbonyl and olefin groups. We tested this by performing the transfer hydrogenation of 5-methyl-5-hexen-2-one (entry 10). Transfer hydrogenation of this substrate proceeds to 81% conversion after 24 h to afford a mixture of 5-methyl-5-hexen-2-ol, 5-methyl-5-hexen-2-one and 5-methyl-5-hexen-2-ol in a 1:0.09:0.13 ratio, respectively, with a 66% yield of 5-methyl-5-hexen-2-ol. Further increasing the steric environment around the olefin provides high chemoselectivity. Transfer hydrogenation of 6-methyl-5-hexen-2-one provides 6-methyl-5-hexen-2-ol as the exclusive transfer hydrogenation product in 95% yield (entry 11). This highlights the ability of the catalytic system **4.1**/KO^{t}Bu to differentiate between steric environments and double bonds, and consistent with prior reports of metal-mediated bifunctional catalysis.[1b,e]
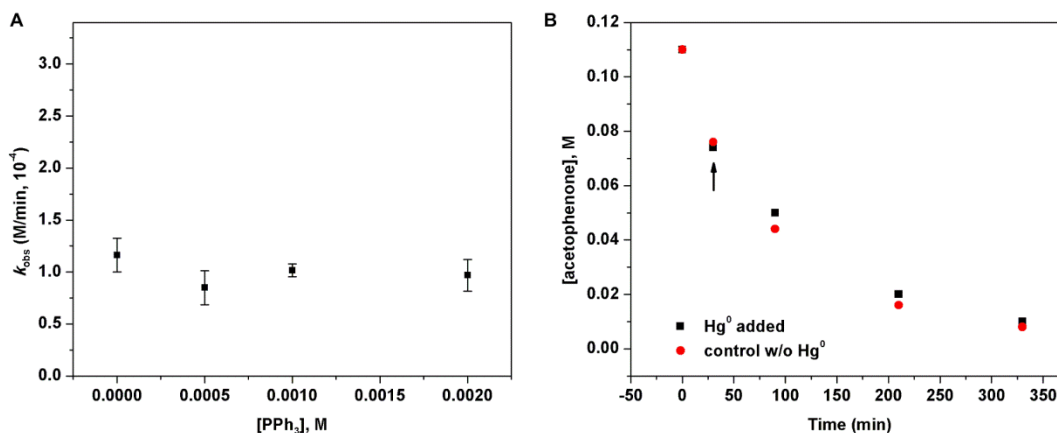
Figure 4-4. Effect of PPh$_3$ concentration on initial rate of acetophenone transfer hydrogenation catalyzed by 4.1 (A) and Hg^0 poisoning experiment during catalysis by 4.1 (B).

Ligand dissociation is a common initiation step for most Ru-based inner-sphere hydrogenation catalysts.[16] Thus, we examined whether exogenous PPh$_3$ hindered catalytic transfer hydrogenation mediated by **4.1**. We hypothesized that, for an outer sphere mechanism, conditions suited to suppress the loss of PPh$_3$ would not inhibit catalysis. Indeed, when an excess of PPh$_3$ (2-8 eq.) is added to the reaction mixture, the rate of transfer hydrogenation catalyzed by the **4.1**/KO^{t}Bu system is not significantly affected (Fig. 4-4A). This result suggests that PPh$_3$ dissociation is not involved in the rate-limiting step of transfer hydrogenation, and is consistent with a catalytically-active species that retains both PPh$_3$ ligands. Moreover, the addition of Hg^0 (*ca.* 1.4 x 10^4 eq.) during transfer hydrogenation has no effect on the reaction profile (Fig. 4-4bB). The mercury poisoning experiment, as well as the highly reproducible reaction kinetics provide evidence consistent with a homogeneous ruthenium catalyst.[17] The stoichiometry of transfer hydrogenation was also examined by quantifying the formation of acetone, relative to 1-phenylethanol, during the reduction of acetophenone, which revealed that equimolar quantities of acetone and 1-phenylethanol are produced concomitantly during the transfer hydrogenation.

4.2.2 Catalyst deactivation and variants

During the course of our subsequent studies on ketone transfer hydrogenation catalyzed by **4.1**, it became apparent that the efficiency of **4.1** was impeded by catalyst deactivation. This was evident by the formation of a deeply colored precipitate emerging as the reaction neared completion. Fortuitously, we were able to isolate this material and identify the structure of the deactivation product through solution (NMR) and solid-state (X-ray and IR) techniques. The deactivation product (**4.1-d**) is a ruthenium aquo-bridged dimer in which the Ru-(OH$_2$)-Ru unit is stabilized by intramolecular hydrogen bonding interactions with the deprotonated dhtp ligand scaffold.
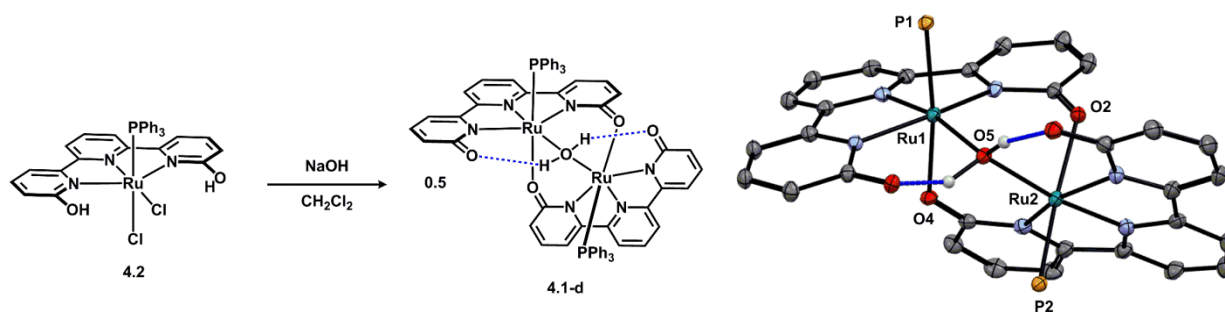
Figure 4-5. Synthesis and solid state structure of the dimer 4.1-d. (30% ellipsoids, solvent and H atoms not involved hydrogen bonding omitted)

Complex **4.1-d** could alternatively be prepared by allowing cis-RuCl$_2$(dhtp)PPh$_3$ (**4.2**) to react with NaOH. Although the solvent used during catalysis (^{i}PrOH) was distilled from CaH$_2$ and dried over activated molecular sieves prior to use, the ppm levels of adventitious water in solution presents a significant hurdle for achieving efficient catalysis since this deactivation product is highly stable and inert to ligand substitution.

We hypothesized that catalyst activity could be optimized by varying the auxiliary ligands on ruthenium and therefore prepared a series of complexes with varying donor sets. Two classes of

complexes were synthesized: one class featuring symmetric auxiliary ligands (**4.3** and **4.4**) and the other featuring asymmetric auxiliary ligands (**4.5** and **4.6**, Fig. 4-6). Complexes **4.3** and **4.4** were prepared by heating benzene solutions of **4.1** with the appropriate PR$_3$ reagent in a sealed vessel. Complexes **4.5** and **4.6** were prepared by allowing complex **4.2** (prepared from the direct reaction of dhtp with RuCl$_2$(PPh$_3$)$_3$ in a non-polar solvent at high temperature) to react with TlPF$_6$ and an excess amount of the desired ligand in dichloromethane solution.
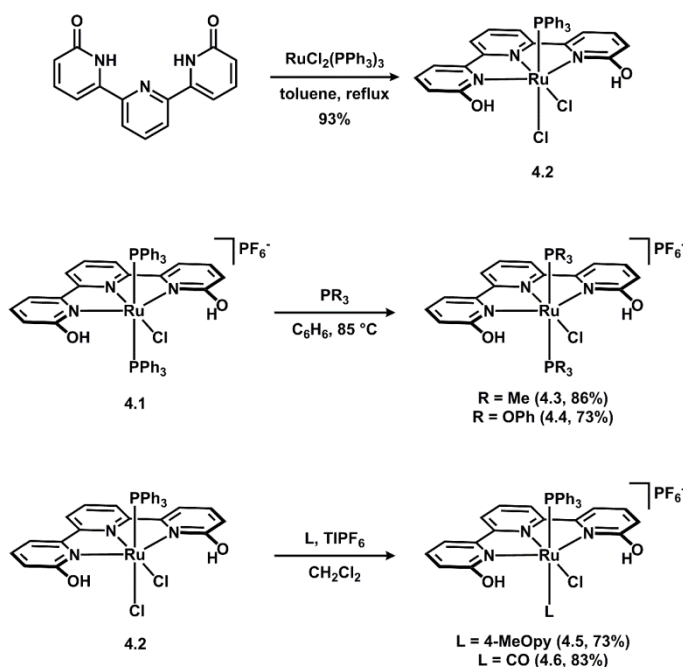
Figure 4-6. Syntheses of ruthenium dhtp adducts.

Both routes allowed for the isolation of the target complexes in high yield and purity, allowing for their characterization by NMR (^{1}H and ^{31}P) and IR spectroscopy. Additionally, crystals of complexes **4.4**, **4.5** and **4.6** suitable for X-ray diffraction were obtained and their solid-state structures are presented in Fig 4-7, along with the structure of complex **4.2**. In general, the solid state structures of these complexes are nearly identical in their primary coordination geometry.

The most notable exception is complex **4.6**, which displays a twisting of the dhtp scaffold, which may be due to an electronic influence from the CO ligand.
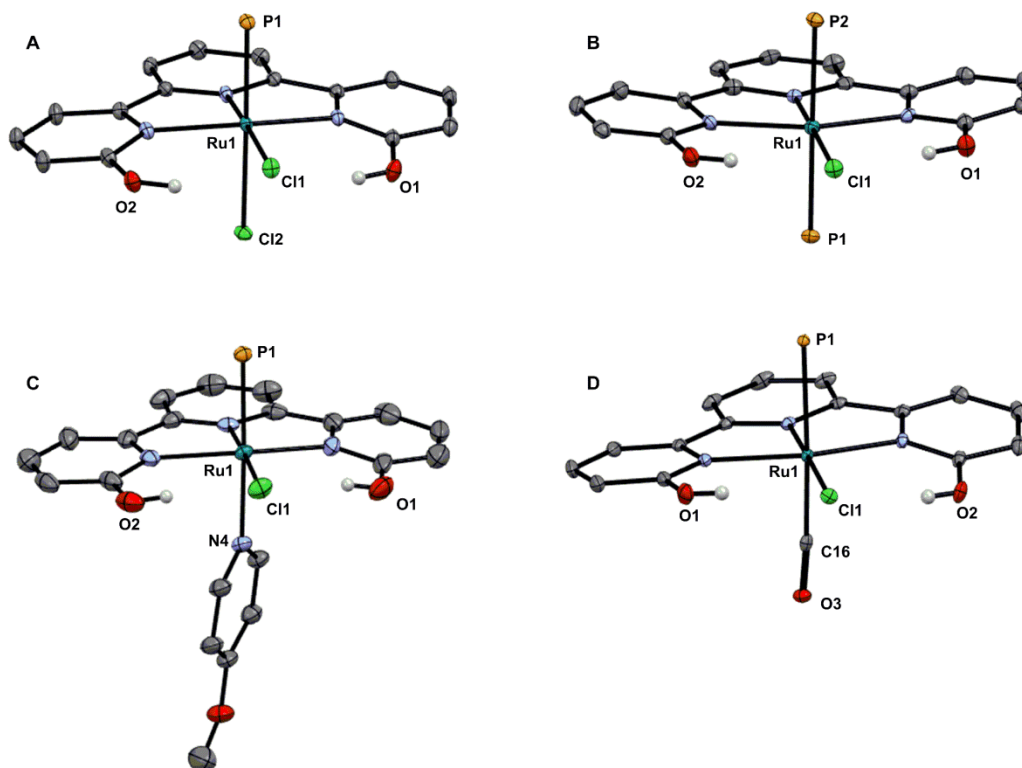
Figure 4-7. Solid state structures of 4.2 (A), 4.4 (B), 4.5 (C) and 4.6 (D). (30% ellipsoids, solvent, counterions, PR$_3$ C atoms and H atoms not involved in hydrogen bonding omitted)

With a series of complexes featuring varying auxiliary ligands in hand, we examined the performance of the ruthenium complexes as catalysts for the transfer hydrogenation of acetophenone. The general conditions previously optimized for complex **4.1** were used and catalysis was allowed to proceed for a total of two hours. The amount of product formed at one hour and two hour time points was quantified using ^{1}H NMR spectroscopy and the results are presented in Fig. 4-8. What is most evident from these data is the stark difference between complex **4.3** and the rest of the series, which is almost completely inactive under the studied conditions. As opposed to catalysis promoted by **4.1**, **4.2** and **4.5**, where precipitation emerges in

the later stages of the reaction, catalytic transfer hydrogenation promoted by **4.6** remains homogeneous throughout the experiment. In order to examine the kinetic profile of transfer hydrogenation catalysis, a homogeneous reaction solution must be maintained. For this reason, we evaluated the details of catalysis through kinetic and mechanistic experiments using complex **4.6**.
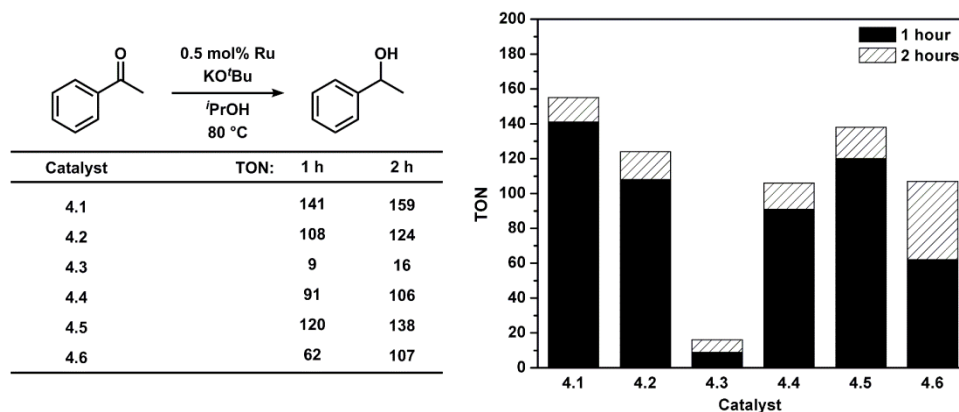
Figure 4-8. Effciency of ruthenium complexes for the catalytic transfer hydrogenation of acetophenone under basic conditions.

4.2.3 Hydride transfer is rate limiting during catalysis

To probe the key mechanistic features of catalytic ketone transfer hydrogenation, we performed kinetic analyses by monitoring reaction progress via ^{1}H NMR spectroscopy; either in situ or by collecting aliquots from reaction solutions at regular time intervals. Product (either acetone or 1-phenylethanol) concentrations were determined by integration utilizing trimethyl(phenyl)silane as an internal standard and all experiments were performed in triplicate to establish error.
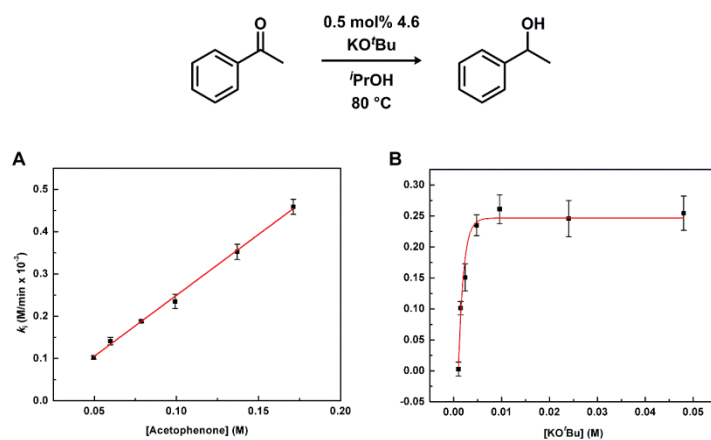
Figure 4-9. Dependence of acetophenone (A) and KO*t*Bu (B) concentrations on the initial rate of acetophenone transfer hydrogenation catalyzed by 4.6.

We first sought to examine the effects of varying substrate and base concentration on the rate of acetophenone reduction. Accordingly, transfer hydrogenation of acetophenone was performed over a range of substrate and base concentrations and the initial rates of substrate reduction were measured. The results of these studies are presented in Fig 4-9. In the case of acetophenone, a linear trend is observed indicative of a first order dependence on acetophenone. For the base concentration, a saturation is observed where a maximum initial rate is observed at a ruthenium:base ratio of approximately 1:10. Beyond this base concentration, the rate remains constant. Note that background measurements were made in the absence of ruthenium catalyst to determine the rate of the base-catalyzed Meerwein-Ponndorf-Verley reduction. These rates were only measurable at high base concentrations (> 0.02 M) and were subtracted from the observed initial rate. The observed base dependence is consistent with a base-accelerated reaction, common for ruthenium-catalyzed transfer hydrogenation reactions. The saturation behavior observed may also be explained by competitive catalyst inhibition by *t*BuOH.
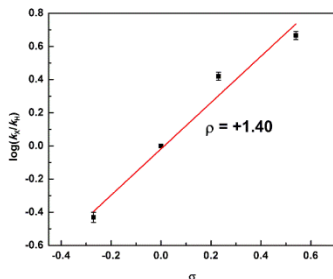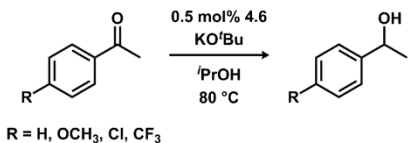
Figure 4-10. Hammett plot for transfer hydrogenation of substituted acetophenones catalyzed by 4.6.

A linear free energy analysis for transfer hydrogenation was conducted to investigate the electronic character of the transition state during catalysis. A Hammett plot was constructed by measuring the initial rates of reduction of para-substituted acetophenone substrates, which yielded a ρ value of +1.40. The positive ρ value indicates build-up of negative charge on the ketone substrate during the rate determining step. Moreover, the magnitude of ρ is consistent with hydride delivery to the ketone substrate in the transition state. This value is lower than that for the reduction of substituted acetophenones by $NaBH_4$ at 30 °C (ρ = +2.02, +3.06)[18,19], reflecting a more anionic nature of the transition state for hydride transfer in the case of BH_4^- reduction.
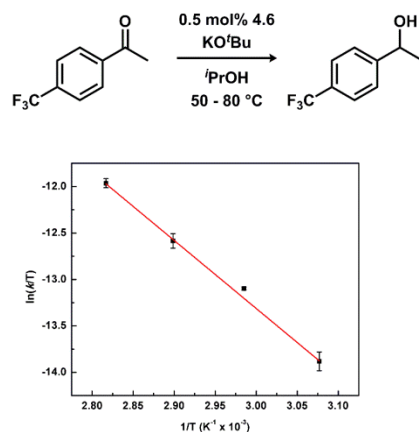
Figure 4-11. Eyring plot for the transfer hydrogenation of 4-(trifluoromethyl)acetophenone catalyzed by 4.6.

The effect of temperature on ketone transfer hydrogenation catalyzed by **4.6** was determined in order to analyze the activation parameters for catalysis. For this study, 4-(trifluoromethyl)acetophenone was used as the ketone substrate since appreciable rates for acetophenone reduction could not be observed at temperatures below 80 °C using our standard conditions. The reaction rates were measured over a 40 °C window and fit to the Eyring equation. This treatment provided $\Delta H^{\ddagger}$ = 15(1) kcal/mol and $\Delta S^{\ddagger}$ = -30(3) eu. At 80 °C, these activation parameters correspond to a free energy of activation ($\Delta G^{\ddagger}$) of 25.3(1) kcal/mol. The negative value of the activation entropy implies that an associative, bimolecular process is operative during the rate determining step. In addition, the magnitude of the activation entropy is suggestive of a highly ordered transition state involving association of substrate with the catalytically-active species. When combined with the first order substrate dependence and the Hammett studies, the kinetic data are consistent with rate-determining hydride transfer to ketone substrate through a transition state which has a highly organized structure.

146

4.2.4 Alkali metal cation effects

We sought to investigate the potential role of the alkali metal cation during catalysis. In order to achieve this, we required a strong, neutral base which would generate ^{i}PrO$^-$ anion in solution without any added metal cations. Under these conditions, we would then be able to examine the effect of added metal cations on catalysis. To meet these criteria, we used Verkade's base (2,8,9-Triisopropyl-2,5,8,9-tetraaza-1-phosphabicyclo[3,3,3]undecane) to generate ^{i}PrO$^-$ anion in solution and salts of the non-coordinating anions $B(C_6F_5)_4^-$ and $B(C_8H_3F_6)_4^-$ to introduce alkali metal cations. Verkade's base is ideal for these purposes since dissolution in ^{i}PrOH quantitatively generates the corresponding phosphonium salt (R$_3$PH$^+$, as determined by ^{31}P NMR), which is expected to be non-reactive toward ketone substrates. Moreover, the tetraarylborate anions should also be stable under the reaction conditions during catalysis.
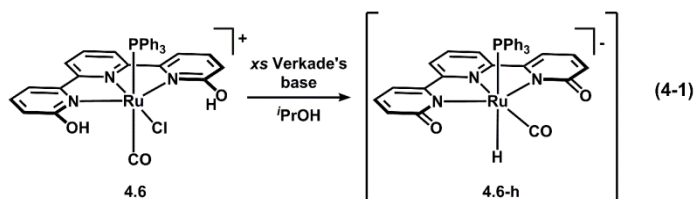
Prior to performing catalysis, we investigated the reactivity of complex **4.6** with Verkade's base in ^{i}PrOH. When a sample of **4.6** is suspended in ^{i}PrOH and treated with excess Verkade's base, the reaction mixture rapidly becomes homogeneous and orange. Analysis by ^{1}H NMR spectroscopy revealed that a new ruthenium hydride complex (**4.6-h**) formed quantitatively under the aforementioned conditions (equation 4-1). In support of this supposition, the ^{1}H NMR spectrum of the reaction of **4.6** with Verkade's base shows that the resonances for the OH groups of the dhtp ligand have disappeared, and a new doublet ($J_{HP} = 105$ Hz) at -8.91 ppm is present. In addition, the ^{31}P NMR spectrum of this reaction mixture exhibits two resonances (in addition to the PF$_6^-$ resonance): a doublet ($J_{PH} = 496$ Hz) at -11.7 ppm, corresponding to protonated

Verkade's base, and a doublet (J_{PH} = 105 Hz) at 33.5 ppm, corresponding to the new ruthenium hydride species. Note that free PPh$_3$ was not observed during the reaction of **4.6** with Verkade's base. Based on the magnitude of the coupling constant between the hydride and PPh$_3$ ligands, and the absence of dhtp OH resonances, the product is formulated as an anionic ruthenium hydride complex, in which the hydride ligand is trans-disposed to the PPh$_3$ ligand.

Moreover, the addition of alkali metal salts to the ruthenium hydride complex **4.6-h** formed *in situ* causes the hydride resonance in the ^{1}H NMR spectrum to shift, dependent on the identity of the alkali metal. Salts of Li$^+$ through Cs$^+$ were added and the chemical shift of the hydride resonance for **4.6-h** was distinct for each metal cation. This is suggestive of coordination of the alkali metal cation to the ruthenium hydride species **4.6-h** in solution. Moreover, the coordination of the cation causes electronic perturbations to the hydride, which could be caused by (a) direct coordination to the hydride or (b) electronic manipulation of the ligand field through cation association. In either case the overall result is the same: added alkali metal cations influence the electron density at the ruthenium hydride, as reflected by the changes in ^{1}H NMR chemical shift.

Beyond altering the room temperature NMR signature of the ruthenium hydride complex, alkali metal cations dramatically impact the rate of acetophenone transfer hydrogenation. When acetophenone is heated to 80 °C in an ^{i}PrOH solution containing 0.5 mol% **4.6**, 10 mol% Verkade's base and 10 mol% tetraaryl-borate salt, the rate of acetophenone reduction is dependent on the identity of the alkali metal cation of the added salt. Salts of Li$^+$, Na$^+$, K$^+$ and Cs$^+$ were analyzed and the initial reaction profiles are presented in Fig. 4-12. Clearly, the results demonstrate that not only does the identity of the metal cation dictate the rate of reduction, but that the rate of reduction increases upon descending through the group. This trend is similar to

that observed by Chen, where the rate enhancement was observed to be greatest for K^{+} and least for Li^{+} when examining Noyori's catalyst during acetophenone hydrogenation.[20]
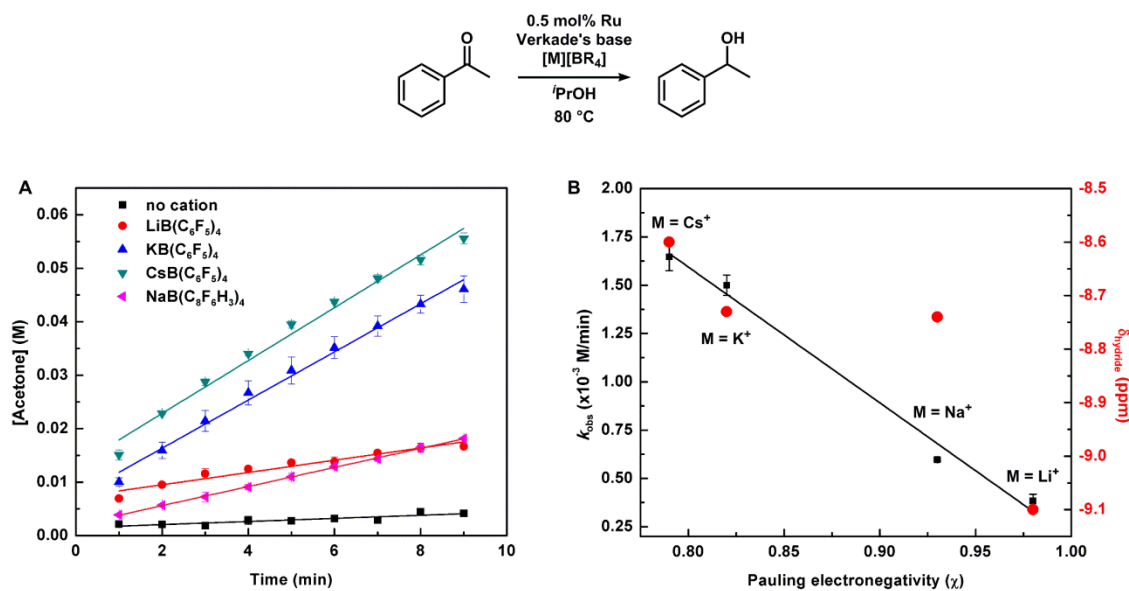
Figure 4-12. Alkali metal effects on the initial profile for acetophenone transfer hydrogenation catalyzed by 4.6 (A) and correlation between the rate of acetophenone reduction and Pauling electronegativity and ^{1}H NMR chemical shift of the hydride resonance and Pauling electronegativity (B).

This finding was rationalized in terms of a higher affinity for K^{+} based on cation-π interactions between the alkali metal and the aryl groups on the ligand scaffold. The origin of the rate enhancement was proposed to be due to substrate coordination to the alkali metal, which serves to increase the susceptibility of the carbonyl group for hydride attack. This hypothesis has been recently supported through computational studies by Dub, Gordon and co-workers[21] as well as through further experimental evidence offered by Bergens and co-workers.[22] When the initial rates of acetophenone transfer hydrogenation catalyzed by **4.6** in the presence of Verkade's base and alkali metals are plotted as a function of the Pauling electronegativity of the metal cation, a linear trend is obtained. Whereas the rate enhancement for Noyori's catalyst plateaus at K^{+}, the rate of catalysis with **4.6** continues to increase beyond K^{+}. This suggests that a preferential

149

binding of the alkali metal due to cation-π interactions is not present. Moreover, the inverse proportionality between the rate of catalysis and the electronegativity of the alkali metal is consistent with a change in electron density at the metal center upon binding the cation *via* an inductive effect, where the least electropositive cation provides the most electron-rich metal center along the series. This notion is supported by the changes in chemical shift of the hydride resonance for **4.6-h** as a function of added alkali metal as the chemical shift of the hydride resonance generally trends with the rate of acetophenone reduction. Since hydride transfer is the rate-limiting step during catalysis, a highly-hydridic hydride is required for rapid insertion into the ketone substrate and an increase in rate with less Lewis-acidic cations is consistent with this hypothesis. Alternatively, the high Lewis acidity of Li$^+$ may inhibit catalysis by stabilizing an alkoxide-bound ruthenium species (*vide infra*) causing a decrese in catalytic rate.

4.2.5 Effect of the location of the OH group on catalysis

Complexes analogous to **4.6** which (a) do not contain OH groups on the terpyridine ligand or (b) contain OH groups in a different position on the ligand are inferior ketone transfer hydrogenation catalysts. We examined two complexes analogous to **4.6** which varied only with respect to the dhtp scaffold: the known terpyridine complex (RuCl(CO)terpy(PPh$_3$)PF$_6$, **4.7**) and a new complex (**4.8**) featuring the 4,4'-dihydroxyterpyridine (4-dhtp) ligand. The 4-dhtp ligand was synthesized in two steps starting from 2-bromo-4-chloropyridine and 2,6-bis(trimethylstannyl)pyridine first through a palladium-catalyzed Stille-coupling, then hydrolysis of the aryl-chloride in a 49% overall yield. When 4-dhtp is allowed to react with RuCl$_2$(PPh$_3$)$_3$ in methanol at 50 °C over 24 hours, complex **4.9** is obtained after salt metathesis, using TlPF$_6$, in good yield. The desired precatalyst **4.8** featuring the 4-dhtp ligand could then be prepared by exposing **4.9** to a CO atmosphere over a 24 hour time period.
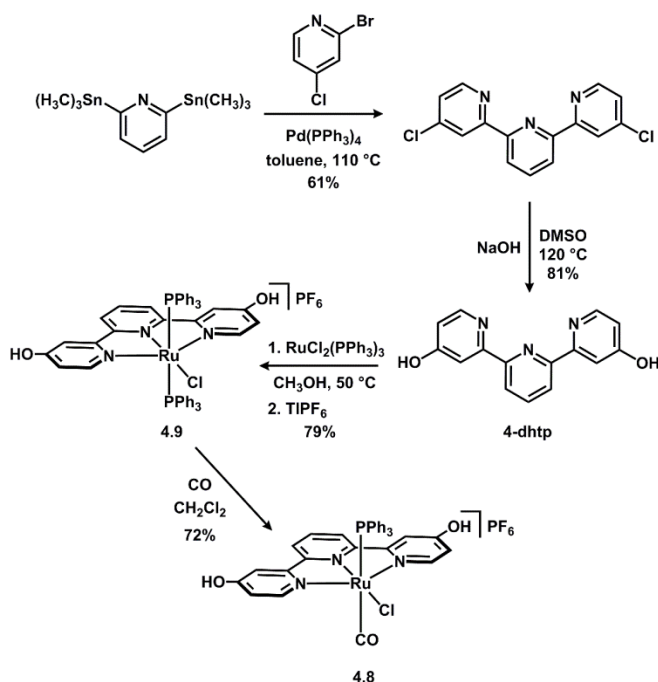
Figure 4-13. Synthesis of 4-dhtp and ruthenium complexes supported by 4-dhtp.

With the series of complexes in hand (**4.6** – **4.8**), we benchmarked ketone transfer hydrogenation catalyzed by **4.7** and **4.8** in the presence of Verkade's base and K^+ ions. Complex **4.7**, devoid of OH groups, is an inefficient catalyst for transfer hydrogenation under the aforementioned conditions, providing only 34 turnovers over two hours. For complex **4.8**, approximately 100 turnovers for ketone transfer hydrogenation were observed over a two hour period. In contrast, complex **4.6** achieves nearly full conversion (96%) of the substrate (191 turnovers) in two hours. Under these conditions, it is clear that the presence and position of OH groups on the terpyridine scaffold has a dramatic effect on transfer hydrogenation efficiency. In the case of the two complexes **4.8** and **4.6**, the location of the OH group has nearly a two-fold effect on the observed catalytic efficiency.
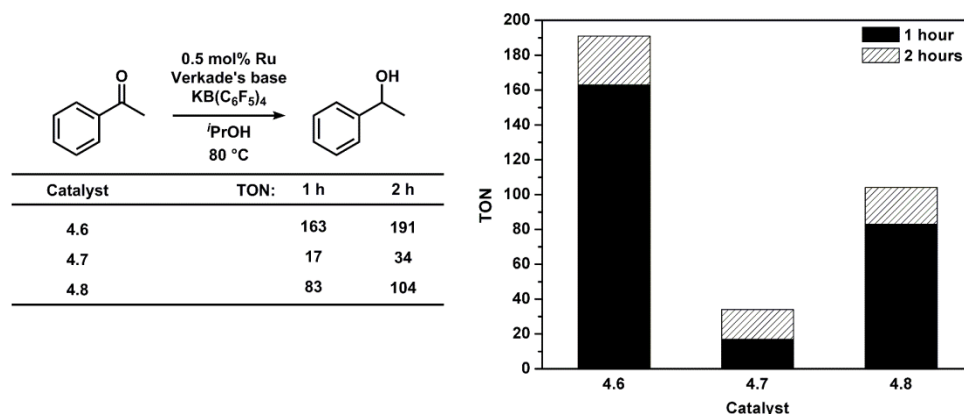
Figure 4-14. Acetophenone transfer hydrogenation efficiency for the ruthenium terpyridine complexes 4.6 – 4.8.

4.2.6 Proposed mechanism for transfer hydrogenation

Based on the above findings, our proposed mechanism for ketone transfer hydrogenation catalyzed by complex **4.6** is depicted in Fig 4-15. Entrance into the catalytic cycle begins with the formation of the hydride complex (A) upon introduction of base and cation (in this case K^+) in ^{i}PrOH solution. In support of this, the hydride resonance in ^{1}H NMR spectrum of the hydride complex **4.6-h** showed a distinct chemical shift dependence on alkali metal. Following hydride formation, attack on substrate proceeds through an intermediate (B) in which the carbonyl group is polarized through interaction with K^+. The large cation effect on reduction rate support a transition state in which the alkali metal is involved in the rate-determining step. Moreover, the large entropy of activation (30 eu) supports a highly organized, associative transition state during hydride delivery. Upon hydride attack on the carbonyl, we postulate a K^+-bound alkoxide (C) is formed, in analogy to Noyori's catalyst as described by several research groups. This alkoxide is likely in equilibrium with a 'bound' form (C'), which would act as an off-cycle loop. A structure similar to C' with ^{t}BuOH likely explains the plateau in activity at high KO^{t}Bu concentrations. Protonolysis of the alkoxide C with ^{i}PrOH to release substrate provides D. This step is likely

152

accelerated under high base concentrations where KO^{i}Pr directly substitutes to release the product alkoxide, which is protonated in the bulk solvent. Hydride abstraction from D liberates acetone and closes the catalytic cycle. Key to this cycle is the position of the cation, which helps to increase activity by orienting the ketone substrate and polarizing the carbonyl for hydride attack. The two-fold enhancement of catalysis with **4.6** over **4.8** supports this notion where the 4-OH ligand would not likely bind cations in an orientation that is suitable for interaction with ketone substrate.
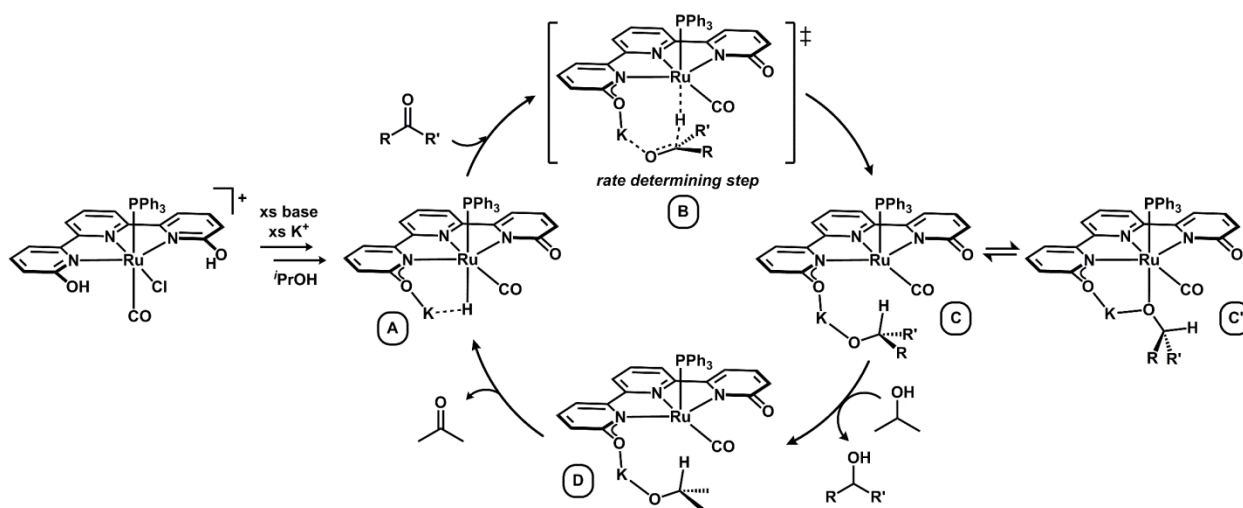
Figure 4-15. Proposed mechanism for ketone transfer hydrogenation catalyzed by 4.6 under basic conditions.

4.3 Dihydrogen adducts supported by the dhtp scaffold

The pendent hydroxyl groups of the dhtp ligand are ideally suited to interact with (and heterolytically cleave) a metal-bound H_2 ligand trans to the central pyridine ring of the terpyridine scaffold, akin to the active site of [Fe]-hydrogenase (*vide supra*). As such, we sought to synthesize complexes which would contain an open coordination site at this position and study their subsequent reactivity toward H_2. We envisioned that placing bulky auxiliary ligands on the metal center would enable us to isolate five coordinate complexes of this type. To test these

hypotheses, we used the ruthenium complex **4.2** as a precursor for investigating deprotonation and ligand substitution reactions. At the outset, *N*-heterocyclic carbene (NHC) ligands were attractive auxiliary ligands to test since the free carbenes are strong bases (pKa ~ 20) and could be used as a single reagent to achieve both dehydrohalogenation of the ruthenium-dhtp precursor and ligation to the metal center.

The reaction of excess NHC **4.10** with the ruthenium-dhtp precursor **4.2** in toluene at ambient temperature provided the desired deprotonated ruthenium complex (**4.11**) supported by two NHC ligands.
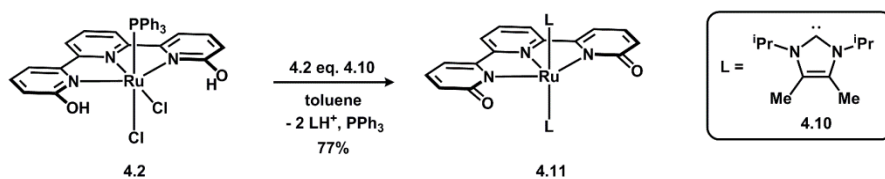
Figure 4-16. Synthesis of the 5-coordinate complex 4.11.

Complex **4.11** was characterized by ^{1}H NMR spectroscopy: the spectrum (CD$_2$Cl$_2$ solution) exhibits a single set of sharp dhtp'' resonances and broad NHC resonances, suggestive of a dynamic process in solution that is best described by a free rotation of the *iso*-propyl groups. No additional resonances were observed that could be assignable to a sixth ligand coordinated to ruthenium, suggesting complex **4.11** is coordinatively unsaturated. The imidazolium salt generated as a byproduct from this reaction could be removed by filtration since **4.11** has high solubility in non-polar solvents. However, this reaction could not be repeated reproducibly multiple times and isolated material occasionally contained mixed phosphine/NHC adducts, imidazolium salt and other unknown byproducts. The origins of the inability to reproducibly prepare **4.11** under these reaction conditions are not currently understood. Nonetheless, the crops of **4.11** produced from successful reactions were used for reactivity studies.

154

Complex **4.11** reversibly reacts with H_2 to form a ruthenium-dihydrogen adduct (**4.12**). Exposing a CD_2Cl_2 solution of **4.11** to 30 psi of H_2 pressure results in the appearance of a broad singlet centered at -1.83 ppm in the ^1H NMR spectrum in approximately 50% conversion from **4.11**. To unequivocally establish the product as a dihydrogen adduct, variable temperature inversion recovery experiments were performed to determine the minimum spin-lattice relaxation time (T_1), which can be used to differentiate hydride and dihydrogen resonances.

Figure 4-17. Reversible H_2 coordination to 4.11 (A), temperature dependence of the T_1 for 4.12 (B) and ^1H NMR spectra of the H_2 and HD resonances for 4.12 and 4.13, respectively (C).

155
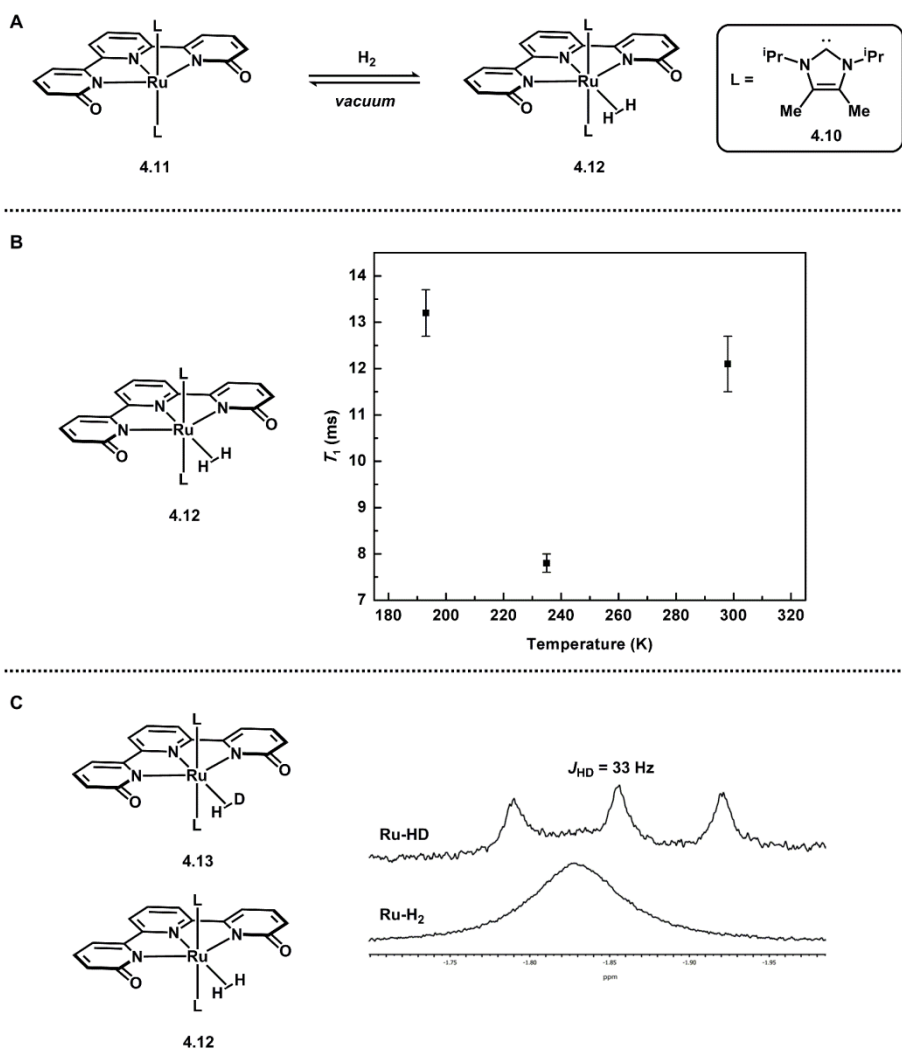
The resonance in question for complex **4.12** has a minimum T_1 value of 7.8(2) ms (Fig. 4-17B), consistent with a metal-bound dihydrogen ligand.[23] Moreover, preparation of the HD isotopologue provides further support. The ruthenium-HD isotopologue (**4.13**) of complex **4.12** was prepared and exhibited a 1:1:1 triplet resonance (-1.85 ppm) in the ^{1}H NMR spectrum (Fig. 4-17C). The magnitude of the H-D coupling constant was used to estimate the H-H bond length and in the case of complex **4.13**, this distance was estimated to be 0.89 Å (J_{HD} = 33 Hz).[23] Free H_2 has a bond length of 0.74 Å and the bond length analysis suggests a weakening of the H-H bond by coordination to ruthenium. We had initially hypothesized that a ruthenium-dihydrogen adduct supported by the fully deprotonated dhtp scaffold would be susceptible to heterolysis by the pendent pyridinoate functionality, in analogy to [Fe]-hydrogenase and other synthetic 2-hydroxypyridine complexes (see Chapter 1). In the case of complex **4.12**, H_2 heterolysis was not observed at ambient temperature or lower and suggests that the pK_a of the H_2 ligand is much greater than that of the pendent pyridinoate, Moreover, the H_2 ligand in complex **4.12** could easily be removed by application of vacuum: this process was repeated to demonstrate the reversibility of H_2 binding. Taken together, these experimental observations point to a weakly bound ruthenium-dihydrogen adduct with no propensity for H-H bond heterolysis across the pyridinoate group.

In contrast, carbon monoxide (CO) irreversibly binds to complex **4.11**. When complex **4.11** is exposed to a CO atmosphere in CD_2Cl_2 solution, the broad ^{1}H NMR resonances of the NHC ligands in **4.11** are replaced with new, sharp peaks for complex **4.14**.
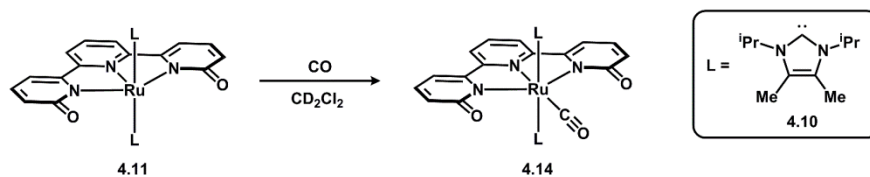
Figure 4-18. Coordination of CO to generate complex 4.14.

The sharp peaks are consistent with the presence of a sixth ligand that blocks rotation of the iso-propyl groups of the NHC ligand. Moreover, the IR spectrum of complex **4.14** shows a sharp ν_{CO} band at 1942 cm^{-1}. The frequency of the CO stretch demonstrates there is significant π-backbonding from the π-basic ruthenium center in **4.14** to the CO ligand. The data from the CO and H$_2$ adducts of complex **4.11** can thus be used to conclude that the 5-coordinate ruthenium complex **4.11** is best described as an electron-rich, π-basic fragment which can bind a sixth ligand; either reversibly (in the case of the σ-donor H$_2$) or irreversibly (in the case of the π-acceptor CO).

4.3.1 Ketone reduction catalyzed by complex 4.11

The competence of complex **4.11** to act as a catalyst for the hydrogenation of ketones was examined. Although no evidence for H$_2$ heterolysis (usually a prerequisite for hydrogenation) was found at ambient temperature, we hypothesized that at elevated temperatures a small population of a heterolysis state might lead to measurable catalytic polar bond hydrogenation.
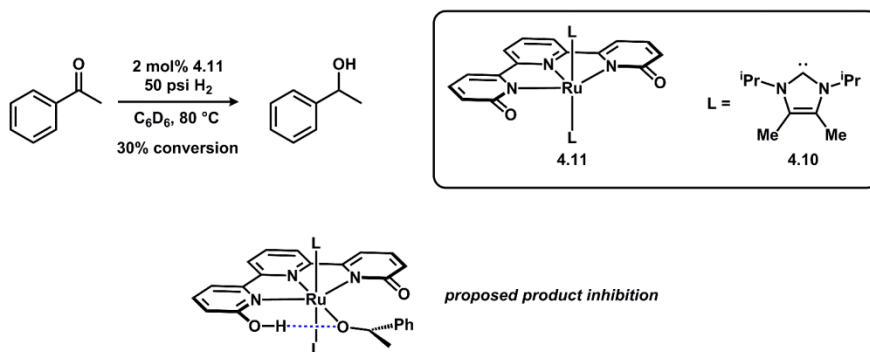
Figure 4-19. Acetophenone hydrogenation catalyzed by 4.11 and a possible catalyst deactivation product.

Accordingly, a solution of complex **4.11** in C_6D_6 was treated with an excess amount of acetophenone (50 equivalents) and heated under H_2 pressure (50 psi) in a re-sealable NMR tube. After five hours at 80 °C, only 30% conversion of the starting ketone was noted and no further reduction occurred over a subsequent 13 hours at 80 °C (Fig. 4-19). The inability to completely reduce acetophenone was hypothesized to be due to competitive binding of the product of reduction, 1-phenylethanol. It seemed likely that the pendent pyridinoate group could engage in stabilizing hydrogen bonding interactions with an alcohol coordinated as a sixth ligand.

To circumvent this issue, we examined the hydroboration of ketones catalyzed by complex **4.11**. In this reaction, the product would be unable to strongly coordinate ruthenium since a Lewis acidic boronate ester group would be bound to oxygen upon reduction. Moreover, the heterolysis of the H-B bond (bond dissociation energy *ca.* 80 kcal/mol) should be more easily accomplished by the pyridinoate group due to the large thermodynamic driving force for forming a B-O bond (bond dissociation energy *ca.* 190 kcal/mol).
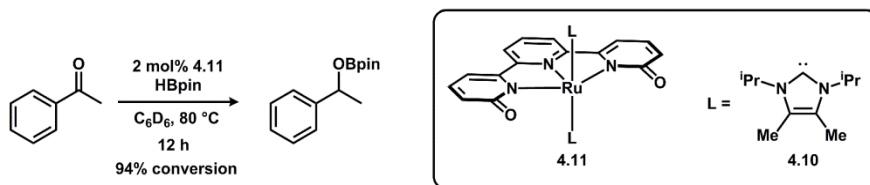
Figure 4-20. Acetophenone hydroboration catalyzed by complex 4.11.

To test this hypothesis, a C_6D_6 solution of **4.11** was treated with excess acetophenone (50 equivalents) and pincaolborane and heated to 80 °C. After 12 hours, nearly complete (94%) conversion of acetophenone to the corresponding hydroborated product was observed. At first glance, the outcome of this experiment supports the hypothesis that alcohol inhibition limits hydrogenation catalyzed by complex **4.11**. However, the large thermodynamic driving force for ketone hydroboration noted above could be a more significant factor in observing complete conversion. The catalytic activity of complex **4.11** for ketone hydroboration surpasses that of Shvo's catalyst under similar conditions,[24] however falls significantly short of a magnesium hydride complex which achieves 980 turnovers in two hours at ambient temperature.[25] Moreover, the inability to reproducibly synthesize complex **4.11** has led to the abandonment of this project until a reliable synthesis can be employed. Nonetheless, these studies demonstrate the ability of the deprotonated dhtp scaffold to mediate E-H bond heterolysis and could be used for future development of catalytic reactions.

4.4 pKa measurements of a homoleptic ruthenium-dhtp complex

To provide insight into the change in electron density at the metal center upon traversing ligand protonation states, a homoleptic ruthenium(II)-dhtp complex was pursued. This complex was targeted to (1) avoid problematic dehydrohalogenation upon deprotonation (if the supporting ligands were chloride) and to (2) circumvent ligand dissociation of auxiliary ligands (such as phosphines) at different protonation states. Additionally, homoleptic ruthenium bipyridine and

terpyridine complexes have been used in a variety of applications, such as photosensitizers for solar cells,[26] electron transfer reagents[27] and as photocatalysts.[28] With this in mind, we also hypothesized that a homoleptic ruthenium dhtp complex could serve any one of these roles and that the properties of the complex could be tuned based on the solution pH to provide distinct reactivity patterns along a H^+ gradient.
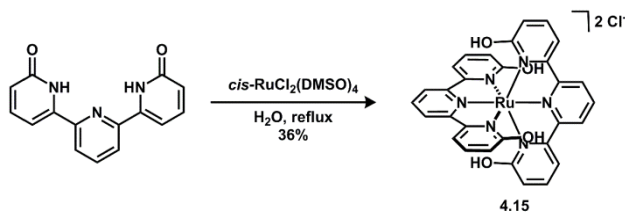
Figure 4-21. Synthesis of the homoleptic ruthenium-dhtp adduct 4.15.

The synthesis of a homoleptic ruthenium dhtp adduct was achieved by refluxing an aqueous solution of cis-RuCl$_2$(dmso)$_4$ with two equivalents of dhtp. After one day, the product, Ru(dhtp)$_2$Cl$_2$ **4.15**, was isolated as an air-stable red powder. Importantly, this complex is soluble in aqueous solutions which made the study of its pH-dependent spectral and electrochemical properties feasible. In order to address how the electronics at the metal center are perturbed upon change in ligand protonation state, we envisioned performing a combined spectrophotometric and potentiometric titration experiment. In this way, the electronic absorption spectrum of the species at varying pH's could be obtained to determine the pKa values associated with protonation events, as well as determine the redox potential of the species in solution.
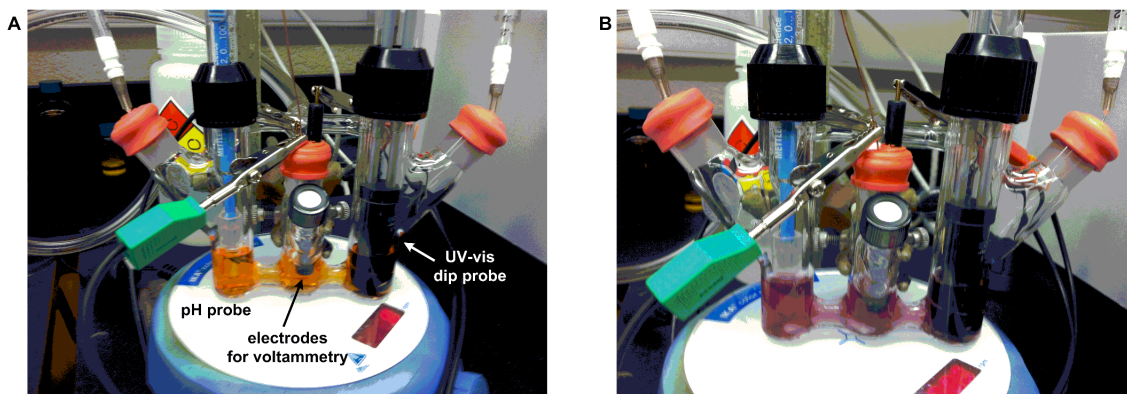
Figure 4-22. Custom cell for measuring pH-dependent UV-vis spectra and electrochemistry under acidic (A) and basic (B) conditions.

In order to achieve this, a custom cell was designed and fabricated which allowed for the suite of experiments (pH measurement, voltammetry and spectroscopy) to be performed on a single solution under an atmosphere of nitrogen, since it became immediately apparent that under basic conditions the complex was easily oxidized by O_2. The cell is depicted in Fig 4-22 containing a solution of **4.15** at low (A) and high (B) pH, and reveals the visible change in color upon change in protonation state.

To collect electronic absorption spectra across a range of pH values, a Britton-Robinson buffer (containing 5% dmso, pH ~ 1.8) was used as the aqueous solution in order to have a linear pH response to added base (NaOH). The electronic absorption spectra of complex **4.15** across a range of pH values are depicted in Fig. 4-23. Using these spectra, two plots were generated from the data collected between the 2 > pH > 7 and 7 > pH > 11 ranges. Monitoring the absorbance at 306 nm for the acidic range and 352 nm for the basic range allowed for a pK_a determination. While one would expect to observe four distinct deprotonation events, we were only able to visualize two; where two H^+ equivalents are lost at each event.
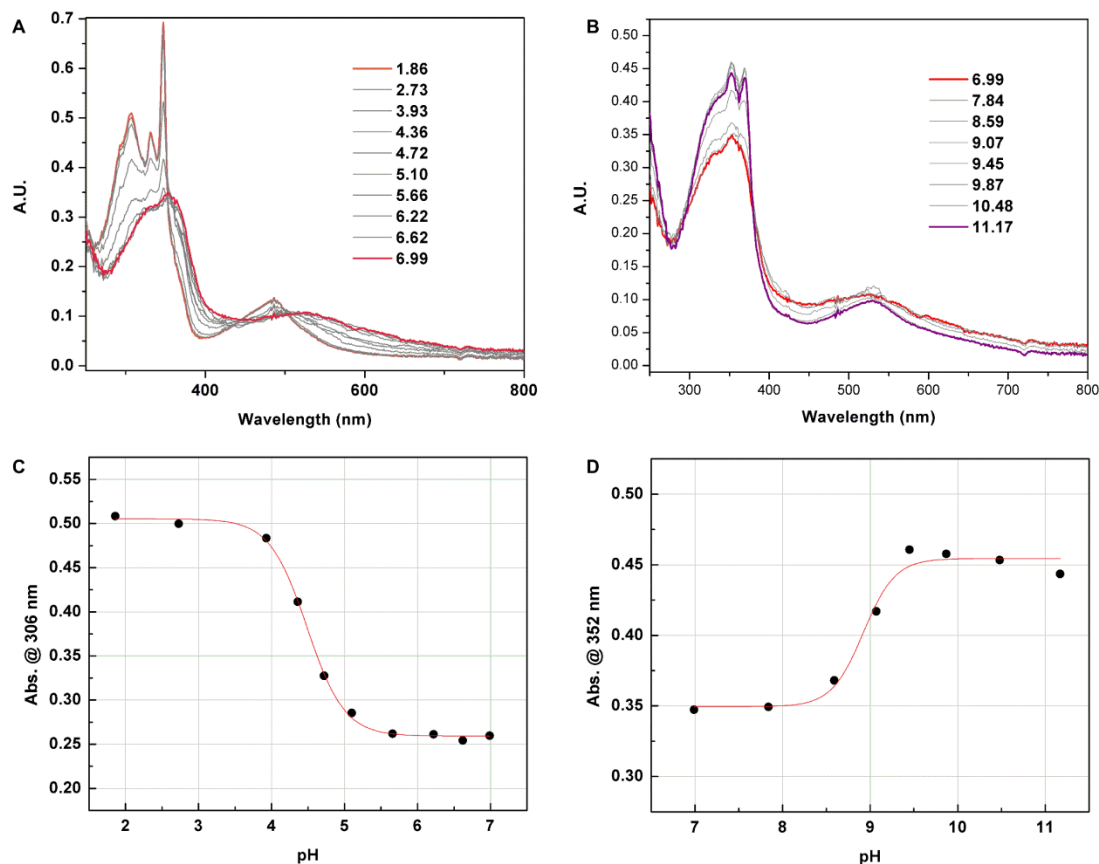
Figure 4-23. UV-vis spectra of 4.15 under acidic (A) and basic (B) conditions, and absorbance plots to determine pKa (C,D).

Most likely, the individual deprotonation events can be decoupled under different conditions or by collecting data at smaller pH increments. However, fitting these plots to sigmoidal curves allows for the determination of the two pK_a values (4.5 and 8.9) which are likely close to (or the average of) the individual values. Based on these pK_a values, a speciation plot (Fig. 4-24) was constructed to visually represent the relative population of each of the three protonation states at a given pH value.
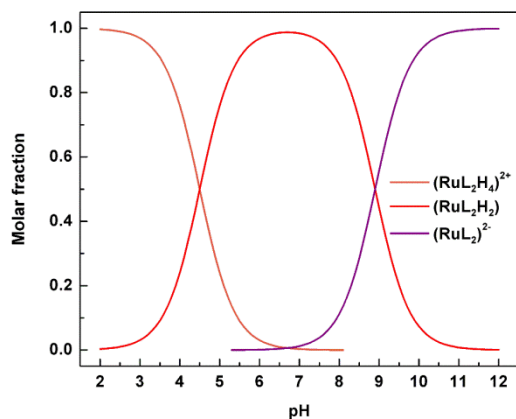
Figure 4-24. pH-dependent speciation diagram for the varying protonation states of complex 4.15.

The concentration required to collect electronic absorption spectra above did not allow for the accurate measurement of redox potentials by either cyclic voltammetry or differential pulse voltammetry (DPV). In order to measure the redox potentials of the species formed at different pH's, a more concentrated solution of **4.15** (~1 mM) was prepared. For this experiment, differential pulse voltammograms (DPVs) were collected since this electrochemical method was more sensitive than cyclic voltammetry and enabled the accurate determination of redox potential. The DPVs of complex **4.15** were collected at three pH values (3, 6.5, and 13), selected based on the above speciation diagram, and showed a cathodic shift upon increasing pH. At higher pH, the ruthenium(III) state becomes more stable relative to ruthenium(II) and reflects an increase in ligand field strength favoring a high oxidation state. Each change in protonation state effected approximately a 0.5 V shift in the redox potential of the complex.
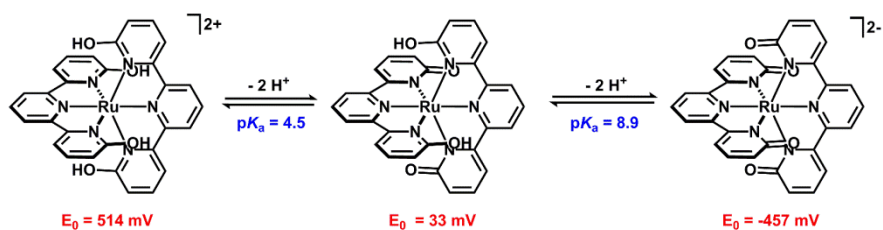
Figure 4-25. Summary of pH-dependent behavior for complex 4.15.

163

This change is notable in that the redox potential of the complex can be modulated by nearly a full volt over a pH range of 3 – 13. To contextualize this redox change, an iron complex supported by a tridentate ligand featuring deprotonatable NH groups was shown to switch the redox potential at the metal center from +0.92 to -0.46 V over a change of 2 pH units (8-10).[29] In this instance, the pK_a's of the NH groups were found to be 8.19, 8.67, 9.86 and 9.93; the first two and last two being only separated by less than 0.5 pK_a units.[29] For the present system, the changes to the redox potential of the metal center are effected over a much broader pH range, which might be used to exploit a differential reaction profile over a wide pH range. The findings from this section are summarized in Fig. 4-25. Using these data, we can estimate the bond dissociation free energies of the OH groups on the ligand scaffold.[30] Although a so-called "square scheme" could not be constructed since two of the pK_a values could not be determined, we can nonetheless provide a first approximation of these values: *ca.* 76 kcal/mol for the first two deprotonation events and *ca.* 59 kcal/mol for the second two deprotonation events.[30] Further work is necessary to (1) understand how the photophysical properties of the complex are altered upon changing pH and (2) exploit this change in ligand field/redox potential for productive chemistry.

4.5 An iron analogue featuring dhtp

Throughout much of this Chapter, and in Chapter 1, the chemistry of [Fe]-hydrogenase is described in detail and referenced when considering 2-hydroxypyridine chemistry. As stated previously, the active site of [Fe]-hydrogenase contains the unusual 2-hydroxypyridine motif and is implicated in H_2 heterolysis and transfer. Up until this point, all of our catalytically-active complexes featuring the 2-hydroxypyridine motif have been based on ruthenium, not iron. As such, we were interested in preparing an iron complex which would be isostructural to the

aforementioned ruthenium complexes and studying its ability to effect H_2 (or E-H) heterolysis and catalytic transfer.
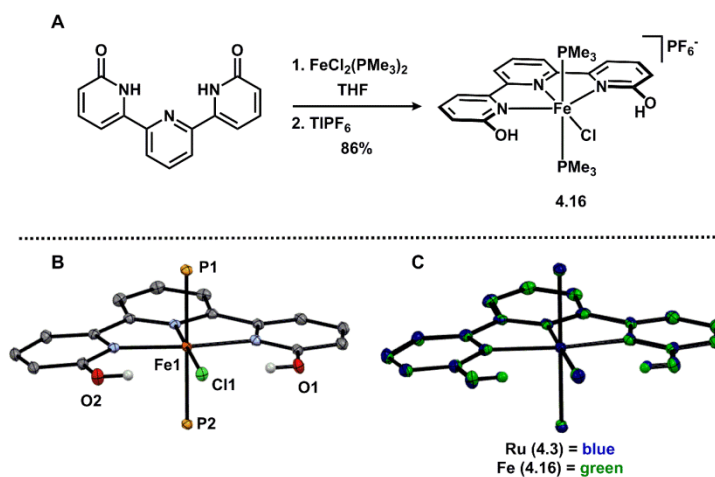
Figure 4-26. Synthesis (A) and solid state structure (B) of the iron complex 4.16, and an overlay of the solid state structures of 4.3 and 4.16 (C). (30% ellipsoids, counterions, PR_3 C atoms and H atoms not involved in hydrogen bonding omitted)

An isostructural iron complex supported by dhtp was synthesized featuring auxiliary trimethylphosphine (PMe_3) ligands. This complex (**4.16**) was prepared by allowing dhtp to react with the iron precursor $FeCl_2(PMe_3)_2$ in tetrahydrofuran, followed by anion metathesis with $TlPF_6$ (Fig. 4-26). Complex **4.16** was isolated as a crystalline, deep purple powder in good yield. The ^1H NMR spectrum of **4.16** (CD_2Cl_2) shows a single set of sharp dhtp ligand resonances along with resonances for two PMe_3 ligands in the normal spectral range (i.e. 0-12 ppm), indicating complex **4.16** is diamagnetic. To evaluate the structural similarity of complex **4.16** to the ruthenium congener **4.3** in the solid state, a crystal of **4.16** suitable for an X-ray diffraction experiment was grown by vapor diffusion of diethyl ether into a dichloromethane solution of **4.16**. The solid state structure of complex **4.16** is highly isostructural to the ruthenium congener **4.3**; an overlay of the two structures is presented in Fig. 4-26C.

4.5.1 Ketone reduction catalyzed by the iron variant

Having demonstrated the structural similarities between the iron and ruthenium congeners, we studied the ability of the iron complex **4.16** to catalytically reduce ketone substrates. Transfer hydrogenation was first surveyed to benchmark the two catalysts. Both complexes were found to be poor catalysts for this reaction and in order to observe significant substrate reduction, 2.5 mol% catalyst and 50 mol% base loading were required.
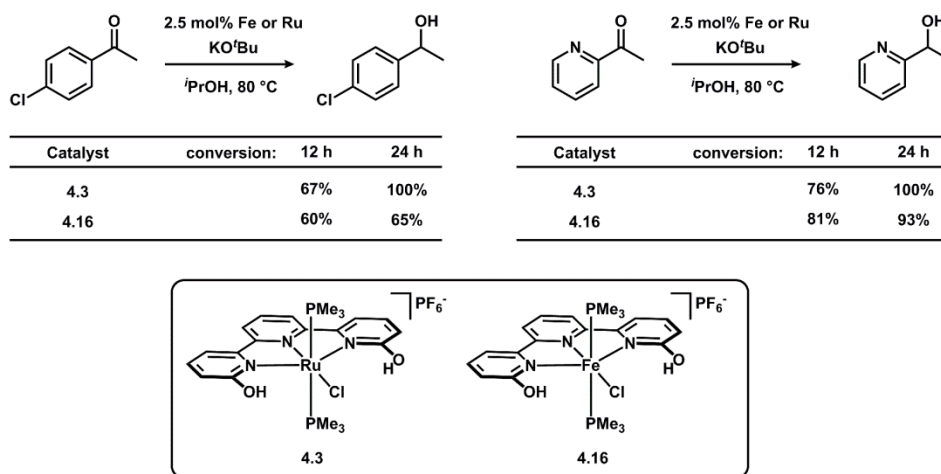
Figure 4-27. Summary of transfer hydrogenation activity for complexes 4.3 and 4.16.

After 12 hours at 80 °C under the aforementioned conditions, both complexes reduced nearly equal amounts of 4-chloroacetophenone (Fig. 4-27). After 24 hours, however, the ruthenium congener **4.3** was able to achieve full conversion, whereas catalysis with the iron complex **4.16** ceased to convert the starting ketone beyond 65% conversion. Most likely, the aryl chloride is incompatible with the iron complex and faciliatates unproductive side reactions. Alternatively, we examined 2-acetylpyridine as a substrate for transfer hydrogenation. Using this substrate, both iron and ruthenium congeners provided similar reactivity over a 24 hour time period. Given their structural similarities, yet large electronic differences (3*d* vs. 4*d* valence shell), it is surprising that the two complexes show similar activity for transfer hydrogenation. Although

166

equal reactivity between iron and ruthenium congeners for catalysis is notable, iron complexes reported by Morris and co-workers have been found to efficiently catalyze enantionselective transfer hydrogenation with as low as 0.02 mol% catalyst in minutes.[31]
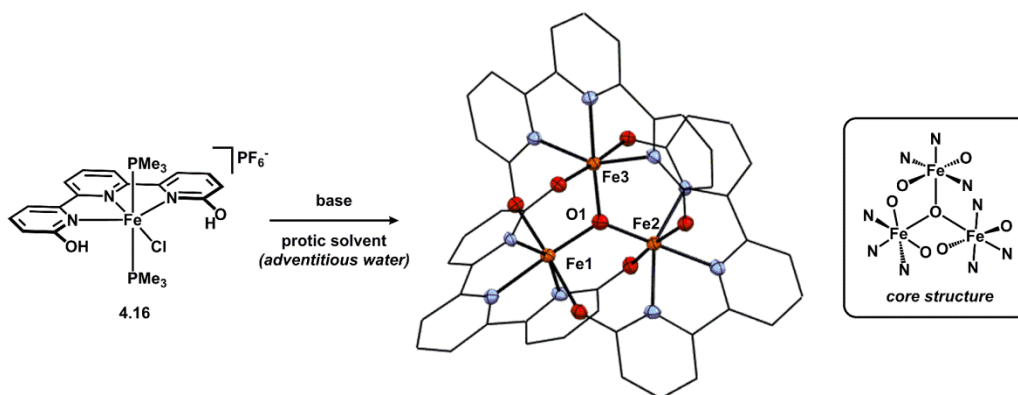
Figure 4-28. Formation of a trimeric iron cluster from 4.16 under basic conditions. (30% ellipsoids, solvent, counterions and H atoms omitted)

Moreover, under basic conditions in protic solvents, the iron complex **4.16** forms a trimeric cluster over time. Fortuitously, a brown crystal of this degradation product suitable for X-ray diffraction appeared from a catalytic hydrogenation experiment in methanol solvent. Although the solvent molecules and potential outer sphere anions could not be rationalized from the diffraction data, the core structure of the complex could be visualized. In the structure, three iron centers supported by the fully deprotonated dhtp ligand are coordinated to a central oxygen atom (Fig. 4-28). Since the residual electron density surrounding the cluster could not be rationalized, the oxidation state at each iron center (+2 vs +3) could not be determined from the diffraction data. Most likely, the iron centers are ferric (+3) and the cluster possesses an overall +1 formal charge, however more characterization data is needed to fully support this hypothesis. Nonetheless, the structure highlights the oxophilicity of iron and the propensity of the dhtp scaffold to form multimetallic ensembles. This cluster is likely the thermodynamic sink of all reactions involving **4.16** with base in protic solvents (which inevitably contain ppm levels of

moisture) since the structure contains six 6-membered rings involving the iron centers. For this reason, we aimed to examine catalysis with iron complex **4.16** in aprotic solvents in the absence of base to avoid the formation of this undesired cluster.

Similar to the ruthenium complex **4.3**, we examined catalytic ketone hydroboration catalyzed by the iron complex **4.16** in aprotic solvent. Since **4.16** is insoluble in benzene, catalysis was investigated in acetonitrile solvent. Excess acetophenone (ca. 100 equivalents) and pinacolborane were allowed to react with complex **4.16** in deuterated acetonitrile at 80 °C. Over the course of one hour, only 10% of the starting acetophenone had been converted to the reduced product. Moreover, the reaction stalled at approximately 30% conversion after two hours and prolonged reaction times did not increase the amount of product formed. The ruthenium congener **4.3**, on the other hand, did not produce any product over this timeframe or over the course of one day.

(4-2)
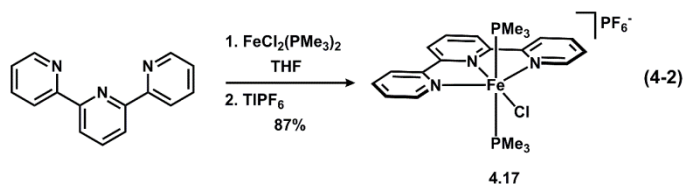
As a control, the analogous parent terpyridine complex **4.17** was synthesized and investigated for hydroboration activity (eq. 4-2). Surprisingly, complex **4.17** is a more active catalyst for acetophenone hydroboration: approximately 80% conversion to the reduced product was noted in one hour under identical conditions tested for the dhtp complex **4.16**.

Catalyst	conversion:	1 h	2 h
4.3		<1%	<1%
4.16		10%	30%
4.17		79%	90%
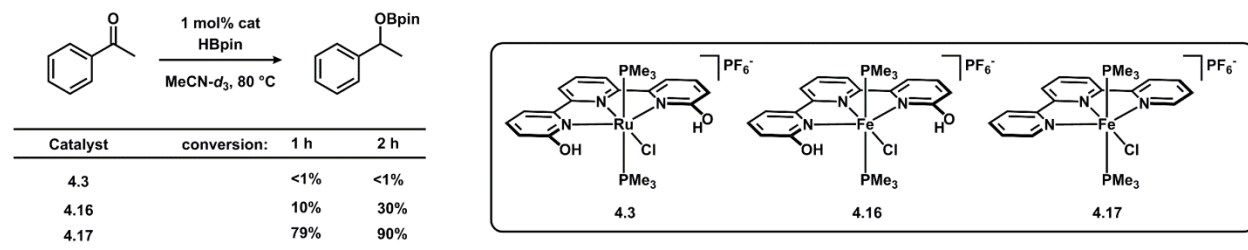
Figure 4-29. Acetophenone hydroboration activity of complexes 4.3, 4.16 and 4.17.

168

The origins of the activity of the terpyridine complex are not understood at present and most likely the terpyridine and dhtp complexes operate through distinct mechanisms to achieve H-B heterolysis and transfer. It is clear, however, that the presence of OH groups on the ligand scaffold serves to deactivate the iron and ruthenium catalysts for hydroboration reactivity. Thus the high activity of the terpyridine complex and low activity of the dhtp complex for catalytic hydroboration have led us to consider other catalyst designs based on iron.

4.6 Experimental section for Chapter 4

General Considerations

All liquid ketones used for transfer hydrogenation studies were either distilled under vacuum or vacuum-transferred from an appropriate drying agent and stored over activated molecular sieves in an inert atmosphere glovebox. All solid ketones were thoroughly dried under high vacuum and stored in an inert atmosphere glovebox. All other commercially-available reagents were used as received without further purification. ^{i}PrOH was distilled from CaH under nitrogen and stored over activated molecular sieves for 24 h prior to use. $LiB(C_6F_5)_4 \cdot 3Et_2O$ was obtained from Boulder Scientific Company and $NaB(C_8H_3F_6)_4$ was obtained from Sigma Aldrich. $RuCl_2(PPh_3)_3$[32], carbene **4.10**[33], complex **4.7**[34] and $KB(C_6F_5)_4$[35] were prepared as previously described. All manipulations were carried out under a purified atmosphere of nitrogen using standard Schlenk techniques or in an MBraun Lab Master 130 or Innovative Technologies Pure Lab^{HE} GP-1 glovebox, unless otherwise stated. NMR spectra were recorded on either a Varian MR400, Varian vnmrs 500 or Varian vnmrs 700 spectrometer and are referenced to residual solvent peaks for spectra collected in deuterated samples. For samples collected in ^{i}PrOH, added trimethyl(phenyl)silane was referenced to 0.1 ppm. IR spectra were collected using a Nicolet iS10 spectrometer equipped with a diamond attenuated total reflectance (ATR) accessory.

GC/MS analyses were performed using a Shimadzu QP-2010 GC/MS. Elemental analysis was performed by Midwest Microlabs, LLC, Indianapolis, IN.

6,6'-di-*tert*-butoxy terpyridine

In a thick-walled Schlenk tube charged with a stirbar, deoxygenated toluene (25 mL) was added to 6,6'-dibromo terpyridine (1.000 g; 2.56 mmol), palladium(II) acetate (0.040 g; 0.18 mmol), 1,1'-bis(diphenylphosphino)ferrocene (0.200 g; 0.36 mmol) and sodium *tert*-butoxide (0.980 g; 10.20 mmol) with stirring. The flask was sealed and stirred at 110 °C for 1 h. The flask was then allowed to cool to room temperature and the resulting mixture was filtered through a small pad of Celite (~4 cm tall x 5 cm diam.) in the open air, and the Celite was rinsed with a minimal amount of toluene. The combined filtrates were concentrated *via* rotary evaporation to give the title compound as a beige solid (0.786 g; 81 %), which was used without further purification. ^{1}H NMR 400 MHz (CDCl$_3$), δ (ppm): 8.29 (d, *J* = 8 Hz, 2H), 8.18 (d, *J* = 7.2 Hz, 2H), 7.91 (t, *J* = 8 Hz, 1H), 7.69 (t, *J* = 8 Hz, 2H), 6.70 (d, *J* = 8 Hz, 2H). ^{13}C NMR 125 MHz (CDCl$_3$), δ (ppm): 163.4, 155.7, 153.5, 139.2, 137.7, 120.5, 113.7, 113.5, 79.5, 28.9. IR, neat (cm^{-1}): 2977, 1567, 1429, 1270, 1248, 1171, 792.

6,6'-dihydroxy terpyridine

6,6'-Di-*tert*-butoxy terpyridine (1.140 g; 3.02 mmol) was dissolved in formic acid (7.0 mL) and stirred for 10 min in the open air. The red solution was then diluted with deionized water (7.0 mL) to produce a thick precipitate. The precipitate was collected on a sintered glass frit and washed with copious amounts of a formic acid/water solution (1:1) until the eluent became colorless. The resulting solid was dried under high vacuum overnight to give the title compound as a pure, white microcrystalline powder (0.640 g; 80 %) with characterization data consistent with that which has been previously reported.[9,10] ^{1}H NMR 400 MHz (DMSO-*d$_6$*), δ (ppm): 12.46

(br s, 2H), 8.06 – 8.22 (m, 3H), 7.59 (app. t, J = 7.8 Hz, 2H), 7.09 (d, J = 6.4 Hz, 2H), 6.49 (d, J = 8.8 Hz, 2H). IR, neat (cm^{-1}): 3087, 1655, 1592, 1475, 1226, 1174, 989, 877, 788. ESI-MS: m/z = 266.0 (100%, MH^{+}).

4,4'-dichloro terpyridine

In a Schlenk tube in the open air, 2,6-bis(trimethylstannyl)pyridine (1.877 g; 4.64 mmol), 2-bromo,4-chloropyridine (2.247 g; 11.68 mmol) and toluene (50 mL) were combined. The tube was sealed and evacuated by three freeze-pump-thaw cycles and refilled with nitrogen. Under a nitrogen atmosphere, Pd(PPh$_3$)$_4$ (0.394 g; 0.34 mmol, dissolved in ca. 40 mL toluene) was added to the solution. The tube was sealed and placed in a 110 °C oil bath and stirred. After three days, the mixture was allowed to cool to ambient temperature and concentrated to dryness on a rotary evaporator. The dark residue was then extracted with boiling ethyl acetate and filtered. Upon standing, crystals of the product emerged from the filtrate and were collected by filtration, washed with a minimal amount of ethyl acetate then hexanes. An additional crop of crystalline product could be obtained by cooling the above filtrate overnight at -25 °C. The obtained material was combined and dried to provide the title compound as a white powder (0.857 g; 61%).^{1}H NMR 400 MHz (CDCl$_3$), δ (ppm): 8.60 (m, 4H), 8.47 (d, J = 8, 2H), 7.98 (t, J = 7.6 Hz, 1H), 7.36 (dd, J = 2 and 5.2, 2H). The 1H NMR characterization data is consistent with a previous report of this compound.[36]

4,4'-dihydroxy terpyridine

In small vial in the open atmosphere, 4,4'-dichloro terpyridine (152.2 mg; 0.504 mmol), NaOH (110.5 mg; 2.76 mmol) and dmso (3 mL) were combined. The vial was sealed with a Teflon-lined cap and the mixture was heated to 120 °C and stirred. After 17 hours, the brown/red reaction mixture was cooled to ambient temperature and H$_2$O (3 mL) was added. The mixture

was then filtered yielding an orange filtrate. Formic acid was added dropwise to the filtrate until a pH of 4 was reached producing a milky suspension. The suspension was cooled in a 5 °C refrigerator and a beige solid settled from the mixture. The solid was collected on a sintered glass frit and washed with H_2O (2 x 5 mL), copious amounts of acetone and then dried to provide the title compound as a beige powder (107.9 mg; 81%). The compound was used without further purification. ^{1}H NMR 500 MHz (CD$_3$OD), δ (ppm): 8.28 (m, 2H), 8.21 (m, 1H), 8.02 (d, J = 7, 2H), 7.30 (d, J = 2.5, 2H), 6.61 (dd, J = 2.5 and 7.5, 2H). ^{13}C NMR 126 MHz (CD$_3$OD), δ (ppm): 181.7, 150.3, 147.3, 141.3, 140.7, 123.5, 117.8, 115.1. HRMS (ESI): m/z = 266.0925 ([M+H]$^+$, predicted: 266.0924).

trans-RuCl(terpyOH)(PPh$_3$)$_2$PF$_6$ (4.1)

In a Schlenk flask charged with a stirbar, deoxygenated methanol (75 mL) was added to the solids 6,6'-dihydroxy terpyridine (0.166 g; 0.626 mmol) and RuCl$_2$(PPh$_3$)$_3$ (0.600 g; 0.626 mmol) with stirring. The mixture was heated to a vigorous reflux for 24 h under a nitrogen atmosphere. The mixture was allowed to cool to room temperature and diluted with methanol (75 mL) and then was filtered through a pad of Celite (~4 cm tall x 5 cm diam.) in the open air. The Celite pad was rinsed with methanol until the eluent became colorless. Solid ammonium hexafluorophosphate (1.700 g; 10.43 mmol) was added to the combined filtrates and the solution was placed in a -25 °C freezer overnight, during which time an orange-colored precipitate emerged. The precipitate was collected, washed with copious amounts of diethyl ether and dried under high vacuum to provide the title compound as a mustard yellow powder (0.448 g; 67 %). ^{1}H NMR, 500 MHz (CD$_2$Cl$_2$), δ (ppm): 10.16 (s, 2H), 7.63 (t, J = 8, 1H), 7.59 (t, J = 8, 2H), 7.50 (d, J = 8.5, 2H), 7.28 (t, J = 7.5, 6H), 7.27 (dd, J = 1 and 7.5, 2H), 7.06 (t, J = 8, 12H), 6.90 - 6.94 (m, 12H), 6.65 (dd, J = 1 and 8.5, 2H). ^{31}P{^{1}H} NMR, 202 MHz (CD$_2$Cl$_2$), δ (ppm): 21.70

(s, PPh$_3$), -144.40 (sep., J = 709, PF$_6^-$). IR, neat (cm^{-1}): 3627, 3100, 1640, 1481, 1434, 1188, 1165, 1090, 833, 788, 744, 695. Anal. Calculated (Found): C, 57.18 (56.95); H, 3.86 (3.87); N, 3.92 (4.04). A crystal suitable for a single crystal X-ray diffraction experiment was grown by vapor diffusion of diethyl ether into a dichloromethane solution of **4.1**.

[Ru(dhtp'')(PPh$_3$)]$_2$OH$_2$ (4.1-d)

Dichloromethane (15 mL) was added to solid 4.2 (54.1 mg; 0.0773 mmol) and NaOH (32.1 mg; 0.803 mmol) and the resulting mixture was stirred. After 24 h, the purple mixture was dried over Na2SO4, filtered and concentrated to a minimal volume. Addition of hexanes to the purple solution produced a precipitate, which was collected on a sintered glass, washed with copious amounts of hexanes and dried to give the title compound as a deep purple powder (29.2 mg; 59%). Crystals suitable for an X-ray diffraction experiment were grown from vapor diffusion of pentane into a benzene solution of **4.1-d**. ^{1}H NMR, 400 MHz (C$_6$D$_6$), δ (ppm): 16.00 (s, 2H), 7.60-7.63 (m, 11H), 6.88-6.93 (m, 21H), 6.77 (d, J = 7.6, 2H), 6.55 (t, J = 8, 2H), 6.45-6.51 (m, 6H), 6.37 (t, J = 7.6, 2H), 6.05 (d, J = 7.2, 2H), 5.95 (d, J = 8.4, 2H). ^{31}P{^{1}H} NMR, 162 MHz (C$_6$D$_6$), δ (ppm): 58.94 (s, PPh$_3$).

cis-RuCl$_2$(dhtp)PPh$_3$ (4.2)

Toluene (*ca.* 150 mL) was added to a mixture of dhtp (0.300 g; 1.13 mmol) and RuCl$_2$(PPh$_3$)$_3$ (1.139 g; 1.19 mmol). The mixture was stirred and heated to a vigorous reflux for 24 h, during which time a magenta precipitate emerged. The mixture was allowed to cool to room temperature and the precipitate was collected on a sintered glass frit in the open air. The solid was washed with toluene until the eluent was colorless, then washed with copious amounts of hexanes and dried to give to the title compound as a dark maroon powder (0.735 g; 93% yield). Crystals suitable for an X-ray diffraction experiment were grown from vapor diffusion of diethyl

ether into a dimethylformamide solution of **4.2**. ^{1}H NMR, 400 MHz (dmso-d_6), δ (ppm): 10.71 (s, 2H), 8.05 (d, $J = 8$, 2H), 7.85 (m, 3H), 7.69-7.77 (m, 2H), 7.29 (t, $J = 8$, 6H), 7.13 (t, $J = 6$, 6H), 6.99 (dd, $J = 2.8$ and 6, 2H), 6.88 (t, $J = 8.8$, 6H). ^{31}P{^{1}H} NMR, 162 MHz (dmso-d_6), δ (ppm): 45.86 (s, PPh$_3$).

trans-RuCl(dhtp)(PMe$_3$)$_2$PF$_6$ (4.3)

Compound **1** (58.4 mg; 0.0545 mmol) was suspended in benzene (*ca.* 10 mL) in a scintillation vial and trimethylphosphine (34 µL; 0.33 mmol) was added. The vial was sealed with a Teflon-lined cap and heated to 85 °C with vigorous stirring for 1.5 h. The reaction was then cooled to ambient temperature and pentane (*ca.* 10 mL) was added to produce a precipitate. The precipitate was collected on a sintered glass frit, washed with copious amounts of pentane and then dried to give the title compound as a bright orange powder (32.8 mg; 86% yield). Crystals of **4.3** suitable for X-ray diffraction were grown from vapor diffusion of diethyl ether into a dichloromethane solution of **4.3** at 5 °C. ^{1}H NMR, 400 MHz (CD$_2$Cl$_2$), δ (ppm): 10.14 (s, 2H), 8.17 (d, $J = 8$, 2H), 8.03 (t, $J = 8$, 1H), 7.97 (t, $J = 8$, 2H), 7.87 (d, $J = 7.6$, 2H), 7.10 (d, $J = 8$, 2H), 0.78 (t, $J = 3.2$, 18H). ^{31}P{^{1}H} NMR, 162 MHz (CD$_2$Cl$_2$), δ (ppm): -5.22 (s, PMe$_3$), -144.48 (sep., $J = 709$, PF$_6^-$)

trans-RuCl(dhtp)(P{OPh}$_3$)$_2$PF$_6$ (4.4)

Compound **4.1** (65.8 mg; 0.0614 mmol) was suspended in benzene (*ca.* 10 mL) in a scintillation vial and triphenylphosphite (97 µL; 0.37 mmol) was added. The vial was sealed with a Teflon-lined cap and heated to 85 °C with vigorous stirring for 1 h. The reaction was then cooled to ambient temperature and pentane (*ca.* 10 mL) was added to produce a precipitate. The precipitate was collected on a sintered glass frit, washed with copious amounts of pentane and then dried to give the title compound as a bright yellow powder (60.8 mg; 85% yield). ^{1}H NMR, 400 MHz

(CD$_2$Cl$_2$), δ (ppm): 9.88 (s, 2H), 7.92 (s, 3H), 7.80 (t, J = 8, 2H), 7.70 (d, J = 7.2, 2H), 7.05 (m, 18H), 6.66 (d, J = 8.4, 2H), 6.55 (d, J = 8, 12H). ^{31}P{^{1}H} NMR, 162 MHz (CD$_2$Cl$_2$), δ (ppm): 101.57 (s, P{OPh$_3$}), -144.29 (sep., J = 709, PF$_6^-$).

RuCl(4-methoxypyridine)dhtp(PPh$_3$)PF$_6$ (4.5)

Dichloromethane (10 mL) was added to a mixture of **4.2** (56.9 mg; 0.0813 mmol) and TlPF$_6$ (31.2 mg; 0.0893 mmol), followed by 4-methoxypyridine (25 µL; 0.25 mmol). The mixture was stirred for 2 h to give an orange suspension. The mixture was filtered and hexane (50 mL) was added to the orange filtrate causing an orange oil to separate. The supernatant was decanted from the oil, which was subsequently triturated with diethyl ether to give an orange solid. The orange solid was collected on a sintered glass frit, washed with copious amounts of diethyl ether and dried to give the title compound as an orange powder (65.2 mg; 73% yield). Crystals of **4.5** with a BPh$_4^-$ counteranion suitable for X-ray diffraction were grown by reacting **4.5** with excess NaBPh$_4$ in dichloromethane and allowing diethyl ether to diffuse into the resulting solution. ^{1}H NMR, 400 MHz (CD$_2$Cl$_2$), δ (ppm): 10.57 (s, 2H), 7.75-7.80 (m, 5H), 7.62 (d, J = 5.2, 2H), 7.54 (d, J = 7.6, 2H), 7.32 (t, J = 7.2, 3H), 7.14 (t, J = 6.4, 6H), 7.01 (t, J = 9.2, 6H), 6.90 (d, J = 8.4, 2H), 6.62 (d, J = 6.8, 2H), 3.71 (s, 3H). ^{31}P{^{1}H} NMR, 162 MHz (CD$_2$Cl$_2$), δ (ppm): 40.31 (s, PPh$_3$), -144.42 (sep., J = 710, PF$_6^-$)

RuCl(CO)dhtp(PPh$_3$)PF$_6$ (4.6)

Dichloromethane (50 mL) was added to a mixture of **4.2** (0.250 g; 0.357 mmol) and TlPF$_6$ (0.132 g; 0.378 mmol) in a Fisher-Porter tube in the open atmosphere. The tube was purged with CO multiple times, then charged to a pressure of 50 psi. The resulting mixture was stirred for 22 hours, during which time the mixture turned from magenta to orange. The mixture was then

filtered through Celite in the open atmosphere into a stirring solution of pentane (ca. 200 mL). The resulting yellow precipitate was collected on a sintered glass frit, washed with copious amounts of pentane and then dried to give the title compound as a bright yellow powder (0.261 g; 87%). ^{1}H NMR, 400 MHz (CD$_2$Cl$_2$), δ (ppm): 10.08 (s, 2H), 8.05 (t, J = 8.4, 1H), 7.87-7.92 (m, 4H), 7.62 (d, J = 7.6, 2H), 7.40 (t, J = 7.6, 3H), 7.21 (dt, J = 1.6 and 8, 6H), 7.03 (d, J = 8.4, 2H), 6.98 (t, J = 9.2, 6H). ^{31}P{^{1}H} NMR, 162 MHz (CD$_2$Cl$_2$), δ (ppm): 16.97 (s, PPh$_3$), -144.40 (sep., J = 709, PF$_6^-$). ATR-IR (cm^{-1}): 2046 (CO).

[RuH(dhtp'')CO(PPh$_3$)][H-PN(CH$_2$N{CH(CH$_3$)$_2$})$_3$] (4.6-h)

A solution of Verkade's base in [i]PrOH (0.48 mL of 0.1 M solution; 0.0048 mmol) was added to solid **4.6** (2.0 mg; 0.0024 mmol), followed by trimethyl(phenyl)silane (5 µL; 0.029 mmol, used as internal standard) in a small vial and stirred for 20 min. The bright red/orange solution was then transferred to re-sealable NMR tube. ^{1}H and ^{31}P NMR spectroscopy revealed quantitative conversion to **4.6-h**. ^{1}H NMR, 700 MHz ([i]PrOH), δ (ppm): 7.51 (t, J = 7, 1H), 7.38 (d, J = 7.7, 2H), 7.04 (t, J = 9.1, 6H), 6.97 (t, J = 7.7, 3H), 6.88 (t, J = 7.7, 6H), 6.80 (t, J = 7.7, 2H), 6.46 (d, J = 7, 2H), 6.12 (d, J = 8.4, 2H), -8.91 (d, J = 106.4, 1H). ^{31}P NMR, 283 MHz ([i]PrOH), δ (ppm): 33.52 (d, J = 105, PPh$_3$), -11.73 (d, J = 496, H-PN(CH$_2$N{CH(CH$_3$)$_2$})$_3^+$)

RuCl(CO)4-dhtp(PPh$_3$)PF$_6$ (4.8)

Complex **4.9** (50.6 mg; 0.047 mmol) was suspended in dichloromethane (20 mL) in a Fisher – Porter tube in the open atmosphere. The tube was purged with CO then pressurized to 60 psi and stirred. After 24 hours, hexanes (20 mL) was added to the mixture in the open air and the resulting precipitate was collected on a sintered glass frit, washed with copious amounts of hexanes and diethyl ether and then dried to provide the title compound as a pale orange powder

176

(30.3 mg; 72%). ^{1}H NMR, 500 MHz (CD$_3$OD), δ (ppm): 8.66 (d, J = 6.5, 2H), 8.03 (d, J = 8, 2H), 7.96 (t, J = 7.5, 1H), 7.63 (d, J = 2, 2H), 7.35 (t, J = 7, 3H), 7.26 (t, J = 8.5, 6H), 7.19-7.22 (m, 6H), 6.99 (dd, J = 2 and 6, 2H). ^{31}P{^{1}H} NMR, 202 MHz (CD$_3$OD), δ (ppm): 13.19 (s, PPh$_3$), -144.61 (sep., J = 707, PF$_6^-$). ATR-IR (cm^{-1}): 2020 (CO).

trans-RuCl(4-dhtp)(PPh$_3$)$_2$PF$_6$ (4.9)

Deoxygenated methanol (30 mL) was added to the solids 4-dhtp (45.8 mg; 0.173 mmol) and RuCl$_2$(PPh$_3$)$_3$ (175.5 mg; 0.183 mmol) under a nitrogen atmosphere. The mixture was heated to 50 °C and stirred. After 24 hours, the reaction was allowed to cool to ambient temperature and solid TlPF6 (64.7 mg; 0.185 mmol) was added and the mixture was stirred for a further hour under nitrogen. The orange mixture was then filtered through Celite in the open atmosphere and diethyl ether (20 mL) and hexanes (200 mL) were added to the filtrate. The resulting orange precipitate was collected on a sintered glass frit in the open atmosphere, washed with copious amounts of diethyl ether and dried to give the title compound as an orange powder (145.9 mg; 79%). ^{1}H NMR, 400 MHz (CD$_3$OD), δ (ppm): 8.61 (d, J = 6.4, 2H), 7.39-7.48 (m, 3H), 7.17-7.27 (m, 20H), 7.09 (t, J = 7.6, 12H), 6.21 (dd, J = 2.8 and 6.4, 2H). ^{31}P{^{1}H} NMR, 162 MHz (CD$_3$OD), δ (ppm): 21.89 (s, PPh$_3$), -144.62 (sep., J = 710, PF$_6^-$)

Ru(NHC)$_2$(dhtp'') (4.11)

Toluene (10 mL) was added to the solids **4.2** (50 mg; 0.071 mmol) and carbene **4.10** (54 mg; 0.30 mmol) in a scintillation vial and the resulting red slurry was stirred. After 13 hours, the dark mixture was filtered through Celite, and the Celite pad was rinsed with toluene until the eluent became colorless. The resulting filtrate was concentrated to a minimal volume and diluted with pentane until a purple precipitate emerged. The precipitate was collected and washed with copious amounts of pentane then redissolved in a minimal amount of dichloromethane and

filtered. The resulting purple filtrate was concentrated to dryness to afford the title compound as a purple solid (40 mg; 77%). Note that this preparation could not be consistently reproduced. ^{1}H NMR, 500 MHz (CD$_2$Cl$_2$), δ (ppm): 7.58 (d, J = 8, 2H), 7.40 (t, J = 7.5, 1H), 7.16 (t, J = 8, 2H), 6.86 (d, J = 6.5, 2H), 6.19 (d, J = 8.5, 2H), 3.80 (br s, 4H), 2.03 (s, 12H), 1.06 (br s, 24H).

Ru(H$_2$)(NHC)$_2$(dhtp'') (4.12)

A sample of **4.11** (ca. 5 mg; ca. 0.007 mmol) was dissolved in CD$_2$Cl$_2$ (0.4 mL) in a re-sealable J. Young NMR tube and an initial ^{1}H NMR spectrum was collected. The tube was then evacuated via freeze-pump-thaw cycles and then charged with 30 psi H$_2$ pressure. The solution immediately turned from red/purple to a red/brown color. Analysis of the resulting solution by ^{1}H NMR spectroscopy showed approximately 50% conversion of complex **4.11** to **4.12**. ^{1}H NMR, 500 MHz (CD$_2$Cl$_2$), δ (ppm): -1.83 (br s, Ru-H$_2$). Depressurizing the tube results in the loss of bound H$_2$ and regenerates **4.11**; this process could be repeated to demonstrate reversible binding.

Ru(HD)(NHC)$_2$(dhtp'') (4.13)

The procedure used to generate **4.12** was repeated except that HD was used. In this experiment, HD was produced by the reaction of NaBH$_4$ (1.9 g; 50 mmol) with MeOD-d_4 (5 mL). The HD produced was vacuum-transferred to the J. Young NMR tube containing **4.11** through a vacuum manifold to generate complex **4.13**.

Ru(CO)(NHC)$_2$(dhtp'') (4.14)

A sample of **4.11** (ca. 5 mg; ca. 0.007 mmol) was dissolved in CD$_2$Cl$_2$ (0.4 mL) in a re-sealable J. Young NMR tube and an initial ^{1}H NMR spectrum was collected. The tube was then evacuated via freeze-pump-cycles and then charged with 30 psi CO pressure. The solution immediately turned from red/purple to dark orange. Analysis of the resulting solution by [1]H

NMR spectroscopy showed quantitative conversion to complex **4.14**. ^{1}H NMR, 400 MHz (CD$_2$Cl$_2$), δ (ppm): 7.79 (m, 3H), 7.09 (t, *J* = 8, 2H), 6.91 (d, *J* = 6.8, 2H), 6.26 (d, *J* = 8.8, 2H), 4.77 (sep., *J* = 6.8, 4H), 2.02 (s, 12H), 0.88 (d, *J* = 7.2, 24H). A solid sample for ATR-IR analysis was obtained by adding pentane to the orange solution to produce a precipitate. The precipitate was collected in the open air, washed with copious amounts of pentane and dried to a red solid (*ca.* 3 mg; *ca.* 0.004 mmol). ATR-IR (cm^{-1}): 1946 (CO).

Ru(dhtp)$_2$Cl$_2$ (4.15)

Deoxygenated H$_2$O (10 mL) was added to solid dhtp (99 mg; 0.37 mmol) and RuCl$_2$(dmso)$_4$ (92 mg; 0.19 mmol) and heated to reflux under nitrogen with stirring. After 16 h, the mixture was allowed to cool to ambient temperature and was concentrated to a red residue. The residue was extracted with methanol and filtered. Diethyl ether was added to produce a precipitate, which was collected on a sintered glass frit, washed with copious amounts of diethyl ether and dried to afford the title compound as a red powder (47 mg; 36%). ^{1}H NMR, 400 MHz (dmso-d_6), δ (ppm): 11.65 (br s, 2H), 8.73 (d, *J* = 7.6, 2H), 8.23 (t, *J* = 8, 1H), 8.14 (d, *J* = 6, 2H), 7.71 (t, *J* = 8.4, 2H), 6.50 (br s, 2H). ESI-MS, m/z: 316.1 (M)$^{2+}$, 631.1 (M-H)$^+$.

trans-FeCl(dhtp)(PMe$_3$)$_2$PF$_6$ (4.16)

In a scintillation vial under N$_2$, tetrahydrofuran (10 mL) was added to dhtp (0.050 g; 0.19 mmol) and FeCl$_2$(PMe$_3$)$_2$ (0.052 g; 0.19 mmol). The resulting purple slurry was stirred briefly (ca. 5 min), then solid TlPF$_6$ (0.070 g; 0.20 mmol) was added and the mixture was stirred for a further 16 h. The mixture was then concentrated in vacuo to afford a purple solid. The solid was extracted with dichloromethane and the extracts were filtered. The resulting purple filtrate was concentrated to a minimal volume and benzene was added to induce precipitation. The deep purple precipitate was collected on a sintered glass frit, washed with copious amounts of benzene

and then pentane, and dried under vacuum to provide the title compound as a deep purple powder (0.105 g; 86%). Crystals suitable for a single crystal X-ray diffraction experiment were grown from vapor diffusion of diethyl ether into a dichloromethane solution of **4.16** at 5 °C. ^{1}H NMR, 400 MHz (CD$_2$Cl$_2$), δ (ppm): 9.85 (s, 2H), 8.00-8.09 (m, 3H), 7.87 (t, J = 7.6, 2H), 7.77 (d, J = 7.2, 2H), 6.80 (d, J = 8.4, 2H), 0.95 (br s, 18 H). ^{31}P{^{1}H} NMR, 162 MHz (CD$_2$Cl$_2$), δ (ppm): 9.82 (s, PMe$_3$), -144.48 (sep., J = 709, PF$_6^-$)

trans-FeCl(terpy)(PMe$_3$)$_2$PF$_6$ (4.17)

In a scintillation vial under N$_2$, tetrahydrofuran (10 mL) was added to terpyridine (0.050 g; 0.22 mmol) and FeCl$_2$(PMe$_3$)$_2$ (0.060 g; 0.22 mmol). The resulting blue-violet slurry was stirred briefly (*ca.* 5 min), then solid TlPF$_6$ (0.077 g; 0.22 mmol) was added and the mixture was stirred for a further 18 h. The mixture was then concentrated in vacuo to afford a blue-violet solid. The solid was extracted with dichloromethane and the extracts were filtered. The resulting blue-violet filtrate was again concentrated to a solid and then redissolved in 1:1 tetrahydrofuran:diethyl ether (*ca.* 5 mL) and placed in a -35 °C freezer overnight. The deposited solid was collected on a sintered glass frit and washed with diethyl ether and dried under vacuum to provide the title compound as a deep violet powder (0.116 g; 87%). ^{1}H NMR, 400 MHz (CD$_2$Cl$_2$), δ (ppm): 8.79 (d, J = 6, 2H), 8.21 (d, J = 7.2, 4H), 7.94-8.02 (m, 3H), 7.55 (t, J = 5.6, 2H), 0.58 (t, J = 4, 18 H). ^{31}P{^{1}H} NMR, 162 MHz (CD$_2$Cl$_2$), δ (ppm): 9.75 (s, PMe$_3$), -144.48 (sep., J = 709, PF$_6^-$).

General procedure for the catalytic transfer hydrogenation of ketones by 4.1

These experiments were typically run in NMR tubes as follows:

In a nitrogen-filled glovebox, a catalyst stock solution of ruthenium complex and base was prepared by adding ^{i}PrOH (10 mL) to ruthenium complex (0.006 mmol) and base (0.12 mmol),

to afford a homogeneous solution. An aliquot of this solution (420 µL; 0.00025 mmol ruthenium and 0.0050 mmol of base) was added to an NMR tube, followed by the ketone substrate (0.05 mmol), trimethyl(phenyl)silane (5.0 µL; 0.029 mmol) as an internal standard and any additives (i.e. $KB(C_6F_5)_4$). The solution was diluted with ^iPrOH to reach a final volume of 0.500 mL. The tube was sealed inside the glovebox and protected with 3-5 layers of electrical tape. The tube was removed from the glovebox and an initial ^1H NMR spectrum was recorded, then the tube was placed in a pre-heated oil bath at 80 °C for 12 h. After this period, a ^1H NMR spectrum was recorded and the NMR yield was calculated using the trimethyl(phenyl)silane resonance as an integration standard.

For kinetics experiments, the tubes were prepared as noted above and then inserted into a pre-warmed NMR spectrometer. Spectra were acquired using the 'UMsetupkinetics' macro and spectra were collected every minute for the first 10 minutes. Baseline corrections for spectra were made using the vnmrj baseline correction command 'fbc' and the acetone resonance was integrated against the interal trimethyl(phenyl)silane resonance.

General procedure for determining chemoselectivity

The general procedure outlined above for the catalytic transfer hydrogenation of ketones was used, except the reactions were performed in a 1 dram vial with stirbar in a nitrogen filled glovebox. Aliquots (20 µL) were taken from the reaction and diluted with dichloromethane (1.0 mL), then analyzed by GC/MS using a Shimadzu QP-2010 GC/MS equipped with a 30 m long DB-5 column with a 0.25 mm inner diameter. The heating scheme used was as follows: 28 °C hold for 15 min, ramp 20 °C/min until 270 °C, and hold 270 °C for 5 min.

Hg[0] poisoning experiment

A related compound, $RuCl_2(PPh_3)_3$, catalyzes transfer hydrogenation *via* formation of Ru-nanoparticles under similar conditions, and in this instance, the addition of Hg[0] significantly affected the reaction profile.[37] To investigate the catalytically-active species derived from **4.1**/KO*t*Bu, we performed a similar experiment. The general procedure outlined above for the catalytic transfer hydrogenation of ketones was used with acetophenone as the substrate and two experiments were run in parallel; one serving as the control reaction. These reactions were performed in re-sealable J. Young NMR tubes. The reactions were monitored *via* ^{1}H NMR spectroscopy to ensure reactions had proceeded past the initiation period (*ca*. 30 min). The NMR tubes were introduced into a nitrogen-filled glovebox and a drop of Hg[0] was added to one tube, re-sealed, and vigorously agitated (the control NMR tube was treated identically, without introduction of Hg[0]). The tubes were removed from the glovebox, returned to the oil bath, and monitored by ^{1}H NMR spectroscopy for a total period of 5.5 h.

4.7 Notes and references

1.   (a) M. C. Warner, C. P. Casey, J.-E. Bäckvall, *Top. Organomet. Chem.* **2011**, *37*, 85; (b) S. Chakraborty, H. Guan, *Dalton Trans.* **2010**, *39*, 7427; (c) R. H. Crabtree, *New J. Chem.* **2011**, *35*, 18; (d) C. Gunanathan, D. Milstein, *Acc. Chem. Res.* **2011**, *44*, 588; (e) T. Ikariya, K. Murata, R. Noyori, *Org. Biomol. Chem.* **2006**, *4*, 393; (f) T. Ikariya, A. J. Blacker, *Acc. Chem. Res.* **2007**, *40*, 1300; (g) A. A. Mikhailine; M. I. Maishan, A. J. Lough, R. H. Morris, *J. Am. Chem. Soc.* **2012**, *134*, 12266; (h) Z. E. Clarke, P. T. Maragh, T. P. Dasgupta, D. G. Gusev, A. J. Lough, K. Abdur-Rashid, *Organometallics* **2006**, *25*, 4113.

2.   (a) *Hydrogen-Transfer Reactions*; J. T. Hynes, J. P. Klinman, H.-H. Limback, R. L. Schowen, Eds.; Wiley-VCH: Weinheim, Germany, 2007; (b) J. I. van der Vlugt, Eur. J. *Inorg. Chem.* **2012**, 363; (c) D. W. Christianson, J. D. Cox, *Annu. Rev. Biochem.* **1999**, *68*, 33.

3.   (a) T. Hiromoto, K. Ataka, O. Pilak, S. Vogt, M. S. Stagni, W. Meyer-Klaucke, E. Warkentin, R. K. Thauer, S. Shima, U. Ermler, *FEBS Lett.* **2009**, *583*, 585; (b) T. Hiromoto, E. Warkentin, J. Moll, U. Ermler, S. Shima, *Angew. Chem., Int. Ed.* **2009**, *48*, 6457.

4.   (a) A. M. Royer, T. B. Rauchfuss, D. L. Gray, *Organometallics* **2010**, *29*, 6763; (b) K.-i. Fujita, N. Tanino, R. Yamaguchi, *Org. Lett.* **2007**, *9*, 109; (c) R. Yamaguchi, C. Ikeda, Y. Takahashi, K.-i. Fujita, *J. Am. Chem. Soc.* **2009**, *131*, 8410.

5.   S. Shima, R. K. Thauer, *Chem. Rec.* **2007**, *7*, 37.

6.   (a) J. F. Hull, Y. Himeda, W.-H. Wang, B. Hashiguchi, R. Periana, D. J. Szalda, J. T. Muckerman, E. Fujita, *Nat. Chem.* **2012**, *4*, 383; (b) W.-H. Wang, J. F. Hull, J. T. Muckerman, E. Fujita, Y. Himeda, *Energy Environ. Sci.* **2012**, *5*, 7923; (c) R. Kawahara, K.-i. Fujita, R. Yamaguchi, *J. Am. Chem. Soc.* **2012**, *134*, 3643; (d) I. Nieto, M. S. Livings, J. B. Sacci, L. E. Reuther, M. Zeller, E. T. Papish, *Organometallics* **2011**, *30*, 6339.

7.   Although previously synthesized, dhtp has not been utilized in transition-metal catalysis (see ref. 9 and 10).

8.   B. G. Hashiguchi, K. J. H. Young, M. Yousufuddin, W. A. Goddard, III, R. A. Periana, *J. Am. Chem. Soc.* **2010**, *132*, 12542.

9.   J. Gatenyo, Y. Hagooly, I. Vints, S. Rozen, *Org. Biomol. Chem.* **2012**, *10*, 1856.

10.   T. J. Donohoe, L. P. Fishlock, P. A. Procopiou, *Org. Lett.* **2008**, *10*, 285.

11.   C. M. Conifer, R. A. Taylor, D. J. Law, G. J. Sunley, A. J. P. White, G. J. P. Britovsek, *Dalton Trans.* **2011**, *40*, 1031.

12   In the absence of base, we observe no reduction of acetophenone. When the amount of base is decreased to 5 mol %, the rate of acetophenone redution is nearly unaffected, however the time required to reach the maximum rate is significantly longer (>200 min vs. <30 min). When 1 mol % base is used, no reduction of acetophenone is observed. These findings are consistent with base-dependent activation of the pre-catalyst: see ref 1g and A. Mikhailine, A. J. Lough, R. H. Morris, *J. Am. Chem. Soc.* **2009**, *131*, 1394.

13.   The maximum TOF for acetophenone reduction catalyzed by **4.1**/KO^{t}Bu (82 h-1) surpasses that observed for the [(η^6-arene)Ru(dhbp)Cl]$^+$ system (7.33 h-1), however the electronic dissimilarity between the two catalyts limits the applicability of comparison based on geometry alone.

14.   S. G. Telfer, N. D. Parker, R. Kuroda, T. Harada, J. Lefebvre, D. B. Leznoff, *Inorg. Chem.* **2008**, *47*, 209.

15.   See experimental section.

16.   S. E. Clapham, A. Hadzovic, R. H. Morris, *Coord. Chem. Rev.* **2004**, *248*, 2201.

17.   J. A. Widegren, R. G. Finke, *J. Mol. Catal. A: Chem.* **2003**, *198*, 317.

18.   K. Bowden, M. Hardy *Tetrahedron* **1966**, *22*, 1169.

19.   R. J. Mullins, A. Vedernikov, R. J. Viswananathan *J. Chem. Educ.* **2004**, *81*, 1357.

20.   R. Hartmann, P. Chen *Angew. Chem. Int. Ed.* **2001**, *40*, 3581.

21.   P. A. Dub, N. J. Henson, R. L. Martin, J. C. Gordon *J. Am. Chem. Soc.* **2014**, *136*, 3505.

22. J. M. John, S. Takebayashi, N. Dabral, M. Miskolzie, S. H. Bergens *J. Am. Chem. Soc.* **2013**, *135*, 8578.

23. G. J. Kubas *Chem. Rev.* **2007**, *107*, 4152.

24. L. Koren-Selfridge, H. N. Londino, J. K. Vellucci, B. J. Simmons, C. P. Casey, T. B. Clark *Organometallics*, **2009**, *28*, 2085.

25. M. Arrowsmith, T. J. Hadlington, M. S. Hill, G. Kociok-Köhn *Chem. Commun.* **2012**, *48*, 4567.

26. K. Kalyanasundaram, M. Grätzel *Coord. Chem. Rev.* **1998**, *77*, 347.

27. M. Hara, C. C. Waraksa, J. T. Lean, B. A. Lewis, T. E. Mallouk *J. Phys. Chem. A* **2000**, *104*, 5275.

28. J. W. Tucker, C. R. J. Stephenson *J. Org. Chem.* **2012**, *77*, 1617.

29. R. F. Carina, L. Verzegnassi, G. Bernardinelli, A. F. Williams *Chem. Commun.* **1998**, 2681.

30. J. J. Warren, T. A. Tronic, J. M. Mayer, *Chem. Rev.*, **2010**, *110*, 6961.

31. W. Zuo, A. J. Lough, Y. F. Li, R. H. Morris *Science*, **2013**, *342*, 6162.

32. P. S. Hallman, T. A. Stephenson, G. Wilkinson *Inorg. Syn.* 1970, *12*, 237.

33. N. Kuhn, T. Kratz *Synthesis* **1993**, *6*, 561.

34. D. Ooyama, M. Saito *Inorg. Chim. Acta.* **2006**, *359*, 800.

35. E. E. Korshin, G. Leitus, L. J. W. Shimon, L. Konstantinovski, D. Milstein *Inorg. Chem.* **2008**, *47*, 7177.

36. G. D. Harzmann, M. Neuberger, M. Mayor *Eur. J. Inorg. Chem.* **2013**, 3334.

37. J. Toubiana, Y. Sasson *Catal. Sci. Technol.* **2012**, *2*, 1644.

Chapter 5 H$_2$ heterolysis using the dhtp platform

5.1 Electronic effects studied in iridium hydrides

In its +3 oxidation state, iridium adopts a low-spin d^6 electronic configuration; directly analogous to ruthenium(II) and low-spin iron(II). Hydride complexes of iridium(III), however, typically exhibit higher stability than first row iron(II) and second row ruthenium(II) hydride complexes.[1] This is in part due to greater M-H bond strengths resulting from interaction with lower lying, more accessible d orbitals in iridium(III) than in ruthenium(II) or iron(II).[1] This beneficial stability has allowed for the isolation of structurally-diverse iridium(III) hydride complexes displaying unique properties.[1] Of particular interest to the proceeding discussion in this Chapter are the class of iridium(III) hydride complexes which display dihydrogen bonding interactions: hydrogen bonding interactions between a partially negatively charged (δ^-) H atom (acceptor) and a partially positively charged (δ^+) H atom (donor). Early examples of complexes of this class were reported by Crabtree and Morris.[2-7] These complexes featured stable (δ^-)H---H(δ^+) adducts that retained the "H$_2$" fragment even upon exposure to vacuum. In these instances, exchange of the H nuclei was not observed and the complexes are best described as static structures.

In contrast to the stable "H$_2$" fragments in the above examples, Crabtree and Eisenstein reported iridium complexes of the general type **5.1** which display reversible H$_2$ binding depending on the supporting phosphine ligand present (Fig. 5-1).[8] For instance, electron-rich

phosphine ligands promoted the formation of iridium dihydrogen adducts (**5.1a**) when complexes of general type **5.1** were exposed with H_2, whereas a more electron-poor phosphine (such as PPh_3) provided the iridium hydride complex (**5.1b**).
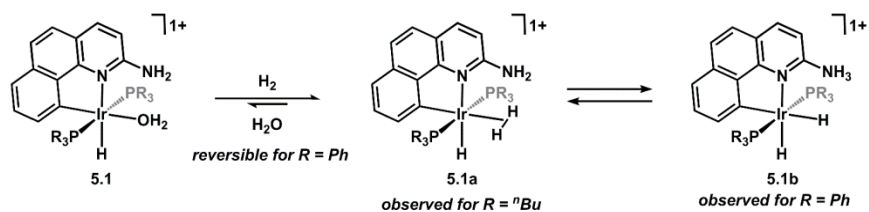
Figure 5-1. Electronic effects of iridium hydride and dihydrogen-adducts observed by Crabtree, Eisenstein and co-workers.

These findings can be rationalized in terms of the acidity of the iridium dihydrogen adducts: the more electron-poor complexes provide a more acidic Ir-(H_2) species which can be deprotonated by the pendent NH_2 group. Interestingly, in no case was an equilibrium between dihydrogen adduct **5.1a** and hydride **5.1b** observed, suggesting that the difference between pK_a's of the putative dihydrogen ligands and NH_2 groups must be greater than two pK_a units.[8] Given that the subtle changes in electronics provided by the different phosphine ligands never allows for the establishment of a dihydrogen/hydride equilibrium, the acidity of the dihydrogen ligand is extremely sensitive to ligand substitution at the iridium center.

5.2 Iridium hydride complexes supported by the dhtp ligand

The synthesis of iridium complexes supported by the dhtp ligand was pursued in order to study H_2 heterolysis mediated by the 2-hydroxypyridine motif. The increased acidity of the ligand OH groups of dhtp, as compared to the NH_2 groups studied by Crabtree and Eisenstein (*vide supra*), would be more likely to establish an equilibrium between dihydrogen adduct and iridium hydride species. Moreover, differences in charge (monocationic for **5.1**) between

previously reported complexes and our targeted, neutral complex (see Fig. 5-2) would allow for a thermodynamically-favored proton transfer from OH group to an iridium-hydride.

The rigid multidentate coordination of dhtp is also ideally suited to maintain a close proximity of the pendent OH groups of the ligand to a *cis*-oriented metal hydride. A synthetic strategy was envisioned whereby reaction of the dhtp ligand with the iridium polyhydride precursor $IrH_5(PPh_3)_2$ could provide either an iridium trihydride complex supported by the neutral dhtp ligand or an iridium monohydride complex featuring the deprotonated, dianionic dhtp ligand and two supporting PPh_3 ligands (Fig. 5-2). In the latter case, the deprotonated dhtp scaffold could be further treated with exogenous acids to generate a cationic iridium hydride complex. At the outset, these complexes seemed ideal targets for studying H_2 heterolysis using the 2-hydroxypyridine motif, in addition to catalysis requiring delivery of multiple H_2 equivalents.
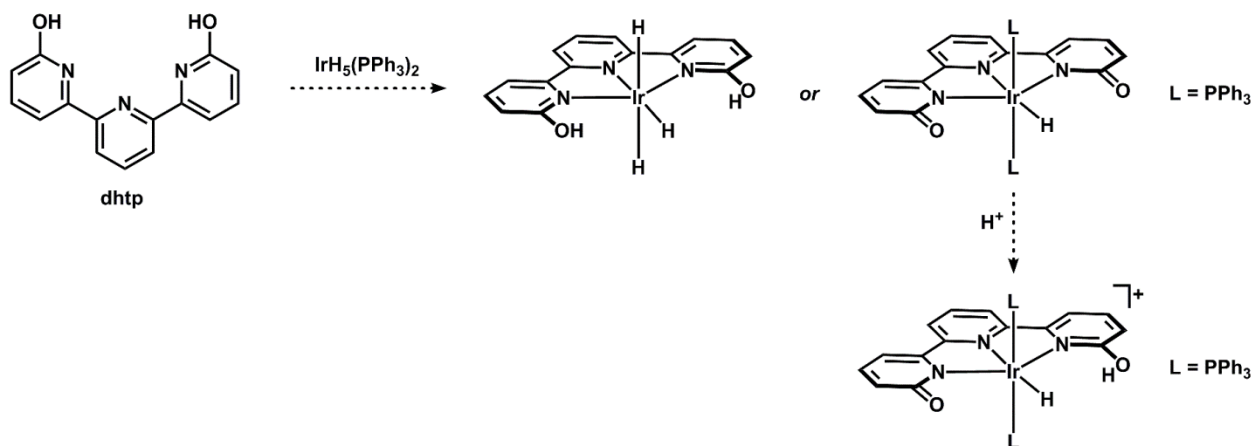
Figure 5-2. Hypothesized iridium hydride complexes supported by dhtp.

When the dhtp ligand was allowed to react with $IrH_5(PPh_3)_2$ at room temperature or above, an unexpected reaction occurred. Rather than isolating either of the hypothesized aforementioned iridium adducts, a cyclometallated product (**5.2**) is formed in which the dhtp ligand is

coordinated to iridium in a bidentate fashion. The structure of **5.2** was confirmed by an X-ray diffraction experiment; dhtp is ligated as a bidentate ligand through a *C,N*-coordination mode (Fig. 5-3). The outer sphere 2-hydroxypyridine motif is in the 2-pyridone tautomeric form, engaging in a hydrogen bonding interaction with the central pyridine ring. The low resolution of the data, however, prohibited the location of the protons and hydrides from the difference map.
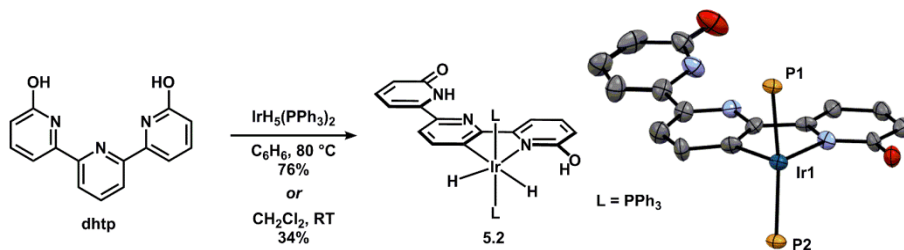
Figure 5-3. Synthesis and solid state structure of 5.2. (30% ellipsoids; solvent, PR$_3$ C atoms and H atoms omitted)

Solution state (CD$_2$Cl$_2$) characterization of **5.2** by ^{1}H NMR spectroscopy revealed that the OH proton and nearest iridium hydride exchange rapidly. At room temperature, the resonances for these two hydrogens are not observable. However, these resonances could be visualized upon cooling the sample below room temperature (Fig. 5-4).
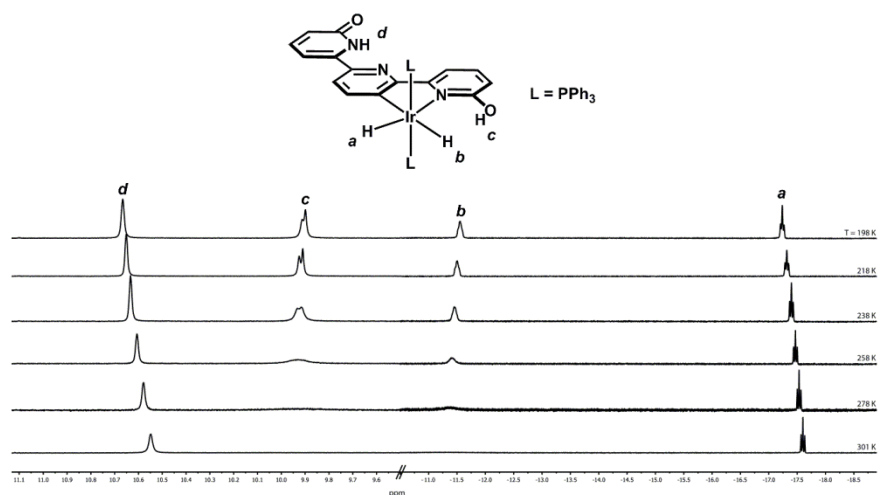
Figure 5-4. Variable-temperature ^{1}H NMR spectra of 5.2. (Hydridic and protic resonances shown for clarity)

189

A set of inversion recovery experiments was performed on a solution of **5.2** at 238 K in order to measure the spin-lattice relaxation time (T_1) of the four resonances associated with the protic and hydridic resonances in complex **5.2**. This analysis was used to confirm that a chemical exchange process between the OH proton (resonance b) and hydride (resonance c) is present.
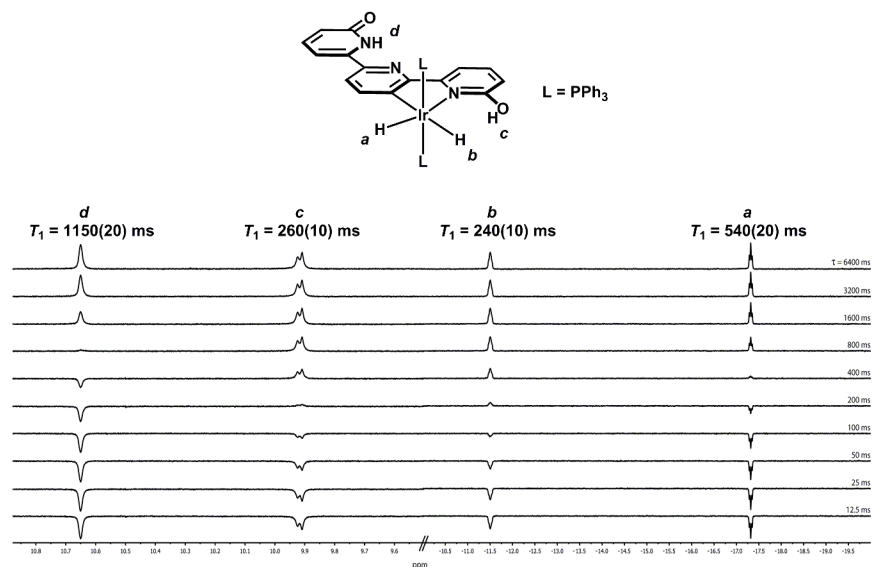
Figure 5-5. Inversion-recovery ^{1}H NMR experiment for complex 5.2. (CD$_2$Cl$_2$, 238 K)

For the N-H resonance (d), a long T_1 value (1150 ms) was obtained, consistent with a protic-type environment. The non-coupled hydride (resonance a) has a T_1 value (540 ms) consistent with a typical metal hydride.[9] The coupled resonances (b and c) have identical T_1 values within error (*ca.* 250 ms), consistent with a chemical exchange process between the two nuclei. The low value of the T_1, with respect to the non-coupled hydride (a), is likely due to a dipole-dipole relaxation mechanism between the two nuclei resulting from their close proximity in space.[8] Furthermore, the temperature dependence of the T_1 values for the four resonances was interrogated by performing inversion recovery experiments on complex **5.2** over a variety of temperatures (Fig. 5-6). Notably, the coupled hydride and OH proton resonances (b and c) have

190

identical temperature-dependent profiles. This is again consistent with two nuclei in rapid chemical exchange on the NMR time scale.
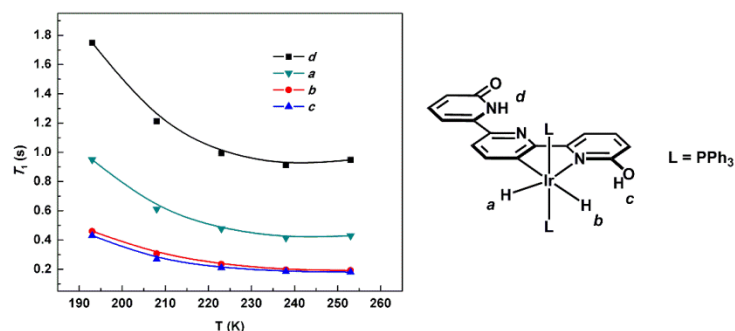
Figure 5-6. Temperature dependence of the T_1 values for the hydridic and protic resonances in complex 5.2.

A chemical description for the mechanism of exchange of the two nuclei in complex **5.2** is presented in Fig. 5-7. This mechanism involves initial proton transfer of the OH proton to the iridium hydride to generate an iridium dihydrogen adduct. Rotation of coordinated H_2 likely has a minimal barrier (< 3 kcal/mol)[10] and is followed by proton transfer to achieve chemical exchange.
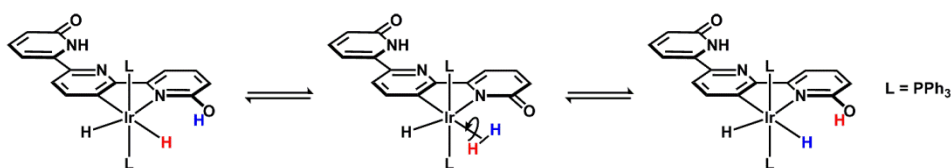
Figure 5-7. Proton/hydride exchange mechanism for complex 5.2.

5.2.1 H_2 heterolysis probed by magnetization transfer

Having confirmed that the protic and hydridic resonances in complex **5.2** are in rapid chemical exchange on the NMR time scale, a quantitative measure of the rate of exchange was pursued. A convenient method to measure chemical exchange rates is by use of exchange spectroscopy (EXSY) techniques *via* ^{1}H NMR spectroscopy. This method relies on the nuclear Overhauser effect (NOE) and probes through-space interactions between nuclei. Much like a

typical one-dimensional nuclear Overhauser spectroscopy (NOESY) experiment, a radio frequency (RF) pulse is applied to one of the resonances in chemical exchange and the effect on the coupled nucleus is observed.
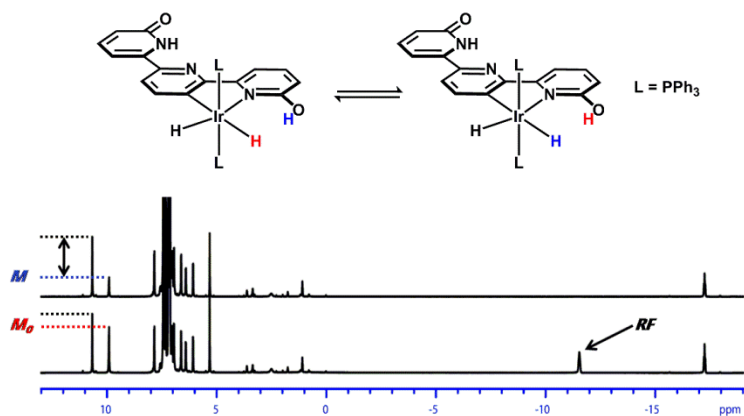
Figure 5-8. Representation of hydride suppression and corresponding OH peak diminishment due to chemical exchange of the two nuclei.

The duration of the RF pulse is selected such that the resonance of choice is completely suppressed and no longer observable in the ^{1}H NMR spectrum. This is represented in Fig. 5-8 where an RF pulse was applied to the coupled hydride resonance at -11.5 ppm. The amount of chemical exchange can easily be determined by integration of the 'coupled' resonance (in this case the OH resonance near 10 ppm) before and after the RF pulse is applied. The extent to which the coupled resonance is diminished (measured *via* integration) can be used to measure a rate for the chemical exchange, based on the T_1 value of the resonances involved according to equation 5.1.[11] Here, M_0 represents the initial magnetization (measured by integration) of the exchanging nuclei and M represents the magnetization after the RF pulse has been applied (Fig 5-8). To measure magnetization transfer in complex **5.2**, integration of the OH resonance using the NH resonance (which is not affected by the RF pulse) as an internal standard allowed for M_0 and M to be accurately determined.

192

$$k = \frac{1}{T_1}\left(\frac{M_0}{M} - 1\right) \quad (5.1)$$

Importantly, this treatment requires that the two resonances of interest have the same T_1 value, which was previously established for complex **5.2**. Since the coupled resonances are observable only below room temperature, these experiments were performed at 238 K and below. At 238 K, magnetization transfer experiments revealed that the two nuclei are rapidly exchanging at a rate of 30.2(3) Hz.

In order to determine the activation parameters for the exchange reaction, this experiment was performed across a series of temperatures below 273 K. The results of these experiments are presented in Fig. 5-9. While a linear trend between $\ln(k/T)$ and inverse temperature exists between 253 and 208 K, at 193 K there is significant deviation from linearity. At this temperature, the OH resonance appears non-Lorentzian and almost resembles a doublet. This behavior can be seen in the spectra in Fig 5-4. The origin of this behavior is unclear; however the trapping of two chemically-similar states (such as the presence and absence of a dihydrogen bond) at low temperature could explain this phenomenon.
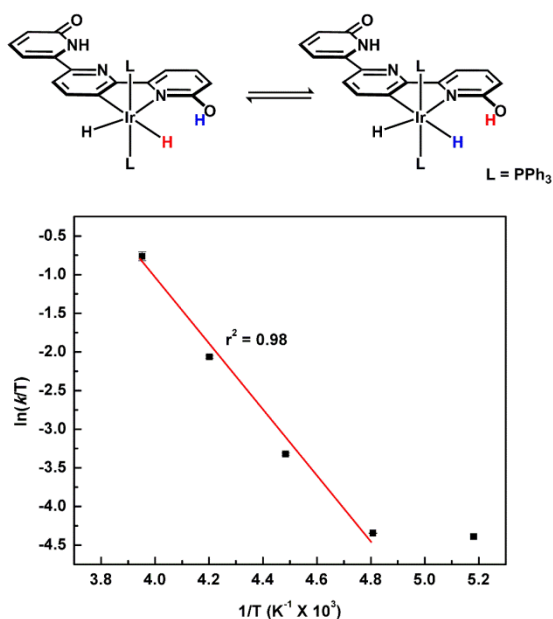
Figure 5-9. Eyring analysis of the hydride/proton exchange in complex 5.2.

Nonetheless, the enthalpy and entropy of activation for the chemical exchange process was estimated by fitting the data from the linear region to the Eyring equation. This treatment provided $\Delta H^{\ddagger} = 8.3(4)$ kcal/mol and $\Delta S^{\ddagger} = -16(2)$ eu. The large negative entropy of activation is surprising, given that little structural reorganization is envisioned to be required to achieve exchange. Moreover, a solvent-assisted exchange mechanism that might account for the observed entropy is unlikely operative since the solvent used for the measurements was CD_2Cl_2. From these parameters, the barrier to net H_2 heterolysis at room temperature could be calculated, thus giving $\Delta G^{\ddagger} = 13.1(1)$ kcal/mol. This barrier corresponds to a rate of exchange, and net H_2 heterolysis, of 1.5×10^3 Hz at room temperature.

5.2.2 DFT-calculated barrier to H_2 heterolysis

To provide support to the assigned mechanism for chemical exchange, DFT calculations were employed to analyze the barrier to net H_2 heterolysis via the mechanism put forth in Fig. 5-7. Accordingly, complex **5.2** was first optimized computationally and compared to the

194

experimental crystal structure. Good agreement between experiment and theory was found using the B3LYP functional and the SDD basis set for iridium and 6-31g(d,p) basis set for all other atoms. The DFT structure of **5.2** is presented in Fig. 5-10, along with the experimental crystal structure. In the DFT structure, the Ir-P distances are 2.397 and 2.416 Å, whereas the Ir-P distances determined by X-ray crystallography are slightly shorter at 2.303(2) and 2.296(2) Å. In the DFT-calculated structure, the Ir-H distances are 1.599 and 1.678 Å , the longer of the two distances being the hydride engaged in a dihydrogen bond (d_{HH} = 1.61 Å). For the Ir-C bond, DFT predicts a distance of 2.115 Å, whereas the experimentally determined value was observed to be 2.087(8) Å.
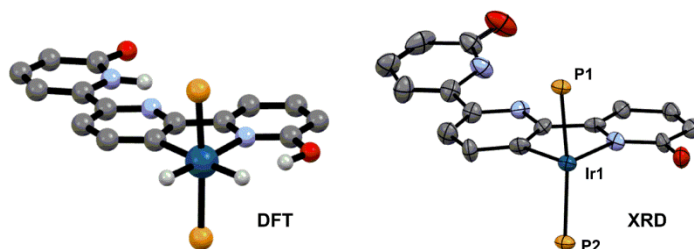
Figure 5-10. Comparison of the DFT-calculated structure of 5.2 and the solid state structure of 5.2 determined by X-ray crystallography.

From this initial starting geometry, a potential energy surface scan was performed in which the separation between the hydride and OH proton was incrementally shortened. This treatment provided an approximation of the barrier for H_2 heterolysis of 13.8 kcal/mol. Note that optimizations of the transition state and resulting iridium-dihydrogen adduct were not performed and this value is therefore an approximation. There is strong agreement between the computationally predicted barrier and the experimentally determined value ($\Delta\Delta G^{\ddagger}$ < 1 kcal/mol), suggesting that the experimentally observed barrier is indeed the barrier to forming an iridium-dihydrogen adduct. The mechanism for exchange, therefore, can be considered to proceed

through three steps as depicted in Fig 5-11. First, proton transfer to the iridium hydride takes place to provide an iridium-dihydrogen adduct. This step is the most energetically costly and therefore rate limiting. According to preliminary computational results, the iridium-dihydrogen adduct is a high energy intermediate. Presumably, rotation of the dihydrogen ligand has a minimal energy barrier (< 3 kcal/mol), as has been determined for other metal-dihydrogen adducts, and therefore rotation is considered to be fast compared to proton transfer.[10] Upon rotation, proton transfer from the dihydrogen adduct provides the exchanged product.
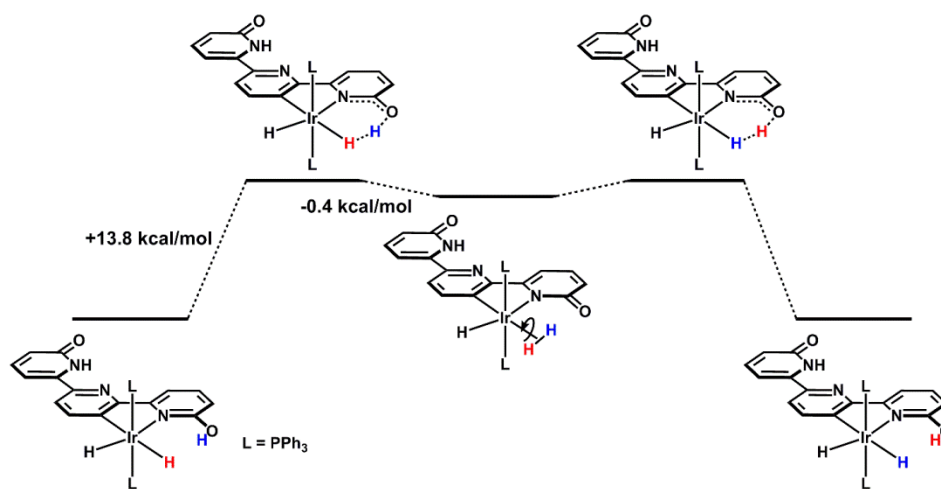
Figure 5-11. DFT-calculated H$_2$ heterolysis and exchange pathway in complex 5.2.

5.3 Effect of remote functionalization on H$_2$ heterolysis rate

Computational studies on Fe-hydrogenase have revealed that electronic perturbations to the iron center have significant consequences on the thermodynamics of the elementary reaction steps during catalysis (i.e. H$_2$ splitting and transfer; see section 1.1). Additionally, Crabtree and Eisenstein have described iridium hydride/dihydrogen complexes whose equilibria are highly sensitive to the electronic parameters of the supporting ligands (*vide supra*). The pendent functionality of complex **5.2**, therefore, is appropriately suited to quantitatively study how remote electronic perturbations to the dhtp ligand affect H$_2$ heterolysis. Specifically,

196

coordination of Lewis acids with varying acidities in the secondary coordination sphere should provide an ideal platform where the primary coordination sphere of the iridium complex is unchanged. In this manner, electronic perturbations are decoupled from local changes in metal geometry.
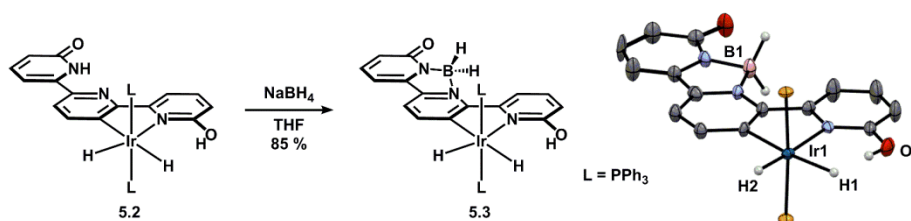
Figure 5-12. Synthesis and solid state structure of 5.3. (30% ellipsoids; solvent, PR$_3$ C atoms and non-hydride H atoms not involved in hydrogen bonding omitted)

Given the steric constraints imposed by the PPh$_3$ ligands, small Lewis acids were attractive to coordinate to the pendent bipyridine-like fragment. Moreover, similarities between the pendent functionality and the well-known BODIPY compounds[12] provided further impetus to study group 15 Lewis acids which would yield a coordinated Lewis acid in a tetrahedral geometry. Initially, a borane adduct was targeted by allowing complex **5.2** to react with NaBH$_4$. Gratifyingly, complex **5.3** was isolated from the reaction mixture and characterized by NMR spectroscopy and X-ray crystallography (Fig. 5-12). The ^{1}H NMR spectrum of **5.3** in CD$_2$Cl$_2$ solvent at room temperature does not contain any resonances corresponding to protic NH or OH groups. Additionally, ^{11}B NMR spectroscopy shows a broad resonance at -2.8 ppm. When a sample of **5.3** was cooled below room temperature, a new protic resonance could be observed in addition to a new hydride resonance; akin to complex **5.3**. The solid state structure of **5.3** reveals the expected coordination mode of the BH$_2$ fragment to the pendent bipyridone fragment: B-N distances 1.594 and 1.542 Å. The structure also reveals the elongation of the Ir-H bond due to the presence of dihydrogen bonding (*ca.* 1.9 vs. 1.4 Å), as predicted by DFT for complex **5.2**.
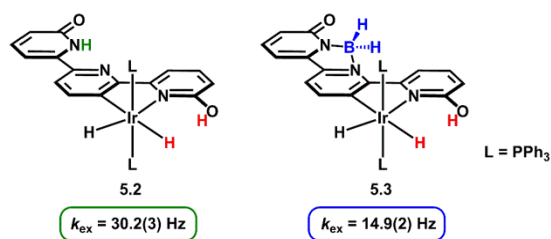
Figure 5-13. Comparison of H₂ exchange rates for complex 5.2 and 5.3 at 238 K.

Using EXSY NMR spectroscopy, the rate of H_2 heterolysis by complex **5.3** was measured.
At 238 K, this rate is 14.9(2) Hz. The rate of H_2 heterolysis in complex **5.3** is approximately half
that of complex **5.2** (Fig. 5-13). This finding is somewhat unsurprising given the "BH_2^+"
fragment should be a considerably weaker Lewis acid than H^+. Regardless, this result confirms
our hypothesis that the rate of H^+/H^- interconversion can be effectively tuned *via* a remote
modification to the seoncdary coordination sphere. More potent Lewis acids able to bind the
pendent bipyridine fragment are therefore expected to impart a substantial increase in exchange
rate. The modifiable exchange rates observed for complexes **5.2** and **5.3**, and related future
complexes, should therefore be an ideal, direct indicator for catalytic competency in reactions
involving rate-limiting bond heterolysis.

5.4 Assessing the catalytic competence of complex 5.2

The ability of complex **5.2**, and its derivatives, to rapidly promote H^+/H^- interconversion led
to the investigation of these complexes to act as catalysts for transformations requiring
heterolytic bond cleavage events. Catalytic cycles for (de)hydrogenation, hydrosilylation and
hydroboration schemes often have rate-limiting steps associated with cleavage of the E-H bond
(E = H for hydrogenation, SiR_3 for hydrosilylation and BR_2 for hydroboration). Given that the
iridium complexes described in this chapter have variable rates for net H_2 heterolysis, it seemed
plausible that the rate of catalysis for a given transformation could be systematically changed

based on the secondary coordination sphere environment. In addition, the rate of H^+/H^- exchange was anticipated to be an indicator of catalytic efficiency: the highest rate of exchange corresponding to the highest rate of catalysis.

To test the above hypotheses, complex **5.2** was examined as a catalyst for a small handful of transformations. Reactions screened to date have included dehydrogenation, hydrogenation, hydrosilylation and H/D exchange (Fig. 5-14A). Unfortunately, complex **5.2** has not been found to be a catalyst for these transformations under conditions tested to date. Higher temperatures are likely required to utilize complex **5.2** as a catalyst for reactions not involving transfer of H_2. Presumably, H_2 liberation from a transient iridium-dihydrogen adduct (Fig. 5-14B) must be highly endothermic and suggests a reactive intermediate capable of either E-H heterolysis or substrate dehydrogenation is not accessible under the reaction conditions examined.
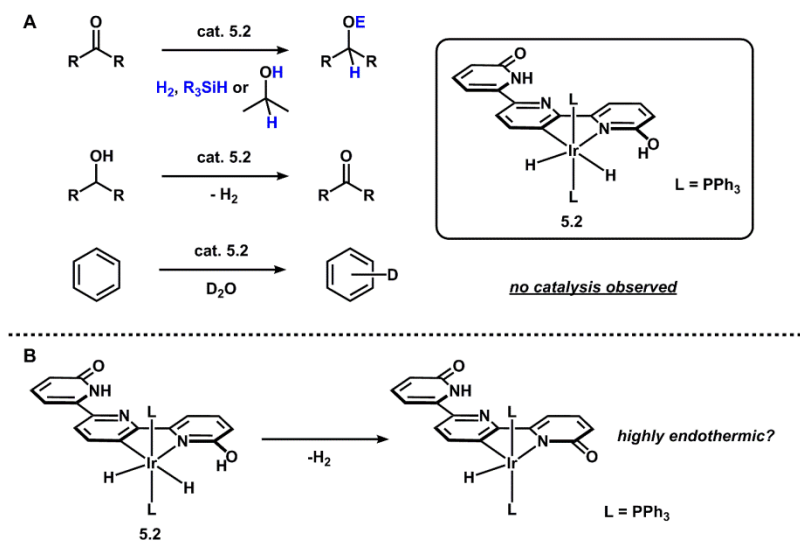

Figure 5-14. General catalytic reactions attempted with complex 5.2 (A) and a potential explanation for a lack of reactivity in complex 5.2 (B).

5.5 Experimental section for Chapter 5

All commercially-available reagents were used as received without further purification. IrH$_5$(PPh$_3$)$_2$ was synthesized as previously described.[13] All manipulations were carried out under a purified atmosphere of nitrogen using standard Schlenk techniques or in an MBraun Lab Master 130 or Innovative Technologies Pure LabHE GP-1 glovebox, unless otherwise stated. NMR spectra were recorded on either a Varian MR400 or a Varian vnmrs 500 spectrometer and are referenced to residual solvent peaks.

Ir(H)$_2$(dhtp')(PPh$_3$)$_2$ (5.2)

Benzene (10 mL) was added to dhtp (28 mg; 0.11 mmol) and IrH$_5$(PPh$_3$)$_2$ (73 mg; 0.10 mmol) in Schlenk tube and sealed. The tube was heated to 80 °C and stirred. After 14 hours, the tube was allowed to cool, and the reaction mixture was diluted with diethyl ether (10 mL). The solids were collected on a sintered glass frit, washed with 1:1 benzene:diethyl ether, then diethyl ether and finally dried to give the title compound as a cream solid (75 mg; 76%). Crystals of **5.2** suitable for X-ray diffraction were grown from vapor diffusion of diethyl ether into a dichloromethane solution of **5.2**. ^{1}H NMR, 500 MHz (CD$_2$Cl$_2$, 238 K): 10.62 (s, 1 H), 9.93 (br s, 1 H), 7.78 (d, J = 6.5, 1 H), 7.42 (m, 13 H), 7.10-7.42 (m, 20 H), 6.92 (d, J = 8, 1 H), 6.60 (d, J = 7, 1 H), 6.41 (d, J = 8.5, 1 H), 6.09 (d, J = 7.5, 1 H), -11.43 (br s, 1 H), -17.41 (t, J = 15.5, 1 H). ^{31}P{^{1}H} NMR, 162 MHz (CD$_2$Cl$_2$, 298 K): 19.3.

Ir(H)$_2$(dhtp-BH$_2$)(PPh$_3$)$_2$ (5.3)

Tetrahydrofuran (ca. 3 mL) was added to **5.2** (6.1 mg; 0.0062 mmol) and stirred to provide a white suspension. To the stirring suspension, NaBH$_4$ (81 µL of 0.08 M solution in dimethoxyethane; 0.0065 mmol) was added, resulting in a color change to bright yellow. After 14 hours, the reaction mixture was filtered and concentrated to dryness to provide the title

compound as a yellow solid (5.3 mg; 85%). The compound was used without further purification. Crystals of **5.3** suitable for X-ray diffraction were grown from vapor diffusion of diethyl ether into a dichloromethane solution of **5.3**. ^{1}H NMR, 500 MHz (CD$_2$Cl$_2$, 238 K): 10.40 (app. d, J = 9, 1 H), 8.18 (d, J = 7.5, 1 H), 7.81 (d, J = 7.5, 1 H), 7.41 (m, 12 H), 7.15-7.26 (m, 20 H), 7.08 (d, J = 7.5, 1 H), 6.70 (d, J = 7, 1 H), 6.44 (d, J = 8.5, 1 H), 6.29 (d, J = 8, 1 H), 3.8 (br s, 2 H), -11.37 (app. d, J = 12.5, 1 H), -16.93 (t, J = 15.5, 1 H). ^{31}P{^{1}H} NMR, 162 MHz (CD$_2$Cl$_2$, 298 K): 19.4. ^{11}B NMR, 128 MHz (CD$_2$Cl$_2$, 298 K): -3.5 (br s).

Exchange measurements by ^{1}H NMR spectroscopy[11]

To measure the exchange rate of the two H nuclei in complexes **5.2** and **5.3**, the following procedure was followed. Prior to performing saturation transfer experiments, the T_1 value of the exchanging resonances were determined at each temperature point. These values were used to determine the necessary saturation pulse width to completely suppress the hydride resonance (5 x T_1). To perform the saturation transfer, a standard PRESAT experiment in vnmrj was used. The preacquisition delay (d1) was modified for each experiment such that the sum of the preacquisition delay and saturation pulse width was a constant 2 seconds throughout the temperature range (d1 + saturation = 2 s). Each PRESAT experiment was performed in triplicate at each temperature point to provide error estimation. Integration against the NH signal provided an internal standard for measuring the extent of exchange (M/M_0). The data were fit to eq. 5-1 to yield rate information at each temperature.

Attempted [i]PrOH acceptorless dehydrogenation promoted by 5.2

In a J. Young NMR tube, complex **5.2** (1.4 mg; 0.0014 mmol) and [i]PrOH (20 μL; 0.26 mmol) were dissolved in C$_6$D$_6$ (0.7 mL). The tube was sealed and heated in an 80 °C oil bath overnight. A ^{1}H NMR spectrum recorded the following day showed ~0.1% conversion of [i]PrOH to acetone.

Attempted hydrosilylation of acetophenone promoted by 5.2

In a J. Young NMR tube, complex **5.2** (1.5 mg; 0.0015 mmol), acetophenone (16 μL; 0.14 mmol) and Et_3SiH (24 μL; 0.15 mmol) were dissolved in C_6D_6 (0.6 mL). The tube was sealed and heated in an 80 °C oil bath overnight. A ^1H NMR spectrum recorded the following day showed no conversion of the starting acetophenone.

Attempted transfer hydrogenation of acetophenone promoted by 5.2

In a J. Young NMR tube, complex **5.2** (4.7 mg; 0.0048 mmol) was suspended in ^iPrOH (0.6 mL) and acetophenone (16 μL; 0.14 mmol) was added. The tube was sealed and heated in an 80 °C oil bath overnight. A ^1H NMR spectrum recorded the following day showed less than 1% conversion of the starting acetophenone.

Attempted H/D exchange of benzene promoted by 5.2

In a thick-walled Schlenk tube, complex **5.2** (4.4 mg; 0.0045 mmol) was dissolved in C_6D_6 (2.0 mL; 23 mmol) and H_2O (75 μL; 4.2 mmol) was added. The tube was sealed and heated in a 150 °C oil bath overnight. Upon cooling the following day, an aliquot (0.5 mL) was removed for NMR analysis and 1,4-dioxane (10 μL; used as an internal standard) was added to the aliquot. The ^1H NMR spectrum recorded showed no increase of the residual proteo-benzene resonance compared to the starting C_6D_6 sample.

Computational details

All calculations were performed using Gaussian 09[14] and visualized using GaussView 5.0.[15] Becke's three-parameter hybrid function using Lee, Yang and Parr's correlation function (B3LYP)[16] was used for all calculations. The SDD basis set[17] was used for Ir atoms and 6-31g(d,p)[18] was used for all other atoms. Structures were freely optimized in C_1 symmetry and

were confirmed to be minima based on the absence of imaginary frequencies in the calculated vibrational spectra.

5.6 References

1. Hartwig, J. F. *Organotransition Metal Chemistry: From Bonding to Catalysis* University Science Books: Sausalito, 2010.

2. Park, S.; Ramachandran, R.; Lough, A. J.; Morris, R. H. *J. Chem. Soc., Chem. Commun.* **1994**, 2201.

3. Park, S.; Lough, A. J.; Morris, R. H. *Inorg. Chem.* **1996**, *35*, 3001.

4. Xu, W.; Lough, A. J.; Morris, R. H. *Inorg. Chem.* **1996**, *35*, 1549.

5. Lee, J. C., Jr.; Rheingold, A. L.; Muller, B.; Pregosin, P. S.; Crabtree, R. H. *J. Chem. Soc., Chem. Commun.* **1994**, 1021.

6. Lee, J. C., Jr.; Peris, E.; Rheingold, A. L.; Crabtree, R. H. *J. Am. Chem. Soc.* **1994**, *116*, 11014.

7. Peris, E.; Lee, J. C., Jr.; Rambo, J. R.; Eisenstein, O.; Crabtree, R. H. *J. Am. Chem. Soc.* **1995**, *117*, 3485.

8. Lee, D.-H.; Patel, B. P.; Clot, E.; Eisenstein, O.; Crabtree, R. H. *Chem. Commun.* **1999**, 297.

9. Crabtree, R. H. *Acc. Chem. Res.* **1990**, *23*, 95.

10. Kubas, G. J. *Chem. Rev.* **2007**, *107*, 4152.

11. Jarek, R. L.; Flesher, R. J.; Shin, S. K. *J. Chem. Educ.* **1997**, *74*, 978.

12. Loudet, A.; Burgess, K. *Chem. Rev.* **2007**, *107*, 4891.

13. Crabtree, R. H.; Felkin, H.; Morris, G. E. *J. Organomet. Chem.* **1977**, *141*, 205.

14. Gaussian 09, Revision D.01, Frisch, M. J.; Trucks, G. W.; Schlegel, H. B.; Scuseria, G. E.; Robb, M. A.; Cheeseman, J. R.; Scalmani, G.; Barone, V.; Mennucci, B.; Petersson, G. A.; Nakatsuji, H.; Caricato, M.; Li, X.; Hratchian, H. P.; Izmaylov, A. F.; Bloino, J.; Zheng, G.; Sonnenberg, J. L.; Hada, M.; Ehara, M.; Toyota, K.; Fukuda, R.; Hasegawa, J.; Ishida, M.; Nakajima, T.; Honda, Y.; Kitao, O.; Nakai, H.; Vreven, T.; Montgomery, J. A., Jr.; Peralta, J. E.; Ogliaro, F.; Bearpark, M.; Heyd, J. J.; Brothers, E.; Kudin, K. N.; Staroverov, V. N.; Kobayashi, R.; Normand, J.; Raghavachari, K.; Rendell, A.; Burant, J. C.; Iyengar, S. S.; Tomasi, J.; Cossi, M.; Rega, N.; Millam, N. J.; Klene, M.; Knox, J. E.; Cross, J. B.; Bakken, V.; Adamo, C.; Jaramillo, J.; Gomperts, R.; Stratmann, R. E.; Yazyev, O.; Austin, A. J.; Cammi, R.; Pomelli, C.; Ochterski, J. W.; Martin, R. L.; Morokuma, K.; Zakrzewski, V. G.; Voth, G. A.; Salvador, P.; Dannenberg, J. J.; Dapprich, S.; Daniels, A. D.; Farkas, Ö.; Foresman, J. B.; Ortiz, J. V.; Cioslowski, J.; Fox, D. J. Gaussian, Inc., Wallingford CT, 2009.

15. GaussView, Version 5, Dennington, R.; Keith, T.; Millam, J. Semichem Inc., Shawnee Mission KS, 2009.

16. (a) A. D. Becke, *J. Chem. Phys.* **1993**, *98*, 5648; (b) C. Lee, W. Yang, R. G. Parr, *Phys. Rev. B: Condens. Matter* **1988**, *37*, 785.

17. Fuentealba, P.; Preuss, H.; Stoll, H.; Von Szentpály, L. *J. Phys. Chem.* **2009**, *113*, 6378.

18. Hehre, W. J.; Ditchfield, R.; Pople, J. A. *J. Chem. Phys*. **1972**, *56*, 2257.

Chapter 6 Summary and outlook

The following contributions have been published as a result of this thesis research:

Moore, C. M.; Szymczak, N. K. *Dalton Trans.* **2012**, *41*, 7886.

Moore, C. M.; Szymczak, N. K. *Chem. Commun.*, **2013**, *49*, 400.

Moore, C. M.; Szymczak, N. K. "Appended Functionality in Pincer Ligands" in *Pincer and Pincer-Type Complexes: Applications in Organic Synthesis and Catalysis*, Szabó, K. J.; Wendt, O. F. (eds.), Wiley-VCH: Weinheim, Germany, 2014, pp 117-147.

Moore, C. M.; Quist, D. A.; Kampf, J. W.; Szymczak, N. K. *Inorg. Chem.*, **2014**, *53*, 3278.

Moore, C. M.; Dahl, E. W.; Szymczak, N. K. *Curr. Opin. Chem. Biol.*, **2015**, *25*, 9.

Moore, C. M.; Szymczak, N. K. *Chem. Commun.*, **2015**, *51*, 5490.

Moore, C. M.; Szymczak, N. K. *Chem. Sci.*, **2015**, *6*, 3373.

Moore, C. M.; Bark, B.; Szymczak, N. K. *to be submitted*.

6.1 Summary

This thesis has demonstrated the utility of hydrogen bonding groups in the secondary coordination sphere of synthetic transition metal complexes to alter primary structure, bonding and reactivity. In Chapter 1, the current state of hydroxypyridine-derived catalysts was thoroughly described along with the motivation to emulate aspects of the metalloenzyme [Fe]-hydrogenase. Catalysts incorporating the 2-hydroxypyridine motif use the pendent pyridinoate groups to aid in H^+ and e^- transfer steps for catalytic hydrogenation, dehydrogenation and water oxidation. Barriers to H^+ transfer can be minimized with an appropriate orientation of the pyridinoate groups to circumvent Grotthuss-type H^+ transfer mechanisms, and thus, lower the entropic contributions to rate-determining steps in catalytic cycles. The principles described for hydrogenation/dehydrogenation will likely be adapted for hydrofunctionalization catalysis, or alternatively, many other reaction types that feature acidic/basic partners, as they may be cooperatively activated/transferred by 2-hydroxypyridine type units. Future frontiers in 2-hydroxypyridine-derived catalysis will involve the development of catalysts featuring earth-abundant metals, structurally-faithful model complexes that exhibit catalytic reactivity of the native enzyme, and the expansion of 2-hydroxypyridine ligands into other catalytic reactions. Moreover, the utility of pincer scaffolds in designing metal-ligand ensembles capable of cooperatively engaging metal-coordinated substrates *via* non-covalent interactions was described. Installed functionality can be directed collinear or orthogonal to a metal-coordinated substrate, and these distinct secondary structures can be targeted for substrate specificity within multifunctional architectures. Because of the potential coordinating ability of the introduced functionality, the selection of metalation conditions requires careful attention to limit multinuclear metal-ligand ensembles. Once metalated, appended functionality can serve to tune a

206

ligand's physical properties and/or promote proton/electron transfer, which may concomitantly modify a pincer's ligand field strength. The recent explosion in reports of cooperative ligand frameworks demonstrates a high interest in the area of metal-ligand multifunctionality, and because of their geometrical constraints as well as unique tunable reactivity, pincer-based ligands are poised to continue to emerge as premier platforms upon which further elaboration is possible to uncover new reactivity profiles for small molecule activation.

In Chapter 2, a tripodal ligand was presented which is capable of promoting hydrogen bonding interactions in the secondary coordination sphere, far removed from the metal center. As a confirmation of this design strategy, we demonstrated CH_3CN coordinated to copper(II) participates in CH–O interactions in the solid state and in solution. This is a powerful finding, given that the CH_3 group of CH_3CN is typically considered to be inert and a poor hydrogen bond donor. Moreover, the design of the ligand scaffold is perfectly suited to engage in hydrogen bonding interactions with groups greater than three atoms away from the metal center.

A proton-responsive tripodal ligand (H_3thpa) was described in Chapter 3 which can engage in hydrogen bonding interactions with atoms directly coordinated to the metal center. When fully protonated, the ligand presents three hydrogen bond donors to a metal-bound substrate. Our results demonstrated that the hydrogen bonds enforce 3-fold symmetry for Cu(I/II) halide complexes in the solution and solid state, and significantly stabilize the Cu-Cl bond in the case of copper(I) chloride. Additionally, our calculations along with vibrational data showed that the strength of the H-bonding interactions between the Cu-Cl and OH groups of H_3thpa are significantly influenced by the oxidation state of copper. These concepts were utilized to stabilize an otherwise highly reactive copper(I) fluoride complex. Chemical reduction of a copper(II) fluoride complex supported by the H_3thpa resulted in the partial dissociation of a F^-

ligand from copper. The resulting copper(I) complex was characterized as containing an outer sphere fluoride anion 'captured' by hydrogen bonds. Notably, the absence of the OH groups resulted in the inability to isolate stable copper(I) fluoride adducts. Apart from demonstrating ground state stabilization of reactive units noted above, the copper(I) fluoride adduct can be used to study H^+ and e^- transfer reactivity. We demonstrated nitrite reduction by a copper complex featuring the H_3thpa ligand. The formation of NO was confirmed by gas-phase IR spectroscopy, isotope labeling, and trapping experiments. DFT calculations predicted that nitrite binds in an η^1-κO fashion to the copper center prior to reduction *via* a H^+/e^- transfer. This reaction, facilitated by the secondary sphere environment, is remiscent to the crucial role of hydrogen bonding residues near the active site of CuNiR, which serve to position nitrite and facilitate electron transfer. This is, to our knowledge, the first synthetic copper system to reduce nitrite in such a fashion.

Chapter 4 highlights a rigid pincer ligand (dhtp) with pendent OH groups which can be utilized for H^+/H^- transfer reactivity. The dhtp scaffold promotes directed interactions with metal-bound substrates, such as halides. Ruthenium(II) complexes efficiently catalyze the transfer hydrogenation of a variety of ketones in the presence of base in 2-propanol. High chemoselectivity was realized in the presence of substituted alkenes. A catalytic cycle for this transformation may involve an outer sphere transfer of hydride with the assistance of substrate coordination to an alkali metal through cooperation of the pendent pyridinoate functionality. Control experiments were performed to demonstrate the necessity of the OH groups for high activity. Additionally, complexes supported by the fully deprotonated form, dhtp'', were shown to be π-bases and bind H_2 reversibly and CO irreversibly.

In Chapter 5, iridium-hydride complexes supported by the cyclometalated dhtp were described. These complexes were shown to rapidly equilibrate H^+/H^- equivalents; effectively considered as H_2 heterolysis. By altering the secondary coordination sphere by coordination of remote Lewis acids, the heterolysis rate can be finely tuned. Although the iridium center is abiological, this finding is reminiscent of DFT results for [Fe]-hydrogenase where the identity of ligands directly coordinated to iron have a dramatic effect on the thermodynamic landscape of H_2 cleavage and transfer. Tuning H_2 heterolysis rates is proposed to be a key indicator for catalytic competency in reactions requiring H-E bond heterolysis.

6.2 Future outlook

The following discussion is a thought experiment where one would consider how hydrogen bonding, or non-covalent interactions in general, at a metal center might be beneficial to promoting either a stoichiometric or catalytic reaction.
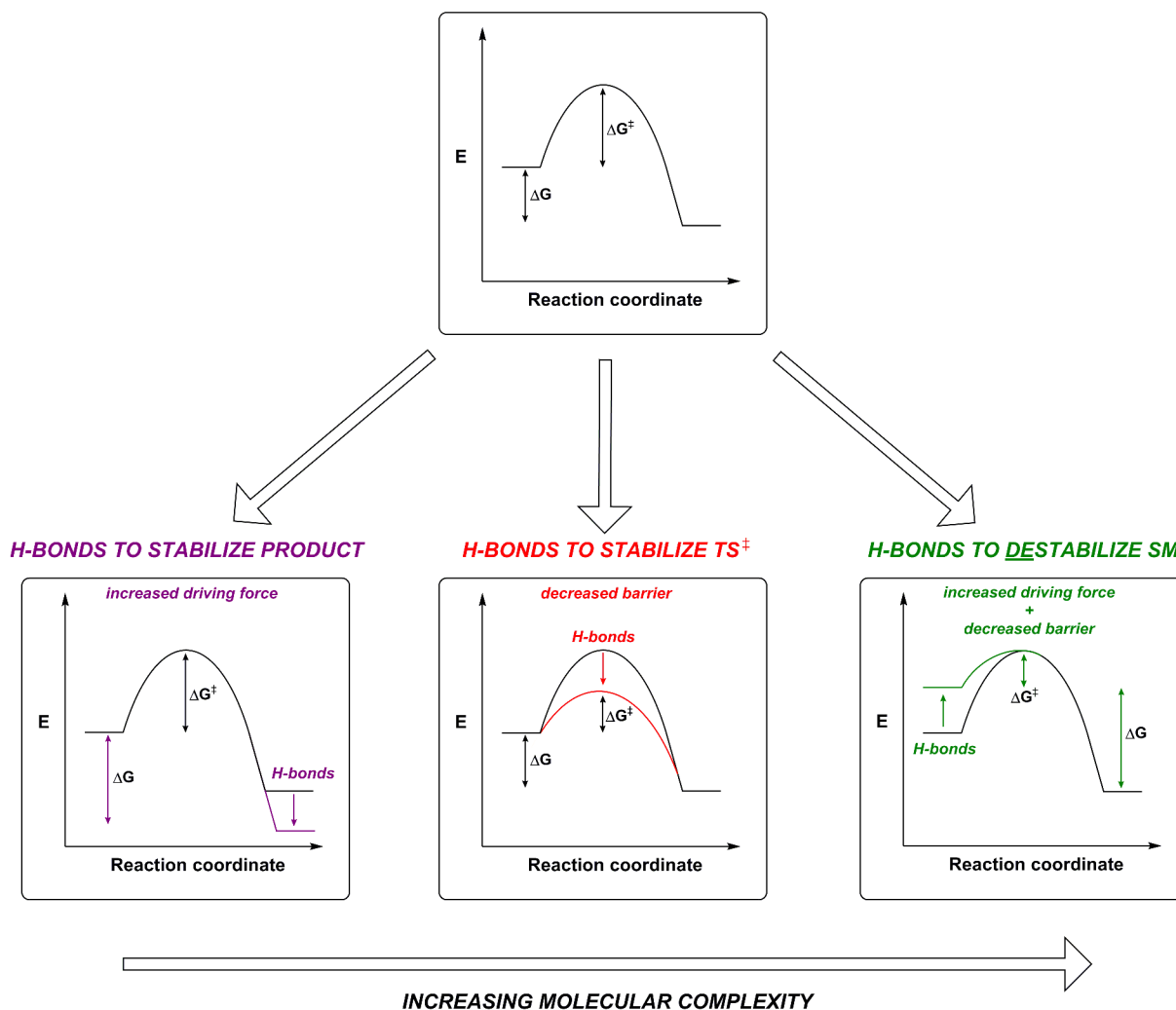
Figure 6-1. Effect of hydrogen bonding on the energy landscape of a hypothetical reaction.
If one were to consider a general reaction coordinate for a simple exothermic reaction such as A
+ B → C, (where A, B, or C may be coordinated to a metal center supported by a ligand
ensemble capable of forming hydrogen bonds), the effects of engineered hydrogen bonding on
the energies of elementary reaction components in three limiting scenarios can be explored (Fig.
6-1).

We should first consider the event where hydrogen bonds are present which stabilize the
product of the reaction, C. In this case, one would envision that a ligand ensemble has been

designed to stabilize product C through hydrogen bonds. The net result of this approach would be to increase the thermodynamic driving force (ΔG) for the given reaction, since product C now has a lower energy due to hydrogen bonding. This approach may be advantageous when considering a stoichiometric reaction at a metal center since the terminal metal-containing product might be of interest. In fact, this approach was demonstrated by the isolation of complex **3.4** in Chapter 3, where the hydrogen bonding groups stabilized a fluoride anion that would otherwise be un-isolable. In the case of a catalytic reaction however, this approach may not be useful given the stability imparted to the product; which may now become a thermodynamic sink in a catalytic cycle.

This scenario changes if we instead examine the case where hydrogen bonds are used to stabilize the transition state of the reaction. In this way, one could imagine a ligand architecture that has been synthesized which engages in interactions with a high-energy intermediate structure: for example, a tetrahedral intermediate formed upon nucleophilic attack at a carbonyl group. This tactic is widely seen in enzyme active sites, where tetrahedral intermediate mimics have been used to isolate and characterize these species. The overall effect of this approach is lower the activation energy ($\Delta G^{\ddagger}$) of the reaction, much the same way that any catalyst functions to lower the barrier to a given chemical transformation. This approach was demonstrated in both Chapters 3 and 4, where hydrogen bonding in complex **3.4** facilitated the rapid reduction of nitrite to nitric oxide and non-covalent interactions in complex **4.6-h** facilitated hydride delivery to ketone substrates, respectively. This general strategy can be effectively applied to studying both stoichiometric and catalytic transformations.

A different, and final approach would be to target interactions with the starting reagents (either A or B) of the reaction. Instead of engineering hydrogen bonding interactions which

would stabilize these species (effectively increasing $\Delta G^{\ddagger}$ and lowering ΔG, thus prohibiting the desired reaction), one could envision *de*stabilizing either species. The effect of this strategy would be to both increase driving force (ΔG) and lower activation energy ($\Delta G^{\ddagger}$). At the outset, this strategy seems unlikely to be achieved, given that hydrogen bonds usually stabilize reactive species. However, one could envision a system in which the metal center has been constrained (via non-covalent secondary coordination sphere interactions) to adopt an unusual coordination geometry and reactive electronic configuration. This, in principle, was demonstrated in Chapter 2 where hydrogen bonding interactions in complex **2.1** influenced the primary coordination geometry. Although the coordination geometry was not unusual (trigonal bipyramidal is common for copper(II) complexes), the strategy is nonetheless validated.

These general principles have been outlined from lowest to highest degree of molecular complexity and specificity. Therefore, as one moves from targeting non-covalent interactions with ground states to excited state intermediate structures, the design required to achieve the intended function is inherently more complex and specific. This is amplified when designing complexes that will destabilize ground states, and the architectures employed to achieve this type of destabilization will likely be of singular use. Exploiting ligand design and hydrogen bonding interactions to generate reactive metal centers *via* ground state destabilization is currently a focus of ongoing work in our laboratory.